CHARGE TRANSPORT IN PROXIMITIZED GRAPHENE

WITHIN VAN DER WAALS HETEROSTRUCTURES

Thèse Nº

Présentée le [date of public defense]

Faculté des Sciences de Base
Laboratoire SuperScience
Programme doctoral en SuperScience

pour l'obtention du grade de Docteur ès sciences

par

Katharina Polyudov

Acceptée sur proposition du jury

Prof. Professeur Mila Frédéric, président du jury
Prof. Kern Klaus, directeur de thèse
Prof. Yazyev Oleg, rapporteur interne
Prof. Maultzsch Janina, rapporteuse externe
Prof. Balasubramanian Kannan, rapporteur externe

Lausanne, EPFL, 2020

EPFL

Problem talk creates problems,
Solution talk creates solutions.
- Steve de Shazer

Acknowledgements

I am very grateful to my thesis advisor **Prof. Klaus Kern** for giving me the opportunity to complete my PhD thesis in the Nanoscale Science Department and for his continuous support during this time.

I would like to thank **Dr. Marko Burghard** for supervising my thesis, for the constant support and the numerous discussions troughout the years.

Thanks to **Prof. Alexander Holleitner** and **Dr. Christoph Kastl** for the great collaboration and the support received from the group at the WSI. I am particularly grateful to **Jonas Kiemle** for the nice and productive time spent together in the labs and for helping out with the measurements.

I thank the Nanostructuring Lab team **Thomas**, **Ulli**, **Marion** and **Achim** for the support in sample fabrication as well as the low temperature service and our technicians **Isabel**, **Marko**, **Wolfgang**, **Peter**, **Mr. Chaikevitch** and **Mr. Siemers** for their help.

Many thanks to the former colleagues **Kristina** and **Roberto** who have introduced me to all the equipment and who are still helping out with any questions and concerns. Thanks to the Quantum Materials subgroup colleagues **Junhong**, **Loc**, **Alessio**, **Karla** and **Lukas** for the nice atmosphere in the labs and the fun lunch and coffee breaks. I am especially thankful to **Soudabeh** for the great collaboration and her scientific input and support.

I want to thank my friends and world's best office mates **Andreas**, **Piotr** and **Patrick**. Thanks for all the fun and nice times in the office, at conferences and also on our movie and karaoke nights.

I am thankful to all former and current members of the **Nanoscale Science Department** for the good times and nice conversations.

I want to thank all my friends and especially **Britta**, **Kathrin**, **Alisa**, **Robin**, **Dana**, **Tabea**, **Magdalena**, **Olga**, **Xenia** and the '**Nanos**' for being a source of strength, motivation and support in so many ways. Special thanks to the best friend in the world, **Katrin**, without you this thesis wouldn't have become reality.

Last, but not least I am thankful to every member of my **family** scattered around the globe for their endless love and moral support!

Abstract

Since their discovery, graphene and other 2D materials have become a subject of intense research in condensed matter physics. Especially the vast possibilities of combining those materials into heterostructures are promising for the discovery of novel physical phenomena. The heterostructures accessible through state-of-the-art techniques have suitably clean interfaces between the layers.

Graphene has gained a lot of attention due to its remarkable mechanical stability and extremely high electron mobility. However, the zero bandgap of graphene is a major bottleneck for implementing this 2D material into most electronic applications. The ability to tune the properties of graphene by proximity effects has shifted the focus of graphene research towards the combination of graphene with other van der Waals materials. The main objective of the present thesis was to explore for two different types of graphene-based van der Waals heterostructure whether fingerprints of electronic proximity effects can be traced in their low temperature magnetotransport properties.

The first part of the thesis deals with heterostructures of graphene and Bi_2Te_2Se (BTS). The strong spin-orbit coupling of BTS makes it a three-dimensional topological insulator with topological surface states which are protected by time-reversal symmetry. At the same time, BTS is promising to exert a pronounced spin-orbit proximity effect on graphene, and thereby to open a band gap and/or introduce a spin texture in the latter. The graphene/BTS heterostructures were fabricated by the direct growth of BTS on graphene to ensure a clean interface between both materials and correspondingly a good electronic coupling between them. Analysis of the weak localization effect observed in the magnetoconductivity revealed the presence of enhanced SOC in the proximitized graphene.

The second part of the thesis focuses on heterostructures wherein graphene is combined with α-RuCl$_3$ which has recently gained a lot of attention as a potential quantum spin liquid system. Previous studies on graphene/α-RuCl$_3$ heterostructures found an unusual temperature evolution of the quantum oscillation amplitude, whose origin remained unclear. The magnetotransport data collected in this thesis point toward two possible origins for this behavior, namely spin fluctuations associated with the magnetic transition into an antiferromagnetic phase at the Néel temperature of approximately 7 K, and the hybridization-induced formation of heavy (flat) bands, both of which are likely to depend on the α-RuCl$_3$ layer thickness. In addition, heterostructures comprising an α-RuCl$_3$ monolayer were found to display an unusual gate dependence of the quantum oscillations, further corroborating the importance of the α-RuCl$_3$ thickness.

Keywords

graphene, van der Waals heterostructures, topological insulators, α-RuCl$_3$, proximity effects, magnetotransport

Zusammenfassung

Seit ihrer Entdeckung sind Graphen und andere 2D-Materialien Gegenstand intensiver Forschung in der Festkörperphysik geworden. Insbesondere die zahllosen Möglichkeiten, diese Materialien in Heterostrukturen zu integrieren, sind vielversprechend für die Entdeckung neuer physikalischer Phänomene. Modernste Techniken ermöglichen die Fabrikation von Heterostrukturen mit ausreichend sauberen Grenzflächen zwischen den Schichten.

Graphen hat aufgrund seiner bemerkenswerten mechanischen Stabilität und der extrem hohen Elektronenmobilität viel Aufmerksamkeit erlangt. Die fehlende Bandlücke in Graphen stellt jedoch eine große Hürde für die Implementierung dieses 2D-Materials in wichtige elektronische Anwendungen dar. Die Möglichkeit, die Eigenschaften von Graphen durch Proximity-Effekte zu beeinflussen, hat den Schwerpunkt der Graphenforschung auf die Kombination von Graphen mit anderen Van-der-Waals-Materialien verlagert. Das Ziel der vorliegenden Arbeit war es, zwei unterschiedliche Arten von van-der-Waals-Heterostrukturen auf Graphenbasis zu untersuchen und Anzeichen für elektronische Proximity-Effekte aus deren Magnetotransporteigenschaften bei tiefer Temperatur zu ermitteln.

Der erste Teil der Arbeit befasst sich mit Heterostrukturen bestehend aus Graphen und Bi_2Te_2Se (BTS). Die starke Spin-Bahn-Kopplung in BTS macht es zu einem dreidimensionalen topologischen Isolator mit topologischen Oberflächenzuständen, die durch die Zeitumkehrsymmetrie geschützt sind. Dies macht BTS zugleich vielversprechend, um einen ausgeprägten Spin-Bahn-Kopplungs Proximity-Effekt auf Graphen auszuüben und dadurch eine Bandlücke zu öffnen und/oder eine Spintextur aufzuprägen. Die Graphen/BTS-Heterostrukturen wurden durch direktes Wachstum von BTS auf Graphen hergestellt, um eine saubere Grenzfläche zwischen beiden Materialien und dementsprechend auch eine gute elektronische Kopplung zwischen ihnen zu gewährleisten. Die Auswertung der schwachen Lokalisierung, die im Magnetwiderstand beobachtet wurde, deutet auf eine erhöhte Spin-Bahn-Kopplung im Graphen hin.

Der zweite Teil der Arbeit befasst sich mit Heterostrukturen, in welchen Graphen mit α-$RuCl_3$ kombiniert ist, wovon letzteres jüngst als potenzielles Quanten- Spinflüssigkeitssystem große Beachtung gefunden hat. In früheren Studien an Graphen/α-$RuCl_3$-Heterostrukturen wurde eine ungewöhnliche Temperaturabhängigkeit der Quantenoszillationsamplituden beobachtet, deren Ursprung unklar blieb. Die in dieser Arbeit gesammelten Magnetotransportdaten weisen auf zwei mögliche Ursachen für diese Abhängigkeit hin, nämlich Spinfluktuationen, die mit dem magnetischen Übergang in eine antiferromagnetische Phase einhergehen (bei einer Néel-Temperatur von ungefähr 7 K) und die Ausbildung schwerer (flacher) Bänder aufgrund elektronischer Hybridisierung. Beide Ursachen sind aller Voraussicht nach von der Schichtdicke des α-$RuCl_3$ abhängig. Außerdem wurde festgestellt, dass Heterostrukturen mit einer α-$RuCl_3$ Monolage eine ungewöhnliche Gate-Abhängigkeit der Quantenoszillationen aufweisen, was die Relevanz der α-$RuCl_3$-Dicke weiter bekräftigt.

Stichwörter

Graphen, van der Waals Heterostrukturen, Topological Isolatoren, α-RuCl$_3$, Proximity effekte, Magnetotransport

Contents

List of Figures

List of Equations

Chapter 1   Introduction

Two-dimensional (2D) van der Waals (vdW) materials have an extended crystalline planar structure held together by strong in-plane covalent bonds and weak out-of-plane van der Waals forces. As a consequence, individual layers can easily be removed by breaking the vdW bonds, accompanied by only little damage either to the extracted layer or the remaining structure. A well-known example is the use of adhesive tape to peel away layers of graphene from bulk graphite. This makes it straightforward to transfer layered materials to any type of substrate for further investigations. While graphene has attracted particularly strong interest owing to its unique band structure and exceptionally high carrier mobility, it is not the best 2D material for every application. In particular, its zero bandgap makes it difficult to use as a semiconductor. Fortunately, the family of 2D materials has grown significantly since the first isolation of graphene [1]. In the meanwhile, this family spans the entire spectrum of electronic properties, as illustrated in Figure 1:1. Within this family, hexagonal boron nitride (h-BN) is an insulator with a bandgap above 5 eV, and the transition-metal dichalcogenides (TMDs) include semiconductors with bandgaps between 0.5 and 3 eV. As documented by a vast amount of research performed during the past ten years, 2D materials enable to explore intriguing new physics in reduced dimensions and to engineer new ultrathin devices [2].
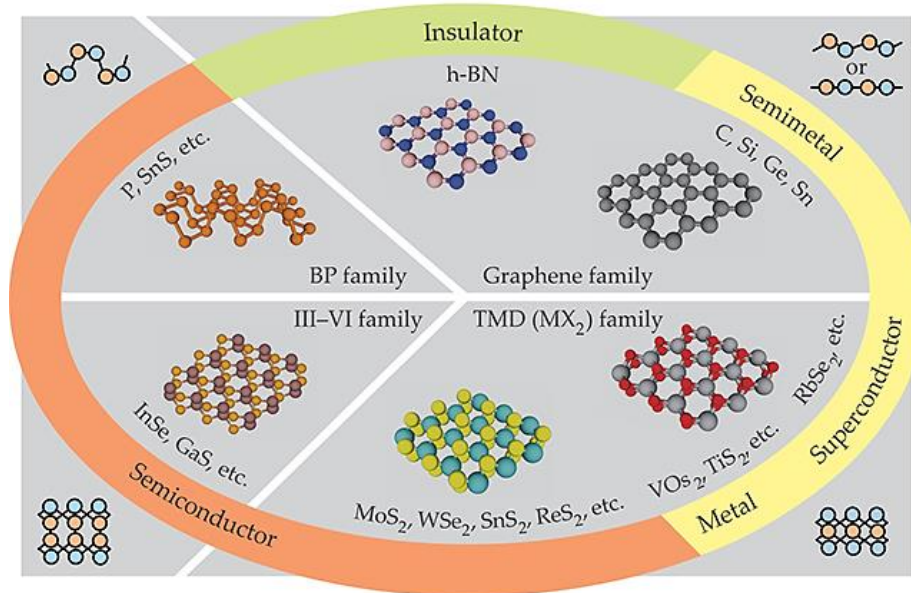
Figure 1:1 The fascinating world of 2D materials comprises graphene and its analogues (e.g., hexagonal boron nitride), the III-VI family of semiconductors, black phosphorus (BP) and its analogues, as well as the transition metal dichalcogenides (TMDs). As indicated by the four corners in the diagram, most of the materials' cross-sectional structures are not strictly planar. Reproduced from [3], with the permission of the American Institute of Physics.

Upon reducing the dimensionality of a system exceptional optical, electronic and magnetic properties often emerge, since the reduction of diminished screening or available phase space can lead to enhanced correlations and quantum effects. With the introduction of quasi-relativistic particles near the corners of the Brillouin zone the quantum mechanical description of graphene's electronic band structure is simplified (see Figure 1:2(a)). At the Brillouin-zone corners (K and K'), where the valence and conduction bands meet in conical valleys, there is a linear dependence of energy on momentum. This relationship is reminiscent of massless particles which are traveling at the speed of light. Hence, graphene's quasiparticles move like electrons which have lost their mass, with the exception that the speed of light is replaced by the approximately three hundred times smaller Fermi velocity. Moreover, graphene's quasiparticles have a pseudo-spin degree of freedom, describing the wave function symmetry on its two triangular sublattices. Accordingly, depending on whether the quasiparticle sits in a K or K' valley, the pseudo-spin is either antiparallel or parallel to the momentum. This chiral nature of charge carriers is responsible for various unusual electronic properties, including the half-integer shift in the quantum Hall effect. Moreover, graphene was also the first system where a nontrivial Berry phase could be detected experimentally, which establishes a connection to the later discovered topological insulators. In bilayer graphene, two graphene layers are stacked together into a staggered honeycomb lattice (see Figure 1:2(b), as a consequence of which the energy dispersion becomes parabolic (i.e., the quasiparticles gain a mass). The energy degeneracy at the K and K' valleys in bilayer graphene is preserved by its inversion symmetry of bilayer graphene, whereby the opening of a bandgap is prevented. Breaking of the lattice's inversion symmetry as in h-BN (see Figure 1:2(c) causes lifting of the degeneracy. The resulting large energy gap at the valleys makes h-BN an extremely good insulator and dielectric.
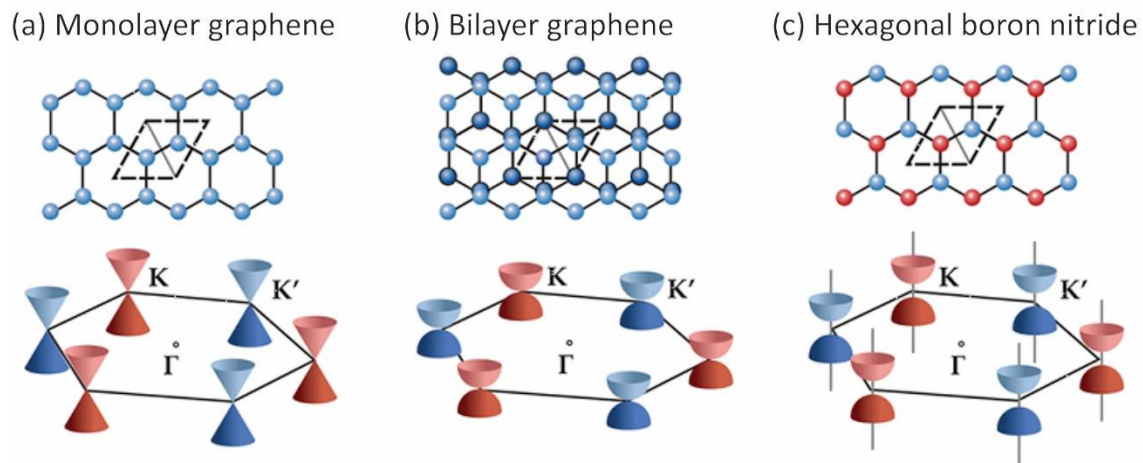
Figure 1:2 Lattice and band structures of (a) monolayer graphene, (b) bilayer graphene, and (c) hexagonal boron nitride (h-BN). The unit cells are indicated by the dashed lines in the lattice diagrams. Reproduced from [3], with the permission of the American Institute of Physics.

By stacking two or more different types of 2D layers on top of each other, a huge variety of vdW heterostructures with atomically sharp interfaces becomes accessible ('Lego assembly'), as schematically depicted in Figure 1:3. At the interface between two 2D layers, proximity effects can occur where one material (partially) borrows the property of another via quantum tunneling or Coulomb interactions. They typically alter the transport of energy and charge, and can lead to intriguing phenomena like interlayer excitons [4] or exotic superconducting states [5]. An additional degree of freedom in vdW heterostructures is the interlayer twisting angle, which can notably influence the physical characteristics. In general, when two lattices are stacked, a periodic, or commensurate, structure is obtained only at particular discrete twisting angles. Nonetheless, even incommensurate heterostructures may form large-scale quasi-periodic Moiré patterns. A

beautiful example of a new interfacial phenomenon engineered in vdW heterostructures is the experimental observation of Hofstadter's butterfly. In 1976, Douglas Hofstadter predicted that subjecting 2D-confined electrons to both a magnetic field and a periodic energy potential leads to a butterfly-shaped fractal energy spectrum [6]. The latter was realized in 2013 based upon quasi-periodic potentials associated with the Moiré pattern between a graphene layer and an h-BN substrate, whose lattice constants differ by only a few percent [7]. In order to probe the energy spectrum, the electrical conductivity of the heterostructure was measured as a function of applied voltage and magnetic field, thereby revealing the predicted fractal quantum Hall effect.
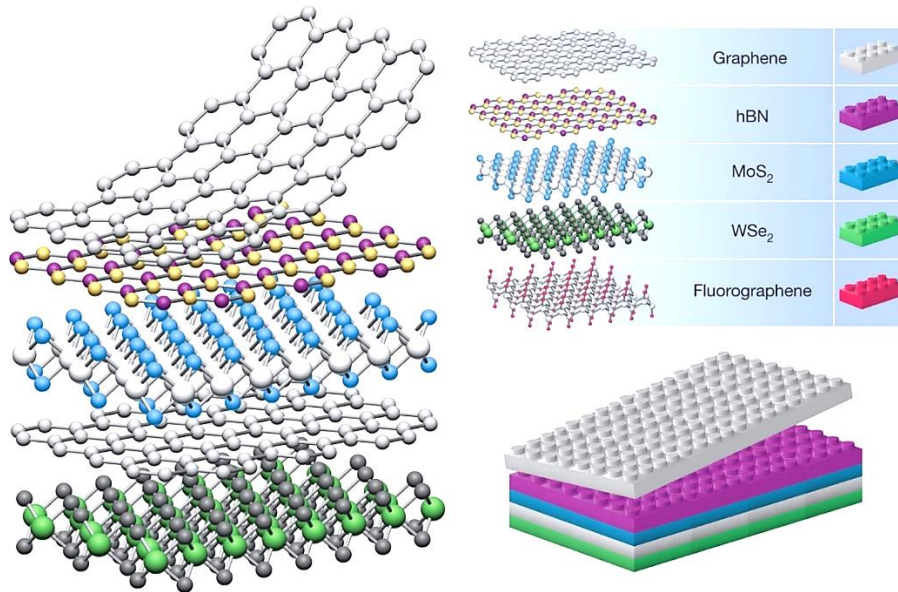
Figure 1:3 Schematic illustration of the formation of vdW heterostructures by stacking of different 2D layers. Such stacking can be conceptually compared to the construction of Lego blocks. Reprinted by permission from [8].

Two major techniques have been established for the assembly of vdW heterostructures. The first one is mechanical transfer, a method pioneered in 2010 for the assembly of high performance graphene devices placed on an h-BN substrate [9]. It starts with the exfoliation of a 2D sheet onto a sacrificial polymer support, followed by aligning and placing it on another sheet, and then removing the polymer. Although the sheets get in contact with the polymer and solvents, subsequent annealing helps to remove the contaminants and attain a reasonable interface quality. The later developed, so-called "pick-and-lift" method is still cleaner [10]. It makes use of a suitable stamp to bring a 2D crystal in contact with another one, which is followed by lifting the two-component stack from the substrate. The second assembly technique is the direct (e.g., chemical vapor deposition, CVD) growth of one 2D material on another [11]. A special case is van der Waals epitaxy, which was first reported more than 30 years ago for the growth of a $NbSe_2$ monolayer on a cleaved MoS_2 bulk crystal surface [12]. Later on, this method was expanded to graphene as vdW epitaxy substrate, as exemplified by the growth of graphene/WSe_2-heterostructures [13].

Of particular relevance for the aims of this thesis is that direct growth often yields a very clean interface between the 2D layers, as it is usually performed at elevated temperature (several hundred °C), under which condition surface contaminations are effectively eliminated. Moreover, vdW epitaxy provides access to heterostructures with nearly perfect crystallographic orientation (lattice match) between the layers. The situation is different for mechanical transfer, in which case surface contaminations tend to remain at the sheet surface, or even additional ones are introduced by the used stamp. In addition, it is much more difficult to obtain lattice-matched (commensurate) heterostructures through mechanical transfer, especially if the sheets do not exhibit well-defined crystallographic edges which could be utilized for rotational alignment.

Heterostructures of 2D materials offer unprecedented possibilities to develop novel electronic, optoelectronic and spintronic devices with intricate functions and high performance [14]. As one example of electronic devices, field-effect transistors (FETs) based on vertical heterostructures are advantageous over their lateral counterparts. In fact, the performance of lateral transistors with a 2D semiconductor material channel is limited by a large contact resistance arising from a high Schottky barrier at the interface between the 2D material and the metal electrodes [15]. By comparison, tunneling FETs based on vdW heterostructures are promising to reduce the supply voltage and hence the power consumption. The first reported tunneling FET consisted of a graphene/h-BN/graphene-heterostructure [16]. The tunneling current and on/off-ratio of such type of device could subsequently be improved by replacing h-BN with a smaller bandgap 2D semiconductor like WS_2 [17]. Furthermore, the fact that 2D materials can retain sharp band edges even at their atomic thickness can be exploited to create vertical p-n junction devices, whose operation relies upon band-to-band tunneling [18]. As distinguished from the conventional planar p-n junction, it is possible to efficiently tune the interlayer band alignment in the vertical p-n junction, thus enabling a subthreshold swing below the thermionic limit over a wide drain current range, as has been documented for instance for MoS_2/Ge tunneling FETs [19].

Besides electronic devices, the extraordinary optoelectronic properties of 2D materials render vertical heterostructures very promising for photodetection applications with ultrafast response speed and ultrahigh sensitivity, both of which are enabled by the ultrashort charge transport path in these devices [20]. For this purpose, a continuously expanding scope of 2D materials is available, including many narrow bandgap semiconductors which are relevant for broadband infrared photodetection. The enhanced matter-light interaction in vdW heterostructures leads to strong optical absorption arising from optical transitions between van Hove singularities in the electronic density of states of 2D materials [21]. In addition, vertical p-n vdW junctions comprise very strong built-in electrical fields, which can accelerate exciton dissociation and suppress dark current, and thus ensure further enhanced sensitivity.

There is also rapidly growing interest in exploiting the properties of the recently discovered, intrinsically magnetic 2D materials for magneto-electric device applications like memories or information storage devices. These 2D materials include ferromagnetic semiconductors and metals, as well as antiferromagnetic insulators [22]. Their magnetism can be tuned through modulation of the carrier concentration, for example via electrostatic gating. VdW magnetic tunneling junction (MTJ) devices based on 2D magnetic insulators display a magnetoresistance exceeding 10^4 at low temperature [23], which is significantly larger than observable for conventional state-of-the-art MTJs. Importantly, akin to other nonmagnetic 2D materials, 2D magnets can be seamlessly integrated with other 2D layers with desired electronic and optical properties, thus opening up rich possibilities for implementing novel device functionalities. By combining magnetic and nonmagnetic materials, the electronic structure of 2D nonmagnetic materials can be engineered through the proximity effect, establishing a tool to realize novel spintronic applications [24].

Along these lines, the major goal of this thesis was to explore two different types of graphene-based vdW heterostructures as potential platforms for the controlled generation, manipulation or probing of spins. In these heterostructures either a three-dimensional topological insulator (3DTI) or a potential 2D quantum spin liquid serve as material that exerts a proximity effect onto graphene. The high carrier mobility, low spin-orbit coupling (SOC) strength, and gate tunability of graphene have shown this 2D material to be a promising spin transport channel in spintronic devices [25]. In fact, graphene exhibits the longest spin relaxation length ever measured at room temperature [26], [27]. The capability of long-distance spin communication is important for the transmission and manipulation of spin signals in multi-terminal device architectures [28], [29]. Spin transport in graphene over long distances has been accomplished by combining it

with h-BN, as the latter reduces the density of charge traps and provides an atomically flat surface. Indeed, spin valves incorporating hBN as substrate, encapsulating layer and tunnel barrier have reached a spin relaxation length of 24 µm owing to improved spin diffusion and enhanced electronic mobility [27]. Most recently, polymer-free spin valves have enabled a record spin relaxation time of 12 ns and spin relaxation lengths exceeding 30 µm [26]. Extending graphene's capabilities beyond spin-conservation requires the implementation of spin-orbit proximity and/or magnetic exchange proximity effects within vdW heterostructures. With recent progress on scaling down of nanostructures and achieving high-quality interfaces, graphene-based vdW heterostructures represent a versatile testbed for low-power spintronics, including devices based on tunnel magnetoresistance [30], spin-transfer torque [31], spin FETs [32], XOR spin logic gates [33] and all-spin logic with built-in memory [34]. As an ultimate vision, future spintronic networks could synergistically combine both spin-conserving (pristine graphene) and spin-generating (proximitized graphene) regions.

Spin-orbit proximity in graphene has been experimentally studied mainly using graphene/TMD-heterostructures. At the present stage, it is well established that the proximity of a TMD layer can notably enhance the SOC of graphene, while simultaneously preserving the high electronic mobility of the latter. The relative strength of the induced SOC has been extracted from magnetotransport data [35], [36], [37], with a lower bound of 0.2 meV reported for high-quality graphene/WSe_2-heterostructures [35]. Besides TMDs, it has been documented that also 3DTIs can strongly enhance the negligible intrinsic SOC of graphene's Dirac states from 10 µeV by two orders of magnitude to approximately 1 meV [38]. However, it is important to note that all of thus far electrically characterized graphene/3DTI-heterostructures were fabricated via mechanical transfer of the TI sheet onto graphene, such that there is only a relatively weak, lattice-unmatched coupling between the two types of layers. By contrast, the present thesis aims to investigate graphene/3DTI-heterostructures where the bismuth chalcogenide-based 3DTI is directly grown onto graphene. Theory predicts that such (commensurate) heterostructures not only display an SOC in the meV range, but also additional functionality like the emergence of a giant spin lifetime anisotropy in the graphene layer (with the in-plane spins relaxing much faster than the out-of-plane spins) [39], [40]. At the same time, it should be possible to tune the SOC proximity strength by electrostatic gating, in close correspondence to observations made on graphene/3DTI-heterostructures fabricated by mechanical transfer [38], [41].

Regarding magnetic proximity effects in graphene, the initial experiments were performed with ferromagnetic insulators like EuS, EuO, or yttrium-iron garnet (YIG), typically in the form of a magnetic substrate. As to be expected, the magnitude of the proximity-induced exchange field was found to sensitively depend on the quality of the interface between graphene and the magnetic insulator. Non-local resistance measurements on a high-quality graphene/EuS-heterostructure revealed the presence of a pronounced magnetic exchange field on the order of 14 T, which is sufficient to split the ground-state degeneracy of graphene in the quantum Hall regime [42]. Hints for a perpendicular magnetic exchange field were also found for graphene on the insulating ferromagnet YIG by measurement of the anomalous Hall effect [43]. Furthermore, effective spin-to-charge current conversion has recently been achieved through the inverse Rashba-Edelstein effect (IREE) in graphene grown by CVD on a YIG substrate [44]. In the latter work, the existence of an (in-plane) induced magnetic moment at the carbon atoms of graphene could be directly proven through magnetic circular dichroism (XMCD) measurements. In all the heterostructures mentioned above, an (out-of-plane) magnetic exchange field is exerted onto the proximitized graphene. However, it is also of interest whether charge transport through proximitized graphene could serve also as a probe of fluctuating magnetic moments in a close-by 2D quantum material. Thus, in the present thesis, graphene is combined with α-ruthenium trichloride (α-$RuCl_3$) as a candidate quantum spin liquid with a 2D layered structure [45], and the magnetotransport characteristics of the heterostructure determined as a function of temperature.

This thesis is organized as follows:

Chapter 2 provides an overview of the fundamental physical concepts, and introduces the electronic properties of the three different components of the investigated vdW heterostructures, specifically graphene, bismuth telluride selenide (BTS) and α-ruthenium trichloride (α-RuCl$_3$).

Chapter 3 summarizes the principles of the relevant experimental techniques, along with details on the preparation of the required 2D sheets, their assembly into heterostructures and the subsequent device fabrication.

In **chapter 4**, the growth characteristic of the graphene/BTS-heterostructures and their investigation by Raman and scanning probe microscopy is described. The Raman data reveals strain and doping effects of the heterostructures and the second harmonic generation microscopy allows to investigate BTS growth orientations on top of graphene.

Chapter 5 deals with the gate- dependant electrical transport properties of the graphene/BTS-heterostructures at low temperatures and under externally applied magnetic fields. Different doping levels of heterostructures are observed and their phase coherence lengths are extracted.

Chapter 6 reports the results of low-temperature charge transport experiments on the graphene/α-RuCl$_3$ heterostructures, with emphasis on the influence of the thickness of the α-RuCl$_3$ sheet in proximity to graphene. The temperature and gate- dependent magneto- oscillation amplitudes are extracted and interpreted.

Finally, **chapter 7** concludes this thesis by highlighting the major results, and furthermore outlines possible directions of future experimental work. Moreover, the use of magneto-optical Kerr measurements to detect charge-to-spin conversion in graphene/BTS heterostructures is described.

Chapter 2   Proximity effects in graphene-based vdW heterostructures

In the following three sections, the basic components of the vdW heterostructures investigated in this thesis will be introduced. These are the 2D Dirac material graphene whose properties are to be modulated through the proximity effect, as well as the 3D topological insulator bismuth telluride selenide (Bi_2Te_2Se) and the quantum spin liquid candidate α-ruthenium (III) chloride (α-RuCl$_3$) which are used as materials exerting a proximity effect onto graphene. Subsequently, the basic physical mechanisms that underlie the spin-orbit and magnetic exchange proximity effects in graphene are described.

2.1   Graphene

2.1.1   Lattice structure and Brillouin zone

Graphene is made of sp^2-hybridized carbon-atoms arranged into a honeycomb lattice, which is C_6 rotation symmetric, as depicted in Figure 2:1(a).
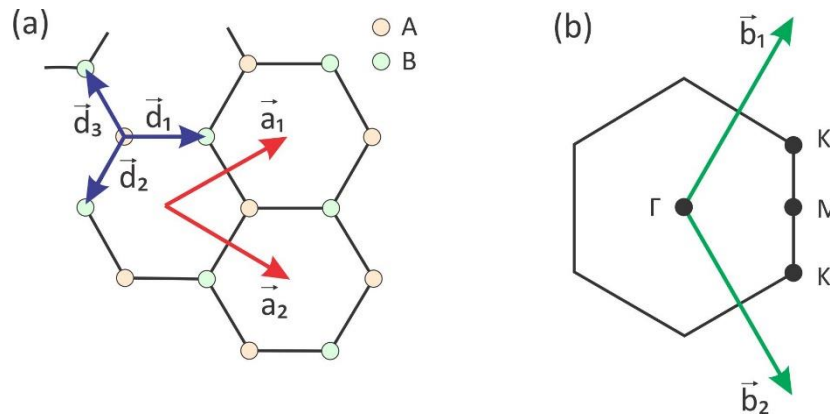
Figure 2:1 Schematic illustration of the graphene lattice in real and reciprocal space. (a) The unit cell is spanned by the two unit vectors $\vec{a}_1$ and $\vec{a}_2$. It contains one atom of the A (orange dot) and B (green dot) sublattice each. (b) First Brillouin zone with the reciprocal lattice vectors $\vec{b}_1$ and $\vec{b}_2$, and the six corners assigned to two inequivalent valleys K and K'.

While the three sp^2-hybridized electrons of each carbon atom are used to form covalent σ-bonds to its neighbours, the last electron remaining in the p$_z$-orbital contributes to the delocalized π-band. The primitive unit cell of the honeycomb lattice, which is spanned by the two lattice vectors

$$\vec{a}_1 = \frac{a_0}{2}\begin{pmatrix} 3 \\ \sqrt{3} \end{pmatrix} \quad \text{and} \quad \vec{a}_2 = \frac{a_0}{2}\begin{pmatrix} 3 \\ -\sqrt{3} \end{pmatrix} \tag{2.1}$$

includes two atoms, commonly labelled as the A and B sublattice. The lattice vectors are given in units of a_0, corresponding to inter-carbon distance of 1.42 Å. The first Brillouin zone of the honeycomb lattice (see Figure 2:1(b)) comprises the two reciprocal lattice vectors

$$\vec{b}_1 = \frac{2\pi}{3a_0}\begin{pmatrix} 1 \\ \sqrt{3} \end{pmatrix} \quad \text{and} \quad \vec{b}_2 = \frac{2\pi}{3a_0}\begin{pmatrix} 3 \\ -\sqrt{3} \end{pmatrix} \tag{2.2}$$

Of special relevance are the so-called Dirac points (DPs) which are located at the K and K' points of the Brillouin zone at the following positions:

$$\vec{K} = \frac{2\pi}{3a_0}\begin{pmatrix} 1 \\ \sqrt{3} \end{pmatrix} \quad \text{and} \quad \vec{K'} = \frac{2\pi}{3a_0}\begin{pmatrix} 1 \\ -\sqrt{3} \end{pmatrix} \tag{2.3}$$

respectively. The nearest-neighbor vectors in real space (see Figure 2:1(a)) are given by

$$\vec{d}_1 = a_0\begin{pmatrix} 1 \\ 0 \end{pmatrix} \quad \text{and} \quad \vec{d}_2 = \frac{a_0}{2}\begin{pmatrix} -1 \\ -\sqrt{3} \end{pmatrix} \quad \text{and} \quad \vec{d}_3 = \frac{a_0}{2}\begin{pmatrix} -1 \\ \sqrt{3} \end{pmatrix} \tag{2.4}$$

2.1.2   Electronic band structure

The low energy electronic states of graphene can be derived with a tight-binding (TB) model [46], assuming that the charge carriers can hop to nearest neighbors. As graphene's unit cell is composed of two atoms, two sets of Bloch orbitals are needed, one for each sublattice:

$$\psi_j = \frac{1}{\sqrt{N}} \sum_{\vec{R}_j} e^{i\vec{q}\vec{R}_j} \, \phi_j\left(\vec{r} - \vec{R}_j\right), \tag{2.5}$$

where N is the number of lattice points, $\vec{q}$ is the wave vector, $\phi(\vec{r})$ is the π-orbital wave function of an isolated atom, j is the sublattice index, and $\vec{R}_j$ is the location of the j-th atom. Due to the two sublattices, the Hamiltonian assumes the form of a 2 x 2 matrix with the following elements:

$$H = \begin{pmatrix} H_{AA} & H_{AB} \\ H_{BA} & H_{BB} \end{pmatrix}. \tag{2.6}$$

The diagonal terms of the Hamiltonian can be calculated from:

$$H_{AA} = \langle \psi_A(\vec{r})|H|\psi_A(\vec{r})\rangle. \tag{2.7}$$

Upon combining equations (2.5) and (2.7), there arises the on-site energy term $\varepsilon = \langle \phi_A(\vec{r})|H|\phi_A(\vec{r}')\rangle$ which is commonly set to zero for undoped graphene. Moreover, as the two sublattices A and B are the same, it follows that $H_{AA} = H_{BB}$. The off-diagonal terms can be calculated from:

$$H_{AB} = \langle \psi_A(\vec{r})|H|\psi_B(\vec{r})\rangle,$$

(2.8)

with $H_{AB} = H^*{}_{AB}$. If only nearest-neighbour hopping (d_i = r - R with i = 1, 2, 3) is taken into account, and the nearest-neighbor hopping energy is defined as t $= \langle \phi_A(r)|H|\phi_B(r)\rangle$ (equaling approximately −2.7 eV [47]), equation (2.8) becomes

$$H_{AB} = t \cdot \left(e^{i\vec{q}\vec{d_1}} + e^{i\vec{q}\vec{d_2}} + e^{i\vec{q}\vec{d_3}}\right) = t \cdot f(\vec{q})$$

(2.9)

and accordingly the full Hamiltonian reads as:

$$H = t \cdot \begin{pmatrix} 0 & f(\vec{q}) \\ f(\vec{q})^* & 0 \end{pmatrix}.$$

(2.10)

Solving the eigenvalue problem yields $E_{\pm} = \pm\sqrt{|f(\vec{q})|^2}$ where the plus (negative) sign accounts for the conduction (valence) band. By inserting the nearest-neighbour coordinates d_1, d_2 and d_3 one obtains the following energy dispersion

$$E_{\pm}(\vec{q}) = \pm t \sqrt{1 + 4\cos\left(\frac{3}{2}q_y a_0\right)\cos\left(\frac{\sqrt{3}}{2}q_x a_0\right) + 4\cos\left(\frac{\sqrt{3}}{2}q_y a_0\right)^2}$$

(2.11)

which is plotted in Figure 2:2(a) for the first Brillouin zone. At zero energy, the valence and conduction band touch at the six DPs, which are distinguished as K and K' valleys. The energy dispersion reveals that graphene is a zero-gap semiconductor. While in pristine graphene, the Fermi energy is located at E = 0, it can be tuned into the valence or conduction band (corresponding to p- and n-type doping, respectively) by introducing a finite on-site energy. Experimentally, such shift can be realized via electrostatic gating (see section 2.1.4). For most charge transport measurements, only the low-energy spectrum of graphene is accessible. In order to approximately describe this range, the full Hamiltonian can be expanded around the K (K')-vector by introducing q = K + k, where $|K| \gg |k|$ and k is the vector measured relative to the corresponding DP. The linearized Hamiltonian around the K and K' points then reduces to

$$H = \pm\hbar v_F \vec{k}\vec{\sigma} = \hbar v_F \begin{pmatrix} 0 & \pm k_x - ik_y \\ \pm k_x + ik_y & 0 \end{pmatrix} \text{ with } \vec{\sigma} = \begin{pmatrix} \pm\sigma_x \\ \sigma_y \end{pmatrix}$$

(2.12)

where the plus (minus) sign is valid for the K (K') valley, $v_F = \frac{3ta_0}{2\hbar} \approx 10^6 \frac{\text{m}}{\text{s}}$ is the Fermi velocity [48], and σ is given by the Pauli matrices σ_x and σ_y. This results in the following low-energy spectrum

$$E_{\pm}(\vec{k}) = \pm\hbar v_F |\vec{k}|$$

(2.13)

where the plus (minus) sign holds for the conduction (valence) band. It is noteworthy that equation (2.13) is independent of the valley, i.e., there is a two-fold valley degeneracy which complements the two-fold spin degeneracy.
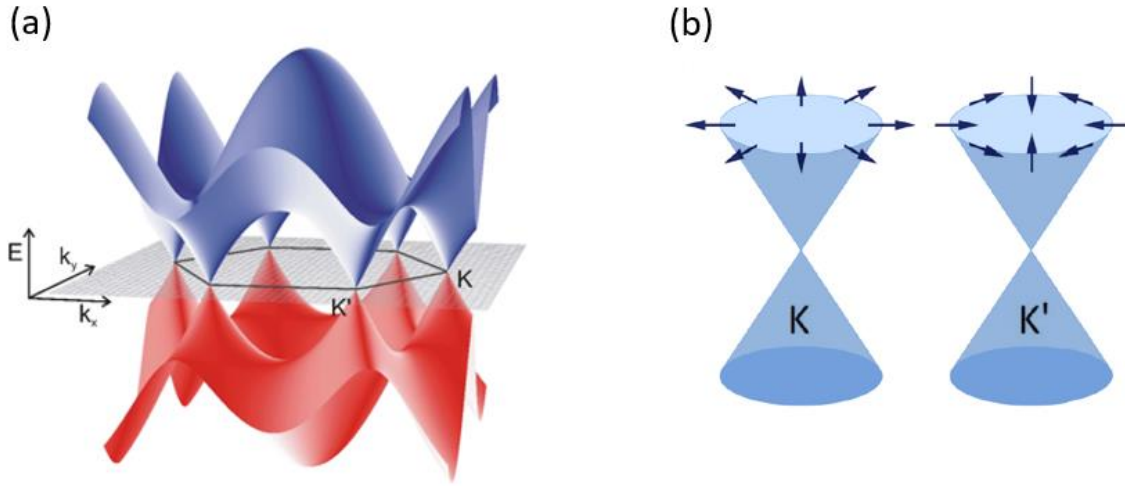
Figure 2:2 Graphene band structure (a) Schematic view of the graphene band structure with the characteristic Dirac cones close to the K and K' points. Reproduced with permission from [49]. (b) Sketch of the pseudospin texture of graphene. Reproduced with permission from [50].

The two-atomic unit cell in graphene imparts an additional degree of freedom onto the charge carriers, commonly called the pseudospin. Using $k = k_F e^{i\theta_{\vec{k}}}$, the Hamiltonian in equation (2.12) can be rewritten as

$$H = \pm \hbar v_F k_F \begin{pmatrix} 0 & \pm e^{i\theta_{\vec{k}}} \\ \pm e^{i\theta_{\vec{k}}} & 0 \end{pmatrix}$$

(2.14)

where $\theta_{\vec{k}} = \arctan(k_y/k_x)$, and the plus (minus) sign relates to the K (K') valley. A possible solution of this eigenvalue and eigenvector problem for this equation are the following normalized eigenvectors in the conduction $|EV_C\rangle$ and valence band $|EV_V\rangle$:

$$|EV_C\rangle = \frac{1}{\sqrt{2}} \begin{pmatrix} e^{\mp \frac{i\theta_{\vec{k}}}{2}} \\ e^{\pm \frac{i\theta_{\vec{k}}}{2}} \end{pmatrix} \quad \text{and} \quad |EV_V\rangle = \frac{1}{\sqrt{2}} \begin{pmatrix} e^{\mp \frac{i\theta_{\vec{k}}}{2}} \\ -e^{\pm \frac{i\theta_{\vec{k}}}{2}} \end{pmatrix}$$

(2.15)

where the plus (minus) sign again relates to the K (K') valley. It is possible to generalize equation (2.15) by introducing the parameter s (the so-called pseudospin) accounting for holes (s = -1) in the valence band, and electrons (s = 1) in the conduction band, which yields

$$|s\rangle = \frac{1}{\sqrt{2}} \begin{pmatrix} e^{\mp \frac{i\theta_{\vec{k}}}{2}} \\ s e^{\pm \frac{i\theta_{\vec{k}}}{2}} \end{pmatrix}$$

(2.16)

Equation (2.16) defines the amplitude of the electronic wave function on the A and B sublattice, respectively. The vector can be understood as the result of a spinor-rotation of $\theta_{\vec{k}}$ around the z-axis, given by

$$R\left(\theta_{\vec{k}}\right) = e^{-\frac{i\theta_{\vec{k}}}{2\sigma_z}} = \begin{pmatrix} e^{-\frac{i\theta_{\vec{k}}}{2}} & 0 \\ 0 & e^{\frac{i\theta_{\vec{k}}}{2}} \end{pmatrix},$$

(2.17)

where σ_z is a Pauli matrix. For a rotation of 2π (corresponding to a charge carrier encircling the origin in k-space) the wave functions picks up a phase, which is the so-called the Berry-phase.

Assuming an initial state $|s_0\rangle$ pointing in the $\pm x$-direction, an arbitrary state (described by equation (2.16)) can be written as:

$$|s\rangle = R\left(\theta_{\vec{k}}\right)|s_0\rangle = \begin{pmatrix} e^{-\frac{i\theta_{\vec{k}}}{2}} & 0 \\ 0 & e^{\frac{i\theta_{\vec{k}}}{2}} \end{pmatrix} \frac{1}{\sqrt{2}} \begin{pmatrix} 1 \\ s \end{pmatrix}$$

(2.18)

with $|s_0\rangle$ being defined for $\theta_{\vec{k}} = 0$. From this equation, it can be seen that the pseudospin is tied to the $\vec{k}$-vector (see Figure 2:2(b)). i.e., in the K cone the pseudospin is parallel to the $\vec{k}$-vector in the conduction band (right-handed Dirac fermions), whereas it is anti-parallel in the valence band (left-handed Dirac anti-fermions). The reverse holds for the K' cone.
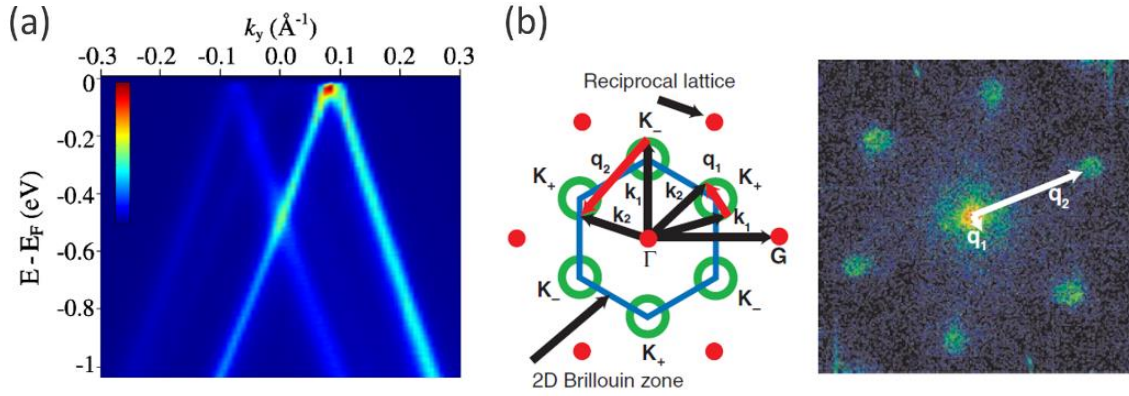
Figure 2:3 ARPES measurements of graphene. (a) ARPES data of single-layer graphene grown on the C face of SiC. The Dirac point is shifted to ~30 meV above the Fermi surface, indicative of weak substrate-induced p-doping. The ghost Dirac cones stem from multiple electronically decoupled graphene monolayers owing to rotational stacking disorder. Reproduced with permission from [51]. (b) The left panel illustrates quasi-particle interference in graphene. The 2D Brillouin zone is shown as blue line and the constant energy contours as green rings at the K$_\pm$ points, along with the two dominant classes of scattering vectors which create the interference patterns. The wave vectors of incident and scattered carriers are denoted as $\vec{k}_1$ and $\vec{k}_2$. Scattering wave vectors $\vec{q}_1$ (short red arrow) connect points on a single constant energy circle, while wave vectors $\vec{q}_2$ (long red arrow) connect points on constant energy circles between adjacent K$_+$ and K$_-$ points. The red circles denote graphene reciprocal lattice points with origin G. The right panel is a Fourier-Transform (FT)-STS image (100 Å × 100 Å) of defective bilayer graphene on SiC. The small ring at $\vec{q} \approx 0$ is associated with $\vec{q}_1$ scattering, whereas the six circular disks at the K$_\pm$ points are associated with $\vec{q}_2$ scattering events. From [52]. Reprinted with permission from AAAS.

Graphene's low-energy band structure is robust for symmetry reasons. The Fermi level of a perfect, un-doped graphene sheet lies between the two symmetrical valence and conduction bands, such that the Fermi 'surface' consists of the two K and K' points where the π- and π*-bands cross. Usually such degeneracy would be prevented by level repulsion opening of a gap at the crossing points. In graphene, however, these points are protected by discrete symmetries, specifically C3, inversion and time reversal symmetry, i.e., unless one of these symmetries is broken, the DPs will remain intact [53]. According to density functional theory (DFT) calculations, adding next-nearest neighbour terms to the Hamiltonian removes the e-h symmetry, while the degeneracy of the DPs remains intact [54]. By contrast, breaking the symmetry between

the A and B sublattices, for instance by a corrugated substrate, will lift the degeneracy at the DPs. This type of symmetry breaking is responsible for the fact that graphene's sister compound h-BN is a band insulator with a large band gap of ~6 eV.

Experimentally, the Dirac energy spectrum of graphene has been confirmed mainly by angle-resolved photoemission spectroscopy (ARPES) and scanning tunneling spectroscopy (STS). ARPES has been widely used to verify the linear Dirac dispersion around the K and K' points in graphene's Brillouin zone. ARPES studies on single-layer graphene have revealed the existence of Dirac cones along with a linear dispersion around them, as exemplified by the ARPES spectrum of epitaxially grown graphene on the C face of SiC [51] in Figure 2:3(a). The spectrum indicates slight p-type doping induced by the substrate. The carrier concentration in substrate-doped graphene can be further modified by chemical doping. Alkali metal deposition induces significant n-doping, which can reach even up to the van Hove singularity where the Dirac cones overlap to form a Fermi surface at the Γ point [55]. Another option is molecular doping, for example by NO_2 adsorption, which has been shown by ARPES to induce hole doping, and thereby to tune the Fermi level through the DP [56]. Besides doping, ARPES has also demonstrated gap opening due to substrate-induced breaking of the (A, B) sublattice symmetry of graphene, e.g., on the Si face of SiC [57].

STS has proven useful for unravelling graphene's energy dispersion via the principle of quasi-particle interference, which at the same time also enables verifying the quasi-particle chirality. For doped graphene, the constant energy contours (CECs) consist of rings around K and K', as depicted in Figure 2:3(b) (left panel). Thus, possible scattering wave vectors may connect points on the same CEC (intra-valley scattering, $\vec{q}_1$), or reach from K to K' (inter-valley scattering, $\vec{q}_2$). According to the nesting condition, Fourier-Transform (FT)-STS is expected to display rings with a radius q = $2k_F$ around $\vec{q} = 0$ and $\vec{q}$ = K − K' (as well as symmetry-equivalent points). This has indeed been observed in quasi-particle interference maps for mono- and bilayer graphene on different substrates, as exemplified in Figure 2:3(b) (right panel) [52]. Moreover, the quasi-particle dispersion manifests itself in the dispersion of the ring radii with applied bias voltage. On this basis, Fermi velocities in the range of $v_F \approx 1.2 - 1.5 \cdot 10^6$ m/s have been determined, in reasonable agreement with results obtained by ARPES [58]. In addition, quasi-particle interference resulting from inter- and intra-valley scattering has also been detected, thus providing access to the chiral properties of the Dirac fermions [59]. The first experimental proof of a Berry phase of π in graphene was provided by the observation of the anomalous half-integer quantum Hall effect [60]. In later experiments on a ballistic, phase coherent graphene p-n-p junction, graphene's Berry phase could be detected as a sudden phase shift at finite B-field in the transmission resonance [61].

2.1.3 Electronic density of states

The density of states (DOS) in graphene can be calculated from $\rho(E) = \partial N(E)/\partial E$ where $N(E)$ is the number of states at energy E. A starting point for deriving $N(E)$ is the equation

$$N(|\vec{k}|) = g \int dV \int_0^k \rho(\vec{k})d\vec{k}$$

(2.19)

where g is the degeneracy of the *k*-states in graphene, V is the volume in k-space, and $\rho(\vec{k}) = (2\pi)^{-d}$ (with d = 2 as the dimensionality of the system). Integration over the Fermi surface (i.e., a circle with radius k) yields p$|\mathbf{k}|^2$, and the above equation becomes

$$N(|\vec{k}|) = g\,\frac{V}{4\pi}\,\lceil\vec{k}\rceil^2.$$

(2.20)

Replacing $\vec{k}$ with the low-energy dispersion relation in equation (2.13) and taking the derivative with respect to the energy then yields

$$\rho(E) = g\,\frac{V}{2\pi}\,\frac{E}{(v_{F\hbar})^2}$$

(2.21)

It follows from equation (2.21) that the DOS in graphene scales linearly with energy E. Moreover, in combination with equation (2.20), $= N(\vec{k})/V$, and $g = 4$ the following dependence of wave vector on carrier density is obtained:

$$|\vec{k}| = k_F = \sqrt{\pi n}$$

(2.22)

2.1.4 Electronic transport in graphene

2.1.4.1 Characteristic length scales and transport regimes

There are several characteristic length scales which play an important role in quantum transport of mesoscopic systems [62], as detailed in the following:

Sample size: L - typically ranging from μm down to nm.

Interatomic spacing: a - typically on the order of a few Å.

Fermi wavelength: λ_F - wavelength of electrons at the Fermi energy. In 2D semiconductor heterostructures, λ_F is on the order of 50 nm; in metals like Cu or Ag it is significantly smaller (a few Å).

Elastic mean free path: l_{el} - average length an electron travels before undergoing elastic scattering into a different wave vector direction. In many materials, l_{el} can be assumed to be approximately temperature-independent. One example is electron scattering at a charged impurity, whereupon almost no energy is transferred. It reaches up to 20 μm in clean two-dimensional electron gases (2DEGs), and can be as short as a few Å (e.g., in disordered alloys).In the low temperature regime, l_{el} dominates the electron scattering (i.e., $l_m \approx l_{el}$).

Inelastic mean free path: l_{in} - the typical distance an electron travels before it experiences inelastic scattering (typically electron-phonon scattering). It depends strongly on temperature.

Phase coherence length: l_φ - the distance over which electrons preserve their phase memory. At distances below l_φ quantum interference of electron paths need to be taken into account. It usually shows a sizable temperature dependence, and can reach tens of μm in 2DEGs, but only up to several nm in regular metals. When spin-flip scattering is negligible, $l_\varphi \approx l_{in}$.

Charge transport regimes can be classified based upon the Fermi wavelength λ_F and the mean free path l_m according to:

$- \lambda_F \ll l_m$: no localization to weak localization regime;
$- \lambda_F \approx l_m$: **localization** regime;
$- \lambda_F > l_m$: **strong localization** regime.

For $\lambda_F \ll l_m$, further classification into the ballistic and diffusive transport regime can be done by involving the sample size L and the phase coherence length l_φ, as summarized in Table 2:1.

	Classical	Quantum
Diffusive	$\lambda_F \ll l_\varphi$, $l_m \ll L$	$\lambda_F \ll l_m \ll l_\varphi$, L
Ballistic	$\lambda_F \ll L < l_\varphi$, l_m	λ_F, $L < l_m$, l_φ

Table 2:1 transport classification

2.1.4.2 Electrostatic gating and field-effect mobility

The device configuration commonly used for charge transport measurements on graphene is the Hall bar structure (see Figure 2:4(a)). For device fabrication, the graphene is transferred to (or mechanically exfoliated onto) a heavily doped silicon wafer covered by a thermally grown SiO_2 insulator layer with a typical thickness of 300 nm. With the aid of a lithographically patterned resist mask, the graphene sheet is then etched into Hall bar geometry through plasma etching, as exemplified in Figure 2:4(b). In a four-terminal electrical measurement, a current I_{14} is driven between electrodes 1 and 4, while detecting the voltage drop V_{23} between electrodes 2 and 3. The resistivity ρ_{xx} of the graphene sheet can be calculated from

$$\rho_{xx} = \left(\frac{W}{L}\right)\left(\frac{V_{23}}{I_{14}}\right)$$

(2.23)

where W is the width and L the length of the graphene channel between the two voltage probes.
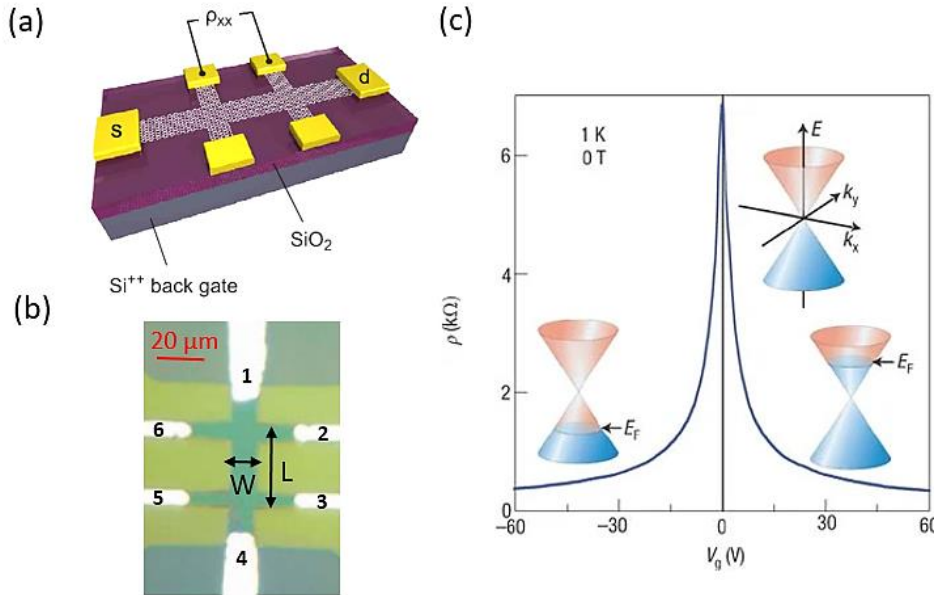
Figure 2:4 Back-gated graphene transistor. (a) Schematic representation of a graphene Hall bar device implemented on a Si/SiO2 substrate. Reproduced with permission from [63]. (b) Optical image of graphene patterned into Hall bar geometry. W is the width, and L the length of the graphene channel. Reprinted from [64], with permission from Elsevier. (c) Tuning of the resistivity of graphene through an electrostatic gate field. Reproduced by permission from [65].

In order to modulate the carrier density (i.e., the Fermi level E_F) in the graphene sheet, a gate voltage V_g is applied between the conducting Si substrate and a contact on the sheet. When the Fermi level of graphene

approaches the DP, the number of carriers decreases and the resistivity reaches a maximum at the DP (see Figure 2:4(c))

The ambipolar transfer characteristic enables investigating electron transport when E_F is above the DP, whereas hole transport can be probed when E_F is below the DP. Shown is the ideal case of the DP being located at V_g = 0 V, which holds only for very clean samples. In practice, there is often unintentional doping introduced during the device fabrication, such that the DP is shifted to positive gate voltages. Such doping can be reduced (and hence the DP moved back close to V_g = 0 V) by removing the surface contaminations for instance via annealing of the device in H_2/Ar atmosphere or ultrahigh vacuum [66]. Alternatively, a high current can be applied in order to achieve Joule heating of the sheet [67]. Although theoretically the carrier density should vanish at the DP, in the experiment one observes a finite residual conductivity on the order of $4e^2$/h. This observation has mainly been attributed to the presence of charged impurities which lead to electron-hole puddles in the graphene sheet [68].

The carrier mobility μ in graphene can be experimentally determined through Hall effect measurements in which the transverse resistivity

$$\rho_{xy} = \left(\frac{W}{L}\right)\left(\frac{V_{26}}{I_{14}}\right)$$

(2.24)

is recorded under an applied perpendicular B-field (V_{26} is the voltage measured between two opposite voltage probes, see Figure 2:4(b)). The carrier density n is then obtainable from

$$n = \frac{B}{e\rho_{xy}}$$

(2.25)

which further yields the Hall mobility via

$$\mu_H = \frac{1}{ne\rho_{xx}}$$

(2.26)

For suspended graphene, impressive Hall mobilities exceeding 200,000 cm^2/Vs have been documented [69]. An alternative approach involves extracting the field effect mobility μ_{FE} directly from the measured transfer curve. To this end, the carrier density is estimated from the surface charge density n induced by the applied V_g:

$$n = \frac{\varepsilon_0\varepsilon_r V_g}{te}$$

(2.27)

with ε_0 as the permittivity of free space, ε_r as the relative permittivity of the dielectric, t as the thickness of the dielectric and e as the electron charge. On this basis, μ_{FE} can be calculated from the gate voltage dependence of sheet conductivity σ using

$$\mu_{FE} = \frac{d\sigma}{dV_g}\frac{1}{C_g}$$

(2.28)

where C_g is the gate capacitance ($C_g = ne/(V_g - V_{gD})$, with V_{gD} as the gate voltage at the DP). For graphene on h-BN, μ_{FE} values larger than 100,000 cm^2/Vs have been found [9].

2.1.4.3   Scattering and transport regimes in graphene

For the specific case of graphene, the main scattering mechanisms involve short and long range scatterers, as well as phonons. Short range scatterers, for which the range of the associated potential is comparable to the unit cell of graphene, include vacancies and edges. Due to the large corresponding wave vector, this

type of scatterers is mainly responsible for intervalley scattering (i.e., scattering from K to K'). In comparison, for long range scatterers like charged impurities the potential decays slowly in space, and the associated short wave vector leads to intravalley scattering. A detailed analysis of the transport characteristics in dependence of n-type doping of graphene has shown that backscattering by phonons is suppressed and instead charged impurity scattering dominates the carrier transport even at room temperature [68]. Such behavior is in contrast to that of most semiconductors, for which acoustic phonon scattering is most relevant under this condition. Charged impurities typically originate from surface adsorbates on the graphene or charge trapping at the graphene/SiO_2 interface. Their influence is strong at low carrier concentration, and decreases with increasing carrier density as a consequence of screening. Scattering by charged impurities can be substantially reduced by implementing h-BN as underlying substrate, or by eliminating the substrate, i.e., rendering the graphene sheet freely suspended [70].The latter approach at the same time removes the coupling to surface phonons of the substrate as another source of scattering [71]. The low-temperature carrier mobility of high quality suspended graphene is ultimately limited by scattering from flexural phonons [72]. In general, the conductivity of graphene devices in the diffusive transport regime is well described by the Boltzmann transport equation

$$\sigma = \frac{e^2 v_{\mathrm{F}}^2 \rho(E_{\mathrm{F}}) \tau(k_{\mathrm{F}})}{2},$$

(2.29)

where τ_{F} is the scattering time at the Fermi level.

In the absence of disorder, charge transport in graphene becomes ballistic. Application of the Landauer formalism shows that the conductance of a graphene strip of width W is given by $G = (4e^2)N/h$, where $N \approx W/\lambda_{\mathrm{F}}$ is the number of modes at large Fermi energies [73]. This further yields for the ballistic conductivity $\propto \sqrt{n}$, from which in turn it follows for the mobility $\mu = \frac{\sigma}{ne} \propto \frac{1}{\sqrt{n}}$, which diverges for $n \to 0$. This implies that for ballistic transport mobility is not a suitable parameter, in contrast to the case of diffusive transport. Experimentally, ballistic transport has been observed on μm length scales in suspended graphene devices [74].

2.1.4.4   Phase coherent transport

There is an intermediate charge transport regime between the ballistic and diffusive regimes, the so-called quantum diffusive or phase coherent transport regime. The latter is characterized by the condition $l_m <$ L, W $< l_\varphi$, such that the carrier momentum gets randomized, but their phase is conserved during multiple scattering events. In analogy to optics, the phase coherence leads to quantum interference effects and correspondingly to a modulation of the carrier transmission. This manifests itself in two major phenomena that can be observed in charge transport experiments on disordered, mesoscopic conductors, namely universal conductance fluctuations and weak (anti)localization.

Universal conductance fluctuations

Universal conductance fluctuations (UCFs) arise when the interference of multiple, complicated paths leads to the accumulation of a random phase upon tuning a parameter such as B-field, as schematically outlined in Figure 2:5(a). The resulting conductance fluctuations are reproducible and aperiodic, and their amplitude around the mean value is on the order e^2/h (see Figure 2:5(b)), independent of the device size and strength of disorder (which is why they are called universal) [75]. The interference pattern can be altered either by modulating the charge carrier wavelength λ_{F} (i.e., via electrostatic gating) or by changing the carrier trajectories via an externally applied B-field (which causes the trajectories to bend). UCFs can be used to extract

the phase coherence length l_φ in single-layer graphene, with values on the order of 1 μm being reported for liquid helium temperature [76].
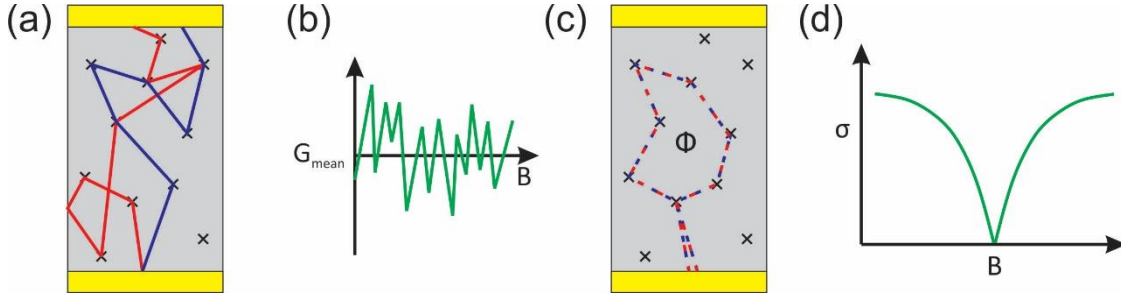
Figure 2:5 Electron trajectories. (a) Two possible trajectories for an electron moving from one electrode to another. (b) UCFs involve conductance fluctuations around an average value G_{mean} in dependence of carrier concentration or applied B-field. (c) Two closed electron trajectories that are related to each other by time reversal symmetry. An applied perpendicular B-field leads to a magnetic flux Φ through the loop defined by the trajectories. (d) Weak localization results in a characteristic dip of conductivity around zero B-field.

Weak localization and weak antilocalization

Another relevant interference effect that occurs in the quantum diffusive regime is coherent backscattering. It can be explained on the basis that the probability amplitude for an electron to travel from a point A to a point B via a trajectory i is given by $a_i a^i e^{i\varphi_i}$. The total probability for travelling from A to B is then obtained by summing over all possible, indistinguishable trajectories [77]:

$$P(A \rightarrow B) = \sum_i |a_i|^2 + \sum_{i \neq j} a_i a_j e^{-i(\varphi_i - \varphi_j)}$$

(2.30)

For open trajectories (i.e., A≠B), the trajectories are uncorrelated and accordingly the second term in the above equation is washed out. This corresponds to the classical result given by the sum of the probabilities of all possible trajectories. In contrast, if the trajectories are closed (i.e., A=B), and under the condition that the two paths i and j are related by time reversal symmetry (see Figure 2:5(c)), it follows that $a_i = a_j$ and $\varphi_i = \varphi_j$, and accordingly $P(A \rightarrow A) = 2\sum_i |a_i|^2$, which signifies an enhanced return probability as compared to the classical case. The increased backscattering probability in turn reduces the conductance. Under an externally applied B-field, the magnetic flux through the trajectory loop (cf. Figure 2:5(c)) introduces a phase difference for the two time-reversed trajectories. Due to the relative phase changes, the interference effects are suppressed upon increasing the B-field and correspondingly the conductivity $\sigma(B)$ increases (see Figure 2:5(d)):

$$\frac{\sigma(B) - \sigma(B = 0)}{\sigma(B = 0)} > 0.$$

(2.31)

This increase of conductivity constitutes the weak localization (WL) effect. For the specific case of graphene, the existence of pseudospin as an additional quantum number renders the constructive interference that underlies the enhanced backscattering into a destructive one. Hence, application of a B-field is expected to cause a conductivity decrease (i.e., a zero-field dip in magnetoresistance), an effect known as weak antilocalization (WAL). However, in the experiment graphene commonly displays WL, an observation which can be ascribed to the presence of short range scatterers which lead to intervalley scattering between the two valleys K and K' of different chirality. Experiments have demonstrated a crossover between WAL and WL, whose details depend on parameters like carrier mobility, carrier density and temperature [78].

Weak (anti)localization can be used to estimate the phase relaxation length in graphene. As W(A)L is independent of the sample length, it is observable even for larger samples and therefore more often used for

this purpose than UCFs. The quantum correction to the magnetoconductivity $\Delta\sigma$ in the absence of SOC is given by:

$$\Delta\sigma(B) = \frac{e^2}{\pi h}\left[F\left(\frac{\tau_B^{-1}}{\tau_\varphi^{-1}}\right) - F\left(\frac{\tau_B^{-1}}{\tau_\varphi^{-1} + 2\tau_{iv}^{-1}}\right) - 2F\left(\frac{\tau_B^{-1}}{\tau_\varphi^{-1} + \tau_*^{-1}}\right)\right]$$

(2.32)

where $F(x) = \ln(x) + \psi\left(\frac{1}{2} + \frac{1}{x}\right)$, with $\psi(x)$ being the digamma function, $\tau_B^{-1} = \frac{4DE}{\hbar}$, where D is the diffusion constant, τ_φ is the phase coherence time, τ_{iv} is the intervalley scattering time, and $\tau_* = \left(\frac{1}{\tau_{iv}} + \frac{1}{\tau_z} + \frac{1}{\tau_w}\right)^{-1}$, with τ_z as the intravalley scattering time and τ_w being a scattering time associated with trigonal warping [79]. Equation (2.32) can describe WL or WAL, depending on the relative magnitude of the involved time scales. While for $\tau_\varphi > \tau_{iv}$, the quantum correction to the magnetoconductivity features WL behaviour, WAL behaviour is obtained in the limit of $\tau_{iv,*} \geq \tau_\varphi$.
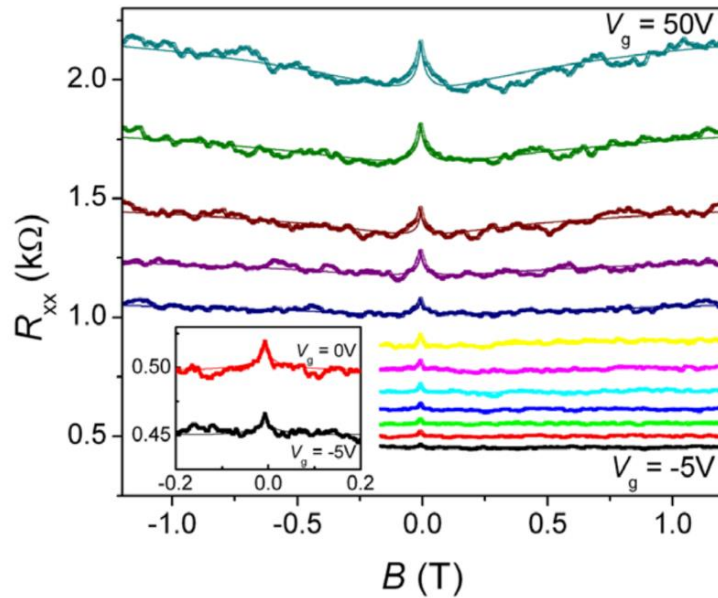
Figure 2:6 Longitudinal magnetoresistance R_{xx} of a graphene device recorded at T = 250 mK for different gate voltages V_g (V_g is varied from 50 to −5 V in steps of 5 V). At all gate voltages, a WL peak is visible near zero B-field. The thin solid lines represent fits to graphene WL theory. In the inset, a zoom into the curves for V_g = -5 and 0 V are shown. Reproduced with permission from [76].

Exemplary magnetoresistance curves of a graphene device are shown in Figure 2:6 together with corresponding fits of the WL effect. The observed decrease of l_φ with decreasing carrier density has been attributed to electron-electron interactions although there might also be an influence of the electron-hole puddles [76].

2.2 Bi_2Te_2Se (BTS)

2.2.1   Crystal lattice

The ternary compound Bi_2Te_2Se (BTS) belongs to the family of bismuth chalcogenide-based three-dimensional topological insulators (3DTIs). Its members are 2D-layered vdW materials with a distinctly anisotropic character. BTS is a distinct line compound in the phase diagram known as "Kawazulite" (and hence not merely a random mixture of Bi_2Se_3 and Bi_2Te_3) [80]. It crystallizes in an ordered tetradymite structure with a rhombohedral unit cell belonging to the space group $R\overline{3}m$. The basic quintuple-layer (QL) unit consists of Te-Bi-Se-Bi-Te, as shown in Figure 2:7, where comparison is made to other members of the tetradymite series. Each QL comprises strong in-plane covalent bonds and is approximately 1 nm thick. The unit cell consists of three QLs, with a stacking sequence of $-[Te-Bi-Se-Bi-Te]_0-[Te-Bi-Se-Bi-Te]_{1/3}-[Te-Bi-Se-Bi-Te]_{2/3}-$ [81]. XRD analysis has shown that there is a ~4% mixing of Se on the Te sites in Bridgman-grown crystals [80].
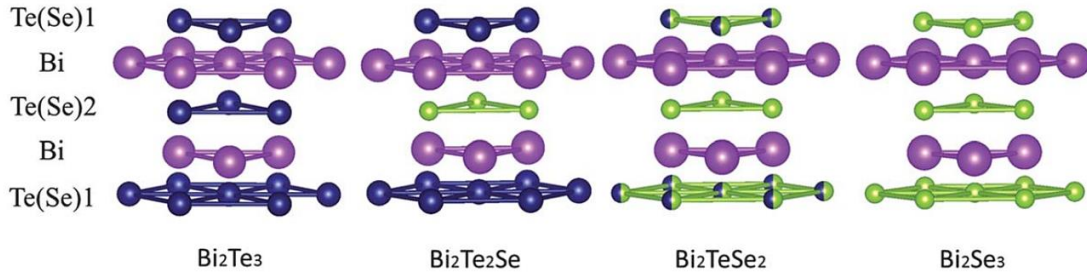
Figure 2:7 Progression of layered crystal structure in the tetradymite series of bismuth chalcogenide-based 3DTIs. In each case, one quintuple layer sandwich is shown. The Bi, Se, and Te atoms are displayed as purple, green, and blue spheres, respectively. Reproduced with permission from [81].

The weak vdW coupling between the QLs makes BTS suitable for standard micromechanical exfoliation and viscoelastic stamping techniques. The natural cleavage plane of BTS lies between two quintuple layers. Alternatively, thin BTS sheets can be obtained by vdW epitaxial growth on various types of substrates such as mica. The latter is a versatile substrate for 2D nanostructure growth owing to its pseudo-hexagonal layered structure and negligible dangling bonds. Thus grown 2D BTS crystals have a triangular shape with a relatively narrow distribution of size and thickness. In addition, they are well-aligned with preferred orientations at multiples of approximately 60°. Also Si/SiO_2 growth substrates are useful, providing access to BTS nanoplates with thickness down to 5 QLs, although they are typically randomly distributed and oriented as a consequence of the amorphous SiO_2 surface [82].

2.2.2   Electronic band structure

Spin-orbit coupling

Topological insulators (TIs) have received strong attention owing to their topological nature and also because they are Dirac materials [83]. They have an insulating bulk but conducting surface states. The latter are protected by time-reversal (TR) symmetry against perturbation and non-magnetic disorder or impurities. Like in a normal (i.e., topologically trivial) insulator, the valence and conduction bands of a TI are separated by a finite energy gap in the entire Brillouin zone of the bulk material. However, the TI surface or any boundary to a normal insulator (including vacuum) hosts Dirac surface states, which close the bulk band gap

unless time-reversal symmetry is broken. As strong spin-orbit coupling (SOC) plays an important role in generating the band structure of TIs, the basic principles of SOC will be outlined in the following.

Spin-orbit coupling (SOC) describes the interaction between the spin and orbital momentum of an electron. Besides being responsible for the emergence of helical Dirac fermions in the energy gap of TIs, SOC acts together with the breaking of inversion symmetry to cause energy splitting in 2DEGs at the surface of a crystalline solid, which is called the Rashba-Bychkov effect [84]. Within a non-relativistic approximation of the Dirac equation, SOC can be described by the Hamiltonian H_{SOC} for an electron in the electrostatic potential V of the nucleus [85]:

$$H_{SOC} = \frac{\hbar}{4m_e^2 c^2} \vec{\sigma} \cdot (\nabla V \times \vec{p})$$

(2.33)

In this equation, the Pauli matrix vector $\vec{\sigma} = \left(\sigma_x, \sigma_y, \sigma_z\right)$ is the spin operator, $\vec{p}$ the momentum operator, m_e represents the free electron mass, and c is the speed of light. The potential gradient ∇V is strongest close to the nucleus and increases with the atomic number Z. Hence, the atomic SOC is particularly strong in high Z elements like Pb or Bi.

The spin-orbit Hamiltonian H_{SOC} implicitly contains the coupling between the spin $\vec{S} = \hbar/2 \cdot \vec{s}$ and the orbital momentum $\vec{L} = \vec{r} \times \vec{p}$. This becomes directly evident for a spherically symmetric potential, which leads to [86]

$$H_{SOC} = \frac{1}{2m_e^2 c^2} \frac{1}{r} \frac{dV(r)}{dr} \vec{L} \cdot \vec{S}$$

(2.34)

.

As a consequence of the coupling of spin S and orbital momentum L, the two momenta S and L by themselves are no good quantum numbers any more, and accordingly [S, L] ≠ 0. By contrast, the total momentum J fulfils the commutation relation [H, J] = 0, and its eigenvalues are also eigenvalues of the Hamiltonian H describing the system. J can assume possible values, J = L ± S, depending on whether the corresponding magnetic moments are aligned parallel or antiparallel. The resulting spin-orbit splitting of energy is observable not only in atoms or molecules, but also in the core levels of solids.

Integer quantum Hall phase

The first example of a quantum state which has no spontaneously broken symmetry and whose behavior depends only on its topology was the quantum Hall (QH) state discovered by von Klitzing in 1980 while exploring the behavior of electrons confined in 2D and subjected to a strong perpendicular B-field [87]. In the QH state, electrons travel only along the sample edge, and there are different "lanes" at the sample's top and bottom edge, wherein the electrons flow in opposite directions (see Figure 2:8(a)). In comparison to a 1D system comprising electrons travelling in both directions, each edge of the QH system contains only half the degrees of freedom. Such spatial separation of the backward and forward movers is the main reason for the topological robustness of the QH effect. In fact, upon encountering an impurity, an edge-state electron simply goes around it because there is no option to reverse its path. An integer QH phase is protected from being deformed into a phase with different topology in the same way a torus is protected from being deformed into a sphere. Such transformation can only occur through a phase transition which is accompanied by the critical closing of the gap in the energy spectrum.
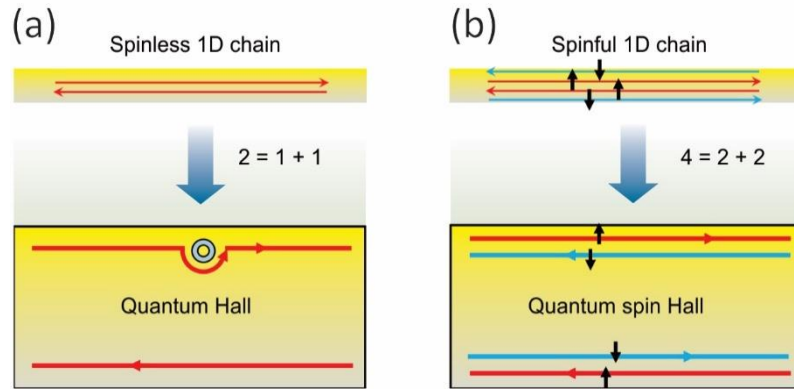
Figure 2:8 Schematic illustration of the hypothetical spatial separation of electron transmission channels in a 1D chain, leading to the quantum Hall (QH) or the quantum spin Hall (QSH) state. (a) For the QH system, the forward and backward mover of a spinless 1D chain undergo spatial separation into a forward mover at the upper edge and a backward mover at the lower, as indicated by the symbolic equation "2 = 1 + 1." Both these states are robust, i.e., they will go around an impurity without scattering. (b) Within a similar picture, for the QSH state the four basic channels within a spinful 1D chain become spatially separated in a pairwise manner, resulting in a forward mover with spin-up and a backward mover with spin-down at the upper edge, and conversely for the lower edge. This type of separation is denoted by the symbolic equation "4 = 2 + 2". Reproduced from [88], with the permission of the American Institute of Physics.

Quantum spin Hall insulators

Importantly, edge states similar to the QH edge states can emerge in a 2D system even in the absence of a TR symmetry breaking B-field. This possibility can be rationalized from the fact that in a real 1D system, there are in total four channels, i.e., one forward- and one backward-moving channel for both spin-up and spin-down electrons (see Figure 2:8(b)). A splitting of these "traffic lanes" in a TR-invariant fashion, in the absence of a B-field, leads to the spin-up forward mover and the spin-down backward mover on the top edge, and conversely for the bottom edge. In this so-called quantum spin Hall (QSH) state a net transport of spin occurs forward along the top edge and in the opposite direction along the bottom edge, in close correspondence to the separated charge transport in the QH state. According to theory, such scenario can be achieved in the presence of SOC [89].
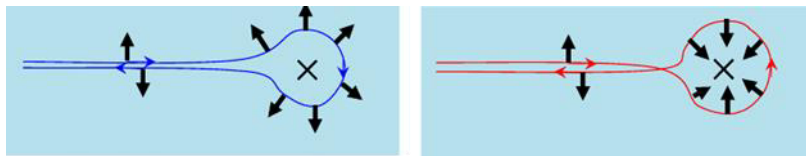
Figure 2:9 Schematic depiction of the mechanism underlying the robustness of QSH edge state against backscattering by non-magnetic impurities (represented by "x"). An electron can be scattered in two directions by such type of impurity. If it goes along the blue curve (clockwise), the spin rotates by π, while in case of the red curve (counter-clockwise) it rotates by −π (the spin direction is indicated by the black arrows). This difference of 2π is associated with a quantum mechanical phase factor of -1, which results in destructive interfere of the two paths, and hence the suppression of electron backscattering. Reproduced from [88], with the permission of the American Institute of Physics..

An intriguing property of the QSH edges is that backscattering by non-magnetic impurities is prohibited. This effect can be understood on the basis that an electron in such an edge state can take either a clockwise or a counter-clockwise turn around an impurity, as illustrated in Figure 2:9. As during this turn, the spin rotates by an angle of π or −π to the opposite direction, the two paths (which are related by TR symmetry) differ by a full $\pi - (-\pi) = 2\pi$ rotation of the electron spin. Accordingly, the two backscattering paths always

interfere destructively, thus ensuring perfect electron transmission. By contrast, if TR symmetry is broken because the impurity is magnetic, the two reflected waves no longer interfere destructively. However, the described scenario holds only if the edge states consist of an odd number of forward movers and an odd number of backward movers. This even-odd effect is connected to the so-called Z_2 topological quantum number, and explains why a QSH insulator is also referred to as a TI [90].

3D topological insulators

The concept of TIs can be generalized to 3D materials. The so-called strong 3DTIs host an odd number of 2D Dirac fermion flavours on each surface [91]. Their surface states consist of a single 2D massless Dirac fermion with an energy dispersion shaped like a Dirac cone, as illustrated in Figure 2:10(a). Similar to the 2D case, the tip of the cone is located at a TR-invariant point and the degeneracy is protected by TR symmetry.
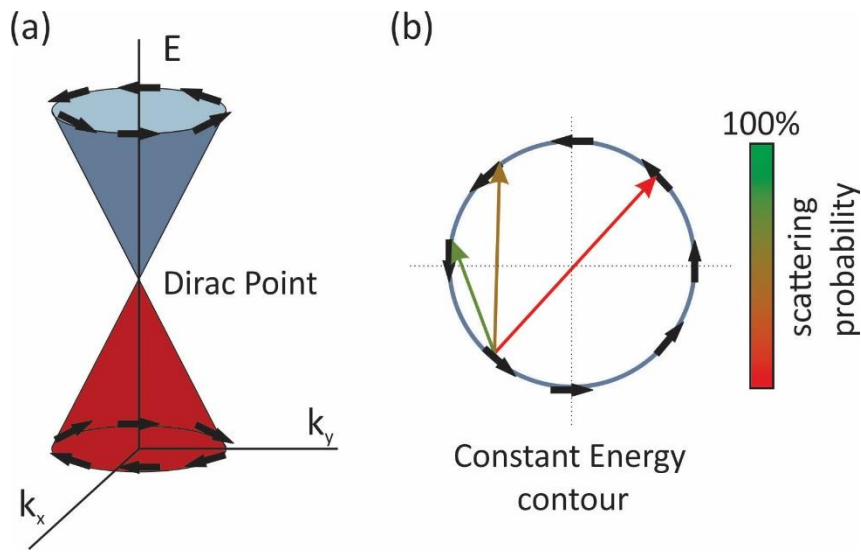
Figure 2:10 3DTI spin texture. (a) The energy dispersion of surface state in a 3DTI is a Dirac cone. The helical spin texture features spin-momentum locking (i.e., spin and wave vector directions are locked at right angles). (b) Exemplary constant energy contour demonstrating that the spin helicity suppresses backscattering by non-magnetic impurities (red arrow). However, scattering at different angles is still possible (green and olive arrows), with a probability that scales as $(1 - \cos(\theta))$, where θ is the scattering angle.

Furthermore, the surface states are spin-polarized with the spin and wave vector directions being locked at right angles, corresponding to a helical spin texture which protects the surface states from backscattering by non-magnetic impurities (see Figure 2:10(b)). Due to the TR symmetry, backscattering requires the electron to undergo a transition from a state $|\mathbf{k},\uparrow\rangle$ to a state $|-\mathbf{k},\downarrow\rangle$, i.e., a spin-flipping process. It is this suppression of backscattering that renders 3DTIs particularly interesting for spintronic device applications, e.g., as spin generator. As apparent from the constant energy contour in Figure 2:10(b), elastic scattering is still possible when the scattering angle is smaller than 180°, as the projected spin directions of the final and initial state have a finite overlap.

The occurrence of surface states in strong 3DTIs can be understood analogously to the 2D QSH case discussed above. Specifically, the strong SOC drives an energy band inversion at the Γ-point of the bulk energy band structure, thereby reversing the order of bonding and anti-bonding states at the band edge. At the same time, when the material is brought in physical contact with a topologically trivial insulator, the band inversion leads to the formation of a Dirac cone across the bulk band gap (the underlying principle is called bulk-boundary correspondence [92]). Theoretical analysis of the particular case of Bi_2Se_3 has shown that the

SOC affects especially the order of the Bi $6p_z$ and Se $4p_z$ orbitals which are of opposite parity and thus possess different symmetries [93]. When SOC is switched on, the Bi $6p_z$-states are shifted into the valence band, while the Se $4p_z$-states are shifted into the conduction band. This band inversion then gives rise to a non-trivial topological Z_2 index and topologically protected states at the surface.

Density functional theory (DFT)-based band structure calculations on BTS reveal the presence of a singly degenerate gapless Dirac cone centered at the Γ point (see Figure 2:11), testifying that this compound belongs to the $Z_2 = -1$ topological class [94]. Moreover, the numerically predicted bulk band gap is ~0.3 eV.
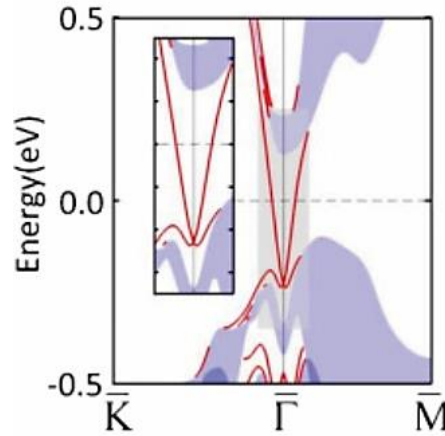
Figure 2:11 Calculated bulk and surface band structures for the (111) surface of BTS. The bulk band projections are represented by shaded areas. Reproduced with permission from [94].

Like for graphene, the electronic band structure of BTS has been experimentally confirmed by ARPES. ARPES maps have revealed the presence of a single Dirac cone with a linear dispersion, in agreement with the theoretical predictions (see Figure 2:12) [94]. Such experiments have furthermore demonstrated that the doping level (chemical potential) of the samples depends sensitively on the growth conditions (cf. Figure 2:12(a)). From the maps, a bulk band gap of ~0.3 eV has been determined for BTS. Moreover, the corresponding 2D constant energy contour plots (see Figure 2:12(b)) reveal a hexagonal shape with the bulk band gap, which gradually transforms into a cycle upon approaching the Dirac node. Close to the DP, the valence band then emerges as a six-fold petal-like pattern. As can be seen from the 3D representation of the electronic structure in Figure 2:12(c), the DP of BTS is not exposed, but rather buried into the bulk valence bands. From the ARPES data, the Fermi velocity v_F is estimated to be $6 \cdot 10^5$ m/s along the $\bar{\Gamma} - \bar{M}$ direction, and $8 \cdot 10^5$ m/s along the $\bar{\Gamma} - \bar{K}$ direction. Both these values exceed those reported for other bismuth chalcogenides Bi_2X_3 [95].

Furthermore, pump-probe photoemission spectroscopy has been used to evaluate the optically excited Dirac surface states in a BTS sample with an insulating bulk (i.e., wherein only the surface states cross the Fermi level). [96]. The observed gigantic optical lifetime exceeding 4 µs is much longer than for most other 3DTIs like Bi_2Se_3 for which lifetimes of a few picoseconds have been reported. The long optical lifetime was found to lead to a sizable surface photovoltage (involving a Fermi level shift of the Dirac surface states) as large as 100 mV, which likewise displays a lifetime on the microsecond scale. These findings suggest the presence of a power-law charge relaxation which is unique to 2D electrodynamics.

The helical spin texture of BTS could be experimentally verified by the detection of spin polarization induced by an electrical current flow through the surface states [97]. In the spin potentiometric measurement, a DC

current was driven between two non-magnetic contacts on a thin BTS sheet, while the spin polarization was detected with the aid of a middle ferromagnetic electrode. Importantly, upon sweeping an in-plane B-field between opposite directions to switch the magnetization of the electrode, the measured voltage signal was found to display a hysteretic step-like change, and furthermore the direction of the hysteresis to reverse upon reversing the current direction, as would be expected based upon the spin-momentum locking of the surface states.
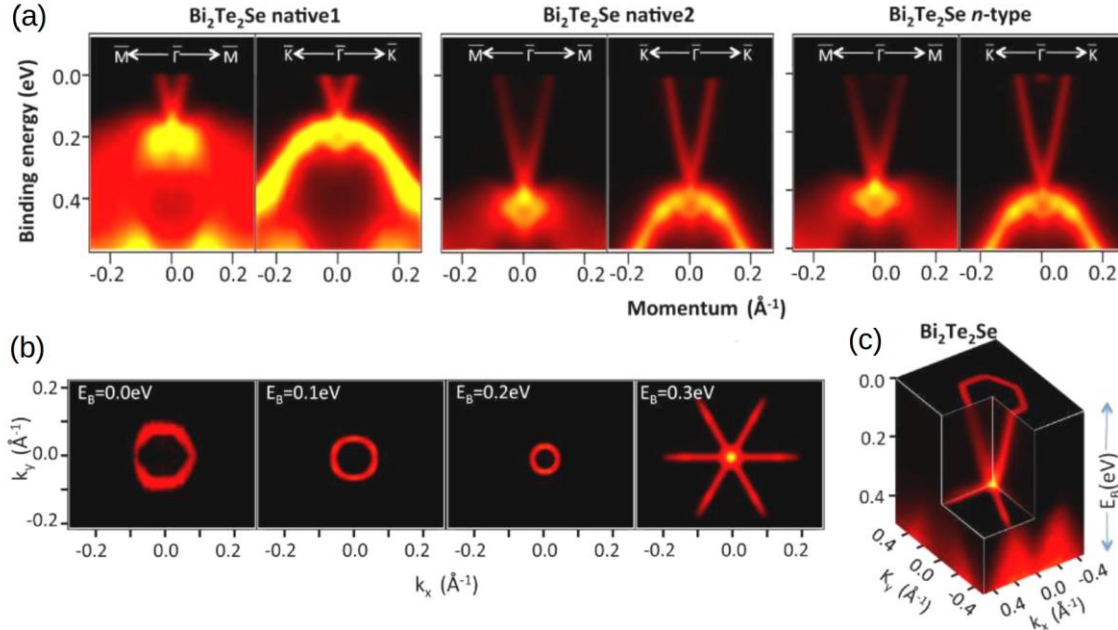
Figure 2:12 ARPES measurements of BTS. (a) ARPES maps of BTS, acquired along the high symmetry directions $\bar{\Gamma} - \bar{M}$ and $\bar{\Gamma} - \bar{K}$ for three different samples that have different doping levels. Each map reveals a single Dirac cone on the cleaved (111)-surface. (b) ARPES maps of constant energy contours at four different binding energies for the "native 2" sample in panel (a). (c) 3D representation of the electronic structure in panel (b). Reproduced with permission from [94].

2.3 α-RuCl$_3$

2.3.1 Crystal lattice

The crystal structure of α-RuCl$_3$ has been subject to some debate. The assignment of the space group is complicated by the presence of stacking faults due to the weakly bound 2D layers (see Figure 2:13). The individual layers are composed of edge-sharing ruthenium ions in a honeycomb arrangement, wherein the RuCl$_6$ octahedra are almost perfectly shaped (cf. Figure 2:13(a)). However, the honeycomb structure is not ideal since there are slightly different distances between the Ru^{3+} ions, specifically one atomic spacing of 3.454 Å (black) and another one of 3.449 Å (green). Recent X-ray have shown that at low temperature, high quality α-RuCl$_3$ crystals have C2/m space group symmetry, and the honeycomb layers exhibit a close-to-perfect ABC stacking [98] (see Figure 2:13(b)). An alternative crystal structure with trigonal (T) space group P3$_1$12 displays ABAB stacking, which is intrinsically faulty (cf. Figure 2:13(c)). In this thesis, high quality α-RuCl$_3$ crystals were used whose crystal structure is close to the C/2m symmetry.
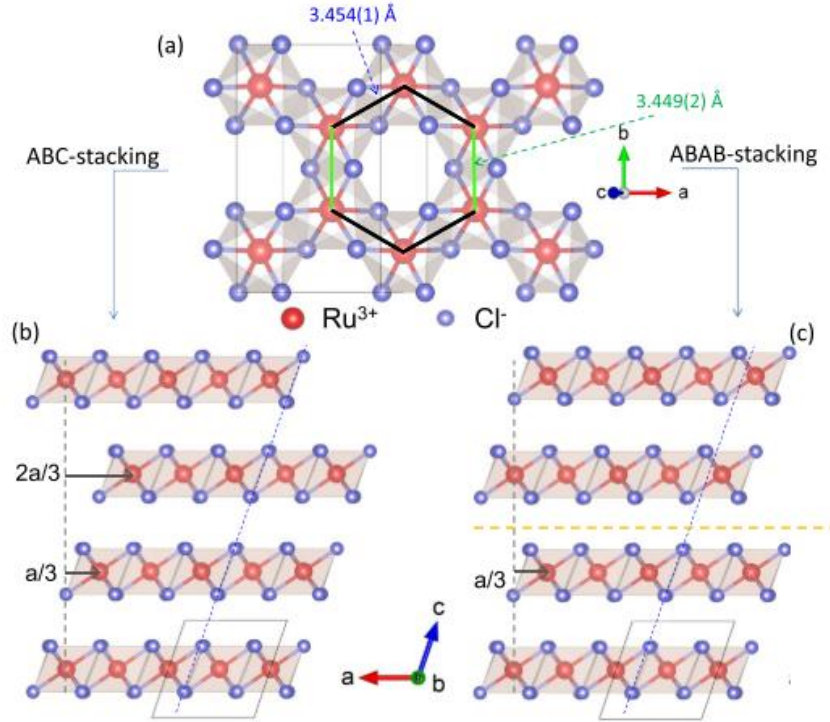
Figure 2:13 Crystal structure of α−RuCl$_3$. (a) In-plane structure of the symmetrical honeycomb lattice of a monoclinic C2/m space group type, consisting of Ru^{3+} ions (red dots) and Cl$^-$ ions (blue dots). Two types of distances are existent between the Ru^{3+} ions, specifically 3.454 Å (blue (1)) and 3.449 Å (green (2)). (b) ABC stacking of α−RuCl$_3$ layers. In the perfect stacking configuration, every fourth layer falls on top of the first layer, as indicated by the dashed black line. (c) ABAB stacking of α−RuCl$_3$ layers. The orange dashed line indicates the presence of a stacking fault. Figure Reproduced with permission from [98].

2.3.2   Quantum spin liquids

The discovery of novel phases of quantum matter has revolutionized condensed matter physics. Concepts like spin-orbit entanglement, electronic correlations and crystal-field effects allow to interpret physical properties from new perspectives [99].

In these systems, topology often plays an important role. In particular, in the weak correlation regime this leads to the emergence of topological insulators and topological semimetals. The influence of the strength of spin-orbit interactions and electronic correlations on the quantum matter phases is summarized in Figure 2:14. Of particular relevance for this thesis is that electronic correlations can drive a spin-orbit coupled Mott insulator into a spin-liquid state [100]. In this strong electronic correlation regime the electrons are localized and the spins are locked due to strong spin-orbit interactions. This leads to highly frustrated magnets where the magnetic moments do not order. A new ground state is formed where all magnetic moments exhibit a long range entanglement[101]. Promising materials to show such a spin liquid phase are the so-called Kitaev materials like Na$_2$IrO$_3$, α-Li$_2$IrO$_3$ or α−RuCl$_3$ which theory predicts to realize the Kitaev honeycomb model [102],[103].
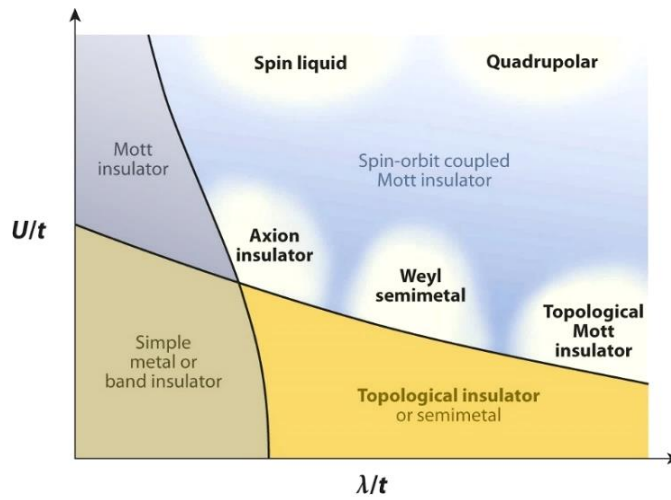
Figure 2:14 Phase diagram of novel types of quantum matter in dependence of electronic correlations (U/t) and spin-orbit interactions (λ/t). Reproduced with permission from [100].

Identifying quantum matter phases and their characteristic properties requires high quality materials and precise measurement techniques. Different experiments have possibly unveiled fractionalized excitations in strongly correlated systems that could hint towards the existence of the theoretically predicted quantum spin liquid (QSL) state [104]. One compound for which fingerprints of such exotic S=1/2 excitations (spinons) have been observed is the spin-1/2 Kagome-lattice antiferromagnet $ZnCu_3(OH)_6Cl_2$ (herbertsmithite). The strongly correlated spins in this system ground state keep fluctuating even for temperatures down to absolute zero, i.e., the magnetic moments do not freeze and no magnetic order develops. The principal possibility to excite spins carrying fractional quantum numbers renders the QSL state of interest for quantum information technology applications.
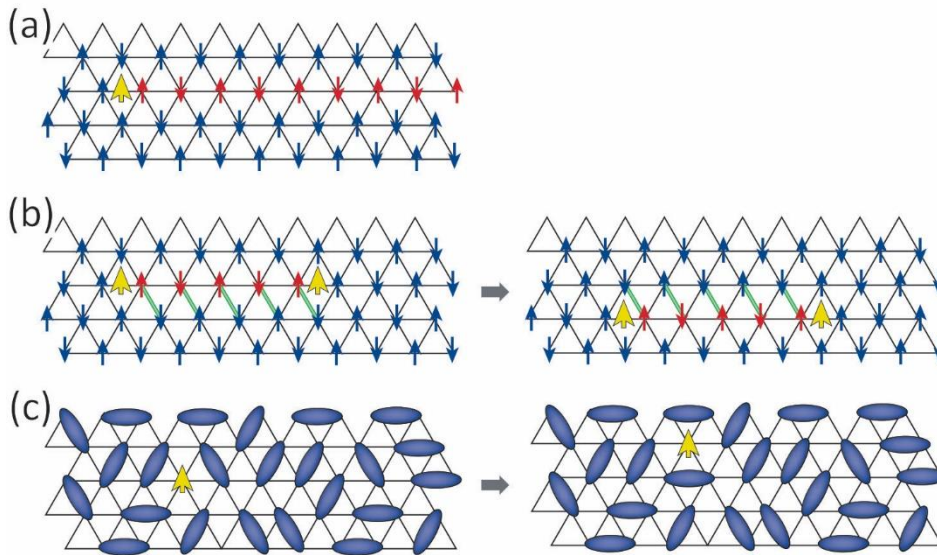
Figure 2:15 Formation of spinons on a triangular lattice. (a) Formation of a spinon (yellow arrow) in an antiferromagnet (spins shown as blue arrows) with flipped spins (red arrows). (b) Movement of two spinons mediated by flipping of the spins between them (red) along the green bonds. (c) Entangled pairs of spins are represented by blue ovals that cover two points in the triangular lattice. Movement of the spinon causes rearrangements of the spin pairs. Reproduced with permission from [101].

In general, the spin liquid state cannot be formed via symmetry breaking of a trivial ground state, but instead depends on long-range entanglement effects. This requires the existence of deconfined spinons (S = 1/2 quantum excitations) [101]. The formation of such spinons on a triangular lattice is illustrated in Figure 2:15 (where the spinon is shown by a yellow arrow). One possibility of spinon formation involves flipping events in one dimension, like the flipping of a string of spins in an antiferromagnet (red arrows), as depicted in Figure 2:15(a).

Movement of spinons requires flipping of another string, as schematically sketched in Figure 2:15(b). The number of spins that need to be flipped (red arrows) can be defined by two bound spinons (yellow arrows). Such movements are possible in 1D systems, as only a finite amount of spins need to be flipped, which requires a finite amount of energy. However, this cannot be realized in 2D or 3D systems where a string is extended to the full length. Spinons in 3D QSL are created by superposition of different pairs of spins in the ground state (blue ovals in Figure 2:15(c)). There is no preference for a specific valence bond configuration in a spin liquid phase and hence the movement of a spinon is just causing a rearrangement of the local valence bonds [101]. Different characters of QSL states have been proposed, including the prominent Kitaev QSLs that have attracted especially strong interest recently [105]. Depending on the lattice, there emerge Kitaev QSLs with different band structures featuring Majorana Fermi surfaces or nodal lines/Weyl points, or gapped QSLs [106].

Kitaev materials rely upon on bond-directional interactions in transition metal compounds with partially filled d-orbitals. The Kitaev type exchange is based on geometric orientations between neighbouring octahedra [102]. Two geometries are possible, namely corner-sharing and edge-sharing geometry. The lattice geometry and the orbital degrees of freedom sensitively influence the resulting Kitaev-type interactions. In the corner-sharing geometry only one charge transfer path is available, which results in a Heisenberg and pseudo-dipolar exchange coupling:

$$\mathcal{H}_{ij} = J_1 \vec{S_i} \cdot \vec{S_j} + J_2 \big(\vec{S_i} \cdot \vec{r_{ij}} \big) \big(\vec{r_{ij}} \cdot \vec{S_j} \big),$$

(2.35)

where $\vec{S_i}$ is the isospin operator (S=1/2), $\vec{r_{ij}}$ is a vector on the ij bond and $J_1 = J_2 = \frac{4}{9} v_{1(2)}$. Isotropic and anisotropic couplings are controlled by the parameters $v_1 = (3r_1 + r_2 + 2r_3)/6$ and $v_2 = (r_1 - r_2)/4$. For the edge-sharing geometry two paths are possible, which interfere destructively. In this case, the exchange interaction is described by the anisotropic part of the Hamiltonian:

$$\mathcal{H}_{ij}^{(\gamma)} = J S_i^{\gamma} S_j^{\gamma},$$

(2.36)

with $J = \frac{4}{3} v_2$ and the bond labeled ij perpendicular to the γ-bond [102]. The edge sharing interactions are believed to represent the Kitaev interactions in honeycomb lattices such as $\alpha-RuCl_3$, Na_2IrO_3 or α- Li_2IrO_3.

2.3.3 α-RuCl₃ as proximate quantum spin liquid
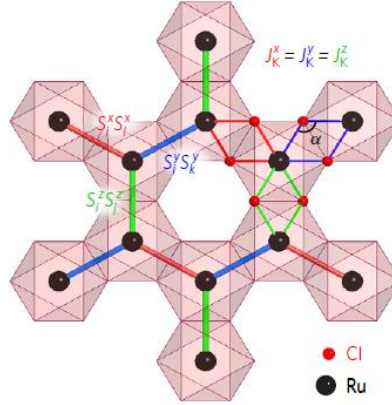
Figure 2:16 Kitaev bonding geometry in the layered honeycomb material α-RuCl₃. The high-symmetry crystal structure leads to isotropic Kitaev interactions $J_K = J_K^x = J_K^y = J_K^z$ with a Ru-Cl-Ru bond angle of 94° maximizing the Kitaev interaction, while the Heisenberg contribution becomes minimal. Reproduced with permission from [107].

The spin-orbit entangled $\alpha-RuCl_3$ with $j_{eff} = 1/2$ Ru^{3+} ($4d^5$) ions is a particularly promising Kitaev QSL candidate [108]. In Figure 2:16, the Kitaev interactions in the hexagonal $\alpha-RuCl_3$ structure are schematically displayed. The high lattice symmetry leads to isotropic Kitaev interactions, and due to the 94° Ru-Cl-Ru bond angle, there is only a minimal Heisenberg contribution. The Kitaev model is exactly solvable for $\alpha-RuCl_3$ and hosts rich and exotic magnetic phenomena.
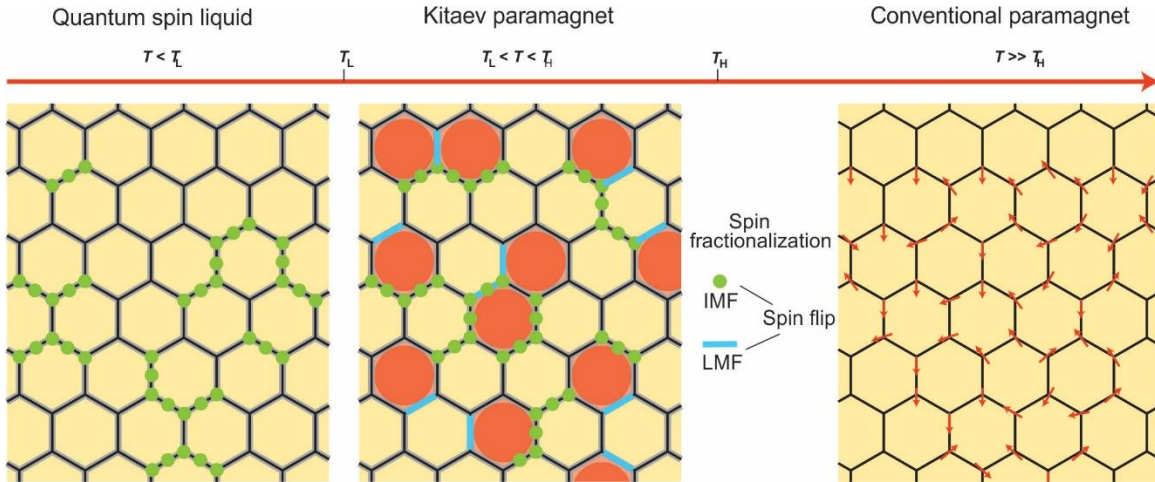
Figure 2:17 Temperature dependent evolution of Majorana fermions in the proximate Kitaev quantum spin liquid α - RuCl₃. (Left) Low-temperature quantum spin liquid phase. (Middle) Kitaev paramagnetic phase. (Right) Conventional paramagnetic phase. (IMF, itinerant Majorana fermions; LMF, localized Majorana fermions). Reproduced with permission from [109].

Theory has predicted that bulk $\alpha-RuCl_3$ assumes an in-plane zig-zag antiferromagnetic order at low temperature, where the magnetic moments of Ru^{3+} are antiferromagnetically aligned with those in neighbouring zig-zag chains, and ferromagnetically aligned with those in the same zig-zag chain [110]. Furthermore, according to recent theoretical studies fractionalization of thermally excited quantum states in the QSL ground state yields two types of Majorana fermions, which are activated at different temperatures [111]. The corresponding temperature dependent evolution, as has been put forward to interpret magnetic specific heat data gained on α-RuCl₃ [107], is schematically depicted in Figure 2:17. In this scenario, below 50 K magnetic

fluxes are frozen in the topologically ordered QSL state and the temperature excites only low-energy itinerant Majorana fermions, while above 50 K, flux fluctuations of localized Majorana fermions also get activated. Upon further increasing temperature, the system finally reaches a conventional paramagnetic phase. Toward implementing α-RuCl$_3$ into vdW heterostructure-based devices, it is important to know how its magnetic ordering changes upon reducing the dimensions from bulk to monolayer. Theoretical calculations have identified four different types of magnetic order in monolayer α-RuCl$_3$ (see Figure 2:18). Although the zigzag AFM phase has the lowest energy among the four spin configurations, the energy difference between the zigzag AFM and FM phases is very small. This is a hint that monolayer α-RuCl$_3$ shows signatures of strong magnetic frustrations and a proximate QSL.
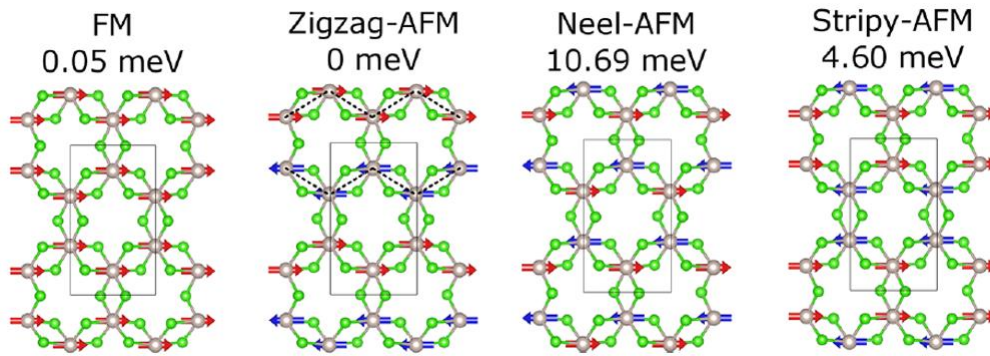
Figure 2:18 Schematic depiction of the supercell and spin configurations of four theoretically predicted magnetic orders in monolayer α-RuCl$_3$, specifically the ferromagnetic, zigzag AFM, Neel-AFM, and stripy AFM phases, together with their relative energies (per formula unit) to the zigzag AFM state. The zigzag chains in the zigzag-AFM phase are represented as dashed lines. Reproduced with permission from [112].

From the experimental side, while early electrical studies on $\alpha-$RuCl$_3$ pointed toward a conventional semiconducting character [113], later resistivity measurements revealed that it is best described as a spin-orbit assisted Mott insulator on a honeycomb lattice [104]. Detailed X-ray absorption studies provided evidence for strong SOC and electronic correlation effects in $\alpha-$RuCl$_3$ and an optical gap of 200 meV was detected by optical spectroscopy [104]. A slightly larger gap of ~250 meV was determined by STS on exfoliated $\alpha-$RuCl$_3$ sheets [114], and ARPES experiments revealed a charge gap on the order of 1.2 eV (at 200 K) [115]. While the SOC strength λ of ruthenium is ~150 meV, the obtained strength for $\alpha-$RuCl$_3$ is slightly weaker (in the range of 100 -130 meV). Magnetic susceptibility measurements on powder samples confirmed that the SOC strength is high enough for the formation of entangled j = ½ moments [116].

The emergence of zig-zag type antiferromagnetic order in bulk $\alpha-$RuCl$_3$ has been experimentally verified by neutron diffraction and magnetic susceptibility measurements. However, the determined critical (Néel) temperature ranges between $T_N \approx$ 6.5 K and 14 K depending on the samples. Neutron scattering and X-ray diffraction measurements on high-quality $\alpha-$RuCl$_3$ single crystals found T_N = 7 K [98]. There is some evidence that samples with stacking faults display rather high T_N values.

First experimental hints for Kitaev interactions in bulk $\alpha-$RuCl$_3$ were gained by neutron scattering [117] and Raman scattering [104] experiments, agreement with calculations based on the Heisenberg- Kitaev model [117]. In the Raman study, fingerprints of Kitaev QSL behavior could be traced in the form of a broad scattering continuum below 100 K which persists in the magnetically ordered state at lower temperatures. Similar spin-phonon scattering has been detected for mechanically exfoliated $\alpha-$RuCl$_3$ nanosheets with a thickness down to ~10 nm, with the onset of Kitaev interactions occurring already below ~180 K [118]. Moreover,

increasingly strong phonon-magnetic scattering as a hallmark of QSLs upon decreasing the thickness of $\alpha-RuCl_3$ nanosheets down to a few layers. This finding has been tentatively attributed to enhanced frustrated magnetic interactions which give rise to a gigantic phonon-magnetic continuum coupling in 2D $\alpha-RuCl_3$ [119].

Overall, the available data indicate that despite the magnetic ordering of $\alpha-RuCl_3$ at low temperatures, QSL features are detectable at temperatures above T_N, testifying the close proximity of $\alpha-RuCl_3$ to the Kitaev QSL model. However, while valuable information about these features is available for bulk $\alpha-RuCl_3$, their detailed dependence on the thickness of $\alpha-RuCl_3$ nanosheets, and if they still persist in the monolayer still needs to be clarified.

2.4   Proximity effects in graphene

2.4.1   Proximity-induced SOC in graphene

2.4.1.1   Spin-orbit proximity

When an electron moves within a solid, it can experience an internal (from the lattice) and/or an external (from a voltage bias applied) electric field, which manifests itself as an effective B-field in the rest frame of reference of the electron. The coupling between the momentum of the electron and the electron spin, representing SOC (see Chapter 2.2.2), provides an indirect means of controlling the spin degree of freedom. While the intrinsic SOC of graphene is rather weak (on the order of 10 µeV [120]), it can be significantly enhanced through the proximity effect that arises upon bringing together graphene with another material that has strong SOC. A special case are vdW heterostructures wherein the other material is also a 2D layer. For a generic vdW heterobilayer, the Hamiltonian can be written as $H = H_1 + H_2 + H_i$, where H_l (l = 1, 2) is the Hamiltonian associated with layer l and H_i accounts for tunneling processes between the two layers [121]. H_1 is given by

$$H_1 = \sum_{k\alpha\alpha'} c_{k\alpha}^\dagger h(k)_{1;\alpha\alpha'} c_{k\alpha'}$$

(2.37)

while H_2 given by

$$H_2 = \sum_{k\alpha\alpha'} d_{k\alpha}^\dagger h(k)_{2;\alpha\alpha'} d_{k\alpha'}$$

(2.38)

In the above two equations, $c_{k\alpha}^\dagger$ and $d_{k\alpha}^\dagger$ ($c_{k\alpha}$ and $d_{k\alpha}$) create (annihilate) single electron states in layers 1 and 2, respectively; moreover, the composite index α describes all other degrees of freedom (i.e., spin, orbital, and particle-hole). If the interlayer tunneling depends exclusively on the difference between the positions, r_1, r_2, of the electrons in the two layers, the crystal momentum is conserved during tunneling and hence

$$H_t = \sum_{k_1 k_2} \sum_{G_1 G_2} \sum_{\alpha_1 \alpha_2} t_{\alpha_1 \alpha_2}(k_1 + G_1)\, e^{iG_2 \cdot \tau_{s_2} - iG_1 \cdot \tau_{s_1}} \times c_{k_1 \alpha_1}^\dagger\, d_{k_2 + (G_2 - G_1)\alpha_2} + h.c.$$

(2.39)

with G_l as the reciprocal lattice vector in layer l, and where the two lattices possess the basis vectors τ_{sl}. A graphene layer with carbon-carbon distance a_0 has two basis vectors $\tau_s = \{(0,0); (a_0, 0)\}$. In a vdW het-

erobilayer, there can be two different kinds of stacking, namely commensurate stacking and incommensurate stacking. In the commensurate case, the bilayer exhibits a periodic structure in real space with a large primitive cell that is commensurate with the primitive cells of both layers. This leads to a well-defined Moiré pattern. By contrast, no such periodicity exists for the incommensurate stacking. Based upon the primitive lattice vectors $a_{li}(i = 1, 2)$ of the two layers, in order for the stacking to be commensurate, four integers m_1, m_2, n_1, n_2 must exist that fulfil the condition:

$$m_1 a_{11} + m_2 a_{12} = n_1 a_{21} + n_2 a_{22}$$

(2.40)

The 2D vectors can be rewritten as complex numbers, i.e., $a_{11} = a_{10}e^{-i\theta_1}, a_{12} = a_{10}e^{+i\theta_1}, a_{21} = a_{20}e^{-i(\theta_2-\theta)}, a_{22} = a_{20}e^{\mp(\theta_2+\theta)}$, where a_{10} is the lattice constant of layer l, $2\theta_l$ is the angle between the primitive lattice vectors of layer l, and θ is the interlayer twist angle. This further leads to the following constrain on the above four integers:

$$\left(\frac{a_{10}}{a_{20}}\right)^2 (m_1^2 + m_2^2 + 2m_1m_2 \cos 2\theta_1) = n_1^2 + n_2^2 + 2n_1n_2 \cos 2\theta_2$$

(2.41)

For commensurate stacking, the twist angle θ is related to the integers according to

$$\theta = \ln \left[\frac{a_{10}(m_1 e^{-i\theta_1} + m_2 e^{i\theta_1})}{a_{20}(n_1 e^{-i\theta_2} + n_2 e^{i\theta_2})}\right]$$

(2.42)

As the size of the primitive cell increases very rapidly with decreasing twist angle θ for $\theta < 5°$, for this regime it is more efficient to use an effective model which keeps only the dominant interlayer tunnelling processes in momentum space, i.e., those for which $|\vec{k}_1 - \vec{k}_2| = |\vec{G}_1 - \vec{G}_2|$ is smallest [122]. If the 2D crystals are triangular lattices and their low energy states are located at the corners (K and K' points) of the hexagonal BZ (like for graphene), then the minimum value of $|\vec{G}_1 - \vec{G}_2|$ is equal to 2K·sin($\theta/2$), where K = $|\vec{K}|$, and there exist three vectors $\vec{q}_i = \vec{G}_1 - \vec{G}_2$ (i = 1, 2, 3) for which this equality is fulfilled. By taking into account all tunnelling processes with $|\vec{k}_1 - \vec{k}_2| = q$, it follows that the higher-order tunnelling processes generate a honeycomb structure in momentum space with the nearest neighbour points connected by the vectors $\vec{q}_i$. In order to introduce spin-orbit proximity to graphene-based vdW heterostructures, a suitable starting point is a generic phenomenological model that describes the Dirac states of graphene with reduced symmetry due to external effects [123]. The corresponding model Hamiltonian reads as:

$$\mathcal{H} = \mathcal{H}_0 + \mathcal{H}_\Delta + \mathcal{H}_l + \mathcal{H}_R + \mathcal{H}_{PIA} + E_D$$

(2.43)

$$\mathcal{H}_0 = \hbar v_F(\tau k_x \sigma_x - k_y \sigma_y) \otimes s_0$$

$$\mathcal{H}_\Delta = \Delta \sigma_z \otimes s_0$$

$$\mathcal{H}_l = \tau(\lambda_l^A \sigma_+ - \lambda_l^B \sigma_-) \otimes s_z$$

$$\mathcal{H}_R = -\lambda_R(\tau \sigma_x \otimes s_y - \sigma_y \otimes s_x)$$

$$\mathcal{H}_{PIA} = a(\lambda_{PIA}^A \sigma_+ - \lambda_{PIA}^B \sigma_-) \otimes (k_x s_y - k_y s_x).$$

The first term $\mathcal{H}_0$ describes a gapless linear dispersion near Dirac points K and K' with two-fold spin-degenerate bands. Here, k_x and k_y are the Cartesian components of the electron wave vector measured from ±K, corresponding to the valley index $\tau = \pm 1$. Moreover, s_i and σ_i are pseudospin matrices, with i = {0, x, y, z}. $\mathcal{H}_\Delta$ describes a mass term which arises when the pseudospin symmetry of graphene is broken when it is placed on a substrate. It leads to the opening of a gap in the spectrum, whose size is modelled by the staggered potential Δ [124]. The pseudospin symmetry breaking depends on the arrangement of graphene above the substrate surface which can be tuned by twisting [125], and on the distance between the layers [126]. Besides the sublattice potential asymmetry, also a Kekulé lattice distortion can open a band gap by introducing nearest neighbour-hopping asymmetry [127].

The term $\mathcal{H}_1$ accounts for the substrate-induced modification of the intrinsic SOC through proximity effects, where λ_1^A and λ_1^B are the sublattice resolved intrinsic SOC parameters.

The terms $\mathcal{H}_R$ and $\mathcal{H}_{PIA}$ account for symmetry breaking due to an electric field vertical to the graphene layer or the presence of a substrate. The term $\mathcal{H}_R$ is the Rashba SOC with parameter λ_R describing the amount of space inversion asymmetry. The term $\mathcal{H}_{PIA}$ is the sublattice resolved pseudospin-inversion asymmetry (PIA) SOC Hamiltonian with parameters λ_{PIA}^A and λ_{PIA}^B reflecting the strength of the mirror plane asymmetry. Interestingly, when the Rashba SOC dominates over the staggered potential, a band inversion occurs, which resembles a time-reversal symmetric version of the quantum anomalous Hall effect [128]. However, this band inversion does not correspond to a topological state, as two (instead of one) pairs of time-reversal symmetric sub-gap helical modes appear at the system boundaries.

With regard to experiments, the possibility to extrinsically enhance SOC in graphene through proximity has thus far mainly been explored by proximity to heavy metal atoms, with the most obvious candidate being the 2D TMDs. It is noteworthy that all thus far investigated graphene/TMD heterostructures in this context were fabricated via mechanical transfer of the TMD sheet onto graphene, which necessarily yields an imperfect heterointerface, and furthermore makes it rather difficult to control the relative lattice orientation. Enhanced SOC in graphene/TMD heterostructures has been observed via weak antilocalization [129] and spin-relaxation measurements [130]. For high-quality graphene/WSe$_2$ heterostructures, a value of 0.2 meV has been reported as a lower bound of the proximity-induced SOC strength, along with a large spin relaxation anisotropy due to the presence of a dominating symmetric SOC [35].

Experiments have also demonstrated the spin generation capability of graphene/TMD heterostructures for both, the use of an electrical current as driving force and through optical control. Evidence for current-induced spin polarization and injection of the generated spin into an underlying graphene layer has been gained for graphene/MoS$_2$ heterostructures, and attributed to a proximity-induced inverse spin Hall effect (ISHE) in graphene, although additional spin-to-charge conversion mechanisms like a proximity-induced inverse Rashba-Edelstein effect (IREE) in graphene or the ISHE within the MoS$_2$ layer may also be operative [131]. More recently, also the Rashba-Edelstein effect (REE) was observed in a graphene/TaS$_2$ heterostructure at room temperature [132]. Optical spin injection into graphene has been achieved for a device wherein a graphene sheet is partially covered by a MoS$_2$ monolayer [133]. Here, illumination of the TMD covered graphene area with circularly polarized light generated spin-polarized carriers due to spin-valley coupling and valley-selective optical absorption. The spin current injected into the graphene could be electrically detected by ferromagnetic electrodes in a non-local geometry at room temperature. The successful injection of optically induced spin currents into graphene has subsequently been confirmed with a graphene/WSe$_2$-heterostructure, in which case the dependence of the non-local spin signal on modulations of the incident light intensity and polarization was studied in detail [134]. Furthermore, electrostatic gating control of spin currents in graphene/TMD heterostructures has been realized even at room temperature. In

the pioneering experiment along this direction, electric field control of the spin current was achieved through gate-tunable spin absorption from graphene into an adjacent MoS_2 layer [135], [136]. Later, it was demonstrated that strong spin-valley coupling in WS_2 or MoS_2 results in a change of over one order of magnitude between the spin lifetimes for in-plane and out-of-plane spins, in good agreement with theoretical predictions [36], [137], [138].

2.4.1.2 Graphene/3DTI heterostructures with spin-orbit coupling

The tetradymite 3DTIs like Bi_2Se_3, Bi_2Te_3, Sb_2Te_3 and BTS have the special property that the lattice constant of the (111) surface has only a small mismatch (<3%) with graphene, as compared to >20% for the TMDs [125]. Correspondingly, graphene and the TI surface can be stacked in a commensurate arrangement, such that the corners of graphene's BZ (K and K') are precisely above the $\bar{\Gamma}$ points of the TI surface BZ, as sketched in momentum space in Figure 2:19(a). In this case, the primitive cell (and BZ) of the heterostructure corresponds to the primitive cell (and BZ) of the TI surface, and the K and K' points of the graphene BZ can be folded back to the $\bar{\Gamma}$ point of the TI (see Figure 2:19)

Figure 2:19 Commensurate graphene and TI stacking configuration. (a) Schematic depiction of the first seven extended BZs of graphene (shown in red), superimposed on the extended BZs of a tetradymite 3DTI (shown in green), for the case of $\sqrt{3} \times \sqrt{3}$ commensurate stacking. (b) Folded BZ for the stacking in panel (a). (c) Real space picture of the $\sqrt{3} \times \sqrt{3}$ graphene-TI commensurate stacking. Reproduced with permission from [125].

The $\sqrt{3} \times \sqrt{3}$ commensurate stacking allows for significant hybridization between the graphene and TI surface states. The calculated electronic bands exhibit a partial lifting of graphene's 4-fold degeneracy (spin and valley degrees of freedom) due to the appearance of two spin-split Rashba bands (cf. Figure 2:20(a)). However, as one sublattice of graphene does not couple to the TI, two of the original graphene states (at the K and K' points) remain spin degenerate. It can furthermore be seen that due to hybridization with the graphene states, the TI surface bands become quadratic at low energy.

The spin texture of the commensurate heterostructure in Figure 2:20(b) resembles the standard Rashba texture, with the in-plane spin being locked perpendicular to the momentum and winding around the $\bar{\Gamma}$ point either clockwise or counter-clockwise. However, DFT-based calculations point toward the emergence of a giant spin lifetime anisotropy in the graphene layer (with the in-plane spins relaxing much faster than the out-of-plane spins) which depends on the Fermi energy [39], as illustrated in Figure 2:21 for the commensurate graphene/Bi_2Se_3 heterostructure.

Figure 2:20 Commensurate graphene/3DTI hybrid bands. (a) Band structure for the commensurate graphene/3DTI heterostructure, as obtained by diagonalization of the corresponding Hamiltonian. The two spin-split Rashba bands are shown in red and blue. Graphene states are shown in grey, the TI surface state bands in green. (b) In-plane spin projection of the eigenstates associated with the bands in panel (a), shown for E = 80 meV. Reproduced with permission from [125].

In particular, the anisotropy is maximal near the graphene Dirac point, reaching values of tens to hundreds, while it decreases to 1/2 at higher energies. This behavior arises because the intrinsic SOC parameters λ_1^A and λ_1^B are almost equal in magnitude but opposite in sign (i.e., $\lambda_1^A \approx -\lambda_1^B$), corresponding to a valley-Zeeman type SOC.

Figure 2:21 Highly commensurate graphene/Bi$_2$Se$_3$ structure. (a-c) Spin texture of the commensurate graphene/Bi$_2$Se$_3$ heterostructure, as obtained from DFT calculations. Each spin component is plotted as a function of angle θ around a constant energy contour. The black, red, and green curves are energy contours corresponding to 34, 100 and 149 meV above the Dirac point of graphene, respectively. (d) Spin lifetime anisotropy of the heterostructure in dependence of energy relative to the Dirac point of graphene. Symbols represent DFT results, solid lines are fits to TB theory. Reproduced with permission from [39].

It should be emphasized that this effect solely relies on proximity-induced SOC and does not require the topological surface states of the TI. Moreover, such gate-tunable spin filtering or charge-to-spin conversion capability cannot be achieved with graphene/TMD heterostructures, for which the much larger lattice mismatch precludes the formation of a small and highly commensurate unit cell.
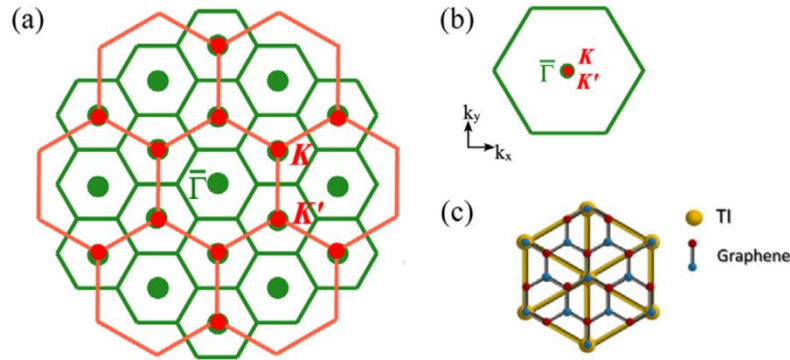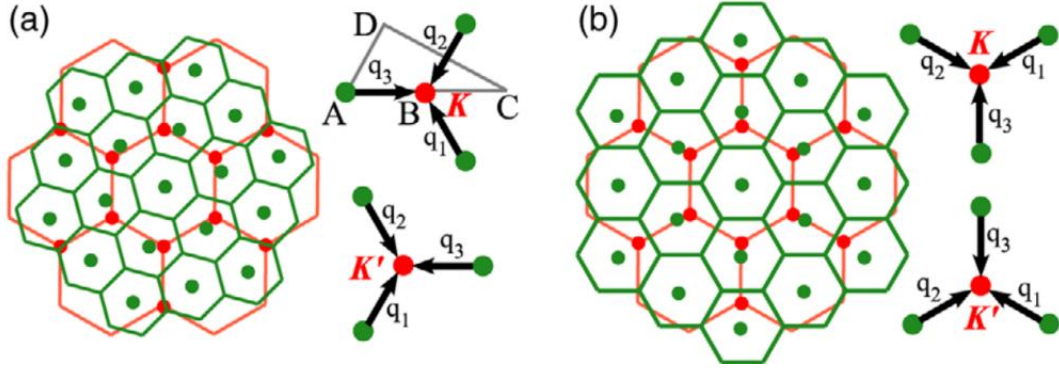

Figure 2:22 Incommensurate graphene and TI stacking configurations. (a) Schematic depiction of the first seven extended BZs of graphene (red) superimposed on the extended BZs of a tetradymite 3DTI (green) for a slight rotation away from $\sqrt{3} \times \sqrt{3}$ commensurate stacking. The vectors $\vec{q}_i$ describe the displacement of the corners of graphene's first BZ from the nearest $\bar{\Gamma}$ points in the TI surface. (b) Corresponding scheme in case of a lattice mismatch between the two components, with the same meaning of the vectors $\vec{q}_i$. Reproduced with permission from [125].

Stacking configurations which deviate from the commensurate stacking can have a mismatch of the graphene and TI lattice constants and/or a small twist angle θ. In Figure 2:22, it is illustrated how the orientations of the TI and graphene BZs are affected in these two cases. In general, due to the conservation of the crystal momentum, the graphene states at the K (K') point now tunnel to the TI surface states with momentum $\vec{q}_i$ (i = 1, 2, 3). In the presence of a twist angle (cf. Figure 2:22(a)), the magnitude of this vector is $\vec{q} = 2K \sin(\theta/2)$, while for the lattice mismatch case, $\vec{q} = |\delta/(1 + \delta)|K$ with δ as the lattice mismatch (cf. Figure 2:22(b)).
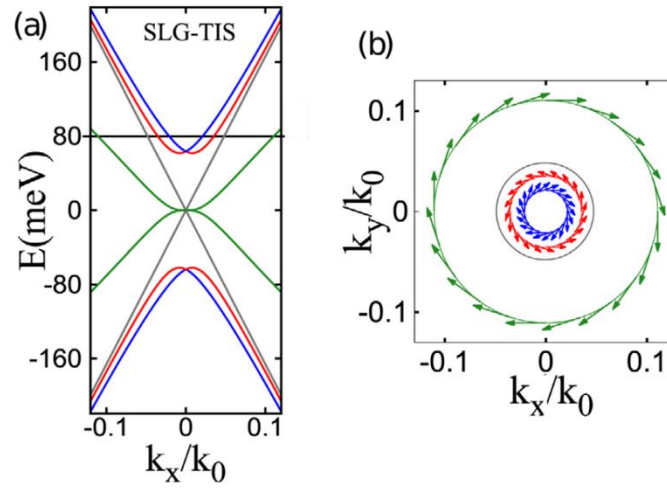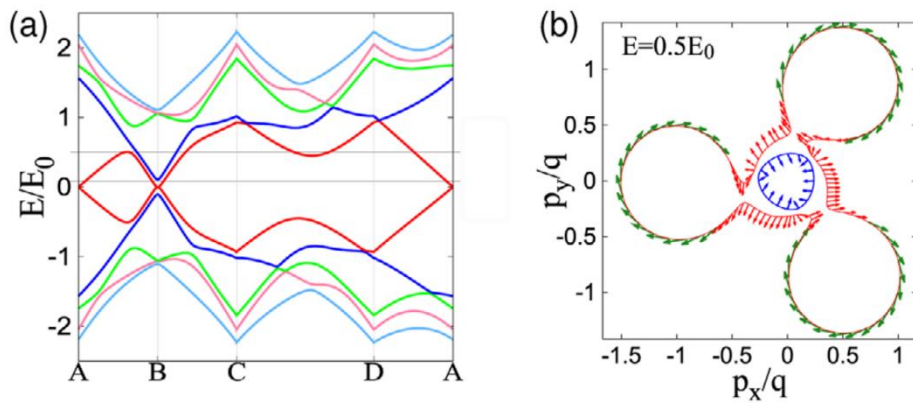

Figure 2:23 Incommensurate graphene/3DTI hybrid bands. (a) Band structure of an incommensurate graphene/3DTI heterostructure with a twist angle of 0.76°, calculated along the path ABCDA in Figure 2:22(a). (b) Corresponding in-plane spin projection of the eigenstates, evaluated at the energy E = 0.5E_0 with E_0 as indicated in panel (a). Reproduced with permission from [125].

The electronic band structure for the interlayer twist angle case is shown in Figure 2:23(a) for a twist angle $\theta = 0.76°$. The corresponding spin texture, as depicted in Figure 2:23(b), is much more intricate than for the commensurate case (compare Figure 2:20(b)). The details of the spin texture can be tuned by the twist angle.
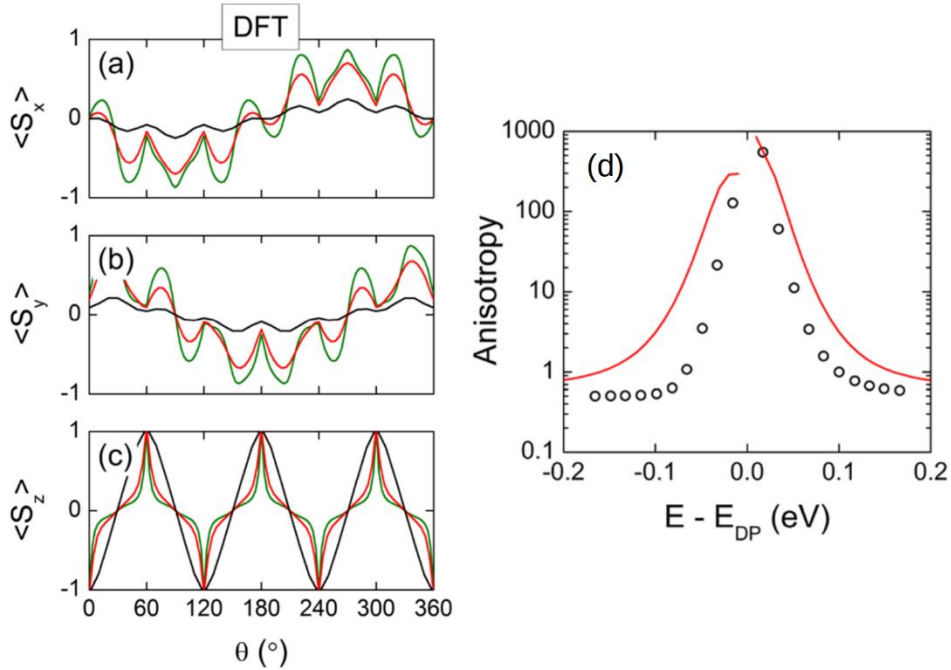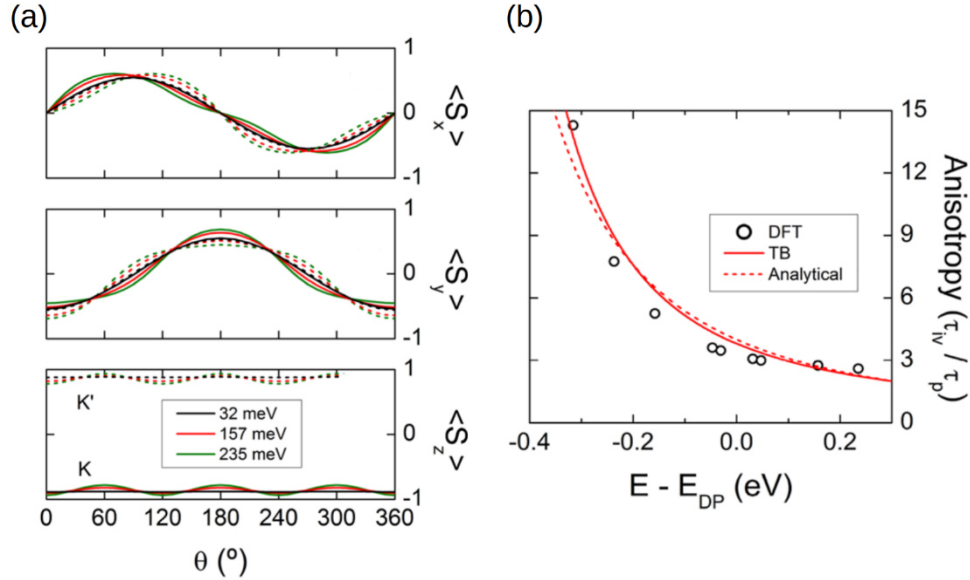

Figure 2:24 Incommensurate graphene/Bi$_2$Se$_3$ structure. (a) Spin texture of an incommensurate graphene/Bi$_2$Se$_3$ heterostructure, as obtained by DFT calculations. Each spin component is plotted as a function of angle θ around a constant energy contour. In each plot, the black, red and green curves are energy contours corresponding to the three indicated energies above the Dirac point of graphene. Solid (dashed) lines are for the K (K') valley. (b) Spin lifetime anisotropy of the heterostructure as a function of energy relative to the Dirac point of graphene. Symbols are the DFT results, solid lines are TB fits, and the dashed line is an analytical expression taken from [139]. Reproduced with permission from [39].

Furthermore, DFT-based calculations indicate that in contrast to the spin relaxation behavior of the commensurate graphene/3DTI heterostructure (cf. Figure 2:21), the spin lifetime anisotropy in the incommensurate case remains high at all Fermi energies and exhibits a strong electron-hole asymmetry, as depicted in Figure 2:24

While many of the above summarized theoretical predictions on graphene/3DTI heterostructures, including the details of the intriguing spin texture, remain to be confirmed by experiment, there are a few studies which clearly testify the presence of proximity-induced SOC, as well as the possibility to tune its strength by electrostatic gating. In a recent magnetotransport study on a hBN-encapsulated graphene/Bi$_{1.5}$Sb$_{0.5}$Te$_{1.7}$Se$_{1.3}$ (BSTS) heterostructure, the carrier density-dependent phase coherence length l_φ was extracted from the observed WAL behavior [140]. In addition, based upon the decrease of l_φ with increasing carrier density, it was concluded that D'yakonov-Perel-type spin scattering in graphene is prevalent, and that a large proximity-induced SOC strength of at least 2.5 meV is present. In another study, by performing spin transport and precession measurements on similar graphene/BSTS heterostructures (although without hBN encapsulation), a sizeable tunability of the spin signal and lifetime through an electrostatic back gate was observed at T = 70 K [38]. Moreover, a spin lifetime on the order of 10 ps was extracted from Hanle data, reflecting a reduction by almost two orders of magnitude compared to pristine graphene devices, which was attributed to the pronounced proximity-induced SOC in the heterostructures.

2.4.2 Magnetic proximity effects in graphene

2.4.2.1 Magnetic proximity

The magnetism arising in graphene by proximity effects induced by an adjacent magnetic insulator can be described by the following discretized Hamiltonian which leaves the linear dispersion of the graphene bands unchanged, except for breaking the valley and electron-hole symmetry, resulting in spin-dependent band splitting and doping, respectively [141]:

$$H = \sum_{i\sigma} \sum_{l} t_{l\sigma} c^{\dagger}_{(i+l)l\sigma} c_{i0\sigma} + \text{H. c.}$$

$$+ \sum_{i\sigma\sigma'} \sum_{\mu=0}^{1} [\delta + (-1)^{\mu} \Delta_{\delta}] c^{\dagger}_{i\mu\sigma} [\vec{m} \cdot \vec{\sigma}] c_{i0\sigma'}$$

$$+ \sum_{i\sigma} \sum_{\mu=0}^{1} [E_D + (-1)^{\mu} \Delta_s] c^{\dagger}_{i\mu\sigma} c_{i0\sigma} \,,$$

(2.44)

where $c^{\dagger}_{i\mu\sigma}$ ($c^{\dagger}_{i\mu\sigma}$) creates (annihilates) an electron of type $\mu = 0$ for A sites and $\mu = 1$ for B sites on the unit cell i with spin $\sigma = \uparrow$ ($\downarrow$) for up (down) electrons; $\vec{m}$ and $\vec{\sigma}$ are unit vectors pointing in the direction of the magnetization and the vector of Pauli matrices, respectively, such that $\vec{m} \cdot \vec{\sigma} = m_x \sigma_x + m_y \sigma_y + m_z \sigma_z$; the anisotropic hopping $t_{l\sigma}$ connects unit cells i to their nearest-neighbour cells $i + l$; the parameters δ, Δ_{δ} and Δ_s describe exchange spin-splittings δ_e (δ_h) of the electrons (holes) and spin-dependent band gaps Δ_{σ} [142]. Finally, E_F indicates the Dirac cone position with respect to the E_F.

Convincing experimental evidence that magnetic proximity can significantly alter the charge transport properties of graphene has been gained for graphene proximitized by the ferromagnetic insulators EuS or EuO. Specifically, the resulting interfacial magnetic exchange field has been reported to exceed 14 T and manifest itself in the anomalous Hall effect [43] or the lifting of the ground state-degeneracy of graphene in the quantum Hall regime [42].

2.4.2.2 Proximity effects in graphene/RuCl$_3$ heterostructures

At the present stage, only very few theoretical investigations are available on graphene/ α-RuCl$_3$ heterostructures. One DFT-based study found that an α-RuCl$_3$ monolayer becomes strained when placed on graphene, whereupon the Kitaev interactions in α-RuCl$_3$ are enhanced by more than 50% in comparison to the unstrained bulk material [143]. At the same time, electron transfer from graphene to α-RuCl$_3$ is predicted to cause n-doping of α-RuCl$_3$ and p-doping of graphene. This leads to an insulator-to-metal transition in α-RuCl$_3$ with the Fermi energy located close to the bottom of the upper Hubbard band of the t_{2g} manifold. This finding points toward the possibility of realizing metallic and even exotic superconducting states.

A second theoretical investigation likewise found that interfacial charge transfer between graphene and α-RuCl$_3$ leads to significant p(n)-type doping of the former (latter), in this case with a degree of about 0.05 e$^-$/Ru atom [144]. The doping is predicted to bring α-RuCl$_3$ considerably closer to the Kitaev point in this system. In this manner, the elusive QSL physics could become accessible to α-RuCl$_3$ without a magnetic field.

It should be mentioned that both theoretical studies above did not explicitly consider spin-orbit proximity effects exerted by α-RuCl$_3$ on graphene, although it is well-established that $\alpha-$RuCl$_3$ has strong SOC (i.e., it is a spin-orbit assisted Mott insulator) [145].
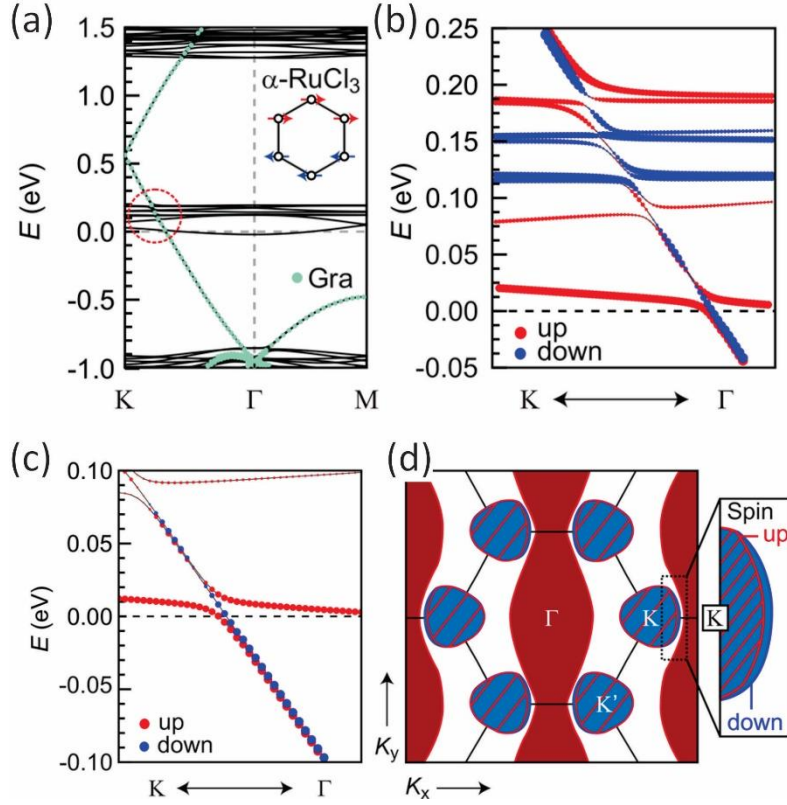
Figure 2:25 DFT-derived band structure of graphene/α-RuCl$_3$. (a) Band structures of graphene (green) and α-RuCl$_3$ in the heterointerface. (b,c) Zoom into the band crossings close to the Fermi level. (d) Calculated electronic structure and Fermi surface of the heterostructure showing the spin up (red) and spin down (blue) Fermi hole pockets around the K and K' points of the graphene Dirac cones. Figure reproduced with permission from [146].

Like for theory, only very few experimental work has thus far been performed on graphene/$\alpha-$RuCl$_3$ heterostructures. In one study, Hall- and magnetoresistance measurements on high-quality heterostructure devices provided evidence for doping and electronic band modification [146]. In particular, the measured transfer curves indicated the presence of an unusually low resistance and strong p-type doping of the graphene. Moreover, fast Shubnikov-de Haas (SdH) oscillations in the longitudinal magnetoresistance were found to display a pronounced beating pattern, which is modulated by the applied gate voltage. Detailed FFT analysis of the oscillations revealed the existence of two different Fermi hole pockets with similar charge carrier densities. Furthermore, the Hall resistance curves displayed non-linear behaviour, indicating the contribution of both holes and electrons to the charge transport. These observations could be rationalized on the basis of DFT calculations which showed that the weakly dispersing bands of $\alpha-$RuCl$_3$ hybridize with the graphene cones at various energies (see Figure 2:25). One of the $\alpha-$RuCl$_3$ bands hybridizes with the graphene band very close to the Fermi energy, which leads to a splitting of the π band states and the formation of Fermi pockets with spin-up or spin-down character around the K and K' points of graphene. Importantly, the spin-down pocket turns out to retain its linear dispersion and to be bigger than the spin-up Fermi pocket which is slightly deformed by the hybridization with the $\alpha-$RuCl$_3$ band. The DFT result furthermore show that the electrons usually occupying the cone between the Fermi level and the Dirac point, now occupy the

$\alpha-$RuCl$_3$ band which is crossing at the Fermi level. This results in a conductive interface system which can account for the very low resistances that were reproducibly observed for all devices.

As another relevant finding, the heterostructures exhibited a zero-field resistance upturn as well as an unexpected damping of the quantum oscillations close to the Néel temperature T_N of $\alpha-$RuCl$_3$. Both these features were tentatively assigned to the onset of additional spin scattering due to spin fluctuations in the $\alpha-$RuCl$_3$.

Evidence for strongly enhanced conductivity, p-type doping of graphene and the presence of multiband transport was also gained by another experimental study of graphene/$\alpha-$RuCl$_3$ heterostructures [147]. In this case, a non-monotonic temperature dependence of resistivity, which is reminiscent of transport in the presence of a magnetic phase transition, was observed between 15 and 40 K, roughly twice as large as T_N of $\alpha-$RuCl$_3$. Overall, the charge transport data were found to be consistent with a picture of inhomogeneous transport where the graphene and $\alpha-$RuCl$_3$ are only intermittently in contact, yielding both highly and lightly doped regions of graphene. This scenario can explain the observation of signatures of slightly doped graphene conducting in parallel to large populations of holes.

Chapter 3   Experimental techniques

Since the discovery of graphene and many other vdW materials, they have been combined into heterostructures which exhibit interesting and new properties that could be useful for various applications. This requires high quality 2D materials of controllable thickness and suitable lateral dimensions. A variety of different techniques such as molecular beam epitaxy (MBE), pulsed laser deposition, thermal evaporation, chemical vapor deposition (CVD) and mechanical exfoliation are available for the preparation of ultrathin sheets [148]. Chapter 3.1 focusses on the CVD growth of BTS for the fabrication of the graphene/BTS heterostructures. Chapter 3.2 describes the methods of mechanical exfoliation and dry transfer of sheets, which are essential for all fabricated devices in this thesis. Chapters 3.3 and 3.4 describe atomic force microscopy (AFM) and Raman microscopy as the most important pre-characterization techniques. The used electrical contact configurations and the required e-beam lithography process are described in Chapters 3.5 and 3.6, respectively. Finally, the heterostructures were electrically characterized (cryogenic charge transport, see Chapter 3.7) and furthermore investigated by different optical techniques such as photocurrent microscopy (Chapter 3.9) and time-resolved Kerr rotation spectroscopy (see Chapter 3.10).

3.1   CVD growth of layered materials

BTS nanoplatelets were grown in a CVD set-up specially adjusted and optimized for this purpose. Compounds like BTS can be synthesized through vapor-solid processes (VS), which require high quality and pure source materials. Here, crystalline powders of ultrapure Bi_2Se_2 and Bi_2Te_3 were used as source materials. The growth process involves sublimation, chemical reaction and deposition, which are controlled by thermodynamics, kinetics and chemistry [149].
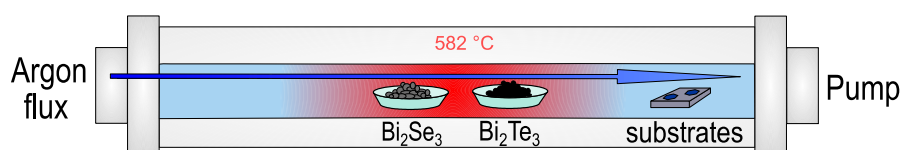
Figure 3.1 Schematic diagram of the CVD set-up for BTS growth. A quartz tube inside the furnace contains the source materials and the growth substrates. Sources are placed in the hot zone (red) and the substrates in a colder zone (blue). The blue arrow indicates the argon flux that carries vapor phase species to the substrates, where the solid BTS crystals form.

The CVD set-up is schematically depicted in Figure 3.1. It mainly consists of a quartz tube inserted into a furnace. The tube can be pumped to a few mbar through a pump connected to one end, while the other end is connected to an argon bottle, allowing to flush the tube with argon or to set a constant argon flux using an additional flow controller. The sublimation temperature of the sources needs to be reached by controlled ramping of the oven temperature using a temperature controller. The temperature profile of the

oven has to be determined in detail beforehand. The evaporated source materials are carried along with the argon flux, whereupon they can undergo chemical reactions. When the vaporized species reach the growth substrates in the colder region, they start to nucleate and form single crystals of different sizes and heights. For the growth of BTS platelets, the following parameters had to be precisely determined and controlled:

Temperature profile of the CVD furnace:
The CVD process takes place in a pumped quartz tube inside a furnace. The furnace temperature is maximal at the center (red colored region in Figure 3.1) and decreases towards both ends of the furnace (blue colored regions in Figure 3.1). A temperature controller sets the maximum temperature and the temperature profile is determined with a suitable sensor for all positions in the tube.

Source quality and position:
The crystal powder of ultrapure Bi_2Se_2 and Bi_2Te_3 is placed at specific positions within the hot center region of the CVD furnace (see Figure 3.1). Wrong positioning would impede optimal sublimation of the sources and prohibit the formation of BTS.

Substrate position:
The temperature gradient is also important for the positioning of the growth substrates. The substrate temperature has a strong impact on the nucleation of the evaporated material, so that BTS crystals grown at colder regions have different sizes, morphologies and quality than those grown at hotter regions.

Pressure:
The quartz tube is pumped and flushed by argon after the sources and growth substrates were mounted into the furnace. It is important to have as little contaminations as possible inside the tube, to avoid oxidation and defects of the synthesized BTS sheets. The vapor of the sources is carried by a constant argon flow towards the substrates. An argon flow controller and the pumping rate control the pressure, which determines how much material is transported.

Step	Set point Temperature	Ramping
1	100°C	25 °C/min
2	400°C	80 °C/min
3	582°C	25 °C/min

Table 3:1 Temperature set points and ramping rates optimized for the growth of BTS.

Heating rate and time:
The heating process is divided into three steps with different ramping rates (see Table 3:1). Especially the heating rate of the third step and the total growth time after reaching the sublimation temperature of 582°C sensitively influence the BTS crystal geometry.

3.2   Mechanical sheet transfer

Scotch tape exfoliation is an easy and fast technique to obtain 2D material sheets of various thicknesses. As the first step, the substrates are cleaned by O_2-plasma and heated to 100°C before the tape with bulk material is pressed on it (Figure 3:2(a)). Such substrates allow for exfoliation of graphene sheets with sizes of up to 30 µm x 30 µm with the so-called 'magic scotch tape' [150]. The contrast of the sheets under the optical microscope is a valuable indicator of the sheet thickness. The Si/SiO_2 substrates with exfoliated graphene are directly used for BTS growth (see Chapter 3.1). For other device configurations, the graphene

sheets need to be transferred onto other 2D materials like hBN, or in between hBN and $\alpha-$RuCl$_3$ sheets (see Chapter 6). Micromanipulators (Figure 3:2(b)) enable exact placement and stacking of different 2D vdW materials [151]. Glass slides coated with PDMS are commonly used to pick up and stack selected sheets in a precise way. Both the sheet on the transparent PDMS stamp and the underlying substrate are visible under the optical microscope, and the substrate can be moved in all directions with the piezo electric xyz-stage. The major micromanipulator components are illustrated in Figure 3:2(b).
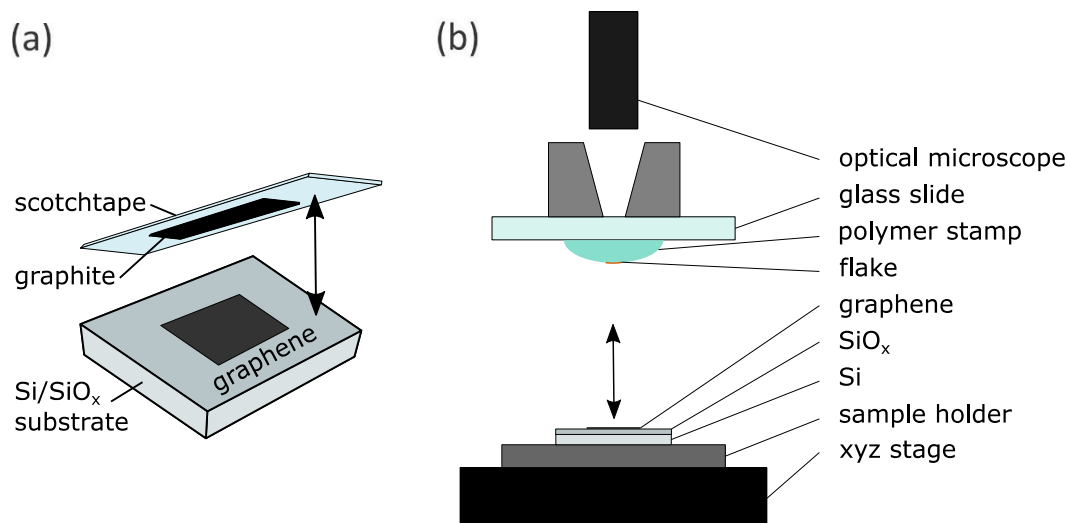
Figure 3:2 Mechanical sheet transfer.(a) Sketch of the scotch tape exfoliation method for graphene. Graphite covered tape is pressed onto a bare substrate and then stripped away again. Graphene (and multi-layers) are left behind on the substrate. (b) Schematic diagram of the micromanipulator used to pick up and stack 2D materials in a precise way.

After successful xy-alignment of the sheets on the PDMS stamp above the substrate, the piezo z-stage is moved until both sheets are in contact. Here parameters like substrate temperature (heater at the xyz-stage), pressure and contact duration are varied depending on whether the sheet on the substrate is picked up, or the sheet on the stamp is stacked on top of the sheet on the substrate. The micromanipulator thus enables the fabrication of heterostructures in a precise and solution-free (dry) manner.

3.3   Atomic Force Microscopy

One important characterization method for heterostructures and the corresponding devices is atomic force microscopy (AFM). All AFM images were taken by the Dimension Icon Scanning Probe Microscope by Bruker. The microscope enables high-resolution surface imaging which yields information about the height and the phase of scanned materials. The excellent height resolution of AFM is crucial for determining the number of layers in the sheets. The AFM allows distinguishing between a graphene mono- (~1 nm height) and bilayer (~2 nm). The principle of measurement is illustrated in Figure 3:3(a). The AFM is composed of a piezo electric xyz-stage onto which the substrate is placed. The region of interest on the substrate is identified with an optical camera. The AFM cantilever which has a sharp tip is scanned over the sample surface with a defined speed. The scan size can be adjusted between ~100 nm and 45 μm. There are two main scanning modes, i.e., the tapping and the contact mode, which operate in different tip-sample interaction regimes (see Figure 3:3(b)). The more common tapping mode is very gentle and fast, with the oscillating tip slightly tapping onto the sample surface. The amplitude of the tip oscillation changes with the sample topography and these changes are tracked by a sensitive detector [152]. In the contact mode, the sample is scanned in constant

physical contact with the tip. For both modes, a laser beam deflected from the cantilever is detected by a photodiode. As the force between tip and sample depends on their distance, the monitored changes are directly related to the topographical height of the sample.
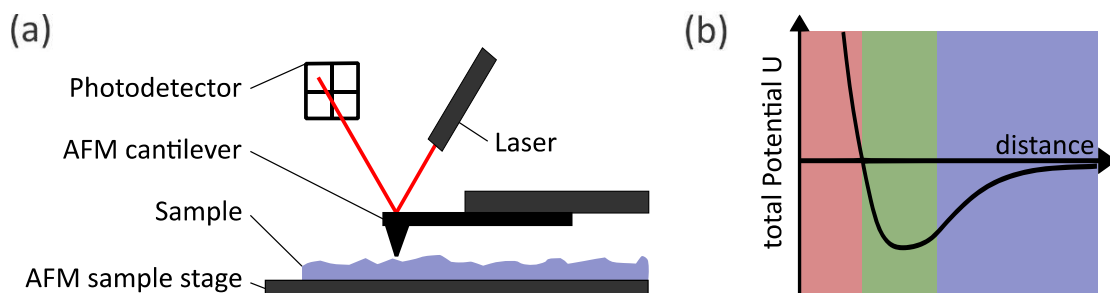
Figure 3:3 AFM operation principle. (a) The cantilever tip scans over the sample surface and the cantilever deflection is detected on a photodetector. (b) Tip-sample potential as a function of tip distance from the sample surface. Depending on the tip-sample distance regime, there are three main operation modes, namely contact mode (red); tapping mode (green); non-contact mode (blue).

3.4 Confocal Raman Microscopy

Another powerful characterization technique for 2D materials and heterostructures is Raman spectroscopy. The used confocal Raman microscope (MonoVista - Spectroscopy & Imaging GmbH) allows choosing between three different laser wavelengths (488 nm, 532 nm and 633 nm). The intensity of the incident laser can be reduced by the ND filter (see Figure 3:4(a)). The incident light interacts with the probed matter locally and the scattered light is analyzed by the spectrometer and collected by a charge-coupled device (CCD). The scattering of light is either elastic (Rayleigh scattering) or inelastic (Stokes and anti- Stokes), as schematically depicted in Figure 3:4(b) [153].
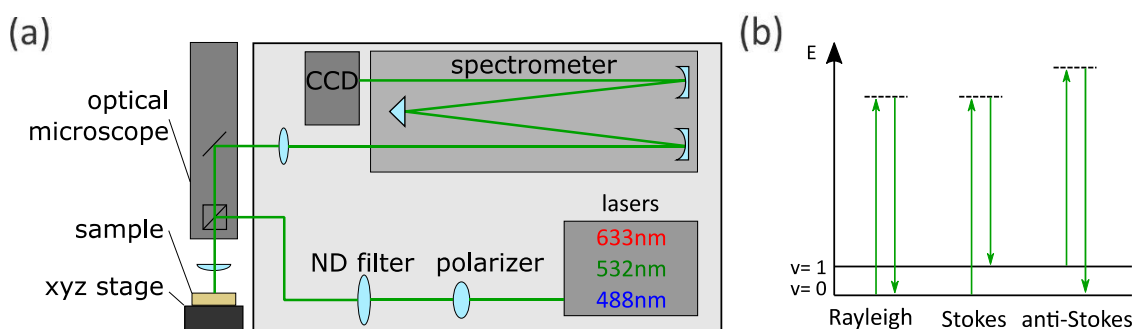
Figure 3:4 Raman microscopy set-up and measurement principle.(a) The sample is illuminated by a laser that is controlled by several filters. The scattered light from the sample collected and analyzed by a spectrometer and a CCD camera. (b) Model of the light scattering processes. The electronic ground state is labeled as v = 0, the first vibrationally excited state with v = 1.

The Raman process involves inelastic scattering of the incident light, where vibrational energy is transferred between the photons and the sample. The probed system can be in the electronic ground state (v= 0) or in the vibrationally exited state (v = 1) prior to the interaction with the incoming light. Incident photons are

absorbed into a virtual electronic state (dashed lines in Figure 3:4(b)). The virtual state undergoes fast relaxation (into the ground state (v=0) or the first vibrationally excited state (v = 1)), which is accompanied by the emission of a photon. Thus the energy between incoming and scattered photons is shifted. The energy of the scattered photon can be lower (Stokes scattering) or higher (anti-Stokes scattering) compared to the incident photon energy (see Figure 3:4(b)). The condition for vibrational modes to be Raman active is a change in polarizability during the vibration. Most of the light is elastically scattered, which is called Rayleigh scattering [153].

The peaks in the Raman spectrum provide useful information about the chemical and structural composition of the sample. A confocal Raman microscope allows acquiring spectra with a spatial resolution (laser spot diameter) on the order of 0.5 - 1 µm, and thus to separately analyze different compounds next to each other. The peak positions, shapes and intensities contain information on defects, strain and doping, and for specific cases also the number of layers (e.g., in a graphene sheet).

3.5 E-beam lithography and device fabrication

All devices for electrical measurements were fabricated by e-beam lithography (EBL) and subsequent metal evaporation. The fabrication process is illustrated in Figure 3:5(a). Compared to EBL, photolithography is faster but the minimal feature size is limited to ~50 nm, and the desired pattern geometry requires appropriate masks. The heterostructure devices investigated throughout this thesis vary in size, shape and position on the substrate, which requires individual patterning with much smaller feature sizes than can be achieved with conventional photolithography methods. EBL is a high resolution patterning technique, which can create nanostructures down to 4 nm in size [154]. Optical and AFM images of the material on the substrate can be loaded into the EBL software in order to design the contact scheme. The substrate is first coated by polymethyl methacrylate resist (PMMA) and then baked on a hot plate at 160 °C. For high resolution and facilitated lift-off, a two-layer PMMA system is used.

(a)
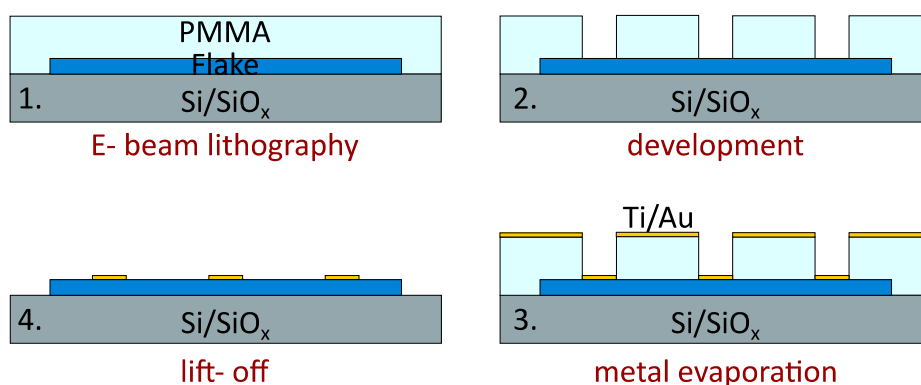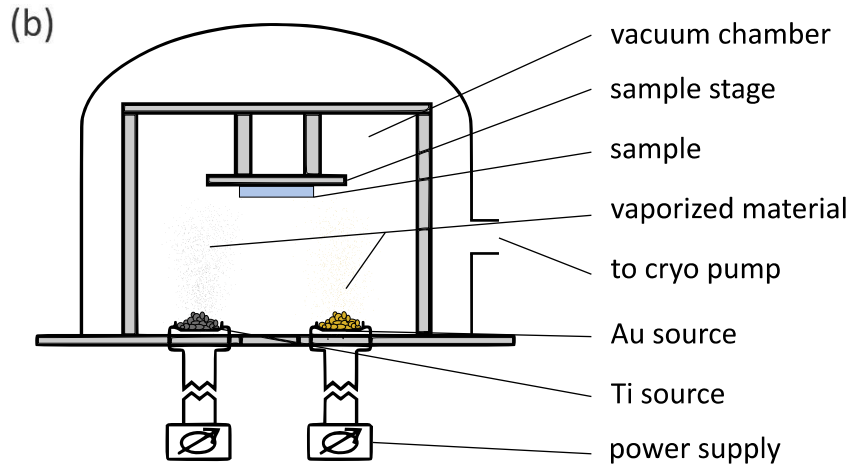
Figure 3:5 E-beam lithography and metal evaporation. (a) Schematic of the device fabrication process. A 2D material flake on a substrate is spin coated with PMMA. After e-beam lithography, the exposed PMMA regions are removed and metal is evaporated on the substrate. Finally, the remaining PMMA and metal is removed. (b) Vacuum chamber for metal evaporation. The sample is mounted on the sample stage. After evacuation of the chamber, metal is evaporated from the electrically heatable boats below the sample.

E-beam exposure causes breaking of the PMMA polymer chains, such that the PMMA in those areas is easily dissolved in MIBK during the development step. The resulting pattern in the PPMA layer on the substrate can be used as an evaporation mask for metals like the commonly used Ti/Au combination. The metal evaporation is performed in high vacuum in a thermal evaporation chamber (see Figure 3:5(b)). The substrate is glued onto a sample holder, which is mounted upside down inside the chamber. Below the sample, there are heatable boats with the two separate metals (Ti and Au) and the chamber is pumped to high vacuum. The metal evaporation rate is precisely measured with a quartz sensor, which is mounted between the boats and the substrate. Depending on the rate and evaporation time, the desired metal thickness is deposited [155]. The chamber is then vented and the substrate immersed in acetone to remove the remaining PMMA together with the metal on top of the PMMA layer. After successful lift-off, all PMMA is removed and the metal remains only in the regions that were patterned by the EBL.

3.6 Electrical measurement geometries

Electrical measurements can be performed in two- or four-terminal configuration. Two-terminal measurements require less device fabrication effort, however, they cannot separate the contact resistance from the intrinsic sample resistance. The two-terminal resistance always contains the two contact resistances plus the sample resistance [75]:

$$R_{2T} = R_{C1} + R_{C2} + R_{sheet} \qquad (3.1)$$

Determining the intrinsic sample resistance is best done with the aid of four contacts. In a four-terminal measurement, the two outer contacts are used as source and drain to pass a current I through the sample, while the two inner contacts measure the voltage drop ΔV (see Figure 3:6(a)). The sample resistance can then be calculated from $R_{4t} = \Delta V/I$.
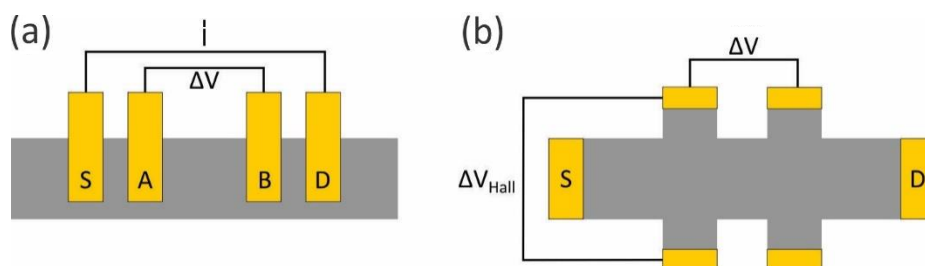
Figure 3:6Electrical measurement geometries. (a) Schematic drawing of a Hall bar geometry with two contact pairs available as voltage probes. (b) Schematic drawing of a four-terminal measurement configuration with the two central contacts serving as voltage probes (A, B).

The Hall bar geometry enables four-terminal longitudinal resistance measurements complemented by Hall resistance measurements (see Figure 3:6(b)). For the latter task, the voltage drop between two opposite contacts is measured and divided by the current passing through the source and drain contacts of the bar. The geometry of the Hall bar must be as accurate as possible to avoid errors in the calculated resistances [75].

3.7 Cryogenic charge transport measurements

The performance of charge transport measurements down to temperatures of a few Kelvin requires cryostats containing cryogenic liquids. All low temperature measurements within this thesis were performed in one of the two available cryostats (one ^{3}He and one ^{4}He cryostat). The ^{4}He cryostat allows measurements down to ~1.3 K (Figure 3:7(a)), whereas the ^{3}He cryostat enables cooling of the sample down to ~250 mK (Figure 3:7(b)) [156]. For both cryostat systems, after mounting of the sample in the sample holder, the insert is either pumped constantly or once before cooling, with a target pressure of ~ $8 \cdot 10^{-6}$ mbar.
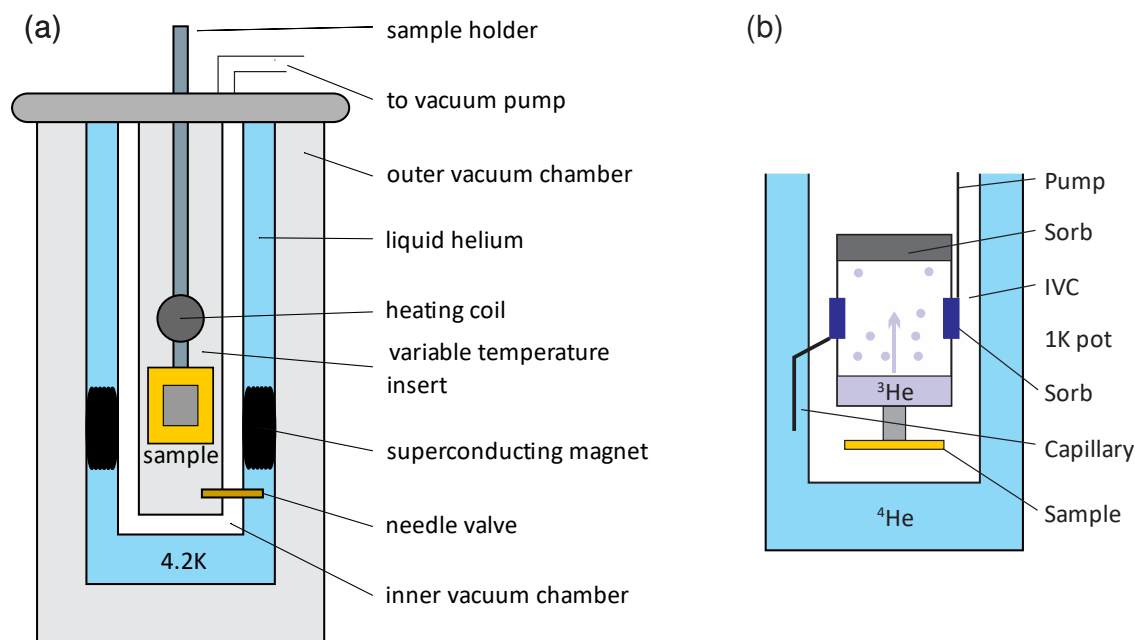
Figure 3:7 Different types of cryostats. (a) Schematic drawing of a cryostat whose reservoir is filled with liquid ^{4}He and the constantly pumped sample space is separated from the liquid by the inner vacuum chamber. In order to reach the base temperature of ~1.3 K, the opening of the needle valve is controlled in order to constantly pump on the ^{4}He. (b) Operation principle of the ^{3}He sorption pump to reach temperatures down to ~250 mK in the ^{3}He cryostat.

The sample is cooled down by controlled opening of the needle valve. For temperature dependent measurements, the temperature can be adjusted through the heating coils that are located close to the sample. In order to perform the electrical measurements, the sample is electrically connected to the set-up via a breakout box. Magnetic fields up to 12 (16) T can be applied through the superconducting magnets within the liquid helium reservoirs. The sample stage is rotatable, thus allowing for angle dependent magnetoresistance measurements in the range of 0.25 K (1.3 K) - 300 K.
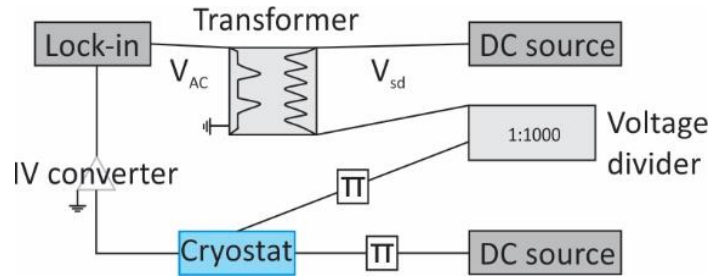
Figure 3:8 Electrical set-up for the cryostats built from a DC voltage source which is modulated by the AC input from the Lock- in. Gate voltages are applied with an additional DC source. The lock-in module records the set current and the voltage drop between the voltage probes .

All devices are fabricated on Si/SiO$_x$ substrates with a metallized bottom surface. They are mounted on gold plated chip carriers with conductive glue, which enables to apply a gate voltage to the sample. The chip carrier is equipped with 20 pins that are wire bonded to the fabricated Ti/Au contacts on the sample. All pins are electrically accessible via the breakout boxes of the cryostat inserts. All measurement modules are connected via low-noise coaxial cables to the breakoutbox. The source current is set by a Keithley 2400 where the amplitude can additionally be varied by the AC input from the 7265 dual phase DSP lock-in amplifier. The same lock-in amplifier is recording the set current and the voltage drops from the probes. The LabView interface allows to control all modules including the B-field and temperature controller as well as the additional Keithley 2400 used to apply gate voltages to the sample.

3.8   Second harmonic microscopy

Second harmonic generation (SHG) microscopy is applicable to structures that lack inversion symmetry. It allows determining the orientations as well as layer stackings of crystalline materials in a fast and non-invasive manner. The SHG signal is detected at half the wavelength of the excitation laser. Polar plots of the SHG signal intensity contain valuable information about the intrinsic symmetry and orientation of the examined layered materials and their stacks [157].

The SHG microscopy experiments were carried out with a cooled Andor Spectrometer (grating 300 g/mm, 500 nm blaze wavelength). The measurement setup is shown in Figure 3:9. The pulses are obtained from a 1064 nm ultrafast fiber laser with a pulse width of ~15 ps. The laser can be tightly focused to a spot size of ~500 nm by an optical objective. For polarization dependent SHG measurements, a λ/2 wave plate is used to change the polarization of the fundamental pulse before it hits the sample.
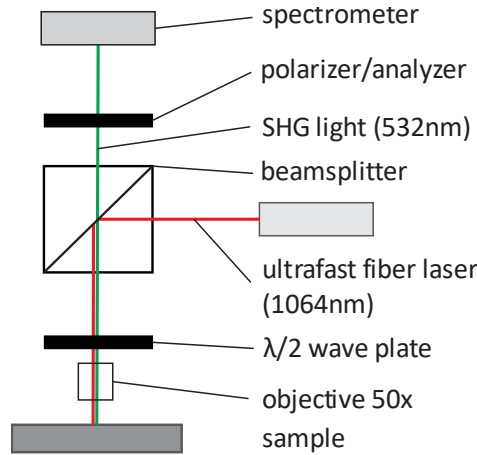
Figure 3:9 SHG and photoluminescence microscopy set up.

The generated SH signal at 532 nm is collected by the same objective lens and sent through a dichroic beam splitter and a linear polarizer/analyzer before being detected by the spectrometer. The orientation of the polarizer/analyzer allows the detection of co-polarized/cross-polarized/unpolarized SHG signals. In the co-polarized configuration the analyzer is aligned to the pump field (emission polarization parallel to the pump field), whereas in the cross-polarized configuration the analyzer is orthogonal to the pump field (emission polarization perpendicular to the pump field). Polarization-dependent photoluminescence spectra are simultaneously recorded. Typically, X-Y maps of a specific sample region are first acquired and then the laser spot is focused onto a specific region of interest on the sample. SHG and PL spectra are collected on the specific spot in dependence of the angle of the λ/2 plate θ and the polarizer/analyzer.

3.9   Photocurrent measurements

Photocurrent microscopy is a powerful tool for exploring the local electronic properties of a contacted 2D material, such as Schottky barriers at the contacts or local doping effects. Photocurrent measurements and spatially resolved photocurrent maps were acquired by scanning the substrate with an electrically contacted nanosheet through a laser spot (with λ = 800 nm for the measurements in this thesis), in dependence of bias voltage and light polarization. The generated photocurrent is detected by a combination of a preamplifier and a multimeter. The spatial resolution of the maps is ~1 μm. For this thesis work, gate-dependent photocurrent maps of the graphene/BTS heterostructures were needed to identify the local CNP (see Chapter 7.1.2) [158].

3.10   Time-resolved Kerr rotation measurements

Time-resolved Kerr rotation (TRKR) measurements based on the magneto-optical Kerr effect discovered by John Kerr in 1877 [159] allow determining the spin dynamics in 2D materials. The Kerr effect consists of a change of polarization and intensity of light upon reflection from a magnetized surface. The detected Kerr-angle θ_K is a measure of the change of polarization between incident and reflected light. The used specially adjusted and optimized TRKR set up allows very sensitive and local measurements of the Kerr effect (see Figure 3:10(a)). Pump (800 nm) – probe (400 nm) pulses are generated at a repetition rate of 80 MHz from a Ti:Sa oscillator. The excitation probe (circularly polarized) and the detecting probe (linearly polarized) are focused and overlapped on the sample region. The more intense pump pulse excites electrons in the sample and induces a net out-of plane spin polarization. This mean magnetization field changes the polarization of

the less powerful probe beam. The reflected pump light is filtered out (by a long-pass filter) and the probe beam is split by a Wollaston beam splitter and analyzed by a photodetector that is balanced by a half-wave plate in a region where no Kerr signal is measurable. The Pump light is sent through an additional delay line, which is a mechanical stage that allows to control the time delay between the pump and probe pulse. The Kerr angle is recorded as a function of the adjusted time delay. The signal difference between the two orthogonal components detected by the two photodiodes is proportional to the Kerr signal.
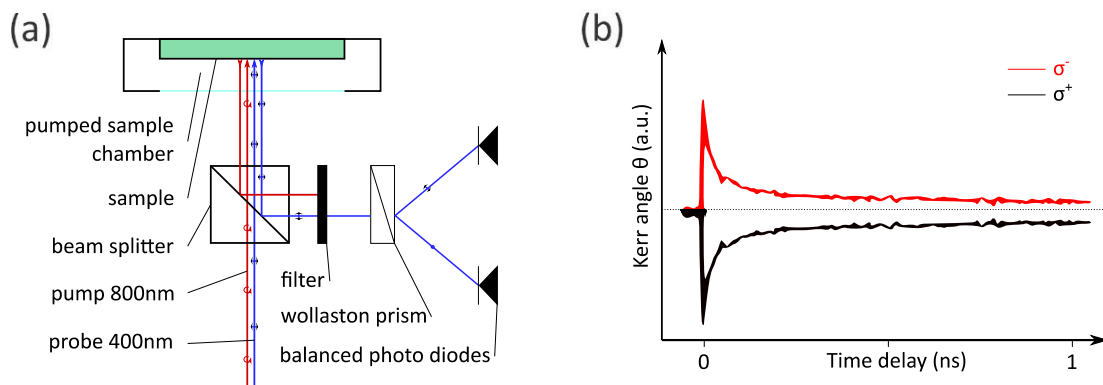
Figure 3:10 TRKR measurements. (a) Schematic drawing of a TRKR setup. Circularly polarized pump pulses and linearly polarized probe pulses are reflected at the sample surface. The pump light is filtered out and the probe pulse is split into two orthogonal components (Wollaston prism) that are detected by two photodiodes. (b) Kerr angle as a function of adjusted time delay between pump excitation and probe detection. The two traces belong to different helicities σ⁺ and σ⁻.

Typical time-dependent Kerr angle traces are shown in Figure 3:10(b). Depending on the pump helicity, the Kerr signal changes its sign and the optically induced polarization decays within a few nanoseconds. The laser spot diameters are ~1 μm and an optical camera allows exact positioning and focusing of the beams in the region of interest on the substrate. The Wollaston prism polarizer needs to be properly aligned in order to split the probe pulse into two orthogonal components. Pump and probe beams are modulated by a mechanical chopper (yielding better signal-to-noise ratios for chopping frequencies in the Hz to kHz range) and detection is made with lock-in amplifiers. The spin relaxation time can be extracted from the Kerr data based upon theoretical model simulations [160].

Chapter 4 Growth and characterization of graphene/Bi$_2$Te$_2$Se heterostructures

In this chapter, the CVD-based growth characteristics of the Bi$_2$Te$_2$Se (BTS) on two different types of graphene sheets are investigated, and the resulting heterostructures are characterized with respect to morphology, as well as the presence of strain and doping effects. The employed vdW epitaxial growth has the potential to yield an intimate coupling between the materials, and to enable commensurate growth in case that the lattices have small mismatch (like for graphene and BTS). The intimate coupling can lead to stronger doping effects than if the same type of heterostructure is obtained by mechanical dry transfer, as in the latter case contaminations at the interface may impede charge transfer between the two sheets. Moreover, even for small lattice mismatch additional factors may introduce significant strain, in particular the influence of the underlying SiO$_2$ surface of the substrate during the growth process. In addition, the growth is expected to sensitively depend on the type and density of defects in the graphene growth substrates. As the vdW epitaxial growth is often performed at higher temperatures (well above 300 °C), it is furthermore important to check to which extent it introduces additional defects into the graphene.

4.1 CVD growth of graphene/Bi$_2$Te$_2$Se heterostructures

The major goal of the CVD growth experiments was to identify the parameters required for obtaining regular BTS nanosheets with defined size and orientation. The individual BTS nanosheets should by crystalline, uniform and have atomically smooth surfaces. These features were evaluated using a combination of optical microscopy, AFM and Raman spectroscopy, as described in the following.
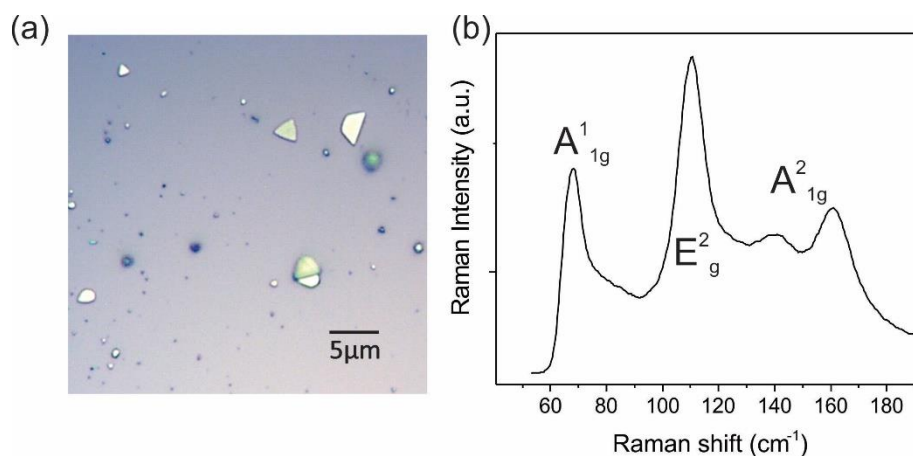
Figure 4:1 CVD growth of BTS on bare Si/SiO$_x$ substrate. (a) Optical micrograph of BTS crystals with different morphologies, lateral sizes and optical contrast depending on their thickness. (b) Representative Raman spectrum (λ_{exc} = 532 nm) of a BTS flake on a Si/SiO$_2$ substrate.

In initial tests, the growth of BTS on bare Si/SiO$_2$ substrates was optimized. Figure 4:1(a) shows several BTS crystals grown on a bare Si/SiO$_2$ substrate. Their stoichiometry could be confirmed by Raman spectroscopy (see Figure 4:1(b)). The characteristic Raman peaks of BTS are in reasonable agreement with the literature. These are the A_{1g}^1 peak (~64.2 cm^{-1}), the E_g^2 peak (~106.8 cm^{-1}) and the A_{1g}^2 peak with two components (~137.8 cm^{-1} and ~153.8 cm^{-1}) [161]. The spectrum was recorded at room temperature with a laser excitation wavelength of 532 nm.
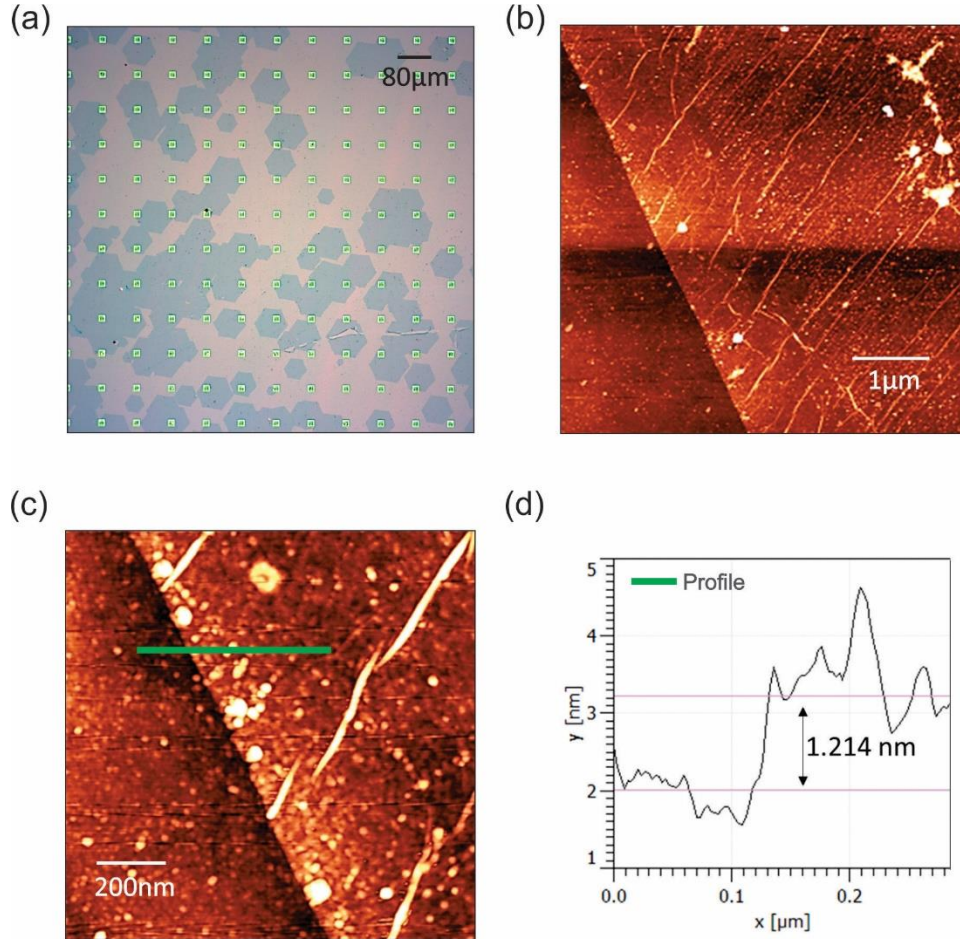
Figure 4:2 Hexagonal shaped CVD graphene. (a) Optical image of hexagonal graphene islands transferred by the wet etching method onto a Si/SiO$_x$ marker substrate. (b) AFM image of part of a hexagonal graphene island. (c) Higher magnification AFM image of the edge region of a graphene island. (d) AFM height profile of the graphene edge region, taken along the green line in panel (c).

For the present thesis, heterostructures comprising BTS on monolayer graphene were most relevant, as theoretical predictions of their electronic properties are available in the literature [139]. The easiest access to large areas of graphene is provided by the transfer of CVD-grown graphene via wet etching techniques onto Si/SiO$_2$ substrates. For this purpose, we compared CVD graphene from two different commercial suppliers (Graphenea Inc., Spain; 2D semiconductors Inc, USA) and from one collaboration group (Prof. Dinh Loc Duong, Sungkyunkwan University, South Korea). The wet etching method in general yielded large areas of pristine graphene monolayers that are suitable for the growth of BTS. For the goal of electrically contacting the graphene sheets for subsequent charge transport and optical measurements, the graphene from the collaboration group was advantageous as it does not cover the entire Cu foil but forms hexagonal islands that are mostly separated from each other. This allows for contacting single sheets of graphene without the

need of an additional etching step. Figure 4:2(a) shows an optical image of such hexagonal graphene islands transferred onto a Si/SiO$_2$ substrate equipped with a position marker array (green squares).

In the AFM image of a graphene island in Figure 4:2(b), a relatively high density of graphene wrinkles is visible, along with PMMA residues stemming from the transfer process. Figure 4:2(c) is a zoom into the edge region of the graphene island, which has an AFM height of ~1.2 nm (cf. Figure 4:2(d)), confirming the presence of monolayer graphene. For the BTS growth, the substrates with transferred CVD graphene were precisely placed at pre-determined positions in the CVD furnace, followed by several cycles of pumping of the quartz tube and flushing it with argon in order to reduce the oxygen concentration. The used growth parameters including growth time, temperature, pressure and argon gas flow are listed in section 3.1 (Table 3:1). The result of a BTS growth on CVD graphene is exemplified in Figure 4:3(a). Although much effort was spent to optimize the growth parameters, BTS nanosheets of good quality could not be achieved. Instead, only small and irregular BTS crystals were obtained. As the lattice mismatch between BTS and graphene is relatively small (~0.9 % [162]), it is unlikely to be responsible for the low quality [163]. Raman spectra of the heterostructures display the peaks expected for BTS and in addition a significantly enhanced D-peak of the underlying graphene (see Figure 4:3(b)). As the intensity of the D-peak is related to the presence of defects in the graphene sheet [164], the unsatisfactory growth is attributable to the high defect density of the CVD graphene which leads to very small BTS flakes with very rough surface morphology. The high defect density stems partially from the transfer process, where the used Cu etchant can introduce additional defects and dopants. Although considerable effort was devoted to optimizing the transfer method for CVD graphene, including the use of bubbling methods [165], reduced etchant concentrations and additional cleaning steps, this could not sufficiently improve the growth quality to render the heterostructures suitable for device fabrication.
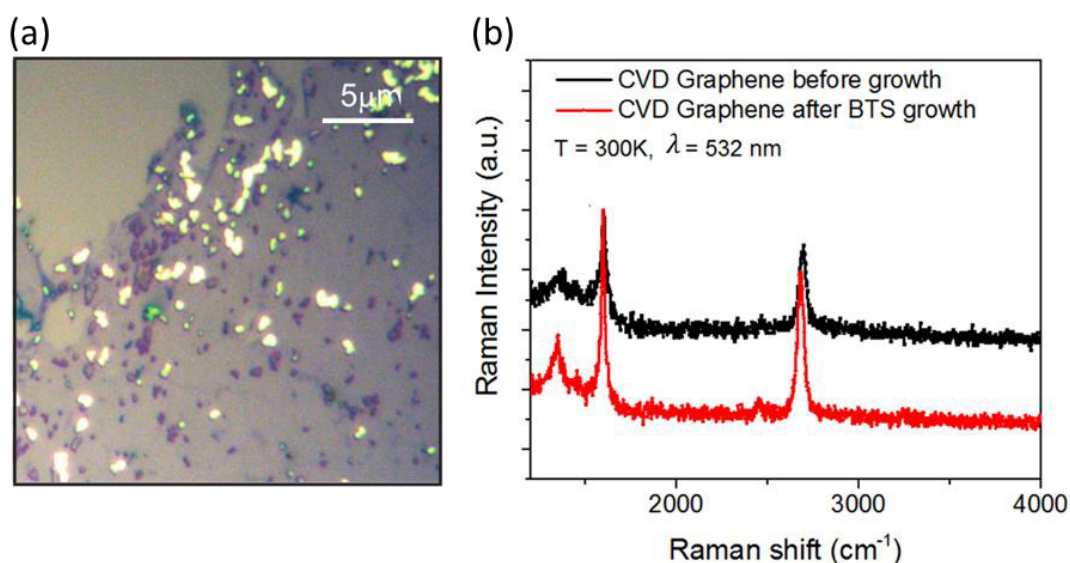
Figure 4:3 BTS growth on CVD graphene. (a) Optical image of a typical BTS growth on top of transferred CVD graphene (hexagonal islands). (b) Raman spectra of CVD graphene before BTS growth (black line) and after BTS growth (red curve).

As an alternative to CVD graphene, we used mechanically exfoliated graphene which has the advantages that is contains less defects and can be obtained in the form of long, regular stripes. However, a disadvantage of exfoliated graphene for the present purpose is the large variety of sheets that are obtained. Hence, monolayers need to be identified using optical microscopy, AFM and Raman spectroscopy before the BTS growth. Usually Si/SiO$_2$ substrates with a position marker array are used to reproducibly find the

same sheets in the various characterization experiments. Unfortunately, the standard gold markers are not compatible with the growth process, since they get completely covered with BTS and hence become un-identifiable. To overcome this hurdle, special markers had to be fabricated, where the gold is coated by a protective SiO_x layer on top.

The exfoliated graphene (the mechanical exfoliation protocol is described in section 3.2) was examined by optical microscopy, and graphene monolayers were selected by optical contrast. Figure 4:4(a) shows a typical exfoliated graphene sheet on a Si/SiO_2 substrate. The upper darker region consists of multilayer graphene, while the lower bright region is a graphene monolayer. Further characterization by AFM revealed the presence of scotch tape residues and other contaminations on the graphene (see Figure 4:4(b)). Nonetheless, in comparison to the CVD graphene, the surface of the exfoliated graphene proved to be much cleaner and to have less wrinkles. The AFM height profiles allowed determining the number of layers in the examined graphene sheets, as exemplified in Figure 4:4(c) where profiles 1 and 2 indicate a single graphene layer (~1 nm height), and with two additional layers stacked on top visible in profile 2.
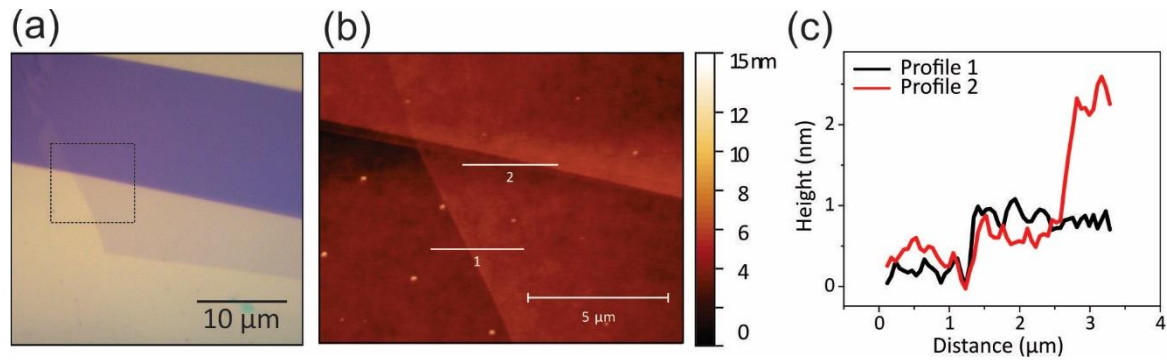
Figure 4:4 Optical and AFM characterization of exfoliated graphene. (a) Optical image of the investigated graphene sheet. The black square indicates the region shown in the AFM image. (b) AFM image revealing sheets regions of different thickness. (c) AFM height profiles taken along lines 1 and 2 in panel (b).

For Raman spectroscopy of graphene on Si/SiO_x (with λ_{exc} = 532 nm), the characteristic Si mode at ~ 520 cm^{-1} was used for calibration. Raman spectra of the graphene in Figure 4:4 are shown in Figure 4:5. They feature two characteristic peaks, specifically the G-peak at ~1580 cm^{-1} and the 2D peak at ~2690 cm^{-1}. The spectrum in Figure 4:5(a) was acquired on a monolayer graphene region, while the one in Figure 4:5(c) belongs to a multilayer graphene region. A clear difference between the two spectra is visible in the shape of the 2D peak. This peak is sensitive to the number of graphene layers and thus helpful for distinguishing between mono-, bi- and multilayers [166]. The 2D peak of the single layer can be fitted by a single Lorentzian peak, while the 2D peak of multiple layers requires the convolution of multiple Lorentzian peaks. The 2D peak and corresponding Lorentzian fits are shown in Figure 4:5(b) for the monolayer case and in Figure 4:5(d) for the multilayer case. While the 2D peak of the monolayer is symmetrical and can be perfectly fitted by one Lorentz fit peak (green line), the 2D peak of the multilayer is highly asymmetric and requires nine Lorentz fit peaks (green lines). Raman spectra of graphene furthermore contain information on amount of defects, strain and doping of the sheets, all of which are important for the interpretation of subsequent measurements on the heterostructures. Details of such analysis are described below in section 4.2.
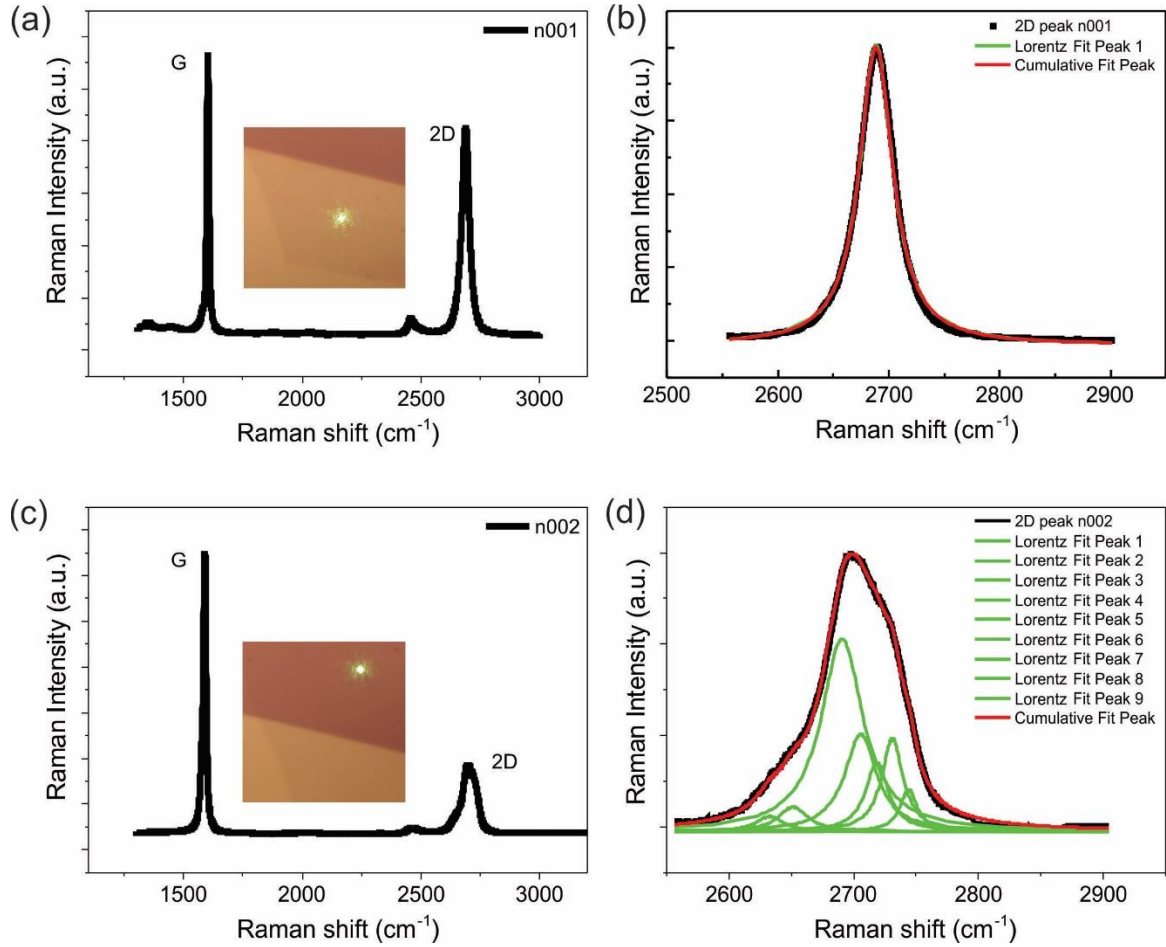
Figure 4:5 Raman spectroscopy of exfoliated graphene flakes. (a) Raman spectrum of monolayer graphene. The measurement position is visible in the optical image (inset). (b) Zoom into the 2D peak of the monolayer graphene spectrum in panel (a). The black curve represents the original spectra; the red curve is a cumulative fit peak to the Lorentzian fit peak (green curve). (c) Raman spectrum of multilayer graphene. The measurement position is visible in the optical image (inset). (d) Zoom into the 2D peak of the multilayer graphene spectrum in panel (c). The black line represents the original spectra; the red curve represents a cumulative fit to the Lorentzian fit peaks (green curves). All spectra were acquired with λ_{exc} = 532 nm, a maximum incident power of 35μW and 10 s acquisition time.

After the successful identification and characterization of monolayer graphene, selected substrates were placed in the CVD furnace for BTS growth. The low pressure and high temperature during the BTS growth helps to remove remaining impurities on the graphene. An example for the successful growth of oriented and relatively large BTS crystals on exfoliated graphene is provided in Figure 4:6. Slow growth rates were found to enable an ordered epitaxial growth, with the formation of triangular shaped BTS flakes (as exemplified by the flakes marked in the AFM image in Figure 4:6(b)) besides spiral-, dendrite- and randomly shaped flakes. The triangular flakes are most likely the result of a smooth, commensurate growth. In general, each growth yielded a variety of BTS flakes of different morphology even on the same graphene sheet. Interestingly, the growth turned out to be strongly favored on multilayer vs. monolayer graphene, an observation which likely reflects the smoother surface of the former sheets. Thinner BTS flakes (thickness below ~5 nm) either have a triangular shape when they have a small lateral size (less than ~4 μm) or a random shape when they are much larger. The triangular nanosheets display uniform colors in the optical images, indicating uniform thicknesses. For essentially all growth conditions, numerous small clusters of BTS are found between the BTS flakes, as concluded from high magnification AFM measurements.

The thickness of the BTS flakes can be estimated from the optical color contrast, with dark purple indicating very thin flakes (height below ~5 nm) and a bright yellow appearance indicating very thick flakes (height above ~20 nm). Many, but not all, triangular nanosheets have the same orientation and are aligned at multiples of 60°, as expected based upon the triangular lattice of BTS. This observation is in accord with the fact that the strength of the vdW interactions between BTS and graphene can locally vary due to the presence of defects and the corrugation of the SiO_2. Very thick BTS flakes often have defined or random orientations.
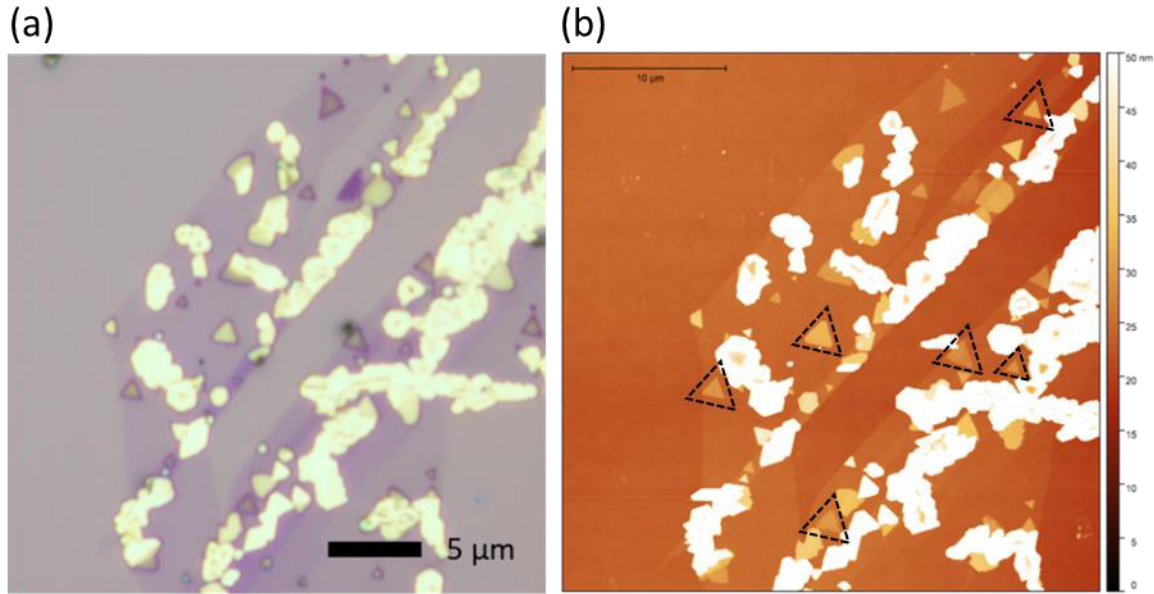
Figure 4:6 BTS growth on top of exfoliated graphene. (a) Optical image of a graphene/BTS heterostructure. (b) AFM image of the same region.

An overview of the major BTS morphologies obtained by growth on exfoliated graphene is given in Figure 4:7. Figure 4:7(d) shows an optical image of a large graphene flake with various BTS flakes grown on top of it. The corresponding AFM image is shown in Figure 4:7(e). Figure 4:7(f) and (g) are zooms into a very thin and a very thick BTS flake. Many of the thick BTS flakes exhibit hole-like features at their center (see Figure 4:7(g)), which are presumably the result of many small triangular crystals laterally growing together, similar to the growth characteristics of MoS_2 [167]. Other thick flakes show spiral structures (cf. Figure 4:7(c)), analogous to the CVD growth of WS_2 [168]. Thin triangular flakes have very uniform thicknesses and smooth surfaces. The thinnest obtained flakes have rough edges and irregular shapes, in some cases featuring a 'frame' at the periphery (see Figure 4:7(f)). The quartz tube remains inside the oven after stopping the growth, such that the substrates cool down quite slowly to room temperature (over a period of ~3.5 hrs.). During the cool down, atoms in BTS are still mobile and can diffuse on the graphene. Such atom diffusion towards thicker BTS flakes can explain both, the irregular shape of the very thin flakes and the ´frame´ that is visible in the AFM images. Figure 4:7(a) -(c) belong to the same graphene/BTS heterostructure: Figure 4:7(a) shows the optical image of a graphene stripe with thick BTS crystals grown on top of it. The white square highlights a BTS crystal that is entirely grown until the edges of the graphene stripe. Figure 4:7(b) shows the AFM image of the highlighted graphene/BTS region. The scalebar of the AFM image is set to low values, in order to recognize the graphene stripe below the BTS. Figure 4:7(c) shows the same graphene/BTS region, but this time the scalebare of the AFM image is set to high levels to make the surface of the BTS crystal visible.

Heterostructures with a well-defined shape of the BTS nanosheets and the underlying graphene were selected for electrical contacting (see Chapter 5.2).
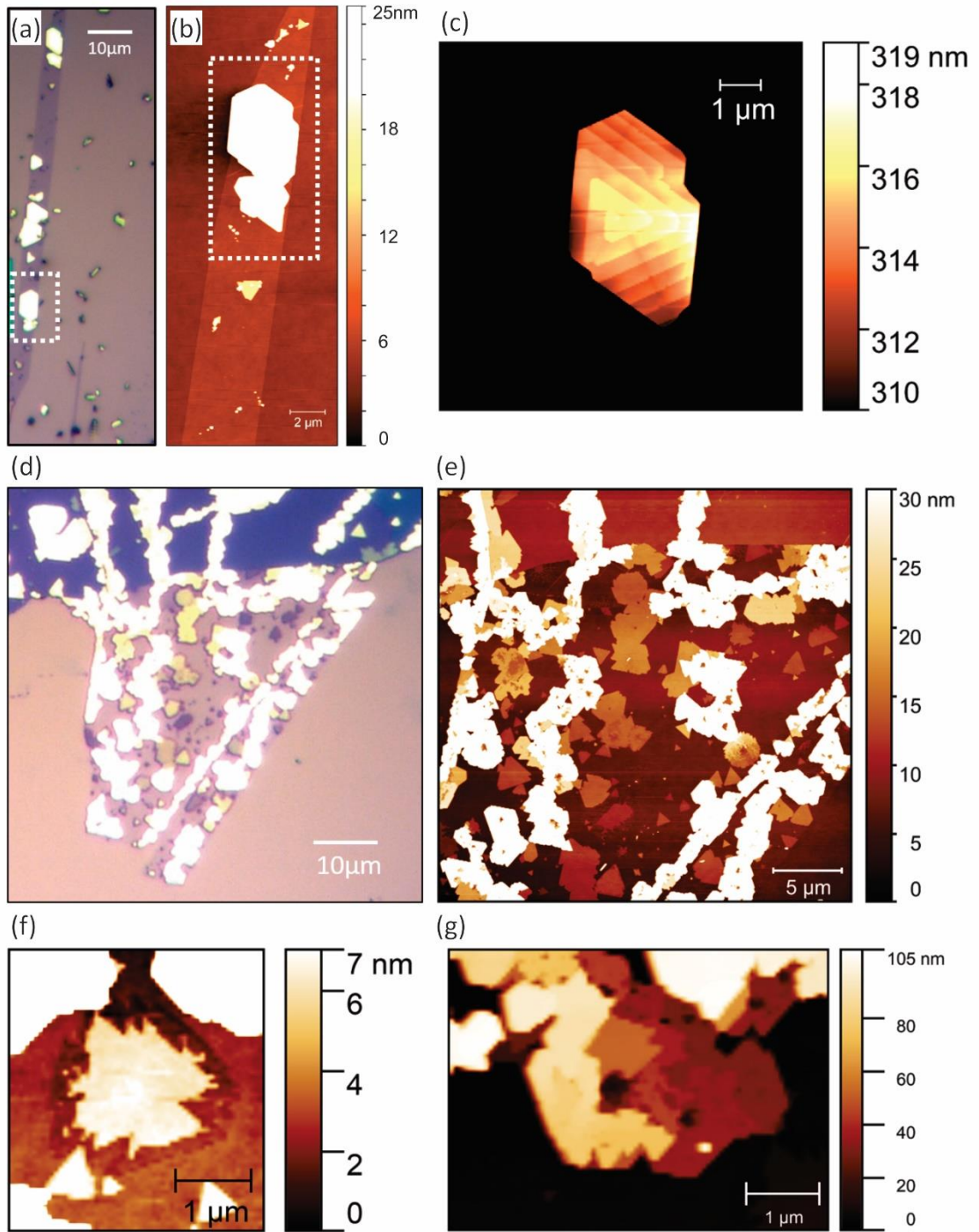
Figure 4:7 AFM images of different BTS growth geometries on graphene. (a) Optical image of a graphene stripe with very thick BTS grown on top. The white square marks the area that is shown in the next AFM image. (b) AFM image of the graphene/BTS heterostructure from a). The scale is chosen very low to make the graphene stripe visible (0nm – 25 nm). The white square marks the area that is shown in the next AFM image. (c) Zoom into the BTS crystal shown in the AFM image from b). The scale is set to values between 310nm and 320 nm in order to see the surface of the thick BTS crystal which resembles a spiral structure. (d) Optical image of a large graphene area connected to a multilayer graphene region. (e) AFM image of the graphene/BTS from figure d). (f) Zoom into a graphene area with very thin BTS growth. The BTS crystal has rough edges and is surrounded by a triangular 'frame'. (g) Zoom into very thick BTS crystals. The 'hole feature' in the center of the flake becomes visible, which indicates a dendrite like growth.

4.2 Strain and doping in graphene/Bi$_2$Te$_2$Se heterostructures

Atomically thin materials are especially susceptible to (unintentional) doping and the introduction of strain. We examine Raman spectra of BTS depending on the thickness of the grown crystals. For evaluating strain and doping effects in the underlying graphene, a correlation analysis of the G- and 2D-peak energies in the graphene Raman spectra was done. Such G-2D plots are commonly used for the characterization of graphene and its heterostructures and allow to separate the effects of strain and doping [169]. All spectra shown below were collected with 532 nm laser excitation, a 100x objective and a low laser power (5% corresponding to ~35 µW), in order to avoid destruction of the BTS crystals through local heating. While the graphene proved to be stable even against high power laser excitation, the BTS degraded much more easily. The sensitivity of the BTS crystals is illustrated in Figure 4:8, where the maximum laser excitation power of the Raman microscope causes destruction of a BTS flake within 10 s. Consequently, a laser power of only 5% of the possible maximum was chosen to minimize degradation of BTS, while the signal is still strong enough.
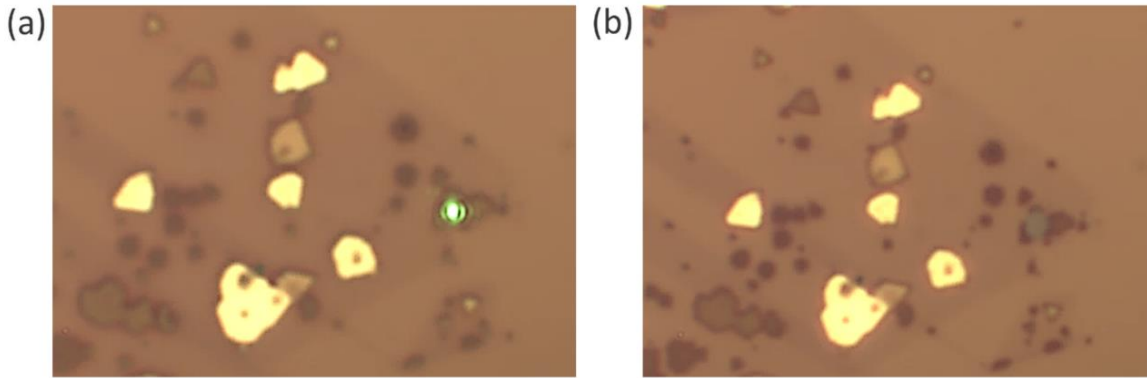
Figure 4:8   Destruction of BTS under the laser spot of the Raman microscope. (a) Optical image taken with the confocal Raman setup. The laser spot is visible in bright green. A spectrum is acquired at this position with the maximum laser power (700 µW) with 10 s acquisition time (λ_{exc} = 532 nm). (b) Optical image of the same area after the Raman spectrum was taken, revealing severe destruction of the BTS crystal.

Figure 4:9(a) shows representative Raman spectra recorded on various BTS flakes (grown on the same graphene sheet) with different thicknesses between 1.7 nm and 25 nm. The exact positions of the laser spot are indicated in the optical image of the graphene/BTS heterostructure in Figure 4:9(b). While the shape of the Raman peaks does not change with flake thickness, there are small differences in intensity and the peak positions. The Raman intensity of the four characteristic peaks is plotted in Figure 4:9(c) as a function of flake thickness. The second thinnest BTS flake (~2.4 nm thickness) shows a clear enhancement of Raman intensity for all of the peaks. A similar observation has been made for thin sheets of Bi$_2$Te$_3$ [170] and Bi$_2$Se$_3$ [171] and can be attributed to crystal- symmetry breaking in thin films [170].

Figure 4:9 d) shows the relation between the peak positions and BTS flake thickness. It is evident that below 5 nm thickness most of the peaks experience a slight downshift, which can be assigned to increasing mechanical stress in the crystals [171].
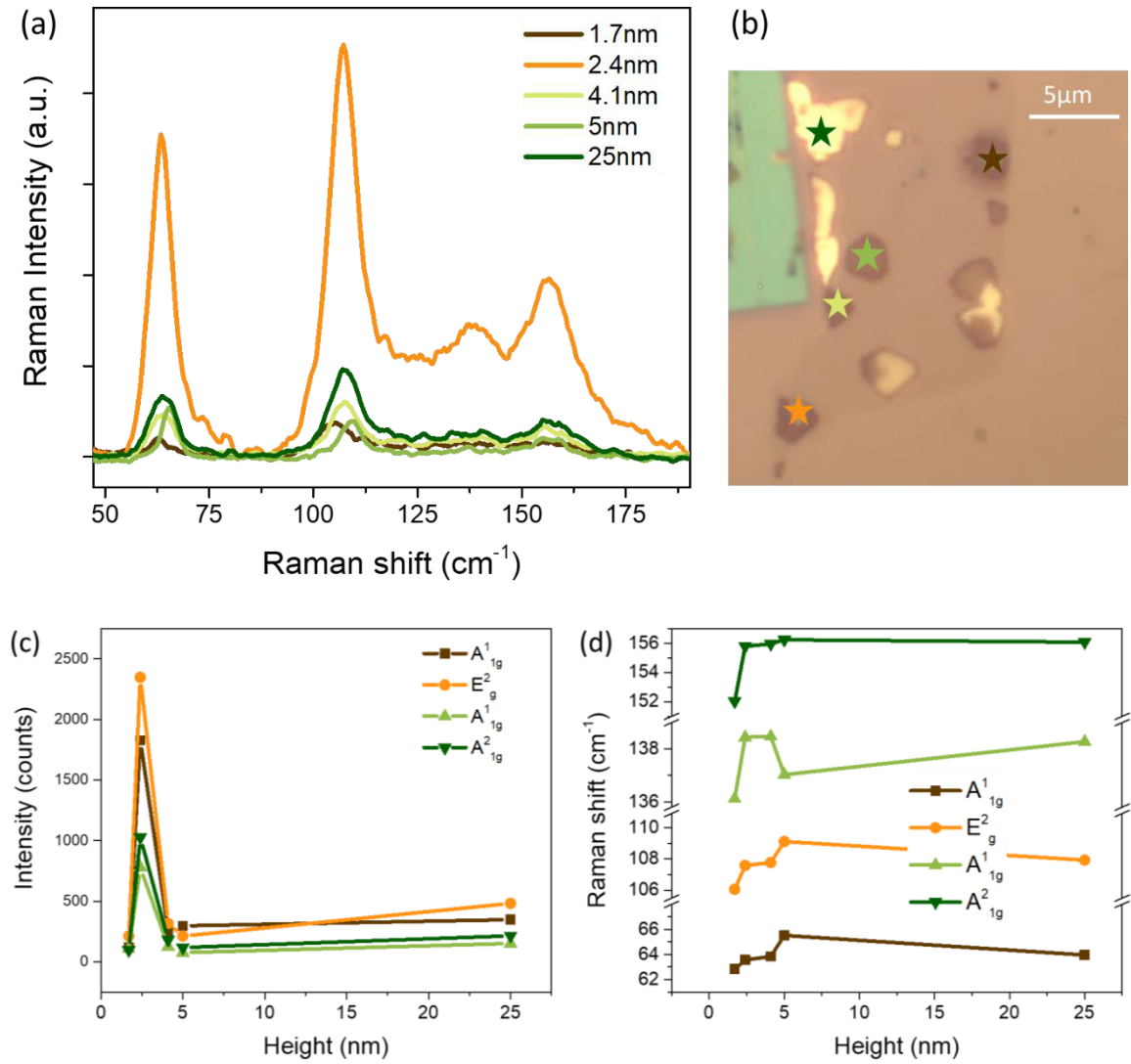
Figure 4:9 Thickness dependence of the Raman peaks of BTS in a graphene/BTS heterostructure. (a) Raman spectra of different BTS flakes grown on the same graphene sheet. The BTS flakes have different thicknesses between 1.7 nm and 25 nm. All spectra were obtained with a 532 nm laser, 10 sec acquisition time and 35μW laser power. (b) Optical image of the graphene/BTS heterostructure used for the Raman characterization. The positions of the laser spots are indicated by star symbols in different colors corresponding to the color of the Raman spectra. (c) Thickness dependent variations in intensity of the four characteristic BTS Raman peaks. (d) Evolution of the energy of the characteristic peaks with BTS thickness.

The high frequency region of the Raman spectra comprises the characteristic graphene peaks (G and 2D). Figure 4:10 compares this region in the Raman spectrum of a bare graphene region (orange spectrum) with that taken on a region of the same graphene sheet that is covered by a ~5 nm thick BTS flake (green spectrum). A small upshift of the 2D band is observed in the latter spectrum, while the G peak position shows no significant change in position. In general, up- or downward shifts of the graphene bands can arise due to strain or doping effects of the graphene. Their respective relevance for the present heterostructures was examined in detail with the aid of G-2D plots.
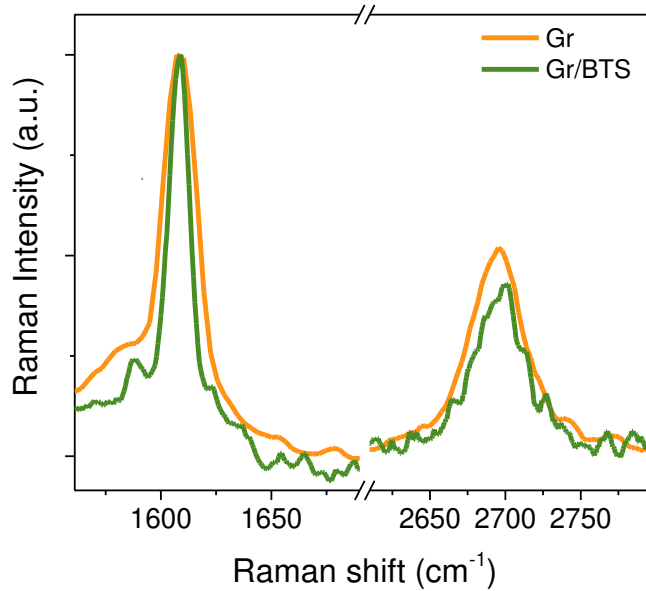
Figure 4:10 Raman spectra of a bare graphene region after CVD growth of BTS (orange line) and the same graphene sheet covered by a BTS flake (green line). Spectra were recorded with a 532 nm laser, 10 sec acquisition time and 35 µW laser power.

The G-2D plots shown below have two independent linear axes; one of them corresponding to constant strain (ε) with increments of 0.1%, and the other one corresponding to constant carrier concentration (n) with increments of $0.5 \cdot 10^{13}$ cm^{-2}. The exact equations for ε and n are given by [172]:

$$\varepsilon = \frac{k_n(\text{G})\Delta\omega_{2\text{D}} - k_n(2\text{D})\Delta\omega_{\text{G}}}{2\gamma_{\text{G}}\omega_{\text{G}}^0 k_n(2\text{D}) - 2\gamma_{2\text{D}}\omega_{2\text{D}}^0 k_n(\text{G})}, \tag{4.1}$$

$$n = \frac{\gamma_{\text{G}}\omega_{\text{G}}^0\Delta\omega_{2\text{D}} - \gamma_{2\text{D}}\omega_{2\text{D}}^0\Delta\omega_{\text{G}}}{\gamma_{\text{G}}\omega_{\text{G}}^0 k_n(2\text{D}) - \gamma_{2\text{D}}\omega_{2\text{D}}^0 k_n(\text{G})}. \tag{4.2}$$

The doping dependencies of the 2D and G peaks are quasilinear for hole doping in graphene, and the lattice strain is determined by the Grüneisen parameter (γ). Accordingly, the two peak frequencies can be expressed as follows:

$$\Delta\omega_{\text{G}} = -2\gamma_{\text{G}}\omega_{\text{G}}^0\varepsilon + k_n(\text{G})n, \tag{4.3}$$

$$\Delta\omega_{2\text{D}} = -2\gamma_{2\text{D}}\omega_{2\text{D}}^0\varepsilon + k_n(2\text{D})n. \tag{4.4}$$

where n is the carrier concentration and $k_n(\text{G})$ and $k_n(2\text{D})$ are empirical constants, $k_n(\text{G}) = -9.6 \times 10^{13}$ and $k_n(2\text{D}) = -1 \times 10^{13}$ [172]. For the Grüneisen parameter for the 2D and G peaks for room temperature uniaxial strain values of $\gamma_{\text{G}} = 1.9$ and $\gamma_{2\text{D}} = 2.6$ are taken. Moreover, ω_{G}^0 and $\omega_{2\text{D}}^0$ represent the frequencies at zero strain and zero doping, for which $\omega_{\text{G}}^0 = 1578 \text{ cm}^{-1}$ and $\omega_{2\text{D}}^0 = 2679 \text{ cm}^{-1}$ is assumed [173].

Pristine graphene exfoliated onto Si/SiO$_2$ substrates is known to be slightly to moderately p-doped, depending on the details of sample fabrication [174]. In the following maps, the magnitude of hole concentration is displayed in negative units of 10^{13} cm^{-2}. Moreover, the values on the strain axis are displayed in percentage units, with negative values corresponding to compression and positive values to tensile strain of the graphene sheet.

The goals of the Raman experiments were to determine the quality of the pristine graphene directly after exfoliation and to detect the changes induced by the subsequent CVD growth of BTS on top of it. To this end, six representative samples were selected, where the exfoliation of graphene was performed with the same graphite source and the conditions during the exfoliation were identical. Each of the following G-2D maps contains three reference graphene values belonging to pristine graphene flakes directly after exfoliation. The same parameters were used for the acquisition of the Raman spectra of pristine graphene and the heterostructures.
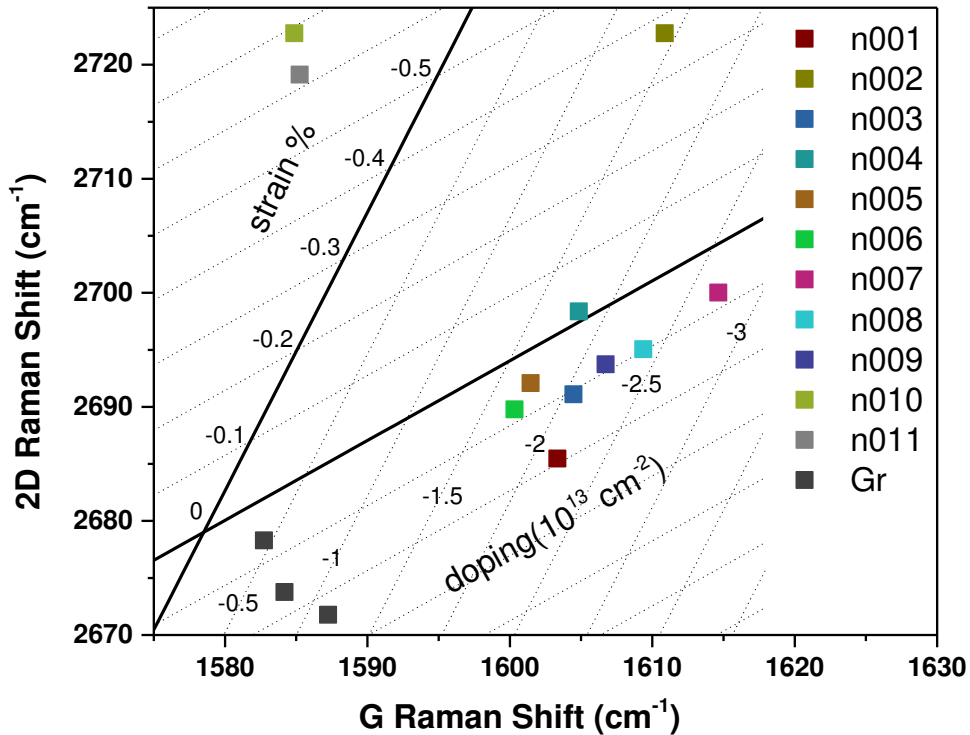
Figure 4:11 Strain – doping plot for the sample K3197. The dark grey square data points correspond to pristine graphene (Gr) before BTS growth. Each data point n001 – n0011 correspond to a Raman spectrum that was obtained on a different spot on the graphene/BTS heterostructure. Exact laser positions are indicated by black arrows in Figure 7:14.

In order to introduce the basic principle of the approach, Figure 4:11 shows Raman data collected from the first investigated sample (K3197), on which two different graphene monolayers locally covered by BTS crystals were examined (see Appendix Figure 7:14(a) and(b)). The numbers in the legend of Figure 4:11 correspond to the numbers in Figure 7:14(a) and (b), which indicate the laser illumination positions for recording the Raman spectra.

In the above map, there is only little and almost constant p-type doping and also only little strain for the pristine exfoliated graphene sheets (dark grey squares). The slight variation of the strain is likely due to local variations of the SiO_2 surface corrugation.

Positions n001 – n005 in Figure 4:11 were located on the first graphene flake (Figure 7:14(a)). In comparison to the pristine graphene reference (dark grey squares), the data points indicate stronger p-doping with hole concentrations on the order of $-2 \cdot 10^{-13}$ cm^{-2}, whereas the strain is similar. In the present heterostructures, graphene as the growth substrate is located below the BTS, which makes it difficult or even impossible to record Raman spectra from graphene regions which are covered by very thick BTS flakes. Nonetheless, it was still possible to perform measurements on a sufficient number of different positions to allow for a reliable analysis. Measurements n001 and n005 were obtained on bare graphene regions as well as on graphene in proximity of BTS crystals of different thicknesses and orientations on top. Data points n002 and n003 both originate from thin BTS flakes on graphene. While point n003 is really close to the values obtained on graphene next to BTS flakes, n002 shows surprisingly high compressive strain ($\sim$-0.4%). The latter could either be induced by the BTS flake, which is only $\sim$2 nm thick and therefore could experience significantly larger stress than the slightly thicker BTS flakes n003 $\sim$3 nm. Indeed no stress is seen for the graphene in proximity with the thick BTS n004 $\sim$23nm.

Measurements n006 – n011 were acquired on a second graphene/BTS heterostructure on the same substrate (K3197). The grown BTS at the various investigated positions had quite different morphology. Specifically, at spots n006, n007 and n009 there was a very thick layer of single BTS crystals that completely covered the graphene layer. Despite this thick BTS layer, graphene Raman spectra could be recorded from some positions. From the plot in Figure 4:11, the highest doping level is found for n007 ($\sim$-2.75$\cdot 10^{13}$ cm^{-2}) which corresponds to a very thin BTS region, and the lowest doping level is obtained for the very thick BTS ($\sim$-1.75$\cdot 10^{13}$ cm^{-2}) at n006. The strain in both positions is comparable to the strain in position n008 which corresponds to a graphene area not directly covered by BTS. Measurements n010 and n011 were obtained on a multilayer graphene area and show a very different correlation of 2D and G peak positions that are easy to separate from the monolayer measurements.

In order to provide a detailed overview of the strain and doping effects induced by the BTS in the underlying graphene, and to enable a comparison of their relative strengths, the data of all measured spots on all the investigated substrates were collected in one graph (see Figure 4:12). The corresponding plots for each single sample together with the optical images can be found in the Appendix Figure 7:4 - Figure 7:13. In the following, the five different types of structures (distinguished by differently colored regions in the graph) are discussed separately.
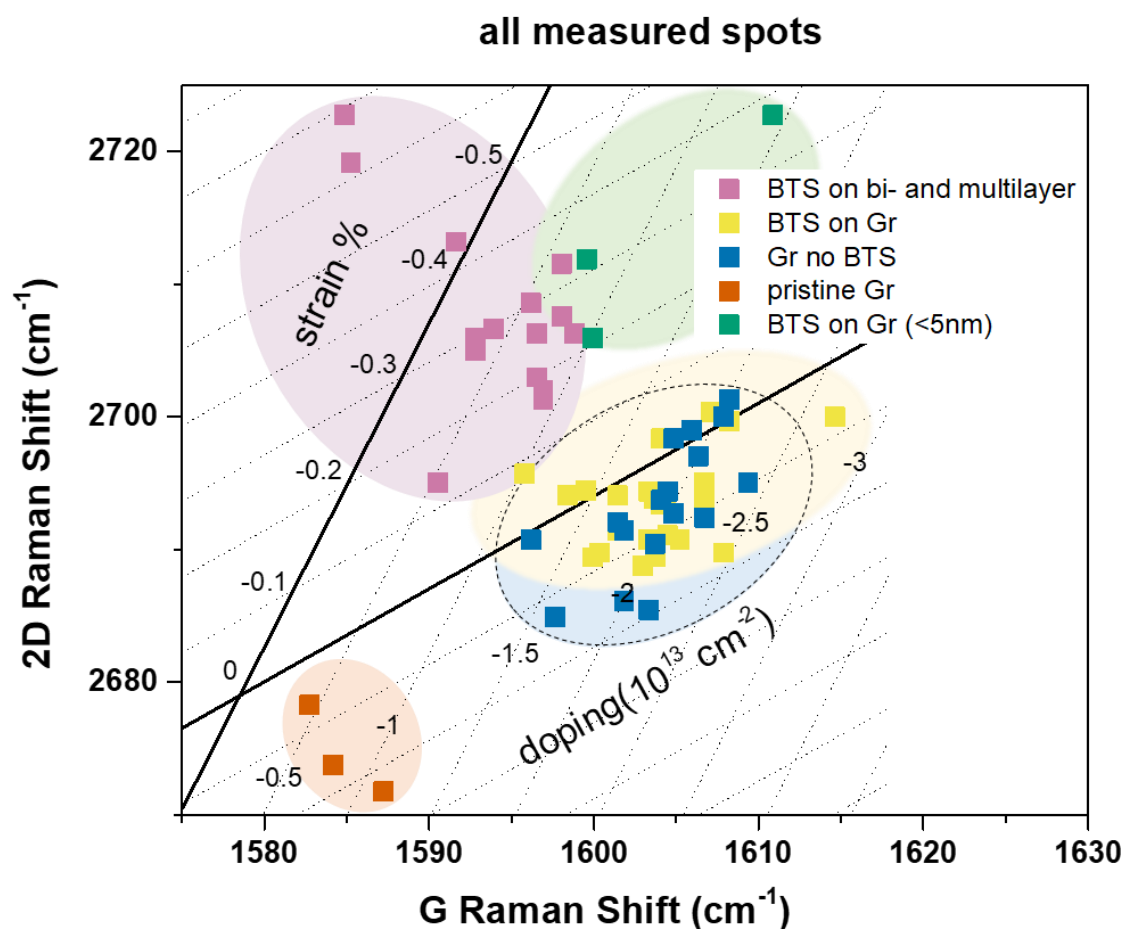
Figure 4:12 Summary of the collected Raman data measured on graphene before the CVD growth of BTS (orange squares), on bare graphene regions after the CVD growth of BTS (blue squares), on graphene covered by BTS sheets (yellow squares), on bilayer and multilayer graphene covered by BTS (pink squares) and on very thin BTS sheets grown on top of graphene (green squares).

Pristine graphene (orange squares):

The data points of pristine graphene fall into a region which is clearly distinct from that of graphene after the CVD growth of BTS. The three reference graphene values reflect only little p-type doping and strain. Specifically, the hole doping concentration is only on the order of $0.75 \cdot 10^{-13}$ cm^{-2} and the tensile strain reaches only up to 0.25%. These levels of p-type doping and strain are consistent with previous reports on pristine graphene on Si/SiO$_2$ [172], and hence these samples were used for subsequent BTS growth. The presence of strain can be explained by the adaption of the graphene sheets to the SiO$_2$ surface topography which is typically corrugated with a height variation of a few nm [175]. Mechanical exfoliation can introduce additional strain, in particular upon pressing the sheets onto the Si/SiO$_2$ [175]. The small p-doping is largely due to molecules like water or oxygen trapped underneath the graphene.

Bare graphene after BTS growth (blue squares):

The map reveals a strong influence of the CVD growth of BTS on the doping level of monolayer graphene (see blue squares in the region surrounded by the black dashed circle). The bare graphene regions show generally much stronger p-doping than the pristine graphene, but relatively low strain. The strain has mostly tensile character and is on average lower than the tensile strain observed in pristine graphene sheets. This small decrease of strain can be explained by the annealing of graphene during the CVD growth [169].

BTS on graphene (yellow squares):

The strain and doping levels of the graphene covered by BTS that is thicker than 5 nm are only little different from the values of the bare graphene after BTS growth. In fact, the blue and yellow regions almost coincide, which could be an indicator of commensurate growth of BTS on the underlying graphene. It may be that the commensurate growth only sets in after a certain minimum number of BTS quintuple layers have grown.

BTS on graphene (<5 nm) (green squares):

The growth of very thin BTS flakes is quite rare. Although the Raman data collected on BTS flakes that are distinctly thinner than 5 nm is quite scattered, the region into which they fall is nonetheless set apart from the other ones. Thin BTS flakes in the here investigated heterostructures generally do not show oriented growth, which is suggestive of appreciable lattice mismatch between them and the underlying graphene. The lattice mismatch can explain the presence of higher stress in graphene, which seems to be correlated with the emergence of stress within the BTS flakes (as manifested by the Raman peak shifts for flake thicknesses below 5 nm in Figure 4:9).

BTS on bi- and multilayer graphene (pink squares):

Reliable values for strain and doping cannot be obtained for the bi- and multilayer graphene sheets, since the present 2D – G peak plots are fully valid only for the monolayer case. However, such type of plot is still useful to differentiate between graphene monolayers and multilayers, as apparent from the distinct character of the latter region.

4.3   SHG microscopy of graphene/BTS heterostructures

In addition to the AFM and Raman characterization of the heterostructures, SHG measurements were performed with the aim of identifying commensurably grown BTS with a twist angle of 30° between the BTS and graphene lattices. In general, surfaces and interfaces that are lacking inversion symmetry are amenable to SHG generation, which should be fulfilled for the graphene/BTS heterointerface.
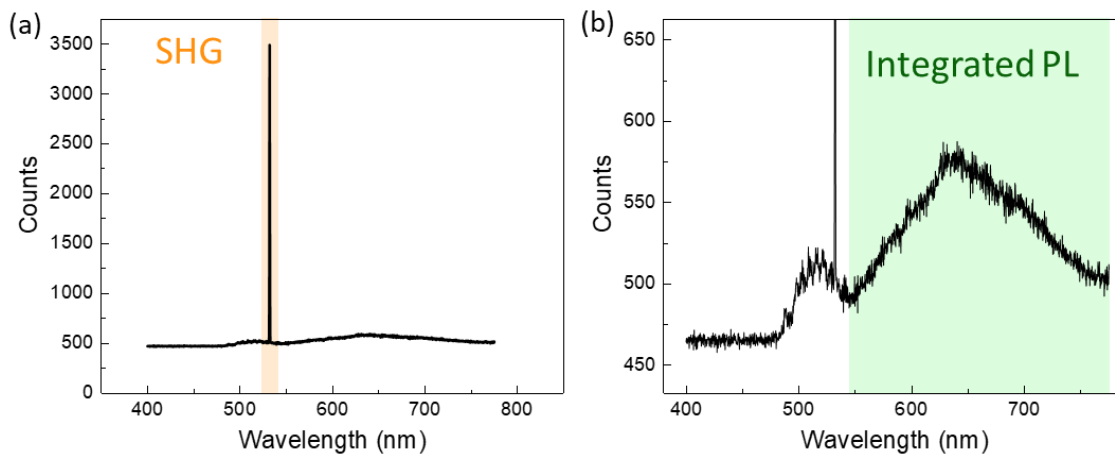
Figure 4:13 SHG and photoluminescence collected from a graphene section covered by thin BTS (the region is shown in Figure 4:14(a). (a) Sharp SHG signal peak collected at 532 nm (highlighted in orange) from the sample upon excitation with a 1054 nm laser. (b) Photoluminescence spectrum acquired from the same spot. For the plots and maps in Figure 4:14 and Figure 4:15 the Pl intensity was integrated over the entire area that is highlighted in green.

The laser spot position for recording the spectra in Figure 4:13 is marked by the white squares in Figure 4:14(b-d). The region comprises a monolayer graphene stripe where a BTS flake of approximately triangular shape is grown on top. The AFM image in Figure 4:14(a) is a zoom into the region and reveals a smoothly grown BTS flake with a thickness of ∼5.7 nm and a clean surface of the underlying graphene stripe. From the optical image one can see that this is the thinnest BTS flake grown on the two graphene stripes in this area. Other BTS crystals have a bright optical contrast, indicating a BTS thickness of > 50 nm.
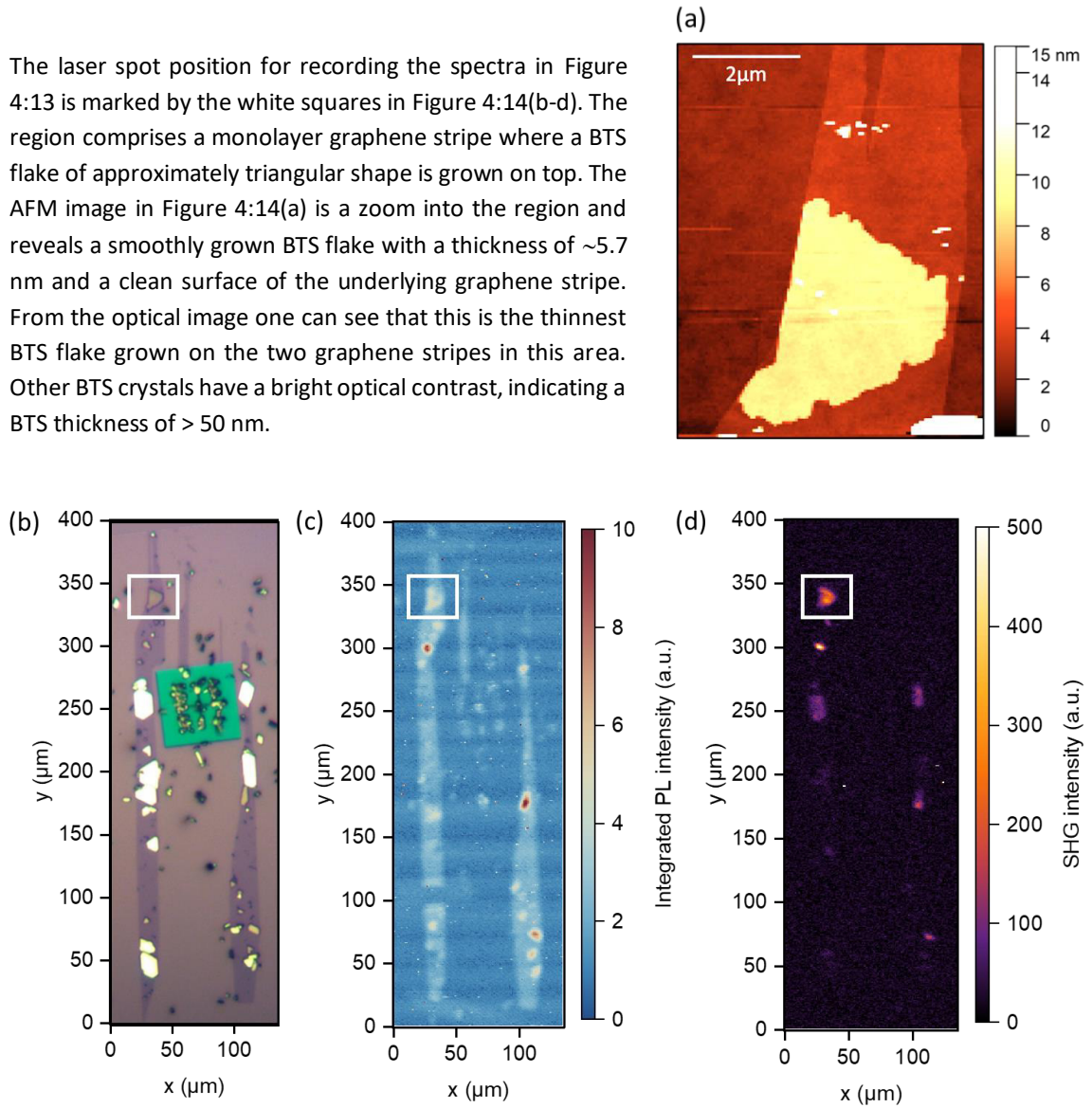
Figure 4:14 SHG and PL maps recorded from a graphene/BTS heterostructure sample. (a) AFM image of the region with the thinnest BTS crystal grown on top of graphene. This graphene/BTS region is highlighted by a white square in panels (b) to (d). (b) Optical image of the two examined graphene/BTS stripes. (c) X-Y PL map of the same sample region as in panel (b). The PL intensity is integrated from 550 nm - 780 nm. (d) X-Y SHG map of the same sample region as in panels (b) and (c). The white square highlights the thin graphene/BTS section which displays the most intense SHG signal in this region.

There are also smaller BTS crystals that are randomly grown on the graphene stripes and on the SiO_2 surface. Figure 4:14(c) shows a PL map obtained from the same sample region as shown in the optical image (cf. Figure 4:14(b). The graphene stripes are clearly visible in the PL map. The PL is further enhanced in the graphene section covered by the thinnest BTS crystal (marked by a white square). One can further recognize a few intense PL spots, which originate from small BTS clusters grown on the graphene. The SHG map (see Figure 4:14(d)) shows strongest intensity for the region marked by the white square. Comparison with the optical image (Figure 4:14(a)) evidences that pronounced SHG signals only stem from graphene that is covered by BTS, and the intensity of the SGH is significantly reduced for thick BTS crystals. By comparison, no SHG signal is visible for bare graphene regions or BTS crystals that are grown on the SiO_2 surface. These observations confirm that the detected SHG signals originate from the graphene/BTS heterointerface. The above PL and SHG maps were recorded for an unpolarized configuration. In a further measurement, the

laser spot was focused on the region with the thin BTS (white square) in order to record polarization dependent PL and SHG spectra. Thus obtained polar SHG intensity plots are shown in Figure 4:15.

Unpolarized detection

Cross-polarized detection

Co-polarized detection
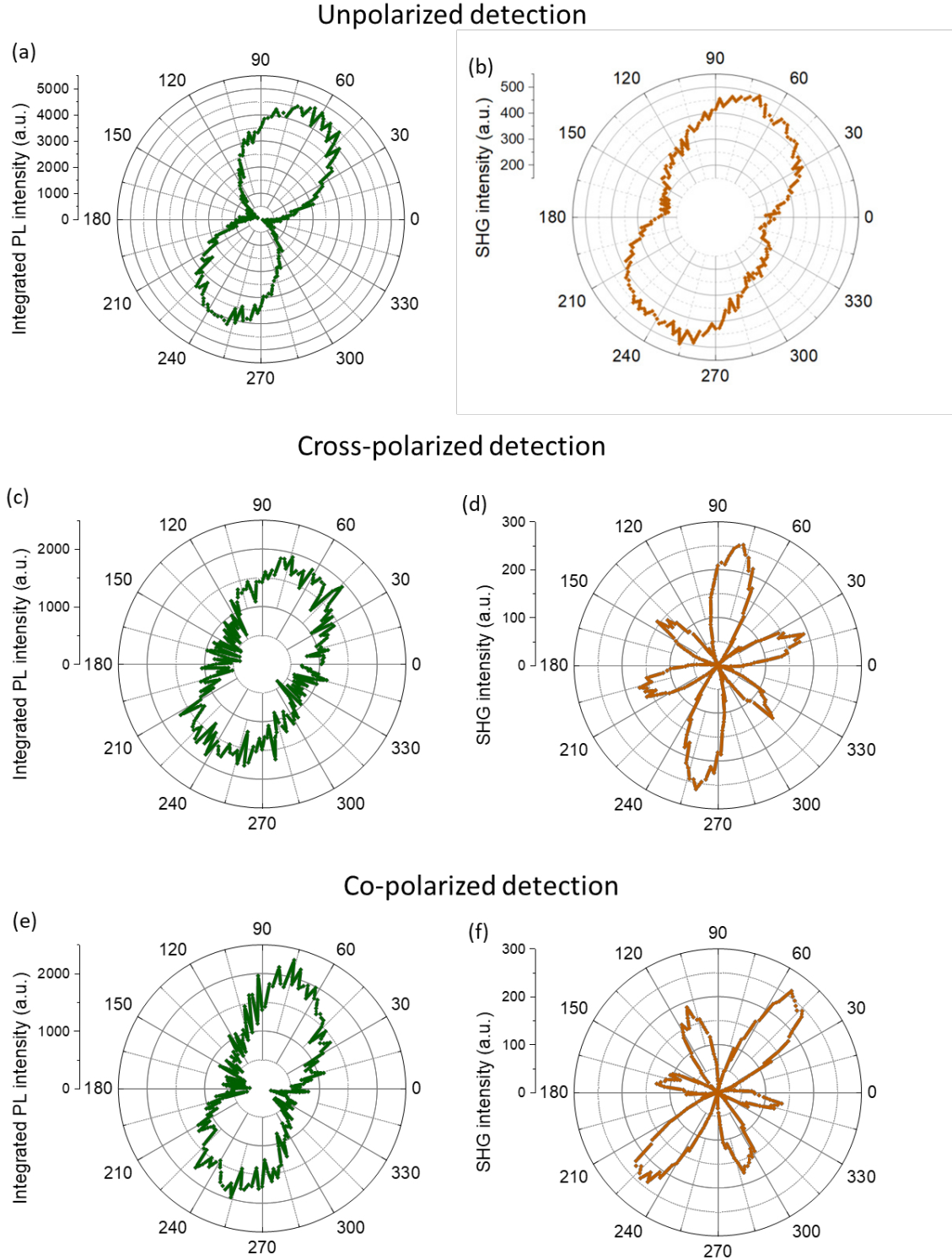
Figure 4:15 Polar plots of the detected PL (green) and SHG (orange) intensities measured in three different polarization configurations, i.e., unpolarized (a, b), cross-polarized (c, d), and co-polarized (e, f).

The plots belong to three different polarization configurations, i.e., unpolarized detection where no additional analyzer is used in front of the spectrometer (see Figure 4:15(a) and (b)); co-polarized detection, where the analyzer is oriented parallel to the pump field (see Figure 4:15(c) and (d)); cross-polarized detection, where the analyzer is oriented perpendicular to the pump field (see Figure 4:15(e)+(f)).

The photoluminescence intensity collected from the graphene/BTS region shows for all three detection configurations a similar, anisotropic shape (see Figure 4:15(a), (c) and (e)). The PL signal of the heterostructures may arise from two-photon absorption processes, in analogy to observations made on graphene quantum dots. This explanation would require that the BTS leads to a local quantum confinement in the underlying graphene, which appears possible in view of the combined strain and doping introduced into the latter (see Chapter 4.2).

The SHG response shows clear differences depending on the detection configuration. In case of the unpolarized detection, there are no well-developed petals visible in the polar plot (see Figure 4:15(b)). By contrast, for both the co- and cross-polarized detection, one clearly observes petals with 60° rotational symmetry. Moreover, the petals are rotated by 30° when the detection configuration is changed from cross-polarized (maximal intensities at ~15°, ~75°, ~135°, ~195°, ~255° and ~315°) to co-polarized (maximal intensities at ~45°, ~105°, ~165°, ~225°, ~285° and ~345°). The 60° rotational symmetry hints towards the formation of a commensurable graphene/BTS heterostructure by a highly oriented growth of the BTS crystal on top of the graphene.

It is furthermore evident that not all of the six petals in Figures Figure 4:15(d) and (f) have the same size. In fact, two pairs have almost equal, smaller size and one pair has a larger size. A similar pattern has been reported for CVD-grown MoS_2 sheets composed of at least two layers, whereas the monolayer exhibits a symmetric pattern [176]. In that case, this difference was attributed to the presence of broken inversion symmetry in the 3R-multilayers with rhombohedral symmetry. It is plausible to assume that the intrinsic lack of inversion symmetry of the graphene/BTS heterointerface can likewise explain the polarization enhancement for selected petals in the SHG response.

Chapter 5   Charge   transport   in   graphene/Bi$_2$Te$_2$Se heterostructures

5.1   Gate-dependent charge transport properties

This chapter summarizes the results of charge transport measurements on the graphene/BTS heterostructures performed in dependence of an applied gate field and an applied perpendicular magnetic field. In these experiments, heterostructures obtained from either CVD graphene or mechanically exfoliated graphene were used (see section 4.1 for a detailed description of the CVD graphene transfer and the mechanical exfoliation method). Towards electrical measurements in 4 probe-configuration, focus was laid on stripe-like graphene geometries covered by continuous BTS sheets that laterally extend to the edges of the graphene. The major objective was to explore the extent to which the proximity of graphene to BTS causes doping, alters the carrier mobility, or enhances the SOC strength.

5.1.1   CVD graphene

For electrical transport experiments on CVD graphene/BTS heterostructures, the hexagonal shaped graphene was etched into stripes before the growth of BTS. Figure 5:1(a) shows a hexagonal CVD graphene sheet transferred on top of a Si/SiO$_2$ substrate before the patterning process. Patterning into stripes with widths in the range of 300 nm to 2 µm was done by e-beam lithography followed by oxygen plasma treatment (100 W, 0.3 mTorr, 5 s). Figure 5:1(b) depicts the resulting graphene stripes after PMMA removal. Subsequent BTS growth resulted in a partial coverage of the stripes, as apparent from the optical image in Figure 5:1(c).

More details on the growth morphology are visible in the AFM image in Figure 5:1(d). The grown BTS crystals have a big variation in size, shape and thickness. For the following transport measurements, regions were chosen where the BTS crystals have a maximum lateral size of 1-2 µm and where high magnification AFM images confirm that the diametral BTS crystal edges reach the edges of the underlying graphene stripe (like for the crystals marked by green arrows in Figure 5:1(d). The four Ti/Au contacts were placed close to such BTS crystals, as exemplified in Figure 5:2(b)-(d) by three different devices. In case of device 1 (see Figure 5:2 (b)), the BTS crystals grown on the 2 µm graphene stripe have various thicknesses and shapes. There is almost no bare graphene areas left after the BTS growth. For device 2 (see Figure 5:2(c)), the graphene stripe has half the width of that in device 1, and the BTS is grown much thicker and denser. Device 3 (see Figure 5:2(d)) comprises the narrowest graphene stripe (300 nm width), which is covered by very thin BTS crystals, with bare graphene sections in between.
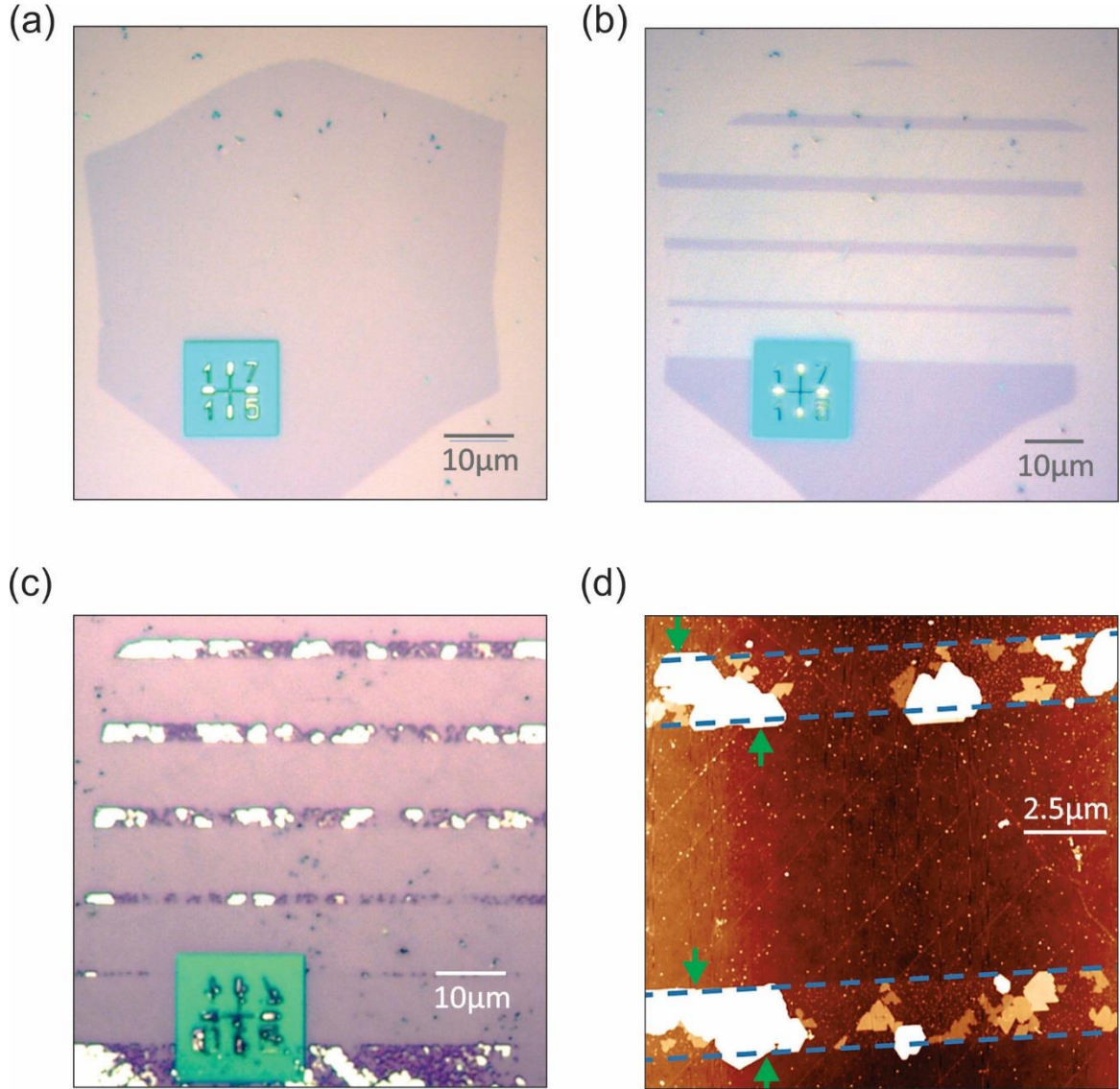
Figure 5:1 Patterning of CVD graphene/BTS heterostructures for subsequent device fabrication. (a) Transferred CVD graphene sheet on top of a Si/SiO₂ substrate. (b) The same graphene sheet patterned into stripes by e-beam lithography and oxygen plasma treatment. (c) Optical image of a patterned graphene sheet after BTS growth on top. (d) AMF image of graphene stripes after BTS growth. Graphene stripes are highlighted by the blue dashed lines along their edges. Green arrows point towards BTS crystals that are grown entirely till the edges of the graphene stripes.

Transfer curves obtained from three different graphene/BTS heterostructure devices are shown in Figure 5:2. The four probe conductivity (σ_{xx}) for each device is plotted as a function of applied gate voltage V_g. All CVD graphene/BTS heterostructures displayed relatively low conductivity and very flat slopes of the transfer curve. In the transfer curves (Figure 5:2(a)), the Dirac point is not visible, i.e., no minimum of σ is reached even at the highest positive gate voltage (V$_g$ = + 70 V). This observation evidences strong p-type doping of the graphene. Although the precise location of the Dirac point remains unknown, it is clear that it must occur at a gate voltage larger than +70 V. For this gate voltage, one can estimate the gate-induced hole concentration using the equation

$$n = \frac{\varepsilon_0 \, \varepsilon_{\mathrm{SiO_2}} \, V_g}{t \, e},$$

(5.1)

where ε_0 is the vacuum permittivity, ε_{SiO_2}= 3.9 is the permittivity of SiO_2, e is the elementary charge and t is the SiO_2 layer thickness of the Si/SiO_2 substrates (300 nm) [177]. This yields a minimum hole concentration of $5 \cdot 10^{12}$ cm^{-2} [+70 V] due to the p-type doping by the BTS for all three devices in Figure 5:2.

The field-effect mobility for the graphene/BTS devices was calculated according to the following equation:

$$\mu = \frac{\sigma(V_g)}{en(V_g)}.$$

(5.2)

From the linear slopes of the three different transfer curves in Figure 5:2(a), the following room temperature hole mobilities were obtained: 234 cm^2/Vs (device 1), 74 cm^2/Vs (device 2) and 54 cm^2/Vs (device 3). The low mobility for device 3 may be due to the fact that the narrow graphene stripe is covered only by very thin BTS crystals which are likely to have reduced crystalline order, thereby leading to enhanced carrier scattering.
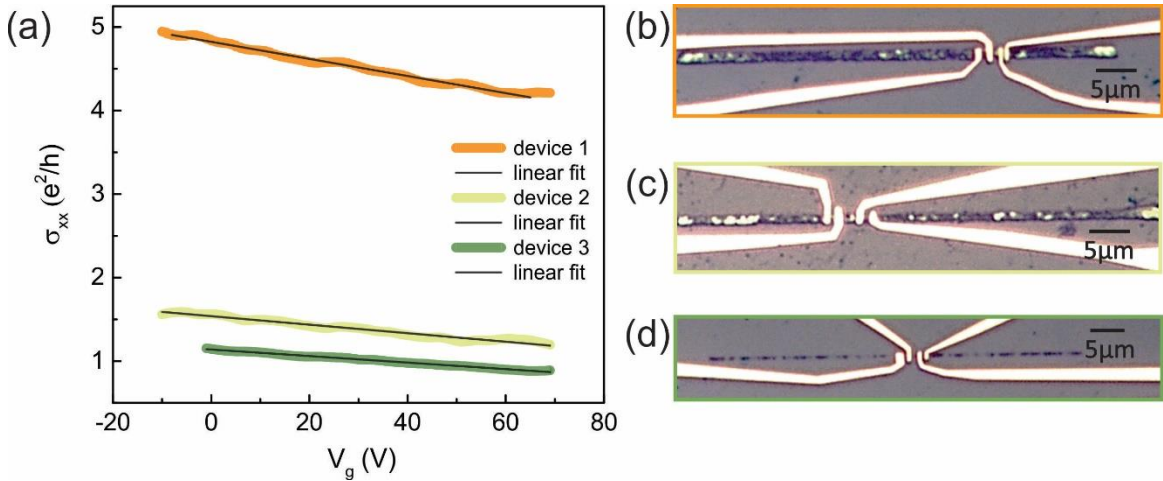
Figure 5:2 Three different CVD graphene/BTS heterostructure devices, each with four Ti/Au contacts. (a) Gate dependent conductivity (σ_{xx}) in units of e^2/h for device 1 to 3 at room temperature. The black lines are linear fits for extracting the charge carrier mobility. (b) Optical image of device 1. The graphene stripe width is ~2 μm. (c) Optical image of device 2. The graphene stripe width is ~1 μm. (d) Optical image of device 3. The graphene stripe width is ~0.3 μm.

Although device 1 features the highest conductivity among the three devices, the hole mobility of 234 cm^2/Vs is still insufficient for meaningful magnetotransport experiments. Hence, for further experiments the focus was shifted toward the heterostructure devices based on mechanically exfoliated graphene, as the latter enables a significantly better BTS growth (see section 4.1).

5.1.2 Exfoliated graphene

For device fabrication, graphene was first exfoliated onto Si/SiO_2 substrates and suitable sheets were selected by the optical microscope. The quality and thickness of the graphene was confirmed by AFM and Raman measurements (see section 4.1). In the following subsections, the charge transport behavior observed for three different device configurations is presented.

5.1.2.1   Graphene decorated with BTS clusters

In the initial experiments, devices made of graphene covered by small BTS clusters were investigated. That even in the absence of larger, continuous BTS nanosheets proximity-induced charge transport features could be detectable was motivated by a recent charge transport study which reported that random decoration of graphene by small particles of Bi_2Te_3 leads to sizable proximity-enhanced SOC in graphene, with an induced graphene band gap of ~6 meV [178].

As a first step, the substrate with exfoliated graphene sheets was placed at slightly colder regions in the CVD furnace to achieve the growth of small clusters instead of extended BTS sheets. Graphene sheets that are homogeneously covered by small BTS clusters were then identified by AFM and subsequently patterned into a Hall bar structure, as exemplified by the AFM images in Figure 5:3(a) and (b). The patterning was done in an extra e-beam lithography step followed by oxygen plasma treatment. It turned out that longer plasma times are needed due to the graphene coverage by the BTS clusters, as the latter are not fully removed by the oxygen plasma. Best results were obtained with a total oxygen plasma treatment time of 10 - 15 sec depending on the density of the BTS clusters. In the AFM image, the original edges of the graphene sheet are still visible as faint lines. Raman analysis confirmed that the graphene in the plasma-treated regions was successfully removed, and moreover revealed that the BTS clusters are oxidized. In the next step, the Hall bar was provided with Ti/Au contacts. In Figure 5:3(c), the measured four probe conductivity is plotted against the applied gate voltage. In this case, the transfer curve displays a minimum at $V_g \approx 30$ V, again indicating p-type doping of the graphene. The Dirac point position yields a doping concentration of $2.1 \cdot 10^{12}$ cm^{-2}, while from the linear slopes of the transfer curve a hole mobility of ~-3275cm^2/Vs and an electron mobility of ~3328 cm^2/Vs are derived.
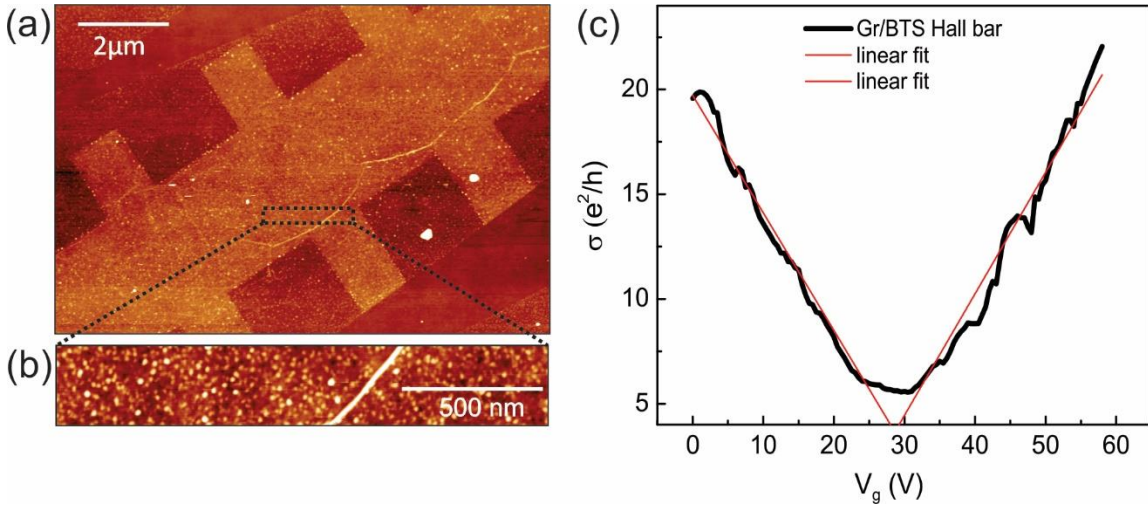
Figure 5:3 Exfoliated graphene Hall bar device decorated with BTS clusters. (a), (b) AFM images of the graphene after growth of small BTS clusters (small white dots) and after patterning into a Hall bar. (c) Gate dependent conductivity (σ_{xx}) in units of e^2/h, recorded at room temperature. The red lines are linear fits.

The high hole mobility of the present heterostructure, as compared to the BTS-decorated CVD graphene (Figure 5:2), testify the better structural quality of the exfoliated graphene and that the patterning process involving three times longer oxygen plasma time as usual does not significantly deteriorate the graphene. At the same time, the weaker p-doping is attributable to the presence of small clusters instead of compact

BTS crystals, which is expected to lead to reduced charge transfer between the two components. The device in Figure 5:3 was further used for magnetotransport measurements (see subsection 5.2.1.1).

5.1.2.2   Graphene/BTS stripe with four-terminal contact configuration

In order to avoid additional etching steps, narrow graphene stripes directly formed during exfoliation were used for fabricating further devices. In this manner, it became possible to define the electrical contacts directly after BTS growth onto the stripes, which ensured less doping and contaminations of the graphene. Graphene stripes with suitable dimensions (300 nm to 1 μm in width, and a minimum length of 10 μm) were selected under the optical microscope and characterized by AFM and Raman spectroscopy before the growth of BTS.
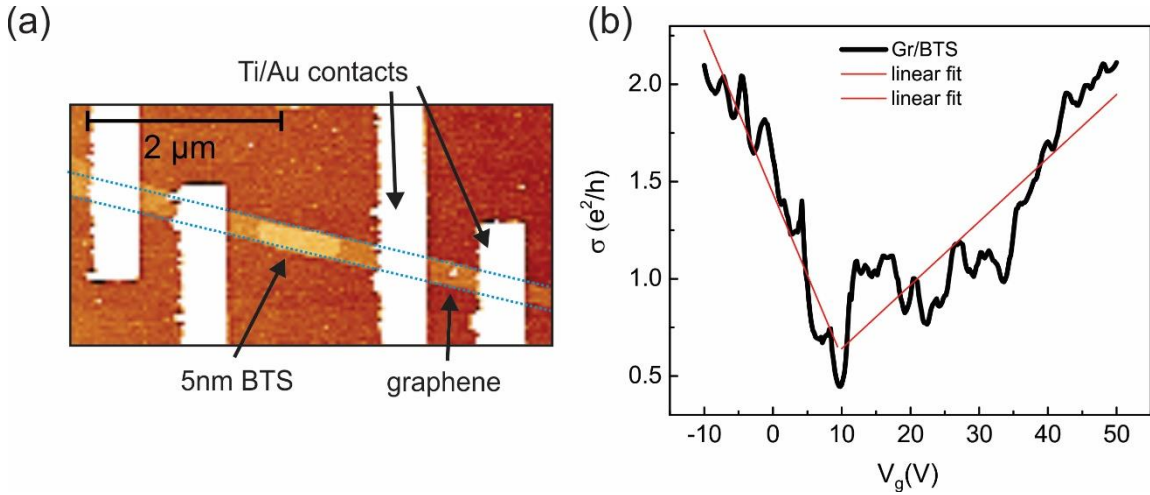
Figure 5:4 Exfoliated graphene stripe device with BTS grown over the entire width of the graphene stripe. (a) AFM image of the graphene stripe with a small BTS crystal between the two middle Ti/Au contacts. (b) Gate dependent conductivity (σ_{xx}) in units of e^2/h. The red lines are linear fits.

Figure 5:4(a) shows a typical exfoliated graphene stripe/BTS device. The width of the graphene stripe is approximately 300 nm. The BTS crystal grown on top of the stripe is very thin (~5 nm AFM height) and has small lateral dimensions of $W \cdot L = 300$ nm $\cdot$ 1 μm.

The conductivity of this device is considerably lower in comparison to the above graphene Hall bar device (see Figure 5:3). The conductivity vs. gate voltage plot (i.e., the transfer curve) deviates strongly from a smooth, linear dependence (cf. Figure 5:4a). Accordingly, the position of the Dirac point can only be estimated to be at $V_g = +10$ V, which corresponds to p-doping with a hole concentration of $7 \cdot 10^{11}$ cm^{-2}. Likewise, a rough estimate of 420 cm^2/Vs (for holes) and 233 cm^2/Vs (for electrons) was obtained for the room temperature field-effect mobility, based upon two very approximate linear fits (red lines). One possible explanation for the low mobility and low doping level of this specific device is the small thickness of the BTS sheet (~5 nm). In fact, it has been predicted by theory [179] and also experimentally confirmed [180] that below a thickness of ~6 nm, the top and bottom surface states of a 3DTI hybridize and consequently a band gap is opened. In addition, the sheet could even be physically segmented into several smaller crystallites, which may account for the rich features in the transfer curve (Figure 5:4(b)). Nonetheless, owing to its advantageous low doping level the device was also used for further magnetotransport experiments (see subsection 5.2.1.2).

5.1.2.3   Device with voltage probes at BTS edges

Further exfoliated graphene/BTS heterostructure devices were fabricated with a different arrangement of the Ti/Au contacts. Specifically, the voltage probes were now placed in direct contact with the BTS flake grown on the graphene stripe. Here it was again ensured that the selected BTS flake is grown entirely over the width of the graphene stripe. The benefit of this alternative four-terminal configuration is that only the electric potential drop over the graphene section that is fully covered by the BTS flake is measured, instead of probing a series of bare graphene sections (or graphene covered by small BTS clusters) and a graphene section fully covered by BTS. A schematic cross-section, optical and AFM image of such a device is shown in Figure 5:5(a). The two voltage probes close to the endings of the BTS flake were designed to cover both the edges of the BTS and also the graphene below. Another novel feature of this device is the thickness of the BTS crystal. AFM measurements yielded a BTS height of ~9.5 nm. The width of the exfoliated graphene stripe below the BTS crystal is ~600 nm. The BTS crystal on top of the graphene stripe has lateral dimensions of $W \cdot L$ = 600 nm $\cdot$ 1.3 µm.
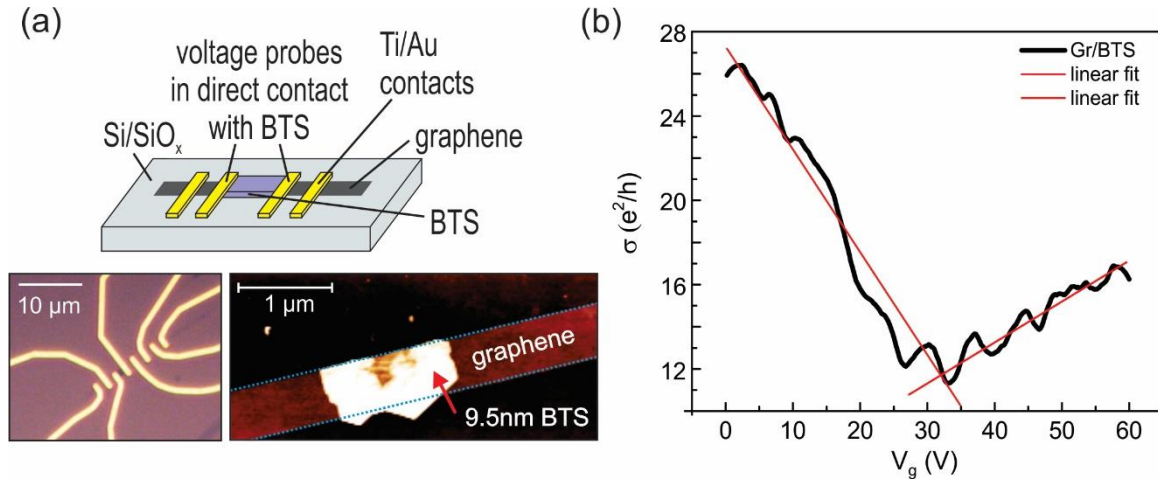
Figure 5:5 Exfoliated graphene stripe device with voltage probes on the BTS. (a) Schematic cross-section, optical and AFM image of the device, revealing two central Ti/Au contacts on the BTS crystal edges and the graphene. Additional Ti/Au contacts are placed on the bare graphene. (b) Gate dependent conductivity (σ_{xx}) of the graphene/BTS section in units of e^2/h. The red line is a linear fit.

The obtained values, plotted in Figure 5:5(b) as a function of gate voltage, are slightly higher than those for the graphene Hall bar decorated by BTS clusters (see Figure 5:3). In this transfer curve, the Dirac point is located at $V_g \approx$ +34 V, indicating a hole doping concentration of 2.4·10^{12} cm^{-2}. Based upon the two linear fits (red lines), values of ~4000 cm^2/Vs are obtained for the field-effect mobility of holes (~3750 cm^2/Vs for electrons). The device was further characterized by magnetotransport measurements (see subsection 5.2.1.3).

5.1.3   Evaluation of doping and carrier mobility

All the graphene/BTS heterostructures devices described above display p-type doping of graphene. Such doping is in agreement with the work function difference between the two materials. In fact, the work function of BTS has been reported to be ~5 eV according to theory and 5.2 eV as found by experiment (ARPES measurements) [181], whereas the experimental value for graphene is 4.5 eV [182]. Moreover, DFT calculations have predicted pronounced p-doping for both the commensurate graphene/BTS heterostructure and the one with the larger unit cell, with the Dirac point of graphene being located a few hundreds of meV

above the Fermi level [39]. However, it needs to be emphasized that there is a notable variation of the doping extent between the present heterostructures, the detailed origin of which remains to be clarified.

Some carrier mobilities determined for the above devices are significantly lower than the values of at least 1000 cm^2/Vs documented for graphene on Si/SiO$_2$ [183], and also lower than those reported for similar graphene-based heterostructures [184]. At the present stage, however, it cannot be distinguished whether the reduced mobility is the consequence of enhanced scattering due to the proximity of BTS [185], or possible changes of the graphene lattice during the BTS growth at elevated temperature (582°C, see section 3.1), or both.

5.2 Magnetotransport measurements

5.2.1 Exfoliated graphene

Magnetotransport measurements were carried out only on the heterostructure devices based on exfoliated graphene (see section 5.1.2), as the devices comprising CVD graphene (see section 5.1.1) were of too low quality. For all the devices below, the corrected ($\Delta\sigma_{xx} = \sigma_{xx}(B) - \sigma_{xx}(B = 0)$) low-field magnetoconductivity consistently diplayed weak localization (WL) behavior. For determining the (gate-dependent) phase coherence length, the data were fitted using the theoretical model proposed by McCann and Fal´ko [79]:

$$\Delta\sigma(B) = \frac{e^2}{\pi h}\left[F\left(\frac{B}{B_\phi}\right) - F\left(\frac{B}{B_\phi + 2B_i}\right) - 2F\left(\frac{B}{B_\phi + B_i + B_*}\right)\right]$$

(5.3)

where $F(z) = lnz + \psi\left(\frac{1}{2} + \frac{1}{z}\right)$ and $B_{\phi,i,*} = \frac{\hbar}{4e}l_{\phi,i,*}^{-2}$. A reasonable fit quality was achieved within the low B-field range of ±3-15 mT, with the precise width of the range depending on the device.

5.2.1.1 Graphene decorated with BTS clusters

The magnetoresistance of the above described graphene Hall bar decorated with BTS clusters (see Figure 5:3) was measured in dependence of applied gate voltage at T = 1.3 K under applied perpendicular B-field. From these data, the magnetoconductance was then calculated by accounting for the distance between the voltage probes and the channel width. The corrected magnetoconductance data are shown in Figure 5:6(a). For all gate voltages, WL behavior with superimposed universal conductance fluctuations (UCFs) is observed. The phase coherence length l_φ extracted from the fits according to equation (5.3) is plotted in Figure 5:6(b) as a function of back gate voltage. There is a maximum of l_φ (reaching a value of ~280 nm) between V_g = 20 and 30 V, which is close to the Dirac point of this device (see the transfer curve in Figure 5:3). For lower and higher gate voltages, l_φ is seen to decrease to approximately 100 nm.
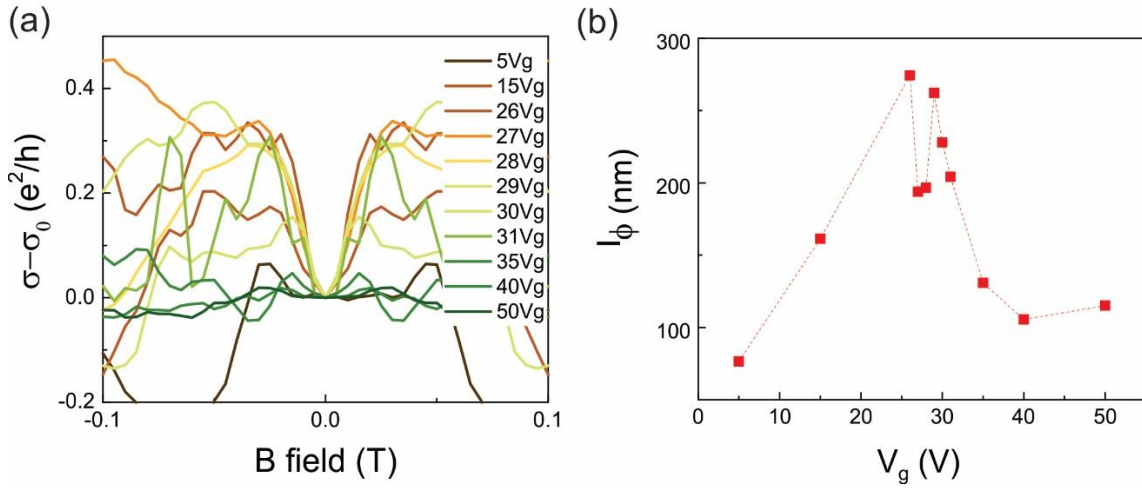
Figure 5:6 Exfoliated graphene Hall bar device decorated with BTS clusters. (a) Magnetoconductance of the exfoliated graphene Hall bar device decorated with BTS clusters (see Figure 5:3) recorded at 1.3 K under perpendicular B-field for a range of gate voltages. (b) Phase coherence length in dependence of gate voltage, obtained by fitting the low B-field data in panel (a) using the McCann-Fal'ko model [79].

5.2.1.2 Graphene/BTS stripe

The gate-dependent magnetoconductance of the above described graphene/BTS stripe-like device (see sub-section 5.1.2) is shown in Figure 5:7(a). In this case, there is a smaller UCF contribution than for the above Hall bar device (see Figure 5:6). Again, WL behavior is observed for the entire gate voltage range ($V_g = 0 - 50$ V). The extracted l_φ values are plotted in Figure 5:7(b) as a function of gate voltage.
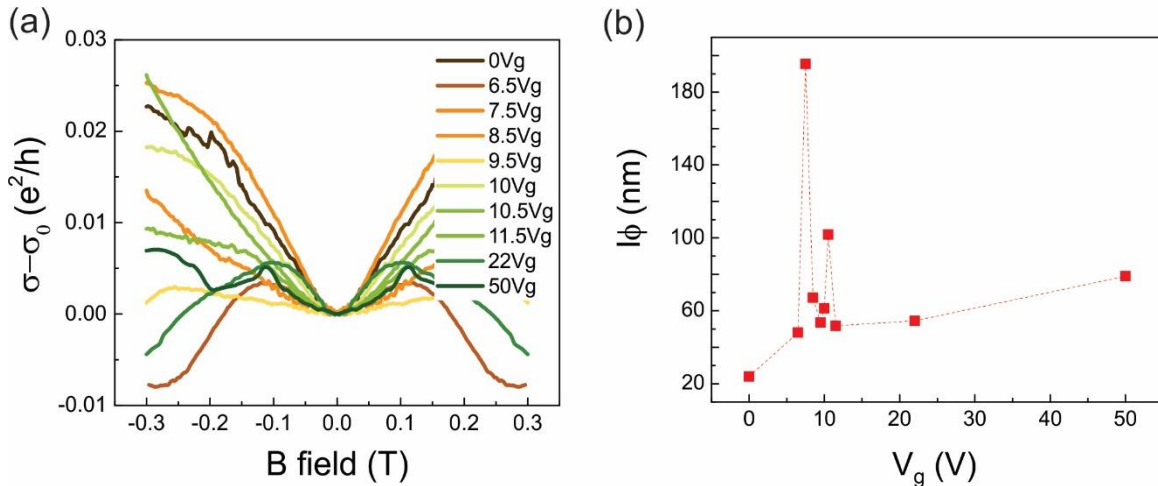
Figure 5:7 Exfoliated graphene stripe device with BTS grown over the entire width of the graphene stripe. (a) Magnetoconductance data for the exfoliated graphene stripe device with BTS grown over the entire width of the stripe (see Figure 5:4), recorded at 1.3 K under perpendicular B-field for a range of gate voltages. (b) Phase coherence length in dependence of gate voltage, obtained by fitting the low B-field data in panel (a) using the McCann-Fal'ko model [79].

From the feature-rich transfer curve of this device, the Dirac point could only be estimated to occur around $V_g = 10$ V. Like for the device above, the maximum of the phase coherence length is found to approximately coincide with this gate voltage, although l_φ considerably scatters within the relatively small gate voltage range of $V_g = 6.5 - 11.5$ V, wherein it reaches values between 50 nm and 190 nm.

5.2.1.3 Graphene stripe with direct contacts to BTS

The magnetoconductance of the above described graphene/BTS device with direct contacts to the BTS (see subsection 5.1.2.3) is presented in Figure 5:8(a). Also here WL behavior is observed for all gate voltages (V_g= 0V − 55V).
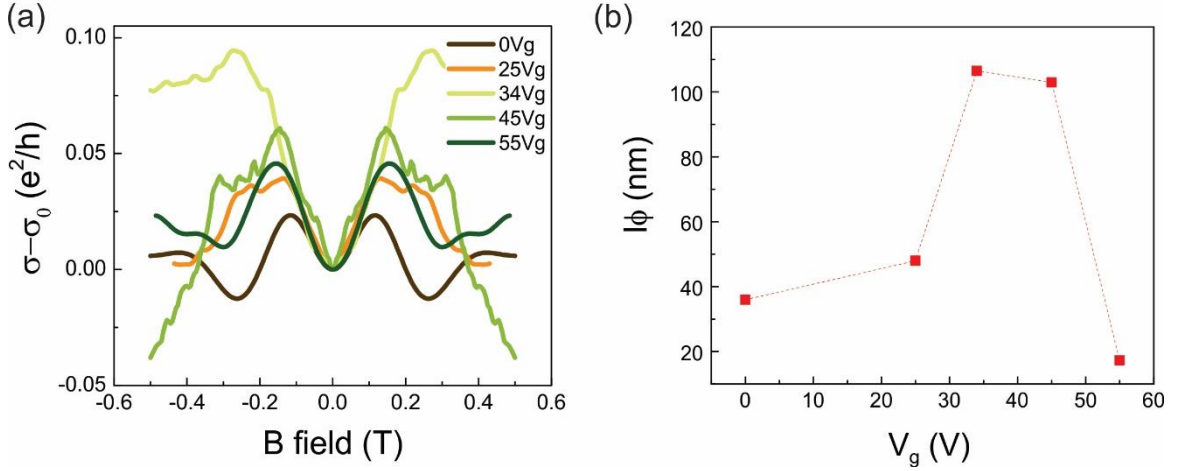
Figure 5:8 Magnetoconductance of the exfoliated graphene stripe device with direct contacts to the BTS (see Figure 5:5). (a) Magnetoconductance data for the bare graphene area recorded at 1.3 K under perpendicular B-field for a range of gate voltages. (b) Phase coherence length in dependence of gate voltage, obtained by fitting the low B-field data in panel (a) using the McCann-Fal'ko model [79].

The extracted phase coherence lengths of the graphene/BTS section, plotted in Figure 5:8(b), exhibits an increase of l_φ around $V_g \approx$ 34-45 V, which coincides with the Dirac point of this section (see Figure 5:5). By contrast, for bare graphene a minimum of l_φ is characteristic, as has been observed in various previous works [79].

5.2.2 Discussion of magnetoconductivity

The major finding for the gate-dependent phase coherence length l_φ of the three different devices is that while for bare graphene l_φ was reported to display a minimum at the Dirac point, for all the BTS-coated graphene an opposite trend is reproducibly observed, i.e., l_φ reaches a maximum at the Dirac point. A very similar behavior has been reported for graphene/$Bi_{1.5}Sb_{0.5}Te_{1.7}Se_{1.3}$ heterostructures at low temperature [41]. In close analogy, the present trend is attributable to the proximity of BTS which imparts D'yakonov-Perel type spin scattering on the proximitized graphene.

Chapter 6 Charge transport in graphene/α-RuCl₃ heterostructures

This chapter summarizes the results of electrical transport measurements that were performed on graphene/$\alpha-$RuCl₃ heterostructures with two major goals. The first main objective was to test whether the application of an in-plane B-field could shine further light on the proposed spin scattering imposed by the $\alpha-$RuCl₃ on graphene [146]. The second major goal was to investigate how the charge transport characteristics are influenced when the thickness of the $\alpha-$RuCl₃ sheet is progressively decreased. This is of interest, as the magnetic ordering, the magnetic fluctuations, as well as the capability to hybridize with the electronic bands of graphene are likely to depend on the number of $\alpha-$RuCl₃ layers. Regarding the magnetic properties, first experimental hints of such dependence have been gained from Raman spectroscopy data [186]. Moreover, for the particular case of an $\alpha-$RuCl₃ monolayer as the minimum possible sheet thickness, due to the absence of interactions between $\alpha-$RuCl₃ layers, the system has been predicted to more closely approach the Kitaev QSL [143], which in turn may manifest itself in the charge transport behavior of the graphene/$\alpha-$RuCl₃ heterostructures.

6.1 Stability of exfoliated ultrathin $\alpha-$RuCl₃ sheets

$\alpha-$RuCl₃ single crystals were synthesized from commercial powder (Ruthenium(III)-chlorid, ROTIMETIC, 99.9%) using a chemical vapor transport growth procedure [187]. Composition and structure of thus obtained big crystals (approximately 3 mm edge length) were confirmed by a combination of SEM (scanning electron microscopy), EDS (Energy Dispersive Spectroscopy) and XRD (X-ray diffraction). The analysis revealed a small percentage (~4%) of stacking faults in the crystal structure [187]. While the weak interlayer vdW interactions in $\alpha-$RuCl₃ make it easy to exfoliate, the compound is quite sensitive against shearing and mechanical stress emerging during exfoliation, stacking and sheet transfer [188].

In order to ensure that also very thin mechanically exfoliated $\alpha-$RuCl₃ sheets are sufficiently stable under ambient conditions as a prerequisite for the subsequent device fabrication, they were characterized by AFM and Raman spectroscopy. The results of an AFM degradation study are presented in Figure 6:1 for a larger exfoliated $\alpha-$RuCl₃ sheet on a Si/SiO₂ substrate. As can be seen from the AFM image contrast and the height profiles, the sheet consists of distinguishable regions that differ in the number of layers.

AFM scans of the same area were repeated at different times after exfoliation, in order to detect possible morphological changes due to the exposure to ambient. The four height scale plots show that for all original sheet thicknesses ranging between 3 and 12 nm, no appreciable height change is visible even after 43 hrs. of exposure to ambient. At the same time, also the surface roughness remains mostly unchanged, further testifying the stability of the sheets against ambient.
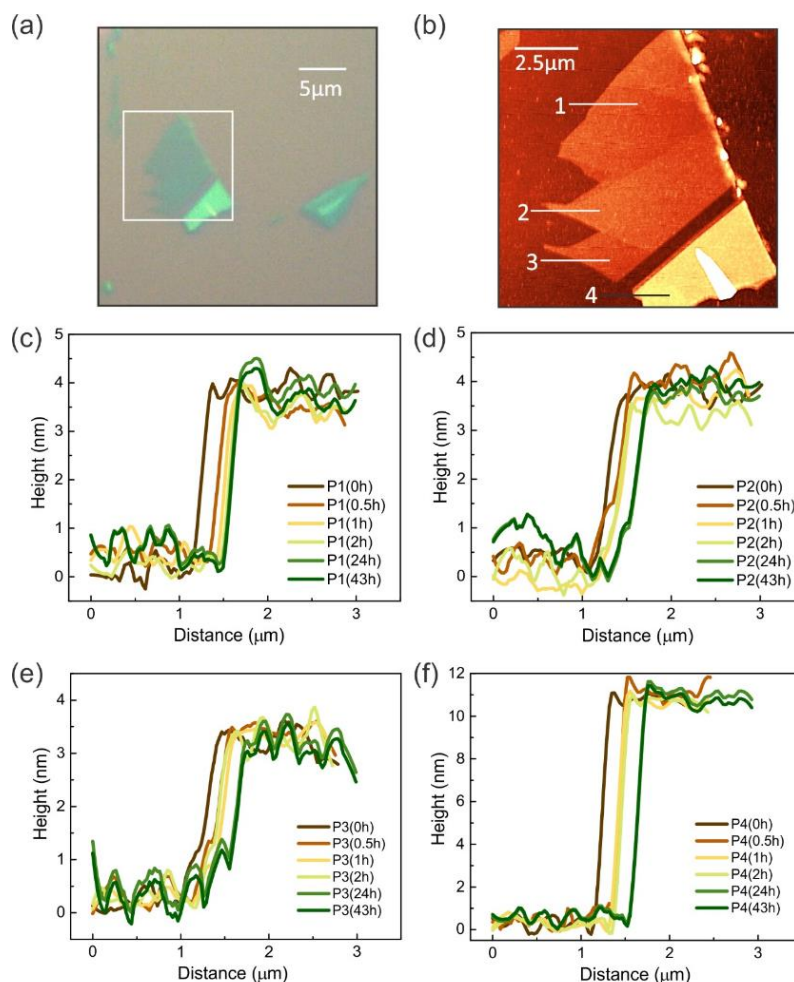
Figure 6:1 AFM degradation study of an $\alpha-$RuCl$_3$ flake kept under ambient conditions. (a) optical image of the examined $\alpha-$RuCl$_3$ flake. (b) AFM image of the examined $\alpha-$RuCl$_3$ flake. (c–f) AFM scans were acquired directly after exfoliation, and then after periods of 30 min, 1 hr, 2 hrs, 24 hrs and 43 hrs after exfoliation of the flake. Height profiles along lines 1 and 3 indicate a thickness of ∼3.5 nm, height profile along line 2 a slightly larger thickness of ∼4 nm, and height profile along line 4 a larger thickness of ∼12 nm.

The stability of the $\alpha-$RuCl$_3$ sheets could be further corroborated by Raman spectroscopy. In Figure 6:2, Raman spectra taken under ambient from the same spot on an approximately 5.5 nm thick $\alpha-$RuCl$_3$ flake are displayed. It is apparent that the spectral features, i.e., peak position and intensity, remain unchanged after up to 42 hrs of ambient exposure.
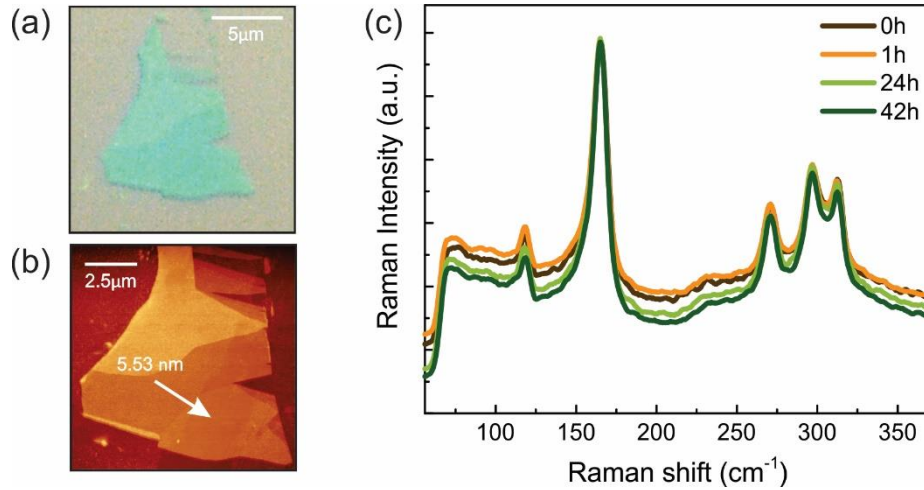
Figure 6:2 Raman degradation study of a mechanically exfoliated 5-6 nm thick $\alpha-$RuCl$_3$ flake under ambient. (a) optical image of the examined $\alpha-$RuCl$_3$ flake. (b) AFM image of the examined $\alpha-$RuCl$_3$ flake. (c) Spectra were taken at the same spot on the flake directly after exfoliation, and subsequently 1 hr, 24 hrs and 42 hrs afterwards. The spectra reveal no significant change of peak intensity and position (excitation wavelength λ= 532nm).

Further optimization of the mechanical exfoliation technique provided access to sufficiently large $\alpha-$RuCl$_3$ sheets down to bilayers and monolayers, as exemplified by the AFM image and height profiles in Figure 6:3. However, it remained challenging to obtain entirely free-standing monolayers which are not attached to a bigger and thicker flake.
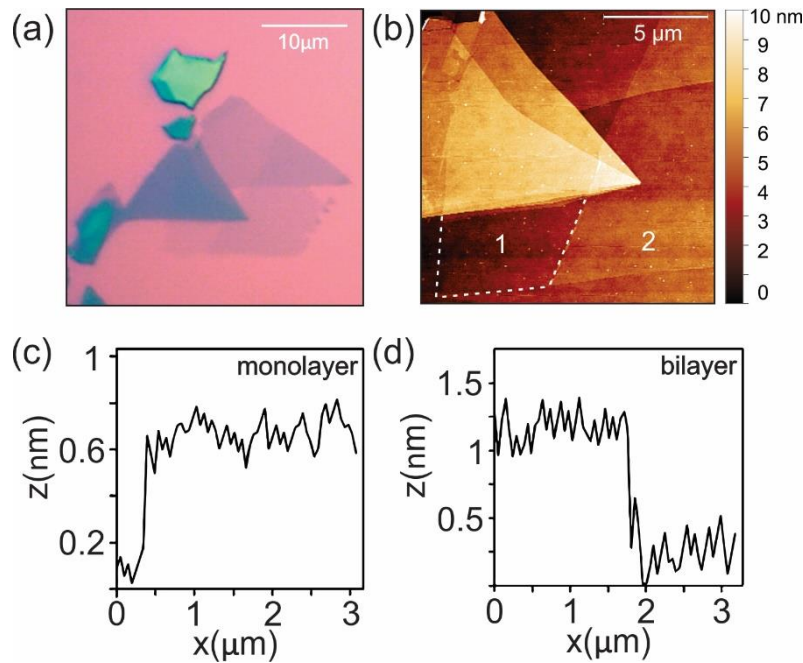
Figure 6:3 Mono- and bilayer $\alpha-$RuCl$_3$ sheets. (a) Optical micrograph and (b) AFM image of $\alpha-$RuCl$_3$ sheets composed of a different number of layers. The area marked by the white dashed line is a monolayer (labeled as '1'), while the area labeled as '2' is a bilayer. (c, d) AFM height profiles taken from area 1 (panel c) and area 2 (panel d). The thickness of the monolayer is about 0.7 nm.

6.2   Device fabrication

For fabricating the graphene/$\alpha-$RuCl$_3$ heterostructure devices, exfoliated sheets were stacked together using a similar dry transfer process as reported previously [146]. A micromanipulator equipped with an optical microscope and a piezo-controlled XYZ-stage was used for precise alignment of the sheets (see section 3.2). An example of a completed device is provided in Figure 6:4(a), together with a schematic illustration of the device cross-section in Figure 6:4(b).
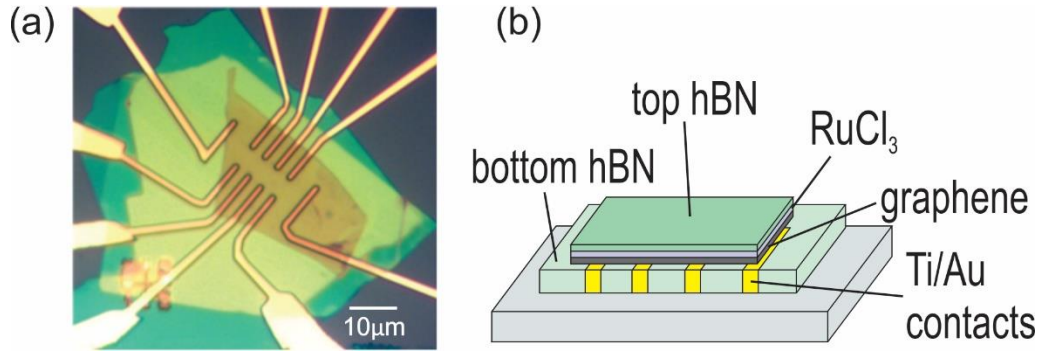
Figure 6:4 Graphene/α-RuCl$_3$ heterostructure device. (a) Optical image of a graphene/α-RuCl$_3$ heterostructure device comprising a 4 nm thick α-RuCl$_3$ sheet. Device fabrication involved the transfer of a top-hBN layer, an α-RuCl$_3$ sheet and graphene onto the bottom hBN where gold electrodes have been integrated before. (b) Schematic cross-section of the device.

As $\alpha-$RuCl$_3$ is documented to undergo chemical degradation upon exposure to acetone [146], the standard e-beam lithography (EBL) process (see section 3.5) needs to be modified. The subsequent steps of the adjusted protocol are as follows:

i. It starts with preparing a substrate with metal contacts embedded into an hBN flake. For this purpose, hBN crystals are exfoliated onto a Si/SiO$_2$ (300 nm oxide thickness) substrate equipped with a position marker array. hBN flakes with a minimum lateral size of 25 x 25 μm^2 are then selected under the optical microscope and their height is examined by AFM. Flakes with a height between 20 nm and 40 nm and displaying a flat and clean surface are selected for EBL.

ii. The mask for the contacts is patterned into PMMA by EBL (see section 3.5). After development in MIBK the substrate is subjected to reactive ion etching (RIE) in order to etch the hBN flake in the patterned regions.

iii. The substrate is loaded for thermal evaporation of first titanium (3 nm), followed by gold whose thickness is adjusted according to the height of the hBN flake (as determined from the AFM topography).

iv. After a successful lift-off, the Ti/Au contacts embedded in the hBN flake are examined once more by AFM (tapping mode). The height of the contacts should exceed that of the hBN flake by maximally 1- 2 nm. Then the Au/hBN region is scanned by the AFM in contact mode in order to clean the surface from PMMA residues [189].

v. For the preparation of polymer stamps for the pick-up of the exfoliated sheets, Elvacite powder (acrylic resin - Elvacite® 2552C High Gloss) is mixed with anisole in a 1:1 ratio. Small drops of the mixture are placed on glass slides and baked on a hotplate at 130 °C for 10 minutes [190].

vi. $\alpha-$RuCl$_3$ crystals are mechanically exfoliated onto Si/SiO$_2$ substrates using PDMS or Nitto adhesive tape [191]. Sheets with a minimum lateral size of 35x35 μm are selected and their height is examined by AFM.

vii.   hBN crystals are mechanically exfoliated onto bare Si/SiO$_2$ substrates, and sheets with minimum lateral size of 50 x 50 μm^2 (and a thickness between 10 and 30 nm) are selected as top hBN layers.

viii.   Graphene is mechanically exfoliated onto bare Si/SiO$_2$ substrates, and sheets with a minimum lateral size of 30 x 30 μm^2 are selected with the aid of an optical microscope.

ix.   The different layers are stacked step-by-step using the micromanipulator. The top hBN layer is picked up first by the Elvacite stamp. The temperature of the substrate stage is set to 70 °C when the stamp is pressed onto the hBN flake. After a few seconds in contact with the hBN sheet, the stamp is slowly lifted such that the sheet is picked up from the Si/SiO$_2$ substrate.

x.   The Si/SiO$_2$/$\alpha-$RuCl$_3$ substrate is mounted onto the sample stage and the substrate temperature is set to 80 °C. Using the optical microscope and the XY-stage of the micromanipulator the top hBN sheet is positioned above the $\alpha-$RuCl$_3$ sheet (all $\alpha-$RuCl$_3$ must be covered by the top hBN) and slowly brought into contact. The $\alpha-$RuCl$_3$ sheet is then picked up by the vdW force acting between $\alpha-$RuCl$_3$ and graphene.

xi.   The same procedure is repeated for the graphene sheet (all graphene must be covered by the $\alpha-$RuCl$_3$ sheet).

xii.   Finally, the hBN bottom electrode is mounted onto the sample stage and the substrate temperature is set to 180 °C. The Elvacite stamp with the graphene/$\alpha-$RuCl$_3$/hBN stack is pressed onto the Au contacts. Due to the high temperature the stamp melts immediately, thus aiding the transfer of the graphene/$\alpha-$RuCl$_3$/hBN stack onto the bottom electrode substrate.

xiii.   Residues of the Elvacite stamp are left on purpose on top of the device in order to avoid any destructive impact of an organic solvent.

xiv.   The device is ready for bonding and electrical measurements.

6.3 Anomalous temperature dependence of magneto-oscillation amplitude

For the low-temperature magnetotransport measurements, it was important that the samples were cooled down very slowly in order to avoid temperature gradients which may cause mechanical stress between the different device components [192].

Previous magnetotransport experiments on graphene/α-RuCl$_3$ heterostructures comprising a relatively thick α-RuCl$_3$ sheet (~20 nm thickness) had revealed a deviation of the temperature dependence of the magneto-oscillation amplitude from conventional Lifshitz-Kosevich (LK) behavior [146]. In general, the LK formula describes quantitatively quantum oscillations for instance in the magnetotransport and allows determining Fermi surfaces. Departures from LK behavior can have different reasons including quantum critical fluctuations [193], non-trivial topologies [194] or the formation of an unconventional Fermi liquid [195]. In order to shine further light on the origin of this deviation, we studied the magnetotransport properties of the heterostructure in dependence of the α-RuCl$_3$ sheet thickness and the direction of the applied B-field with respect to the substrate plane. In the next sections, the temperature dependent behavior of three different graphene/α-RuCl$_3$ heterostructures is presented in the order of decreasing thickness of the contained α-RuCl$_3$ sheet, followed by a discussion of possible mechanisms that may underlie the non-LK behavior.

6.3.1 Heterostructure with 20 nm thick α-RuCl$_3$ sheet

The longitudinal magnetoresistance (recorded under perpendicular B-field, i.e., $\theta = 90°$) of a graphene/α-RuCl$_3$ heterostructure device comprising a 20 nm thick α-RuCl$_3$ sheet is shown in Figure 6:5(a) for various temperatures between 1.3 and 15 K. At all temperatures, the curves display pronounced oscillations as a function of B-field, in accordance with earlier results obtained on graphene/α-RuCl$_3$ heterostructures with a similar thickness of the α-RuCl$_3$ sheet [146]. As mentioned in section 2.4.2.2, these oscillations can be attributed to the formation of two hole pockets upon hybridization between the Dirac bands of graphene and the almost flat bands of α-RuCl$_3$ [146].
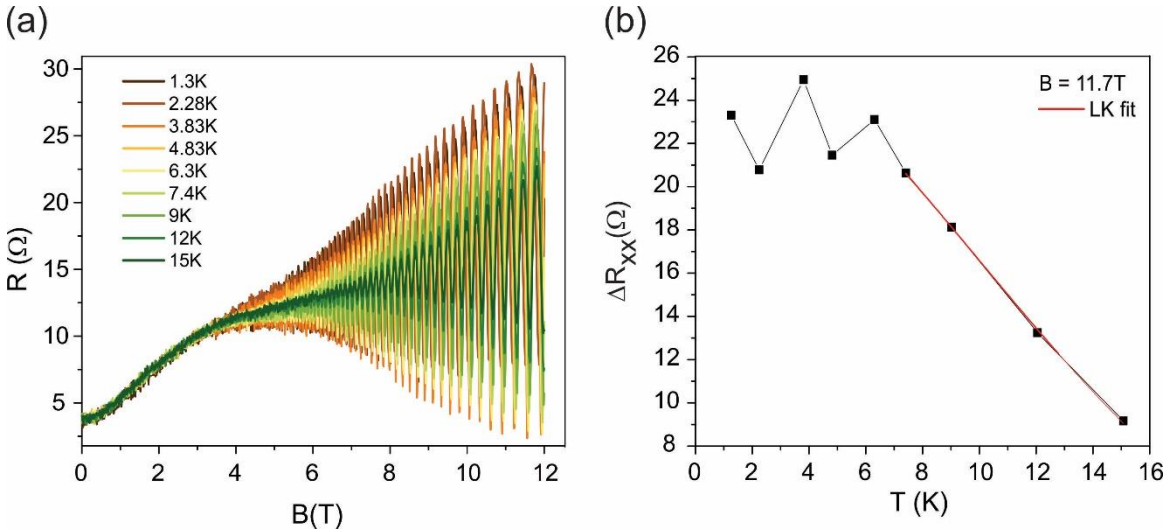
Figure 6:5 Heterostructure with 20 nm thick α-RuCl$_3$ sheet. (a) Longitudinal magnetoresistance R_{xx} of a graphene/α-RuCl$_3$ heterostructure with a 20 nm thick α-RuCl$_3$ sheet, measured at various temperatures between 1.3 and 15 K (V_g = 0 V). (b) Temperature evolution of the magneto-oscillation amplitude (ΔR_{xx}) at B $\approx$ 12 T. The red line is a fit according to the Lifshitz-Kosevich (LK) formula.

The corresponding magneto-oscillation amplitude (at B ≈ 12 T) is plotted in Figure 6:5(b) as a function of temperature. Again in close agreement with previous findings [146], there occurs a deviation from the monotonous amplitude increase at ~6 K, although in the present case the amplitude fluctuates instead of displaying a continuous decrease upon further cooling. The data points could be fitted (red line) down to ~6 K by the thermal damping factor R_T of the Lifshitz-Kosevich (LK) formula

$$R_\text{T} = \frac{\alpha r \mu_c T/B}{\sinh(\alpha r \mu_c T/B)},$$

(6.1)

where $\alpha = 2\pi^2 k_\text{B} m_\text{e}/e\hbar = 14.69\,T/K$ and μ_c is the effective cyclotron mass in relative units of the free electron mass m_e [196].

The magnetoresistance of the same device was again measured with a θ = 45° tilt, in order to introduce an in-plane component of the B-field. The obtained longitudinal magnetoresistance R_{xx} is displayed in Figure 6:6(a) as a function of B·cos(π/4) for various temperatures between 1.3 and 15 K. The temperature dependence of the magneto-oscillation amplitude at B = 11 T (see Figure 6:6(b)) is clearly different from the corresponding plot in Figure 6:5(b) (θ = 90°), as it enables an LK-fit down to ~2.5 K instead of only ~6 K in the latter case. Below 3 K, the amplitude is seen to drop, although only one more data point is available.
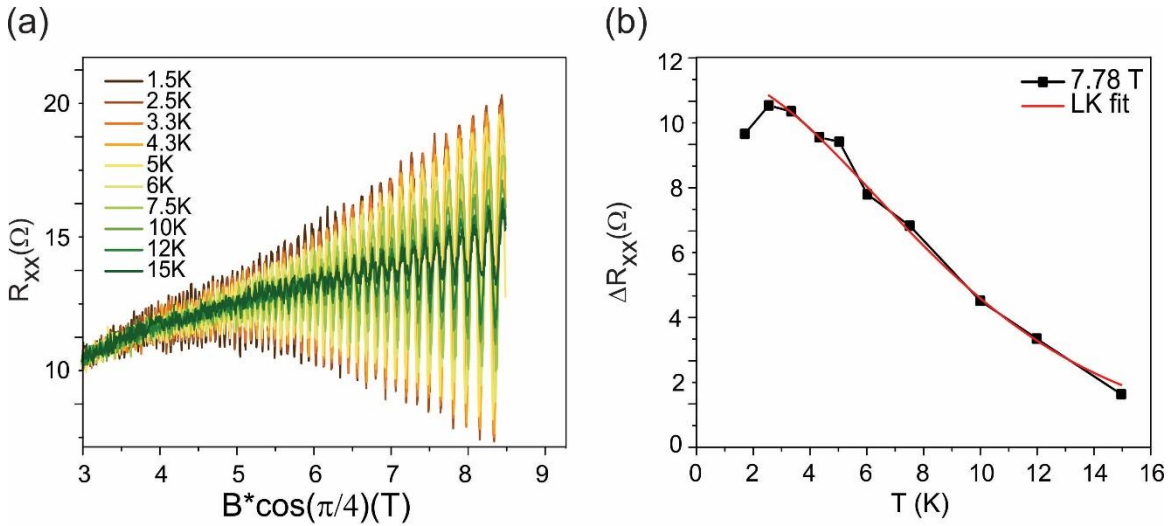
Figure 6:6 Magnetoresistance data of the same heterostructure as in Figure 6:5 (with a 20 nm thick α−RuCl3 sheet), measured under a tilt of θ = 45° (V_g = 0 V). (a) Longitudinal magnetoresistance R_{xx} as a function of the out-of-plane B-field component for various temperatures between of 1.3 and 15 K. (b) Temperature evolution of the magneto-oscillation magnitude (ΔR_{xx}) at B = 7.78 T. The red line represents a fit according to the Lifshitz-Kosevich (LK) formula.

6.3.2 Heterostructure with 4 nm thick α-RuCl3 sheet

The next graphene/α−RuCl3 heterostructure that was investigated contained a 4 nm thick α−RuCl3 sheet (Figure 6:4(a) is an optical image of this device). The longitudinal magnetoresistance R_{xx} is plotted in Figure 6:7(a) for various temperatures in the range of 0.3 to 20 K. Here, the traces were collected in 1 K steps below 10 K, in order to better resolve the low temperature trend. A mentionable difference to the heterostructure device with the 20 nm thick α−RuCl3 sheet (cf. Figure 6:5(a)) is the considerably stronger magneto-oscillation amplitude. The extracted magneto-oscillation amplitude at B = 13.6 T is shown in Figure 6:7(b) as a function

of temperature. Remarkably, the data can now be reasonably well fitted by the LK-formula down to the lowest temperature (T = 0.3 K). The overall fit range notably exceeds that for the 20 nm α−RuCl$_3$ hetero-structure above (cf. Figure 6:5(b)).
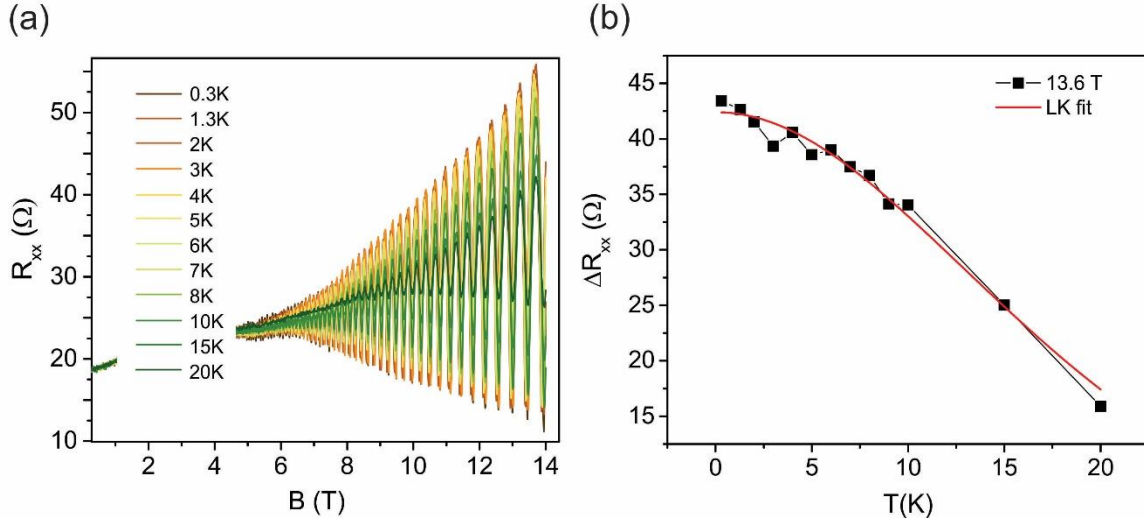
Figure 6:7 Heterostructure with 4 nm thick α-RuCl$_3$ sheet under perpendicular B-field. (a) Longitudinal magnetore-sistance R$_{xx}$ of a graphene/α−RuCl$_3$ heterostructure with a 4 nm thick α−RuCl$_3$ sheet (under perpendicular B-field), recorded at V$_g$ = 0 V for various temperatures between 0.3 and 20 K. (b) Temperature evolution of the magneto-oscil-lation amplitude (ΔR$_{xx}$) at B = 13.6 T. The red line is a Lifshitz-Kosevich (LK) fit of the data.

Like before for the 20 nm α−RuCl$_3$ heterostructure device, the magnetoresistance was then measured under a tilt of θ = 45°. The obtained curves are displayed in Figure 6:8(a) for five different temperatures between 250 mK and 10 K. As a major observation, the trend of the amplitude (at B = 9.82 T) is similar to that in Figure 6:7(b), with a monotonous increase upon cooling.
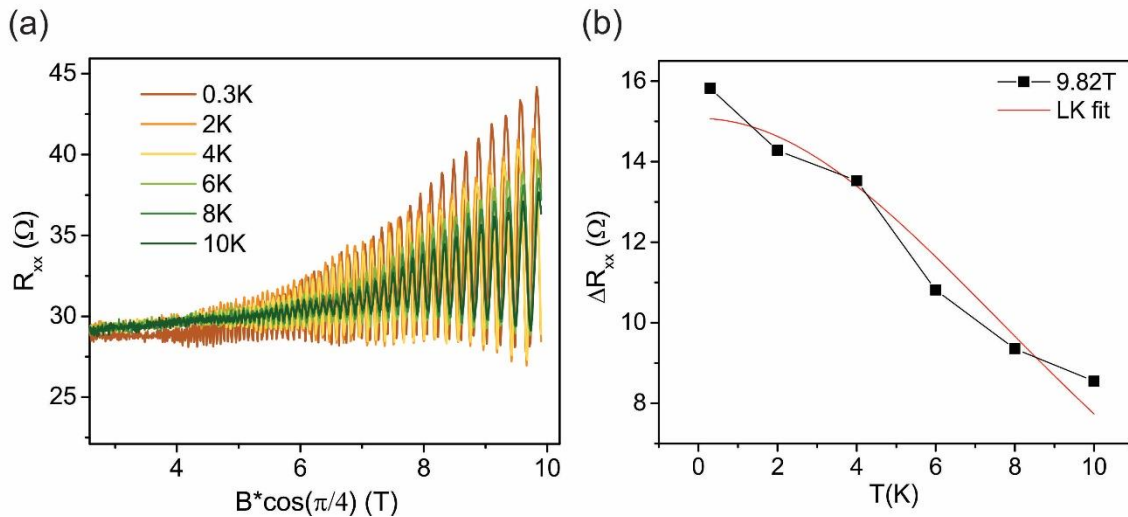
Figure 6:8 Magnetotransport behavior of the above device for a tilt of θ = 45° with respect to the applied B-field. (a) Longitudinal magnetoresistance R$_{xx}$ acquired at various temperatures between 250 mK and 10 K (V$_g$ = +70 V). (b) Plot of the magneto-oscillation amplitude (extracted at B = 9.82 T) vs. temperature.

6.3.3 Heterostructure with α-RuCl₃ monolayer

The fabrication of a graphene/α-RuCl₃ heterostructure with an α-RuCl₃ monolayer proved to be highly challenging, since it is very difficult to pick the latter up from the Si/SiO₂ substrate. Nevertheless, after many failed attempts a first such device could finally be realized.
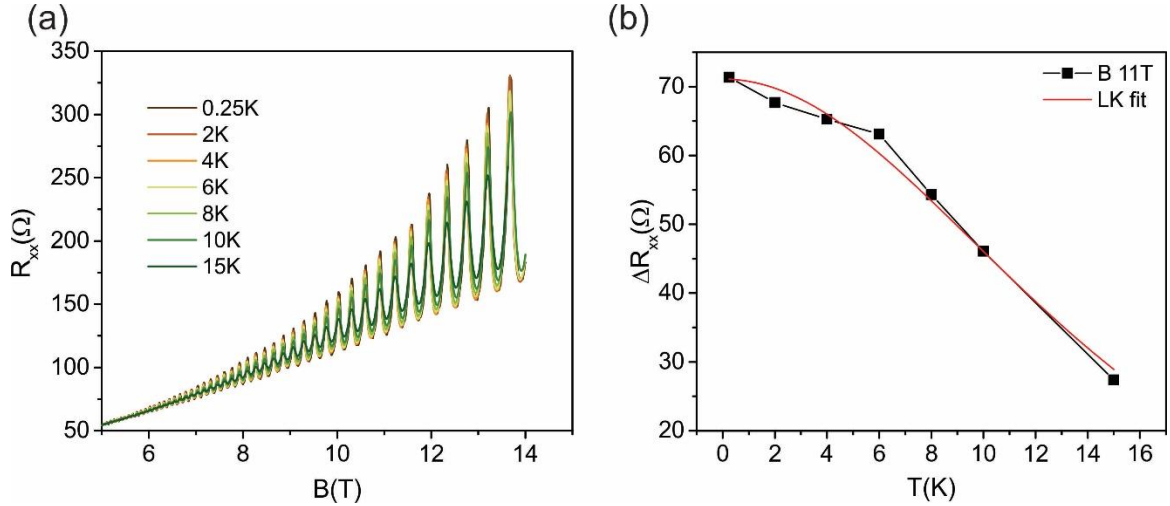

Figure 6:9 Heterostructure with α-RuCl₃ monolayer under perpendicular B-field. (a) Longitudinal magnetoresistance R_{xx} of the monolayer α−RuCl₃ heterostructure at selected temperatures between 0.25 and 15 K, recorded at V_g = 0 V under perpendicular B-field (θ = 90°). (b) Temperature evolution of the magneto-oscillation amplitude at B = 11T.

The longitudinal magnetoresistance of the graphene/α-RuCl₃ heterostructure device with an α-RuCl₃ monolayer (recorded under perpendicular B-field, i.e., θ = 90°) was measured at two different gate voltages, specifically V_g = 0 V and V_g = +70 V. The data obtained at V_g = 0 V is shown in Figure 6:9(a), along with the magneto-oscillation amplitude at B = 11T plotted vs. temperature in Figure 6:9(b). As already mentioned above (section 6.3), no beating pattern is observed at this specific gate voltage. The temperature evolution of the oscillation amplitude displays a monotonous increase upon cooling. However, at T ≈ 6 K there is a clear change of slope, i.e., below this temperature the amplitude continues to rise with a smaller rate. This trend is in contrast to the behavior of the above heterostructures with thicker α-RuCl₃, for the latter of which the oscillation amplitude dropped at least at one point upon cooling.

The temperature dependent magneto-oscillations of the device at V_g = +70 V, where a pronounced beating pattern with several nodes emerges (see section 6.3), is displayed in Figure 6:10(a). In these measurements, temperature was changed in 1 K steps below 10 K, and in 2 K steps above 10 K. The result of FFT analysis in Figure 6:10(b) reveals a strong double peak feature with monotonically decreasing amplitude for both peaks when temperature is increased. For a better overview, the FFT spectra are replotted in Figure 6:10(c) with vertical offset.

Figure 6:10 Magnetotransport behavior of the monolayer α−RuCl₃ heterostructure with FFT analysis of the magneto-oscillation components. The measurements were performed at V_g = +70 V under perpendicular B-field (θ = 90°). (a) Longitudinal magnetoresistance R_{xx} after background subtraction, plotted as a function of inverse B-field (1/B) for various temperatures. (b) Corresponding FFT analysis, revealing a double peak feature whose amplitude decreases with rising temperature. (c) Plot of the temperature dependent FFT spectra with vertical offset for visual clarity. (d) Temperature evolution of the amplitude of the two peaks (F1 - spin up and F2 - spin down).

The temperature dependence of the magneto-oscillation amplitudes of the two peak components is displayed in Figure 6:10(d). The peak with the stronger amplitude (F1) is associated with the spin-up Fermi pocket, and the weaker amplitude peak (F2) with the spin-down hole pocket. For both peaks, one observes a rising trend upon cooling, although for peak F1 the data show some noticeable scatter below 10 K.

Like for the other heterostructures devices before, the magnetotransport behavior of the present device was also measured under θ = 45° with respect to the B-field (again at V_g = +70 V). FFT analysis yielded the temperature dependent spectra in Figure 6:11(a). Compared to the above measurements under θ = 90° it is now more difficult to distinguish the two peaks belonging to the two different Fermi hole pockets. The temperature evolution of the peak amplitudes, depicted in Figure 6:11(b), very similar to the one observed for θ = 90° (cf. Figure 6:10(d)). In the present case, the monotonous amplitude rise upon cooling is more clear-cut, as the data of the F1 peak are less scattered. The only small difference between the two B-field orientations is a common observation with the 4 nm α-RuCl₃ heterostructure, but distinct from the behavior of the 20 nm α-RuCl₃ heterostructure.
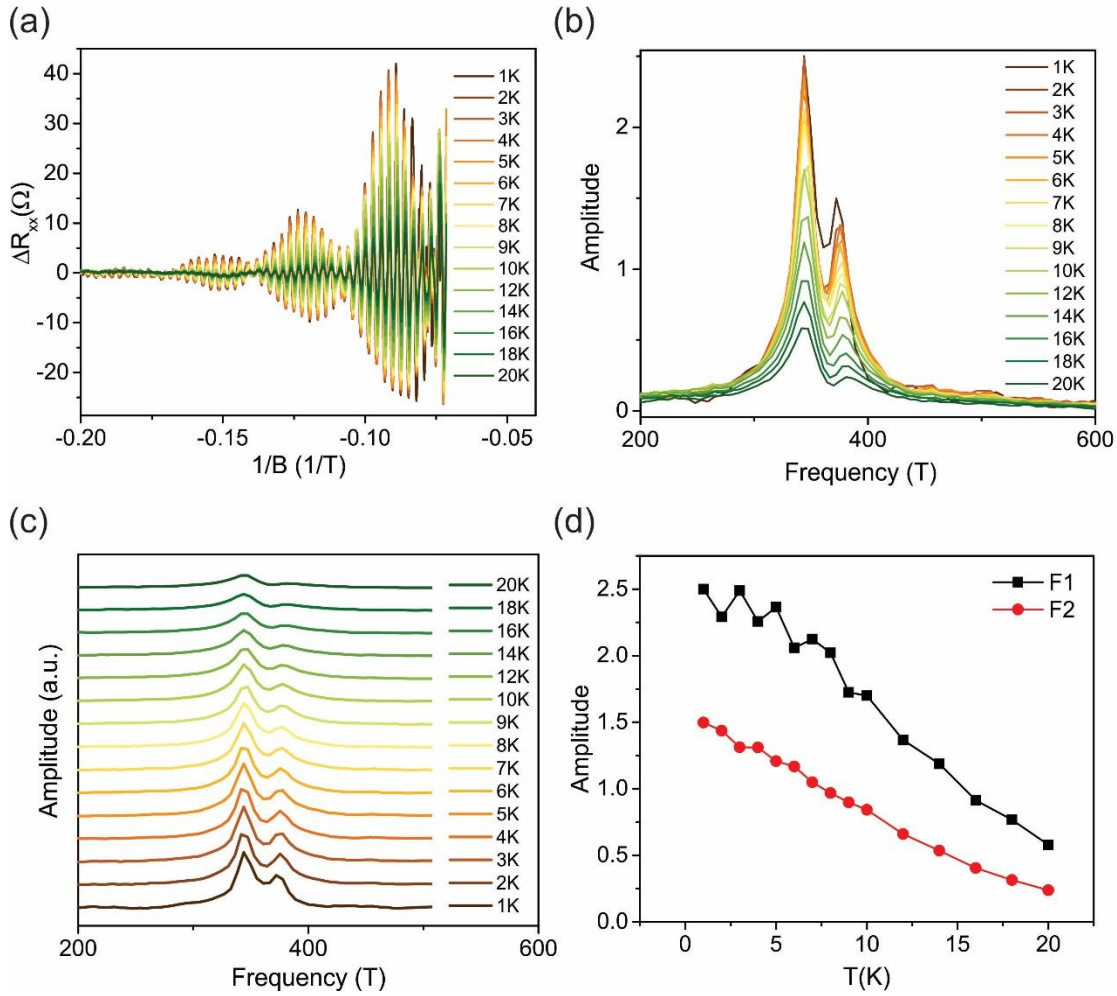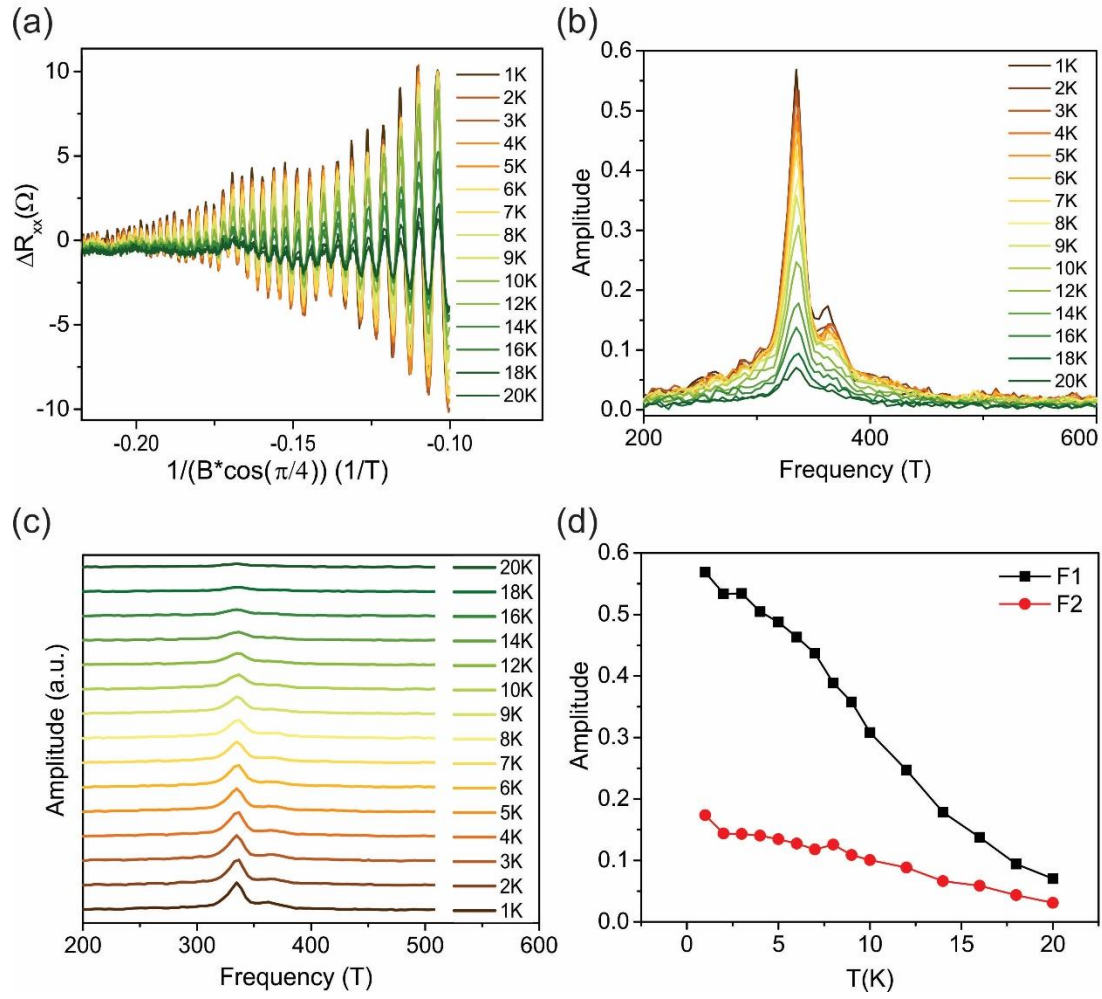
Figure 6:11 Magnetotransport behavior of the monolayer α–RuCl₃ heterostructure with FFT analysis of the magneto-oscillation components. The measurements were performed at V_g = +70 V under tilted B-field (θ = 45°). (a) Longitudinal magnetoresistance R_{xx} after background subtraction, plotted as a function of inverse B-field (1/B) for various temperatures in the range of T = 1 to 20 K. (b) Corresponding FFT analysis, revealing a double peak feature whose amplitude decreases with rising temperature. (c) Plot of the temperature dependent FFT spectra with vertical offset for visual clarity. (d) Temperature evolution of the amplitude of the two peaks (F1 - spin up and F2 - spin down).

6.3.4   Possible origin of non-LK behavior

Overall, the above described temperature dependent magnetotransport behavior of the graphene/α-RuCl₃ heterostructures with three different thicknesses of the α-RuCl₃ sheet exhibits the following two major trends:

- With decreasing thickness of the α-RuCl₃ sheet, the range over which the temperature dependence of the magneto-oscillation amplitude can be fitted by the LK equation extends towards lower temperatures (compare Figure 6:5(b) with Figure 6:7(b),Figure 6:9(b) and Figure 6:10(d)).
- Upon application of an in-plane B-field component, the LK fitting range of the magneto-oscillation amplitude extends towards lower temperatures (compare Figure 6:5(b) with Figure 6:6(b)). When the LK fitting works already at perpendicular B-field for the entire temperature range, application of an in-plane B-field component does not impart any significant change (compare Figure 6:7(b) with Figure 6:8(b), and Figure 6:10(d) with Figure 6:11(d)).

There are two possible (mutually not exclusive) mechanisms that may explain the non-LK behavior and the aforementioned trends. The first mechanism involves interfacial spin scattering due to spin fluctuations that emerge in $\alpha-RuCl_3$ upon its transition to the zig-zag antiferromagnetic ground state at the Néel temperature T_N [146]. This assumption gains some support by the fact that T_N lies in a similar temperature range as the observed onset of deviation from LK theory. For bulk $\alpha-RuCl_3$, the magnetic phase transition at low temperature is preceded by a structural phase transition occurring at ~150 K [197]. It is assumed to involve a transition from a monoclinic to a trigonal structure, similar to observations made on the 2D magnet $CrCl_3$ [188]. The magnetic transition behavior of bulk $\alpha-RuCl_3$ crystals has been found to depend on their structural perfection. In particular, crystals with minimal stacking faults exhibit $T_N \approx 7$ K, whereas crystals with higher percentages of stacking faults show an additional magnetic transition at ~14 K [98]. For the specific bulk $\alpha-RuCl_3$ used here as starting material for mechanical exfoliation, magnetic susceptibility measurements revealed two magnetic transitions at T_{N1} = 7 K and T_{N2} = 13 K [187], indicating the presence of some disorder. At the present stage, it remains unknown how T_N evolves when bulk $\alpha-RuCl_3$ is decreased to thin sheet and how it precisely depends on the number of $\alpha-RuCl_3$ layers. Nonetheless, Raman studies suggest enhanced frustrated magnetic interactions in few layered $\alpha-RuCl_3$ sheets in comparison to bulk $\alpha-RuCl_3$ [119]. In this context, it is furthermore noteworthy that recent charge transport measurements on other graphene/α-RuCl3 heterostructures revealed peaks and dips in the first derivative of the temperature dependence of resistivity (i.e., dρ/dT vs. T-plots) at low temperature [147]. These features occurred in the range of 12 – 35 K, roughly corresponding to the higher T_N in non-perfect bulk α-RuCl3 crystals. However, why there is no additional feature at lower temperatures in their resistivity data remains unclear.

For the present devices, spin fluctuations associated with the magnetic transition in the α-RuCl3 sheet may indeed account for the non-LK behavior visible below ~6 K in the 20 nm α-RuCl3 heterostructure (cf. Figure 6:5(b)), as this temperature fits quite well to the lower T_N. In this scenario, the absence of an additional change between 10 and 15 K could be explainable by the absence or reduced number of stacking faults in the thin sheet. At the first sight, this may sound unlikely as mechanical exfoliation has the tendency to introduce additional disorder into crystals due to the mechanical shear forces that act on them. However, it could also be that during exfoliation preferably sheets of high internal order and hence strong cohesion are separated from the larger crystal structure. On this basis, the extended LK fitting ranges for the 4 nm and monolayer α-RuCl3 heterostructures could then be understood if T_N would decrease with decreasing thickness of the α-RuCl3 sheet. Testing this assumption would require independent measurements of T_N for α-RuCl3 sheets in dependence of thickness, which however are not available at the present stage.

In contrast to the α-RuCl3 thickness dependence, it seems more difficult to explain the magnetotransport data acquired under 45° tilt by the proposed spin scattering mechanism. Magnetic susceptibility measurements on bulk α-RuCl3 have revealed that /It has been documented that the application of a sufficiently strong in-plane B-field suppresses the antiferromagnetic phase, resulting in a paramagnetic phase instead [198]. As can be seen from the corresponding magnetic phase diagram in Figure 6:12, this transition requires an in-plane B-field above ≈ 8 T within the relevant temperature range below 10 K. In the present experiments, however, the in-plane B-field component B·cos(45°) remains just below this value, thus pointing against such B-field induced suppression of antiferromagnetic ordering as the origin of the extended LK behavior.
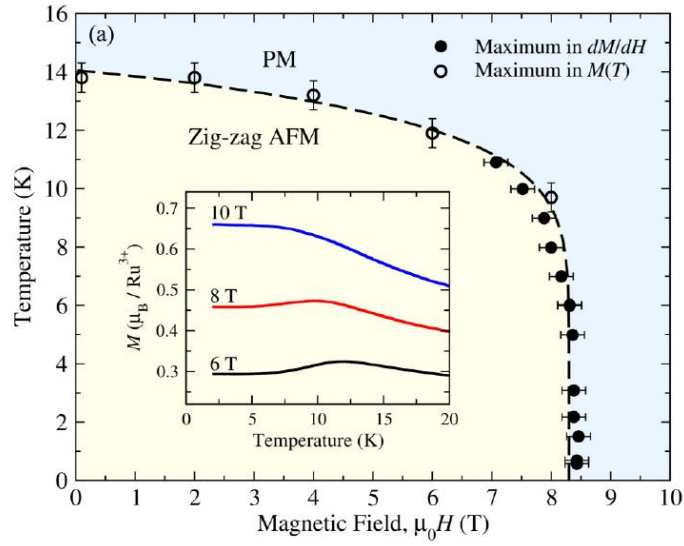
Figure 6:12 Magnetic phase diagram of single-crystal α-RuCl₃ under a B-field perpendicular to the stacking axis c*. The dashed line is a guide to the eye, marking the phase boundary between the zig-zag antiferromagnetic phase (yellow shading, AFM) and the paramagnetic (PM, blue shading) phase. Reproduced with permission from [198].

The second possible mechanism that could account for the non-LK behavior relates to the fact that the hybridization-induced bands associated with the two Fermi hole pockets (see section 2.4.2.2 and Figure 2:25) have a heavy (flat) character. The presence of heavy bands has been invoked to explain the anomalous temperature dependence of the quantum oscillation amplitude for the heavy fermion compounds $CeCoIn_5$ [193] and SmB_6 [195]. Theoretical modelling for SmB_6 has shown that band hybridization leads to an amplitude maximum at low temperature, whose prominence depends on the hybridization strength and the Fermi level position [199]. The key principle underlying the emergence of the maximum is that the quantum oscillations originating from the flat (heavy) band regions contribute with larger amplitudes to the weighted average over different chemical potentials from a window proportional to temperature. The experimental features in Figure 6:6(b), Figure 6:7(b). Figure 6:8(b), Figure 6:9(b) and Figure 6:11(d) indeed resemble the possible (calculated) shapes of the maximum, which underscores that this mechanism contributes to or even is mainly responsible for the observed dependence on α-RuCl₃ thickness (which may change the details of hybridization) and also on the tilt with respect to the applied B-field (which may alter the Kondo coupling parameter with a cosine-like angle dependence).

It is important to emphasize that the fine details of the temperature dependence of the magneto-oscillation amplitude of the above devices could be subtly influenced by doping, strain and the relative orientation of the two lattices. All these parameters are difficult to control for the used mechanical transfer method. In total, there arises an intricate picture, where not only both the magnetic phase transition of α-RuCl₃ and the hybridization-induced heavy bands in the graphene/α-RuCl₃ heterostructure could simultaneously contribute to the non-LK behavior, but where also sample-to-sample variations are likely to be important.

Further hints that the band hybridization indeed depends on the thickness of the α-RuCl₃ sheet in proximity to graphene could be gained especially for the monolayer case, as manifested in a distinct gate depen-dence of the magneto-oscillations, which was not observed before for the other heterostructure devices with thicker α-RuCl₃. This is described in more detail in the next section.

6.4 Gate-dependent magneto-oscillations in the heterostructure with an α-RuCl₃ monolayer

The longitudinal magnetoresistance R_{xx} under perpendicular B-field (θ = 90°) of the α-RuCl$_3$ monolayer heterostructure is shown in Figure 6:13 for B-fields up to 14 T and applied gate voltages between -70 V and +70 V in steps of 10 V. All measurements were done at ~300 mK. In comparison to the heterostructures with thicker α-RuCl$_3$ sheets (cf. Figure 6:5(a) and Figure 6:7(a)), there is a pronounced beating pattern which is effectively modulated by the applied gate voltage. Only at V_g = 0 V, no beating pattern is observed, while for all positive and negative gate voltages different numbers of nodes appear depending on the gate voltage value.
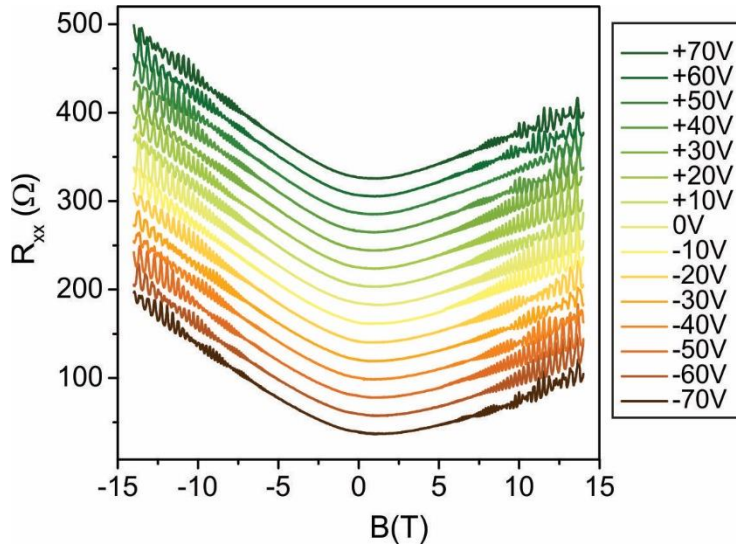
Figure 6:13 Longitudinal magnetoresistance R$_{xx}$ of a graphene/α-RuCl$_3$ heterostructure with an α–RuCl$_3$ monolayer, measured at T ≈ 300 mK under perpendicular B-field (θ = 90°) for various gate voltages in the range of -70 V to +70 V. The original data can be found in the Appendix (Figure 7:3).

The magnetoresistance of the device is replotted in Figure 6:14(a) as a function of 1/B, together with the gate-dependent FFT spectra in Figure 6:14(b). Similar to previous observations on a heterostructure with a ~20 nm thick α-RuCl$_3$ sheet [146], the spectra comprise two close peaks, which can be ascribed to the two Fermi pockets in the hybridized band structure. As a general trend, the double-peak feature shifts towards higher frequency for increasingly negative gate voltage, again in agreement with the previously reported behavior [146]. However, the present device is different in that there seems to be a 'crossing' of the two FFT peaks, i.e., while one of the peaks always occurs at the same frequency, the other one occurs at higher (lower) frequency for negative (positive) gate voltages. This is highlighted in Figure 6:15(a), where the double peak feature at V_g = +70 V is compared to the one at V_g = -70 V.
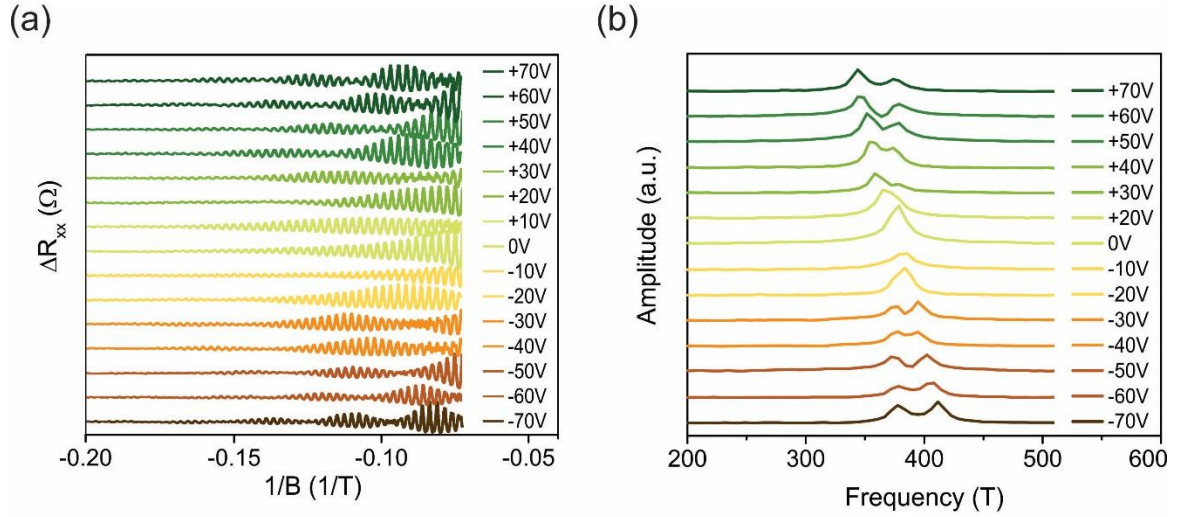
Figure 6:14 FFT analysis of the gate- dependent magneto-oscillation components. (a) Magnetotransport data in Figure 6:13 replotted as a function of 1/B. A nonlinear background was subtracted and the curves were vertically offset for clarity. (b) Corresponding FFT spectra revealing two close peaks which shift in dependence of the applied gate voltage.

From the gate-dependent peak frequencies, the respective carrier concentrations were calculated, which are plotted vs. gate voltage in Figure 6:15(b). Here, the carrier concentration derived from the lower frequency peak is denoted as n_1 (black line) and the carrier concentration derived from the higher frequency peak as n_2 (red line). Importantly, the (hole) concentrations on the order of $1.8 \cdot 10^{13}$ cm^{-2} match well with the values determined for the heterostructures with thicker α-RuCl$_3$, and indicate very strong p-doping which cannot be explained otherwise than being due to strong interaction with the α-RuCl$_3$. This finding strongly supports that the α-RuCl$_3$ monolayer is indeed present and intact in the investigated device. Such confirmation is particularly important since it is notoriously difficult to pick up and transfer the monolayer, and a direct microscopic proof that these steps were successful is rather difficult to provide.
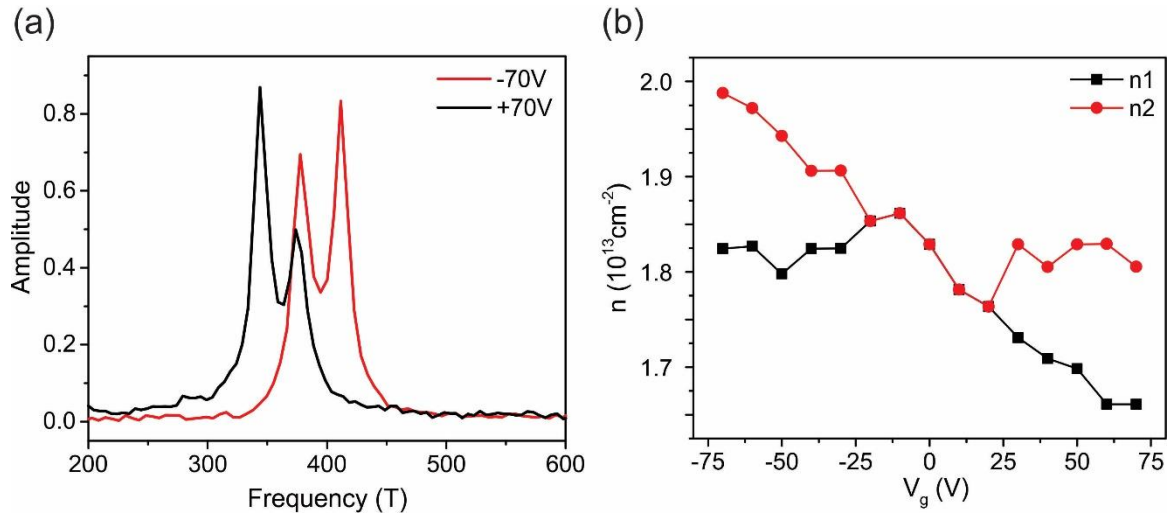
Figure 6:15 FFT amplitudes and carrier concentrations for the gate magnetotransport data in Figure 6:14. (a) Comparison of the double peak feature for Vg = +70 V and Vg = -70 V. (b) Carrier concentrations calculated from the two FFT peak frequencies, plotted as a function of applied gate voltage. Concentrations n1 and n2 are derived from the lower and higher frequency peak, respectively.

The plot in Figure 6:15(b) directly mirrors the above mentioned 'crossing' behavior, with the carrier concentration of one of the pockets remaining constant while the other one rises or decreases with the applied gate voltage, and is clearly distinguished from the behavior of the previously studied 20 nm α-RuCl$_3$ heterostructure [146]. In the latter case, both hole concentrations monotonously decrease in parallel with increasing gate voltage. The crossing observed for the present device is unlikely to be simply the result of sample-dependent variation of the doping level, but must rather be due to a change of the (hybrid) band structure. For a complete picture, however, additional possible effects have to be taken into account. As one possibility, mechanical strain may be introduced into an α-RuCl$_3$ monolayer when it is placed on graphene [143]. Another option is that a structural transformation into a distorted honeycomb lattice occurs when the α-RuCl$_3$ approaches a single layer, as suggested by recent Raman spectroscopy experiments [186]. There is also some evidence gained by low-energy electron diffraction (LEED) that the surface monolayer of α-RuCl$_3$ undergoes a crystal structure reconstruction that breaks inversion symmetry [200].

Chapter 7   Summary and Outlook

The unique properties of graphene makes it a promising candidate for technological applications, for instance in the area of spintronics and valleytronics [201]. A big advantage of graphene is the ability to tune its properties via proximity effects with other 2D vdW materials, such as transition metal dichalcogenides (TMDs), TIs and magnetic insulators [202]. This thesis was aimed at exploring proximity effects exerted on graphene by two different types of 2D materials, specifically BTS as a 3DTI and the antiferromagnetic Mott insulator (and proximate Kitaev quantum spin liquid) α-RuCl$_3$. In both cases, novel device fabrication approaches were developed in order to achieve a sufficiently strong electronic coupling between the two components, either through direct growth of the material onto graphene or through significant improvements of the mechanical transfer method used to stack the material onto graphene.

The first part of the thesis dealt with BTS crystals directly grown by CVD on top of graphene. Heterostructures combining graphene with BTS are of particular interest for enhancing the SOC in graphene in order to implement spin generation and manipulation functionalities [203].
The quality of the obtained graphene/BTS heterostructures was found to be sensitively influenced by the graphene source as well as the detailed growth parameters. The initial growth experiments were carried out with CVD graphene transferred onto the Si/SiO$_2$ substrates using a wet etching method. This type of graphene offers the advantage that the transferred sheets are not only very large, but also consist mostly of monolayer regions. However, the relatively high defect density of these sheets turned out to significantly impede the BTS growth on top. As another disadvantage, the CVD graphene sheets often exhibited pronounced p-doping due to the different etchants, solutions and polymers used during the transfer process. The resulting non-uniform and irregular shaped BTS on the CVD graphene was not suitable for device fabrication. Much better results were obtained with mechanically exfoliated graphene, which provided access to large BTS crystals with defined orientations (see Chapter 4.1).

The exfoliated graphene/BTS heterostructures were thoroughly characterized by a combination of optical microscopy, AFM, Raman spectroscopy and second harmonic generation (SHG) microscopy. The characteristic Raman peaks obtained from the BTS flakes confirmed their crystalline order and chemical composition. Detailed analysis of the Raman peak positions revealed the presence of tensile stress in BTS crystals with a layer thickness below ~5 nm. This tensile stress was found to be associated with compressive stress in the underlying graphene sheet. By comparison, graphene regions with thicker BTS crystals exhibited only minor strain, and at the same time consistently strong p-doping. Interestingly, p-doping was observed not only for the BTS covered graphene, but also for bare graphene sections after the BTS growth (see Chapter 4.2).

Information regarding the interface symmetry and lattice match in the graphene/BTS heterostructures could be gained from optical SHG microscopy. The polarization-dependent SHG signals revealed for some, but by far not all, BTS/graphene regions broken inversion symmetry and a 30° relative orientation between the graphene and BTS lattices, corresponding to a commensurate growth (see Chapter 4.3).

Charge and magnetotransport experiments on the graphene/BTS heterostructures were performed in different contact configurations. Despite the sizeable variation of p-doping level from device-to-device, the gate dependent phase coherence lengths could be extracted from the low temperature magnetotransport data. Thus derived phase coherence length displayed a maximum at the CNP in graphene/BTS, in contrast to pristine graphene displaying a minimum at the CNP (see Chapter 5). This behavior can be taken as evidence for an SOC enhancement of graphene by the BTS proximity, in analogy to similar graphene/3DTI heterostructures with an estimated graphene SOC strength of ~2.5 meV [41].

The second part of the thesis is dedicated to graphene in proximity to α-RuCl$_3$. Previous studies on graphene/α-RuCl$_3$ heterostructures reported an intriguing magnetotransport behavior which according to DFT calculations could be attributed to the resulting hybrid band structure [146]. The hybridization between the bands of graphene and α-RuCl$_3$ induces strong hole doping in graphene and the formation of two Fermi hole pockets. The major objective of the experiments presented in Chapter 6 was to shine more light on the origin of the anomalous temperature dependence of the magneto-oscillation amplitude in the graphene/α-RuCl$_3$ heterostructures. This task was addressed by (i) investigating further graphene/α-RuCl$_3$ heterostructures wherein the α-RuCl$_3$ thickness is smaller than the 20 nm in the original report (possibly down to the monolayer limit), and (ii) performing magnetoresistance measurements under a tilt of 45° with respect to the applied B-field, in order to introduce an in-plane B-field component which may suppress the onset of the deviation upon cooling down the device.

Considerable effort was devoted to improving the heterostructure fabrication process which involves exfoliation of the crystals with scotch tape, followed by pick- up and stacking steps using polymer stamps. In this manner, a graphene/α-RuCl$_3$ heterostructure device comprising an α-RuCl$_3$ monolayer could ultimately be achieved.

The magnetotransport measurements revealed that both decreasing the thickness of the α-RuCl$_3$ sheet and the application of an in-plane B-field extend the range over which the temperature dependence of the magneto-oscillation amplitude can be fitted by Lifshitz-Kosevich theory towards lower temperatures. Based upon the available data, it was not possible to single out one specific mechanism to explain this trend. As the most plausible scenario, both a suppression of the magnetic phase transition of α-RuCl$_3$ and the hybridization-induced heavy bands in the graphene/α-RuCl$_3$ heterostructure can simultaneously contribute to the non-LK behavior, with the fine details of the temperature evolution being influenced by sample-to-sample variations of doping, mutual orientation of the two lattices, and the quality of the heterointerface.

Due to the quite challenging device fabrication and the rather time consuming magnetotransport measurements, it proved difficult to obtain a good device statistics necessary to unequivocally interpret the device behavior. This limitation vividly expresses the major strength and weakness of the mechanical transfer approach to vdW heterostructures. On the one hand, it can provide access to heterostructures with intriguing physical properties, which would be difficult or even impossible to realize by alternative methods. For the specific case of α-RuCl$_3$, there is currently no vapor phase method available that would allow direct growth of α-RuCl$_3$ on graphene. On the other hand, the lack of efficient control over the interface cleanliness and the relative lattice orientation unavoidably leads to fabrication-related differences between the devices, which are difficult to pin-down due to the lack of straightforward methods for determining these structural characteristics.

Based on the above summarized results, there arise several possible directions of future research which could help to shine further light on the electronic properties of the investigated graphene-based hetero-

structures, and how these could be exploited for spintronic device applications. In the following two sections, these perspectives are outlined separately for the graphene/BTS and the graphene/α-RuCl$_3$ heterostructures.

7.1 Follow-up experiments on graphene/BTS heterostructures

7.1.1 More detailed Raman studies

The Raman spectroscopic detection of strain and doping effects in the graphene/BTS heterostructures has so far been limited by the thickness of the grown BTS sheets. For graphene covered by thicker BTS (>15 nm), no Raman signal could be obtained because of significant absorption of the incoming (and backscattered) laser light by the BTS. This may be improved in further experiments by flipping of the graphene/BTS stacks. The flipping could be achieved by spin-coating PMMA onto the substrate with the graphene/BTS sheets, followed by placing the sample for a few hours in hot water (90°C) so that the PMMA/BTS/graphene stack separates from the Si/SiO$_x$ substrate and floats on the water surface. The stack could then be fished by a PDMS stamp and the PPMA dissolved in acetone. Finally, the PDMS/graphene/BTS stack would be pressed onto a clean Si/SiO$_2$ substrate and be ready for the Raman experiments.

More detailed studies of the strain and doping effects for a wide range of BTS flake thicknesses and orientations could help to better understand the appreciable variation of the local doping levels. The flipping method would furthermore allow transferring the graphene/BTS heterostructures onto TEM grids. TEM analysis could help to confirm the crystalline quality of the grown BTS crystals, and to identify the parameters required for the commensurate growth of BTS on graphene.

7.1.2 Probing the spin texture

Theory predicts a gate-tunable spin texture for the commensurate graphene/BTS heterostructures, which would represent a highly valuable functionality for spintronic applications [39]. Based upon the ability to determine the interface symmetry using SHG microscopy, it would be very interesting to experimentally probe the spin lifetimes anisotropy in the heterostructures. For this purpose, we have performed first time-resolved Kerr rotation (TRKR measurements) in close collaboration with the group of Alexander Holleitner (WSI TUM München). Details on the optical set up and the principle of measurement can be found in Section 3.10.

Figure 7:1 depicts a first graphene/BTS heterostructure that was examined by TRKR microscopy. The optical image in Figure 7:1(a) and the AFM image in Figure 7:1(b) show the same region of the device. Especially the thick BTS sheets (appearing as shiny yellow flakes in the optical image and white flakes in the AFM image) exhibit regular shapes and defined growth orientations. For the thinner sheets (purple contrast in the optical image) it is more difficult to assess the quality of the growth. For the TRKR measurements, the circularly polarized pump laser and the linearly polarized probe laser need to be perfectly aligned on the same spot on the sample surface. To achieve better precision for the positioning of the laser pulses, photocurrent X-Y maps are first recorded. A photocurrent map acquired from the graphene/BTS region is shown in Figure 7:1(d). Photocurrent signals of different strength and signs are obtained from the BTS flakes.

For the following TRKR measurements, three different spots were selected on the graphene/BTS heterostructure; the first one on a smoothly grown, relatively thin BTS flake (height ~6 nm), the second one on a less oriented and slightly thicker BTS flake (height ~8 nm), and the third one on a graphene section not covered by BTS as reference. The three spots are marked by arrows in the optical and AFM image. The gate

dependent two-probe resistance of the graphene/BTS heterostructure was recorded before and after acquiring the X-Y photocurrent map of the sample. There is an unexpectedly large shift between the two transfer curves. Specifically, in the first transfer curve the CNP is not visible for gate voltage up to V_g = +60 V due to the strong p- doping of the graphene, which was also observed in charge transport measurements on similar graphene/BTS heterostructures (see Chapter 5), whereas in the transfer curve recorded after the X-Y photocurrent map acquisition, the Dirac point is located at V_g = +20 V. Such drastic doping changes could be explained by UV light-induced detachment effects in graphene [174]. In the present case, irradiation with the 400 nm probe laser upon recording of the photocurrent map may remove oxygen adsorbates as a major source of p-doping from the graphene surface. The reduced p-doping is highly advantageous as it opens the possibility to detect the spin lifetimes also close to the CNP.
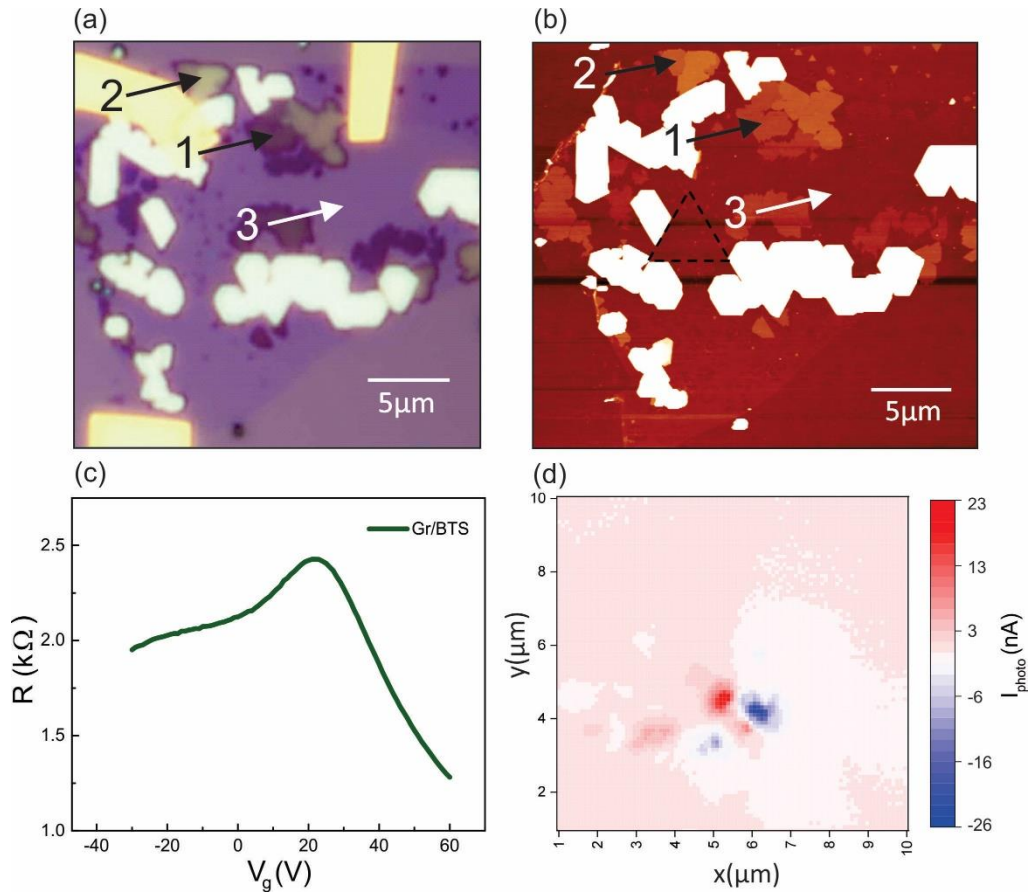

Figure 7:1 Pre-characterization of a graphene/BTS heterostructure used for TRKR measurements. (a) Optical image of the electrically contacted heterostructure with various BTS flakes. The labeled arrows mark the laser positions for the subsequent TRKR measurements. The three different spots include a ~6 nm thick BTS flake (spot 1), an ~8 nm thick BTS sheet (spot 2), and a graphene section without BTS (spot 3). (b) AFM image of the same region as in the optical image, with spots 1, 2 and 3 marked accordingly. (c) Gate dependent two-probe resistance curve of the graphene/BTS heterostructure measured at room temperature in a weak vacuum and after acquisition of an X-Y scan of the heterostructure with a 400 nm laser. (d) X-Y photocurrent map of the heterostructure.

During the TRKR measurements, the examined spots are exposed to the 800 nm and 400 nm laser over hours, which can result in further shifts of the CNP. Thus, for an accurate correlation between the local CNP and the detected Kerr angle the photocurrent signals were recorded in parallel. For each scan, the local graphene CNP is accessible from the sign change of the photocurrent.
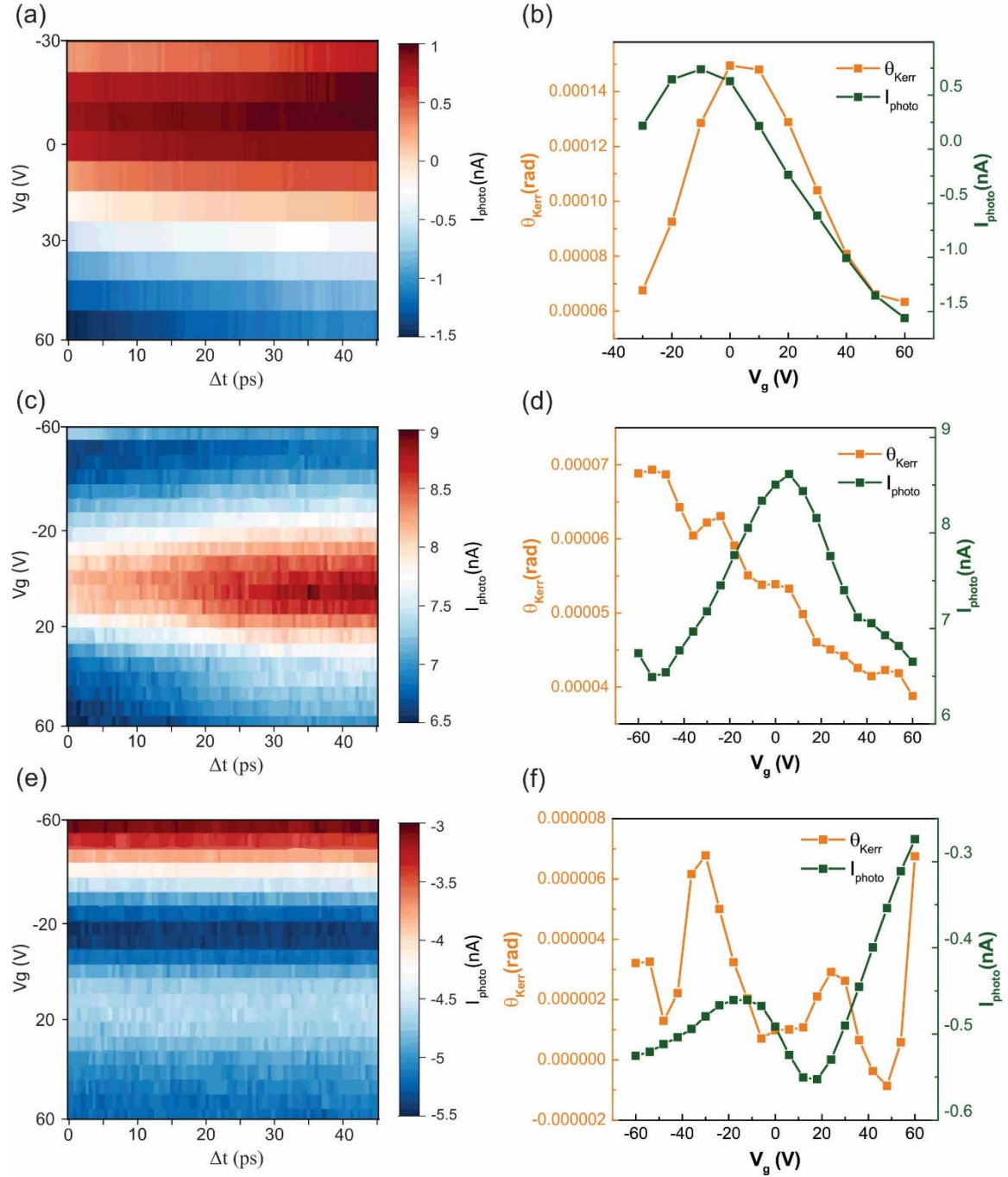
Figure 7:2 TRKR measurements taken from the three different spots of the graphene/BTS heterostructure in Figure 7:1. (a), (c) and (e) are gate and time dependent local photocurrent maps detected from spots 1, 2 and 3, respectively. (b), (d) and (f) show the time integrated Kerr rotation signals as a function of applied gate voltage (orange data points). The corresponding local photocurrent values are plotted as well (green data points).

The Kerr data obtained from all three spots on the graphene/BTS device is summarized in Figure 7:2. For each applied gate voltage, the Kerr and photocurrent signals were recorded with an acquisition time of Δt = 50 ps. Figure 7:2(a), (c) and (e) show time dependent photocurrent data recorded from spot 1, 2 and 3, respectively. Figure 7:2(b), (d) and (f) are plots of the corresponding time integrated Kerr angle along with the simultaneously recorded photocurrent as a function of gate voltage.

The photocurrent response at the first spot testifies that the CNP occurs at V_g = +10 V, since at this gate voltage the photocurrent changes its sign (Figure 7:2(a)). Close to the CNP there is a maximum of the Kerr angle (see Figure 7:2(b)). This finding is in good agreement with the theoretical prediction for the highly commensurate structure that the spin lifetime anisotropy is maximal near the CNP [39] (see Figure 2:21(c)).

The data recorded from the second spot is more difficult to interpret, as there is no change of sign in the photocurrent and hence the location of the CNP remains open. Indeed, the subsequent gate dependent two-probe resistance measurement revealed a further, strong shift of the CNP towards negative gate voltages outside the measurable range. In addition to not being able to determine the Kerr angle close to the CNP, the Kerr angles are now significantly smaller than before (see Figure 7:2d). Nonetheless, the monotonous increase of the Kerr angle is in accordance with the theoretically predicted behavior for the non-commensurate heterostructure (see Figure 2:24(b)) [39]. Confirming that the local BTS/graphene section has indeed this structural characteristic would require SHG measurements at this spot.

For the third spot (graphene without BTS) serving as reference, there also appears no sign change of photocurrent, indicating that the CNP was shifted outside the accessible gate voltage range (i.e., below V_g = -60 V). The most important observation is that the collected Kerr signal is very weak in comparison to the two other spots, which ensures that the Kerr signal originates from the heterointerface between graphene and BTS.

Further TRKR experiments could enable gaining a better understanding of the dependence of TRKR signals and the derived spin lifetimes on the thickness and growth orientations of the examined BTS flakes. To this end, it should be possible to repeatedly shift the CNP back by venting sequences which expose the device to ambient. Along these lines, it would also be interesting to study the spin texture of graphene/BTS heterostructures wherein the graphene is located on an underlying h-BN sheet instead of making direct contact with the Si/SiO$_2$ surface. However, this task would require novel growth strategies, as at the present experimental status the BTS growth occurs at random locations on the substrate.

7.2 Follow-up experiments on graphene/α-RuCl$_3$ heterostructures

7.2.1 Enhanced gating

The present charge transport experiments demonstrated that different devices display a different temperature- and gate-dependence of the magneto-oscillations. In order to enable a better correlation between these differences and the thickness of the α-RuCl$_3$ sheet with the heterostructure, and to unravel the extent to which the thickness influences the doping level, further DFT calculations would be highly beneficial.

From the experimental side, it would be worthwhile to study the effect of further enhanced doping on the magnetotransport properties of the graphene/α-RuCl$_3$ heterostructures. Theory predicts that strong n-type doping of the α-RuCl$_3$ can bring it closer to the Kitaev QSL state (see section 2.4.2.2), which may manifest itself in the magnetoresistance behavior. The required strong gating could be achievable with an additional (graphene) gate on top of the α-RuCl$_3$ sheet.

7.2.2 Tunneling spectroscopy of α-RuCl$_3$

Another interesting task would be to probe possible signatures of a Kitaev QSL in α-RuCl$_3$ by 2D-to-2D tunneling spectroscopy. According to theory, magnetic or quantum-order excitations could lead to characteristic features in both the differential conductance and the inelastic electron tunneling spectrum, which in the latter case scale cubically with the applied B-field [204]. The required tunneling devices could be obtained by embedding an α-RuCl$_3$ (mono) layer between two graphite sheets serving as top and bottom electrodes, which should in principle be feasible with the mechanical transfer method.

Appendix

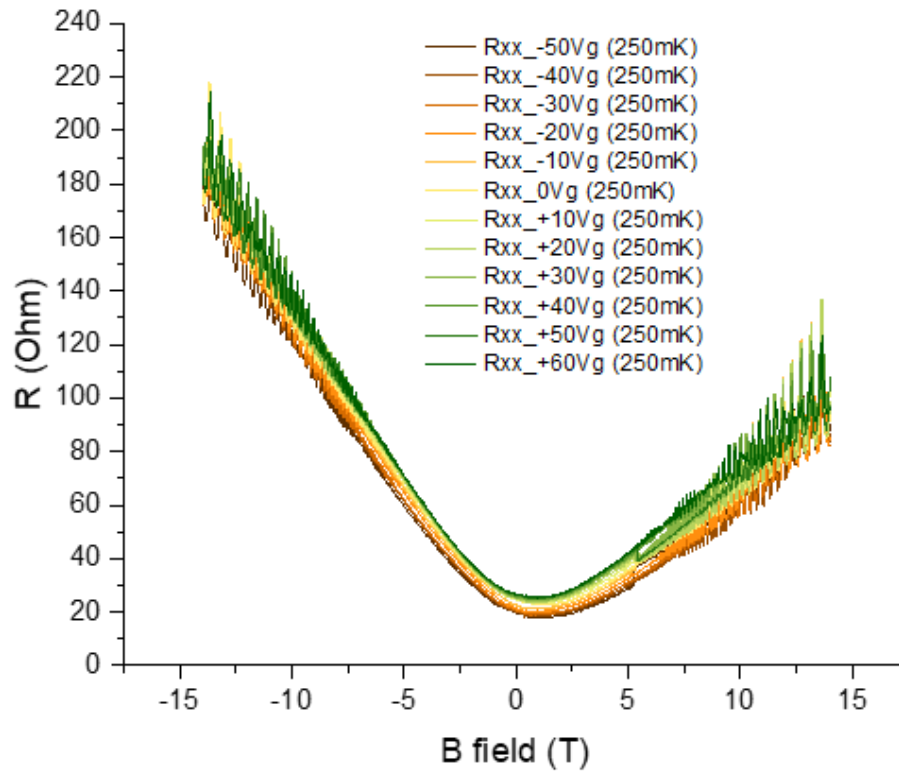Figure 7:3 Magnetoresistance data of a heterostructure with a 4nm thick $\alpha-RuCl_3$ sheet

Figure 7:4 K3189

Figure 7:5 Strain – doping plot for the sample K3189.

Figure 7:6 K3184

Figure 7:7 Strain – doping plot for the sample K3184.

Figure 7:8 K2471

Figure 7:9 Strain – doping plot for the sample K2471.

a)

b)

c)

Figure 7:10 K3176

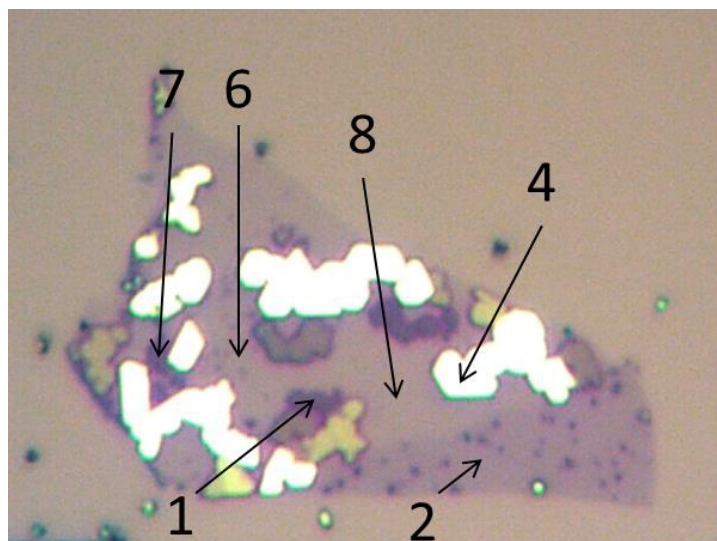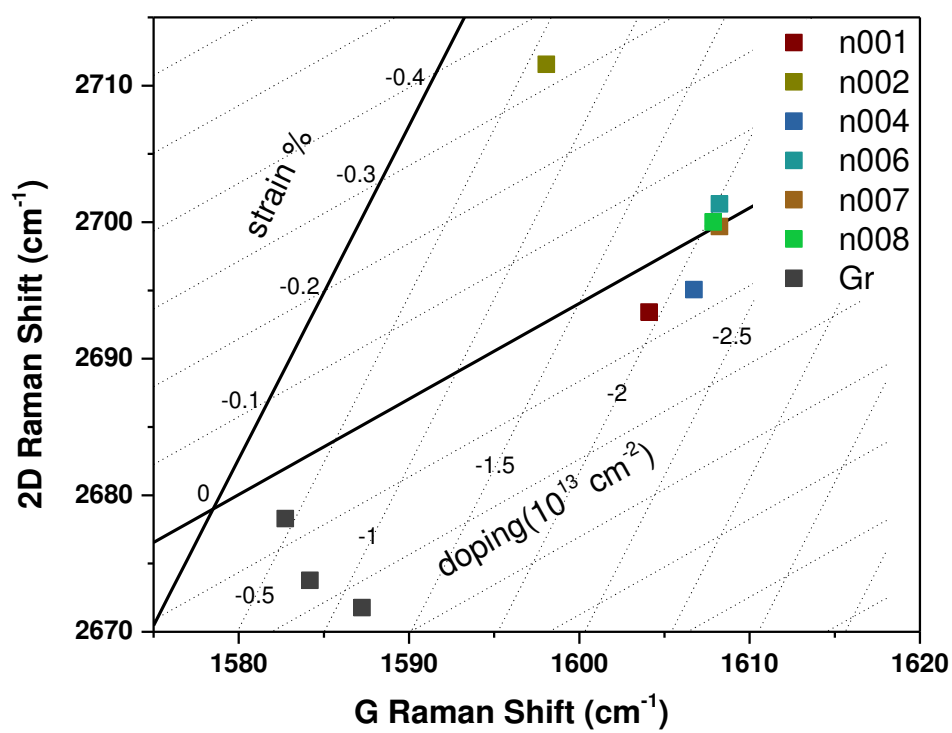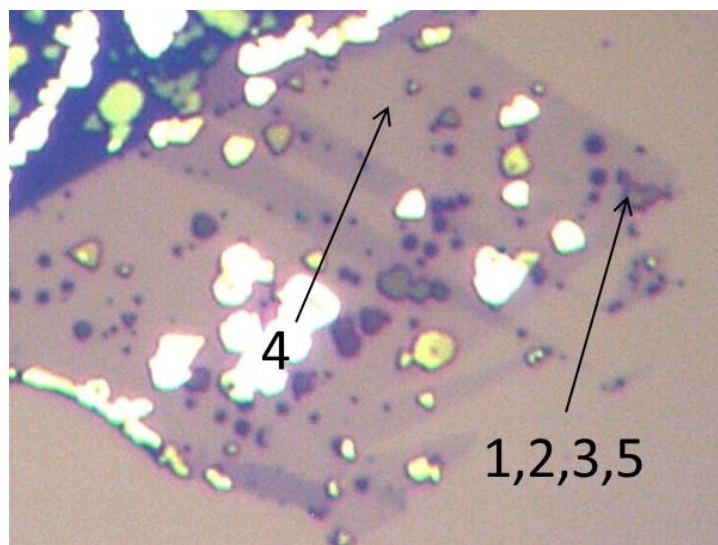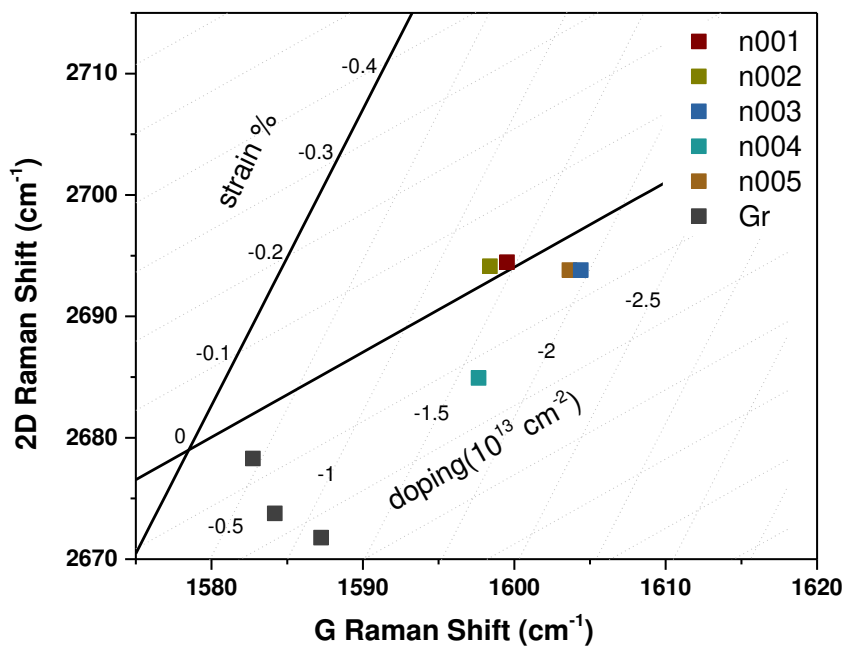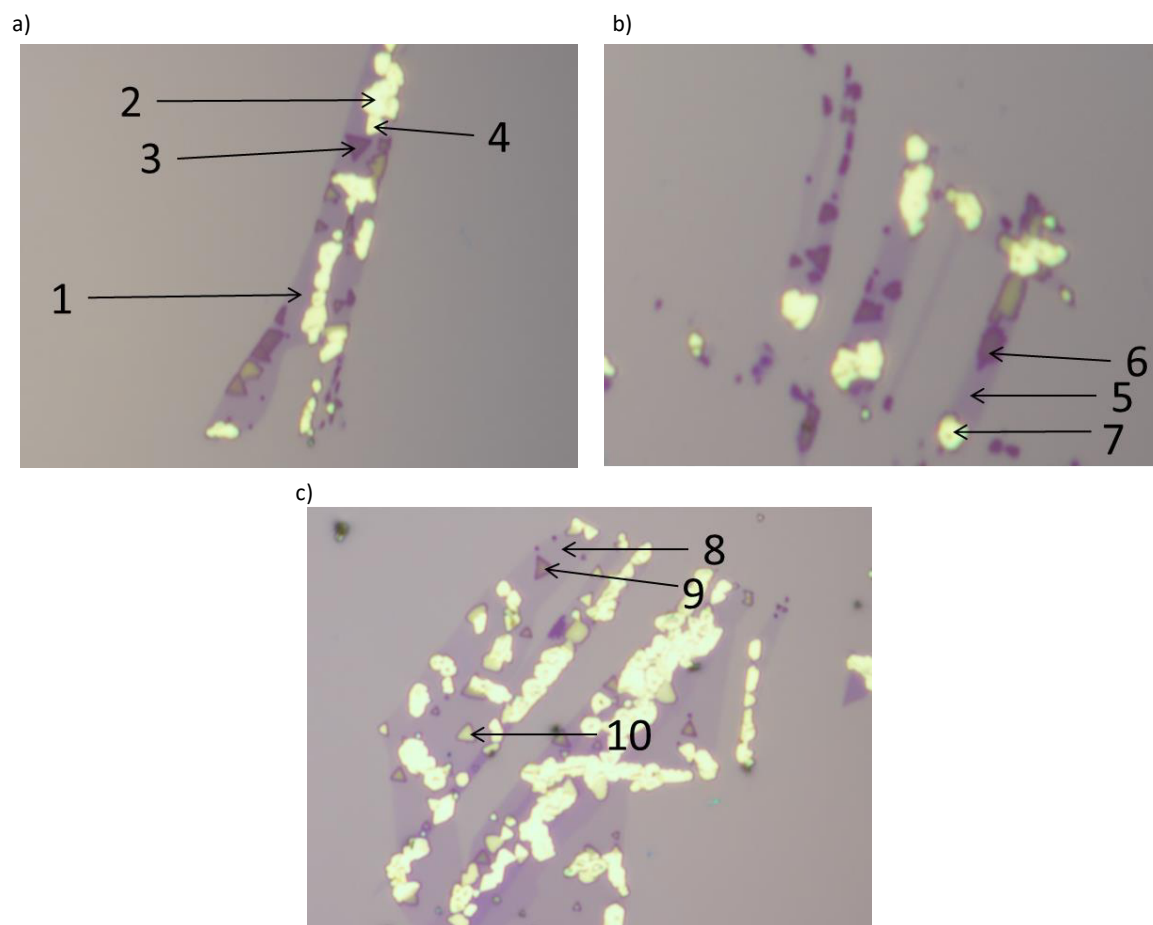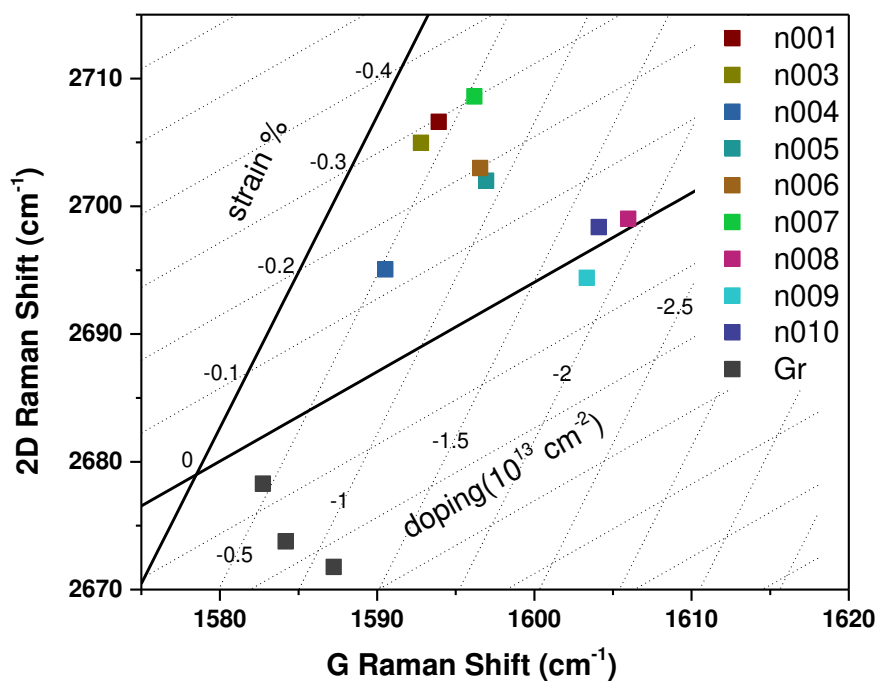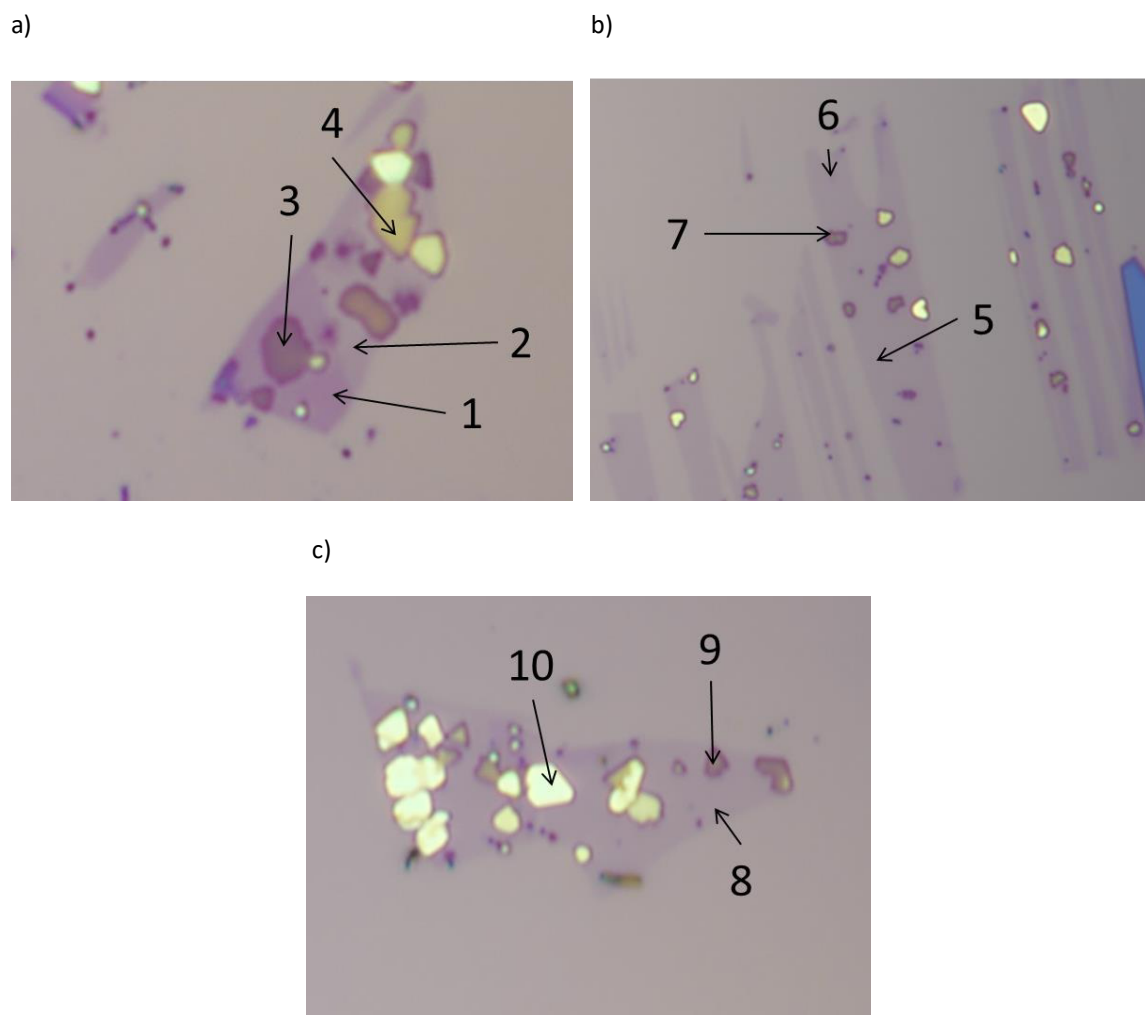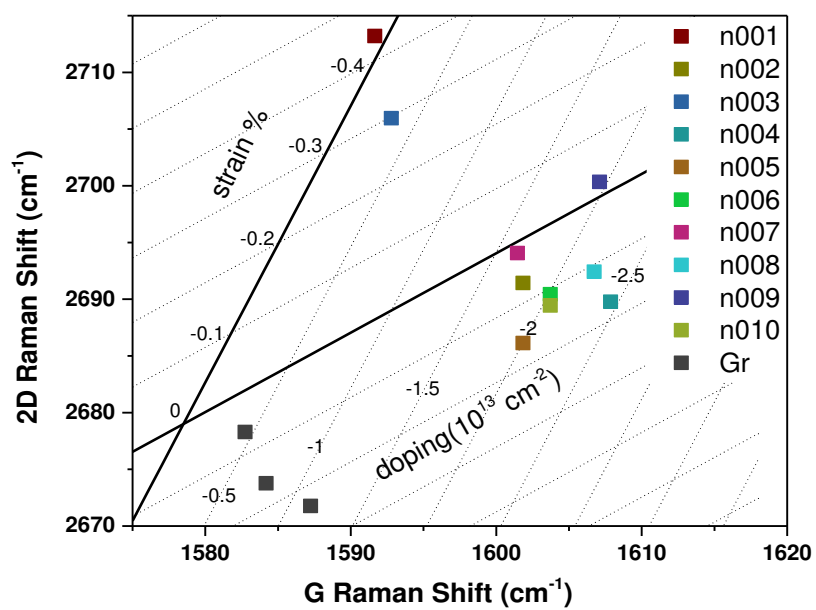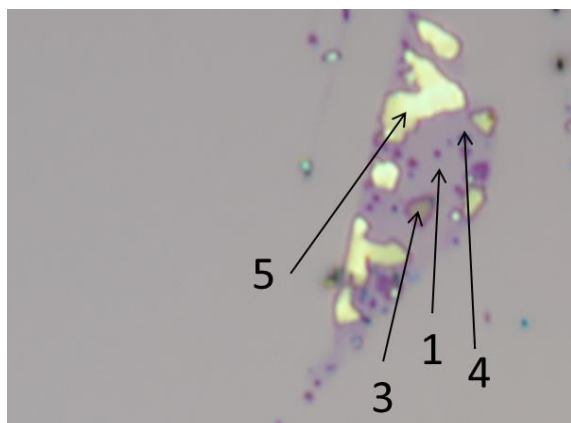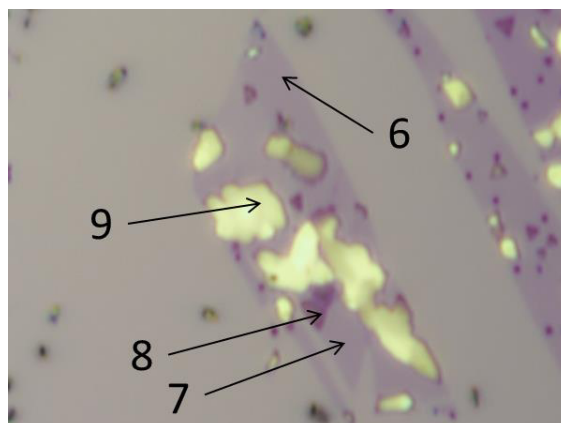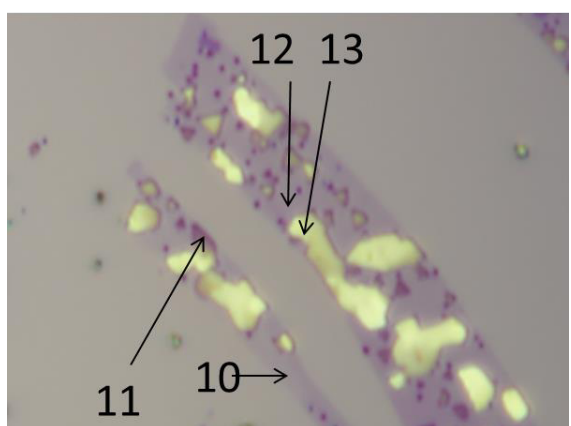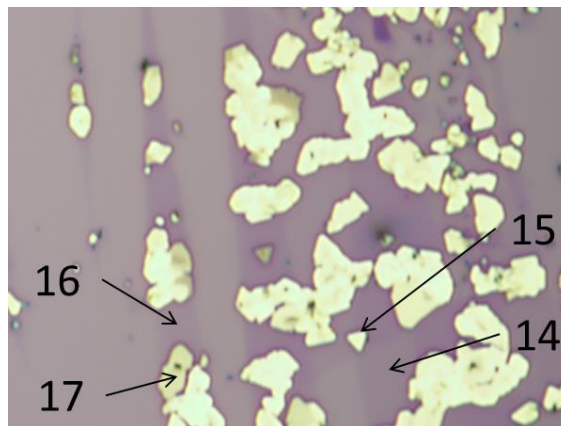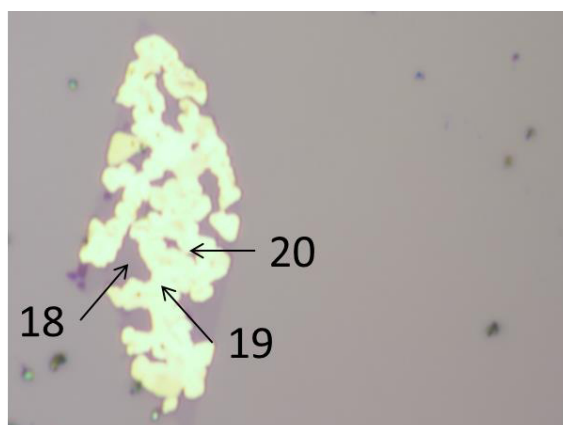Figure 7:11 Strain – doping plot for the sample K3176.
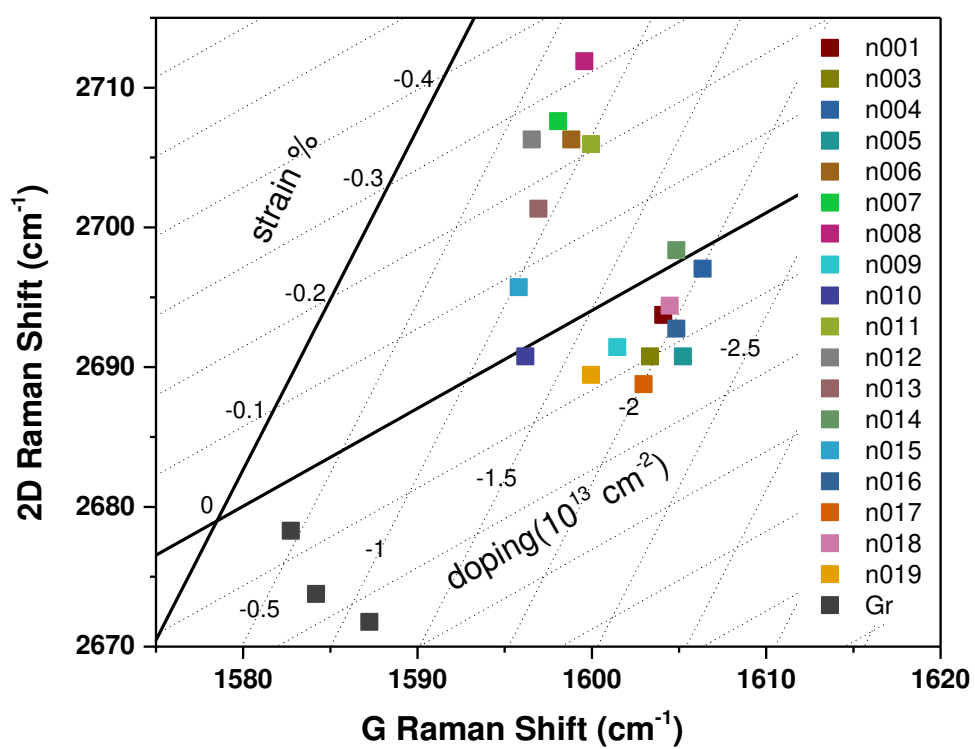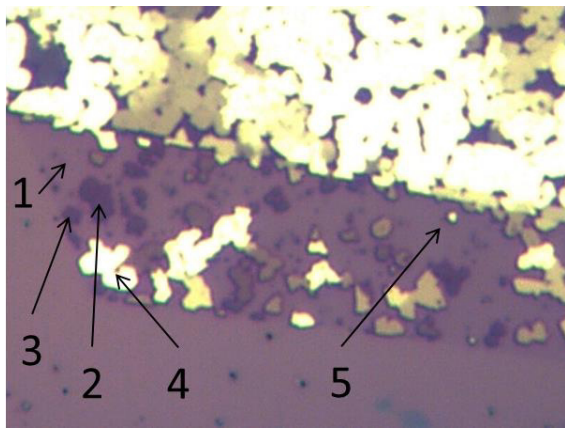
a)

b)

c)

d)

e)

Figure 7:12 K3190

Figure 7:13 Strain – doping plot for the sample K3190.
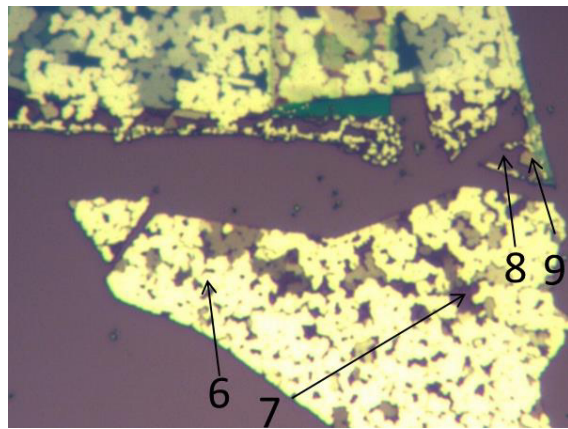
Figure 7:14 K3197

Bibliography

[1]   S. Das, J. A. Robinson, M. Dubey, H. Terrones, and M. Terrones, "Beyond Graphene: Progress in Novel Two-Dimensional Materials and van der Waals Solids," *Annu. Rev. Mater. Res.*, 2015, doi: 10.1146/annurev-matsci-070214-021034.

[2]   K. Khan *et al.*, "Recent developments in emerging two-dimensional materials and their applications," *J. Mater. Chem. C*, 2020, doi: 10.1039/c9tc04187g.

[3]   P. Ajayan, P. Kim, and K. Banerjee, "Two-dimensional van der Waals materials," *Phys. Today*, 2016, doi: 10.1063/PT.3.3297.

[4]   H. C. Kamban and T. G. Pedersen, "Interlayer excitons in van der Waals heterostructures: Binding energy, Stark shift, and field-induced dissociation," *Sci. Rep.*, 2020, doi: 10.1038/s41598-020-62431-y.

[5]   Y. Oreg, G. Refael, and F. Von Oppen, "Helical liquids and Majorana bound states in quantum wires," *Phys. Rev. Lett.*, 2010, doi: 10.1103/PhysRevLett.105.177002.

[6]   D. R. Hofstadter, "Energy levels and wave functions of Bloch electrons in rational and irrational magnetic fields," *Phys. Rev. B*, 1976, doi: 10.1103/PhysRevB.14.2239.

[7]   C. R. Dean *et al.*, "Hofstadter's butterfly and the fractal quantum Hall effect in moiré superlattices," *Nature*, 2013, doi: 10.1038/nature12186.

[8]   A. K. Geim and I. V. Grigorieva, "Van der Waals heterostructures," *Nature*. 2013, doi: 10.1038/nature12385.

[9]   C. R. Dean *et al.*, "Boron nitride substrates for high-quality graphene electronics," *Nat. Nanotechnol.*, 2010, doi: 10.1038/nnano.2010.172.

[10]   R. Frisenda *et al.*, "Recent progress in the assembly of nanodevices and van der Waals heterostructures by deterministic placement of 2D materials," *Chemical Society Reviews*. 2018, doi: 10.1039/c7cs00556c.

[11]   J. A. Robinson, "Growing vertical in the flatland," *ACS Nano*. 2016, doi: 10.1021/acsnano.5b08117.

[12]   A. Koma, "Summary Abstract: Fabrication of ultrathin heterostructures with van der Waals epitaxy," *J. Vac. Sci. Technol. B Microelectron. Nanom. Struct.*, 1985, doi: 10.1116/1.583125.

[13]   Y. C. Lin *et al.*, "Atomically thin heterostructures based on single-layer tungsten diselenide and graphene," *Nano Lett.*, 2014, doi: 10.1021/nl503144a.

[14]   K. S. Novoselov, A. Mishchenko, A. Carvalho, and A. H. Castro Neto, "2D materials and van der Waals heterostructures," *Science*. 2016, doi: 10.1126/science.aac9439.

[15]   A. Allain, J. Kang, K. Banerjee, and A. Kis, "Electrical contacts to two-dimensional semiconductors," *Nature Materials*. 2015, doi: 10.1038/nmat4452.

[16]   L. Britnell *et al.*, "Field-effect tunneling transistor based on vertical graphene heterostructures," *Science (80-.).*, 2012, doi: 10.1126/science.1218461.

[17] T. Georgiou *et al.*, "Vertical field-effect transistor based on graphene-WS 2 heterostructures for flexible and transparent electronics," *Nat. Nanotechnol.*, 2013, doi: 10.1038/nnano.2012.224.

[18] C. H. Lee *et al.*, "Atomically thin p-n junctions with van der Waals heterointerfaces," *Nat. Nanotechnol.*, 2014, doi: 10.1038/nnano.2014.150.

[19] D. Sarkar *et al.*, "A subthermionic tunnel field-effect transistor with an atomically thin channel," *Nature*, 2015, doi: 10.1038/nature15387.

[20] M. Buscema *et al.*, "Photocurrent generation with two-dimensional van der Waals semiconductors," *Chemical Society Reviews*. 2015, doi: 10.1039/c5cs00106d.

[21] L. Britnell *et al.*, "Strong light-matter interactions in heterostructures of atomically thin films," *Science (80-.).*, 2013, doi: 10.1126/science.1235547.

[22] C. Gong and X. Zhang, "Two-dimensional magnetic crystals and emergent heterostructure devices," *Science*. 2019, doi: 10.1126/science.aav4450.

[23] T. Song *et al.*, "Giant tunneling magnetoresistance in spin-filter van der Waals heterostructures," *Science (80-.).*, 2018, doi: 10.1126/science.aar4851.

[24] P. Huang, P. Zhang, S. Xu, H. Wang, X. Zhang, and H. Zhang, "Recent advances in two-dimensional ferromagnetism: Materials synthesis, physical properties and device applications," *Nanoscale*. 2020, doi: 10.1039/c9nr08890c.

[25] W. Han, R. K. Kawakami, M. Gmitra, and J. Fabian, "Graphene spintronics," *Nature Nanotechnology*. 2014, doi: 10.1038/nnano.2014.214.

[26] M. Drögeler *et al.*, "Spin Lifetimes Exceeding 12 ns in Graphene Nonlocal Spin Valve Devices," *Nano Lett.*, 2016, doi: 10.1021/acs.nanolett.6b00497.

[27] J. Ingla-Aynés, M. H. D. Guimarães, R. J. Meijerink, P. J. Zomer, and B. J. Van Wees, "24-μm spin relaxation length in boron nitride encapsulated bilayer graphene," *Phys. Rev. B - Condens. Matter Mater. Phys.*, 2015, doi: 10.1103/PhysRevB.92.201410.

[28] M. V. Kamalakar, C. Groenveld, A. Dankert, and S. P. Dash, "Long distance spin communication in chemical vapour deposited graphene," *Nat. Commun.*, 2015, doi: 10.1038/ncomms7766.

[29] Z. M. Gebeyehu *et al.*, "Spin communication over 30 μm long channels of chemical vapor deposited graphene on SiO2," *2D Mater.*, 2019, doi: 10.1088/2053-1583/ab1874.

[30] H. H. Kim *et al.*, "One Million Percent Tunnel Magnetoresistance in a Magnetic van der Waals Heterostructure," *Nano Lett.*, 2018, doi: 10.1021/acs.nanolett.8b01552.

[31] M. Alghamdi *et al.*, "Highly Efficient Spin-Orbit Torque and Switching of Layered Ferromagnet Fe3GeTe2," *Nano Lett.*, 2019, doi: 10.1021/acs.nanolett.9b01043.

[32] S. Jiang, L. Li, Z. Wang, J. Shan, and K. F. Mak, "Spin tunnel field-effect transistors based on two-dimensional van der Waals heterostructures," *Nat. Electron.*, 2019, doi: 10.1038/s41928-019-0232-3.

[33] H. Wen *et al.*, "Experimental Demonstration of xor Operation in Graphene Magnetologic Gates at Room Temperature," *Phys. Rev. Appl.*, 2016, doi:

10.1103/PhysRevApplied.5.044003.

[34]   B. Behin-Aein, D. Datta, S. Salahuddin, and S. Datta, "Proposal for an all-spin logic device with built-in memory," *Nat. Nanotechnol.*, 2010, doi: 10.1038/nnano.2010.31.

[35]   S. Zihlmann *et al.*, "Large spin relaxation anisotropy and valley-Zeeman spin-orbit coupling in WSe2 /graphene/ h -BN heterostructures," *Phys. Rev. B*, 2018, doi: 10.1103/PhysRevB.97.075434.

[36]   T. Wakamura, F. Reale, P. Palczynski, S. Guéron, C. Mattevi, and H. Bouchiat, "Strong Anisotropic Spin-Orbit Interaction Induced in Graphene by Monolayer WS2," *Phys. Rev. Lett.*, 2018, doi: 10.1103/PhysRevLett.120.106802.

[37]   Z. Wang *et al.*, "Origin and magnitude of 'designer' spin-orbit interaction in graphene on semiconducting transition metal dichalcogenides," *Phys. Rev. X*, 2016, doi: 10.1103/PhysRevX.6.041020.

[38]   D. Khokhriakov *et al.*, "Tailoring emergent spin phenomena in Dirac material heterostructures," *Sci. Adv.*, 2018, doi: 10.1126/sciadv.aat9349.

[39]   K. Song, D. Soriano, A. W. Cummings, R. Robles, P. Ordejón, and S. Roche, "Spin Proximity Effects in Graphene/Topological Insulator Heterostructures," *Nano Lett.*, vol. 18, no. 3, pp. 2033–2039, 2018, doi: 10.1021/acs.nanolett.7b05482.

[40]   A. W. Cummings, J. H. Garcia, J. Fabian, and S. Roche, "Giant Spin Lifetime Anisotropy in Graphene Induced by Proximity Effects," *Phys. Rev. Lett.*, vol. 119, no. 20, pp. 1–7, 2017, doi: 10.1103/PhysRevLett.119.206601.

[41]   S. Jafarpisheh, A. W. Cummings, K. Watanabe, T. Taniguchi, B. Beschoten, and C. Stampfer, "Proximity-induced spin-orbit coupling in graphene/ Bi1.5Sb0.5Te1.7Se1.3 heterostructures," *Phys. Rev. B*, vol. 98, no. 24, pp. 1–6, 2018, doi: 10.1103/PhysRevB.98.241402.

[42]   P. Wei *et al.*, "Strong interfacial exchange field in the graphene/EuS heterostructure," *Nat. Mater.*, 2016, doi: 10.1038/nmat4603.

[43]   Z. Wang, C. Tang, R. Sachs, Y. Barlas, and J. Shi, "Proximity-induced ferromagnetism in graphene revealed by the anomalous hall effect," *Phys. Rev. Lett.*, 2015, doi: 10.1103/PhysRevLett.114.016603.

[44]   J. B. S. Mendes *et al.*, "Direct detection of induced magnetic moment and efficient spin-to-charge conversion in graphene/ferromagnetic structures," *Phys. Rev. B*, 2019, doi: 10.1103/PhysRevB.99.214446.

[45]   A. Banerjee *et al.*, "Excitations in the field-induced quantum spin liquid state of α-RuCl3," *npj Quantum Mater.*, 2018, doi: 10.1038/s41535-018-0079-2.

[46]   P. R. Wallace, "The band theory of graphite," *Phys. Rev.*, 1947, doi: 10.1103/PhysRev.71.622.

[47]   A. H. Castro Neto, F. Guinea, N. M. R. Peres, K. S. Novoselov, and A. K. Geim, "The electronic properties of graphene," *Rev. Mod. Phys.*, 2009, doi: 10.1103/RevModPhys.81.109.

[48]   G. L. Yu *et al.*, "Interaction phenomena in graphene seen through quantum capacitance,"

Proc. Natl. Acad. Sci. U. S. A., 2013, doi: 10.1073/pnas.1300599110.

[49]   M. Orlita and M. Potemski, "Dirac electronic states in graphene systems: Optical spectroscopy studies," *Semiconductor Science and Technology*. 2010, doi: 10.1088/0268-1242/25/6/063001.

[50]   Y. Ren, Z. Qiao, and Q. Niu, "Topological phases in two-dimensional materials: A review," *Reports on Progress in Physics*. 2016, doi: 10.1088/0034-4885/79/6/066501.

[51]   M. Sprinkle *et al.*, "First direct observation of a nearly ideal graphene band structure," *Phys. Rev. Lett.*, 2009, doi: 10.1103/PhysRevLett.103.226803.

[52]   G. M. Rutter, J. N. Crain, N. P. Guisinger, T. Li, P. N. First, and J. A. Stroscio, "Scattering and interference in epitaxial graphene," *Science (80-.).*, 2007, doi: 10.1126/science.1142882.

[53]   J. L. Mañes, F. Guinea, and M. A. H. Vozmediano, "Existence and topological stability of Fermi points in multilayered graphene," *Phys. Rev. B - Condens. Matter Mater. Phys.*, 2007, doi: 10.1103/PhysRevB.75.155424.

[54]   S. Reich, J. Maultzsch, C. Thomsen, and P. Ordejón, "Tight-binding description of graphene," *Phys. Rev. B - Condens. Matter Mater. Phys.*, 2002, doi: 10.1103/PhysRevB.66.035412.

[55]   J. L. McChesney *et al.*, "Extended van hove singularity and superconducting instability in doped graphene," *Phys. Rev. Lett.*, 2010, doi: 10.1103/PhysRevLett.104.136803.

[56]   S. Y. Zhou, D. A. Siegel, A. V. Fedorov, and A. Lanzara, "Metal to insulator transition in epitaxial graphene induced by molecular doping," *Phys. Rev. Lett.*, 2008, doi: 10.1103/PhysRevLett.101.086402.

[57]   J. Liang *et al.*, "Intrinsically stretchable and transparent thin-film transistors based on printable silver nanowires, carbon nanotubes and an elastomeric dielectric," *Nat. Commun.*, 2015, doi: 10.1038/ncomms8647.

[58]   Y. Zhang, V. W. Brar, C. Girit, A. Zettl, and M. F. Crommie, "Origin of spatial charge inhomogeneity in graphene," *Nat. Phys.*, 2009, doi: 10.1038/nphys1365.

[59]   I. Brihuega *et al.*, "Quasiparticle chirality in epitaxial graphene probed at the nanometer scale," *Phys. Rev. Lett.*, 2008, doi: 10.1103/PhysRevLett.101.206802.

[60]   K. S. Novoselov *et al.*, "Two-dimensional gas of massless Dirac fermions in graphene," *Nature*, 2005, doi: 10.1038/nature04233.

[61]   A. F. Young and P. Kim, "Quantum interference and Klein tunnelling in graphene heterojunctions," *Nat. Phys.*, 2009, doi: 10.1038/nphys1198.

[62]   C. W. J. Beenakker and H. van Houten, "Quantum Transport in Semiconductor Nanostructures," *Solid State Phys. - Adv. Res. Appl.*, 1991, doi: 10.1016/S0081-1947(08)60091-0.

[63]   J. Güttinger *et al.*, "Transport through graphene quantum dots," *Reports Prog. Phys.*, 2012, doi: 10.1088/0034-4885/75/12/126502.

[64]   Z. Jiang, Y. Zhang, Y. W. Tan, H. L. Stormer, and P. Kim, "Quantum Hall effect in graphene," *Solid State Commun.*, vol. 143, no. 1–2, pp. 14–19, 2007, doi: 10.1016/j.ssc.2007.02.046.

[65] A. K. Geim and K. S. Novoselov, "The rise of graphene," *Nat. Mater.*, 2007, doi: 10.1038/nmat1849.

[66] M. Ishigami, J. H. Chen, W. G. Cullen, M. S. Fuhrer, and E. D. Williams, "Atomic structure of graphene on SiO 2," *Nano Lett.*, 2007, doi: 10.1021/nl070613a.

[67] J. Moser, A. Barreiro, and A. Bachtold, "Current-induced cleaning of graphene," *Appl. Phys. Lett.*, 2007, doi: 10.1063/1.2789673.

[68] J. H. Chen, C. Jang, S. Adam, M. S. Fuhrer, E. D. Williams, and M. Ishigami, "Charged-impurity scattering in graphene," *Nat. Phys.*, 2008, doi: 10.1038/nphys935.

[69] K. I. Bolotin *et al.*, "Ultrahigh electron mobility in suspended graphene," *Solid State Commun.*, 2008, doi: 10.1016/j.ssc.2008.02.024.

[70] K. S. Novoselov *et al.*, "Room-temperature quantum hall effect in graphene," *Science (80-.).*, 2007, doi: 10.1126/science.1137201.

[71] B. Trauzettel, D. V. Bulaev, D. Loss, and G. Burkard, "Spin qubits in graphene quantum dots," *Nat. Phys.*, 2007, doi: 10.1038/nphys544.

[72] C. Józsa *et al.*, "Linear scaling between momentum and spin scattering in graphene," *Phys. Rev. B - Condens. Matter Mater. Phys.*, 2009, doi: 10.1103/PhysRevB.80.241403.

[73] J. Tworzydło, B. Trauzettel, M. Titov, A. Rycerz, and C. W. J. Beenakker, "Sub-poissonian shot noise in graphene," *Phys. Rev. Lett.*, 2006, doi: 10.1103/PhysRevLett.96.246802.

[74] X. Du, I. Skachko, A. Barker, and E. Y. Andrei, "Approaching ballistic transport in suspended graphene," *Nat. Nanotechnol.*, 2008, doi: 10.1038/nnano.2008.199.

[75] T. Ihn, *Semiconductor Nanostructures: Quantum States and Electronic Transport*. 2010.

[76] Y. F. Chen, M. H. Bae, C. Chialvo, T. Dirks, A. Bezryadin, and N. Mason, "Magnetoresistance in single-layer graphene: Weak localization and universal conductance fluctuation studies," *J. Phys. Condens. Matter*, 2010, doi: 10.1088/0953-8984/22/20/205301.

[77] N. M. R. Peres, "Colloquium: The transport properties of graphene: An introduction," *Rev. Mod. Phys.*, 2010, doi: 10.1103/RevModPhys.82.2673.

[78] F. V. Tikhonenko, A. A. Kozikov, A. K. Savchenko, and R. V. Gorbachev, "Transition between electron localization and antilocalization in graphene," *Phys. Rev. Lett.*, 2009, doi: 10.1103/PhysRevLett.103.226801.

[79] E. Mccann, K. Kechedzhi, V. I. Fala'Ko, H. Suzuura, T. Ando, and B. L. Altshuler, "Weak-localization magnetoresistance and valley symmetry in graphene," *Phys. Rev. Lett.*, 2006, doi: 10.1103/PhysRevLett.97.146805.

[80] S. Jia *et al.*, "Low-carrier-concentration crystals of the topological insulator Bi 2Te 2Se," *Phys. Rev. B - Condens. Matter Mater. Phys.*, 2011, doi: 10.1103/PhysRevB.84.235206.

[81] R. J. Cava, H. Ji, M. K. Fuccillo, Q. D. Gibson, and Y. S. Hor, "Crystal structure and chemistry of topological insulators," *J. Mater. Chem. C*, 2013, doi: 10.1039/c3tc30186a.

[82] Y. Liu *et al.*, "Epitaxial Growth of Ternary Topological Insulator Bi2Te2Se 2D Crystals on Mica," *Small*, 2017, doi: 10.1002/smll.201603572.

[83] M. Z. Hasan and J. E. Moore, "Three-Dimensional Topological Insulators," *Annu. Rev. Condens. Matter Phys.*, 2011, doi: 10.1146/annurev-conmatphys-062910-140432.

[84] Y. A. Bychkov and E. I. Rashba, "Properties of a 2D electron gas with lifted spectral degeneracy," *JETP Letters*. 1984, doi: 10.1088/0022-3719/17/33/015.

[85] J. J. Sakurai and D. Z. Freedman, "Advanced Quantum Mechanics," *Am. J. Phys.*, 1968, doi: 10.1119/1.1974573.

[86] F. Schwabl, *Quantum mechanics (Fourth Edition)*. 2007.

[87] K. V. Klitzing, G. Dorda, and M. Pepper, "New method for high-accuracy determination of the fine-structure constant based on quantized hall resistance," *Phys. Rev. Lett.*, 1980, doi: 10.1103/PhysRevLett.45.494.

[88] X. L. Qi and S. C. Zhang, "The quantum spin Hall effect and topological insulators," *Phys. Today*, 2010, doi: 10.1063/1.3293411.

[89] C. L. Kane and E. J. Mele, "Quantum Spin hall effect in graphene," *Phys. Rev. Lett.*, 2005, doi: 10.1103/PhysRevLett.95.226801.

[90] C. Wu, B. A. Bernevig, and S. C. Zhang, "Helical liquid and the edge of quantum spin hall systems," *Phys. Rev. Lett.*, 2006, doi: 10.1103/PhysRevLett.96.106401.

[91] L. Fu, C. L. Kane, and E. J. Mele, "Topological insulators in three dimensions," *Phys. Rev. Lett.*, 2007, doi: 10.1103/PhysRevLett.98.106803.

[92] M. Z. Hasan and C. L. Kane, "Colloquium: Topological insulators," *Rev. Mod. Phys.*, 2010, doi: 10.1103/RevModPhys.82.3045.

[93] H. Zhang, C. X. Liu, X. L. Qi, X. Dai, Z. Fang, and S. C. Zhang, "Topological insulators in Bi 2 Se 3, Bi 2 Te 3 and Sb 2 Te 3 with a single Dirac cone on the surface," *Nat. Phys.*, 2009, doi: 10.1038/nphys1270.

[94] M. Neupane *et al.*, "Topological surface states and Dirac point tuning in ternary topological insulators," *Phys. Rev. B - Condens. Matter Mater. Phys.*, 2012, doi: 10.1103/PhysRevB.85.235406.

[95] Y. Xia *et al.*, "Observation of a large-gap topological-insulator class with a single Dirac cone on the surface," *Nat. Phys.*, 2009, doi: 10.1038/nphys1274.

[96] M. Neupane *et al.*, "Gigantic Surface Lifetime of an Intrinsic Topological Insulator," *Phys. Rev. Lett.*, 2015, doi: 10.1103/PhysRevLett.115.116801.

[97] J. Tian, I. Miotkowski, S. Hong, and Y. P. Chen, "Electrical injection and detection of spin-polarized currents in topological insulator Bi2Te2Se," *Sci. Rep.*, 2015, doi: 10.1038/srep14293.

[98] H. B. Cao *et al.*, "Low-temperature crystal and magnetic structure of α-RuCl3," *Phys. Rev. B*, vol. 93, no. 13, pp. 1–8, 2016, doi: 10.1103/PhysRevB.93.134423.

[99] D. Pesin and L. Balents, "Mott physics and band topology in materials with strong spin-orbit interaction," *Nat. Phys.*, vol. 6, no. 5, pp. 376–381, 2010, doi: 10.1038/nphys1606.

[100] A. Banerjee *et al.*, "Neutron scattering in the proximate quantum spin liquid α-RuCl3,"

Science (80-.)., vol. 356, no. 6342, pp. 1055–1059, 2017, doi: 10.1126/science.aah6015.

[101] L. Balents, "Spin liquids in frustrated magnets," *Nature*. 2010, doi: 10.1038/nature08917.

[102] G. Jackeli and G. Khaliullin, "Mott insulators in the strong spin-orbit coupling Limit: From Heisenberg to a Quantum Compass and Kitaev Models," *Phys. Rev. Lett.*, vol. 102, no. 1, pp. 2–5, 2009, doi: 10.1103/PhysRevLett.102.017205.

[103] A. Kitaev, "Anyons in an exactly solved model and beyond," *Ann. Phys. (N. Y).*, vol. 321, no. 1, pp. 2–111, 2006, doi: 10.1016/j.aop.2005.10.005.

[104] L. J. Sandilands, Y. Tian, K. W. Plumb, Y. J. Kim, and K. S. Burch, "Scattering Continuum and Possible Fractionalized Excitations in α-RuCl3," *Phys. Rev. Lett.*, vol. 114, no. 14, pp. 1–5, 2015, doi: 10.1103/PhysRevLett.114.147201.

[105] W. Rantner and X. G. Wen, "Electron spectral function and algebraic spin liquid for the normal state of underdoped high Tc superconductors," *Phys. Rev. Lett.*, 2001, doi: 10.1103/PhysRevLett.86.3871.

[106] K. O'Brien, M. Hermanns, and S. Trebst, "Classification of gapless Z2 spin liquids in three-dimensional Kitaev models," *Phys. Rev. B*, 2016, doi: 10.1103/PhysRevB.93.085101.

[107] S. H. Do *et al.*, "Majorana fermions in the Kitaev quantum spin system α-RuCl 3," *Nat. Phys.*, 2017, doi: 10.1038/nphys4264.

[108] C. Broholm, R. J. Cava, S. A. Kivelson, D. G. Nocera, M. R. Norman, and T. Senthil, "Quantum spin liquids," *Science (80-.).*, vol. 367, no. 6475, 2020, doi: 10.1126/science.aay0668.

[109] N. Perkins, "Quantum magnetism: Kitaev physics crystalized," *Nature Physics*. 2017, doi: 10.1038/nphys4298.

[110] I. Rousochatzakis, J. Reuther, R. Thomale, S. Rachel, and N. B. Perkins, "Phase diagram and quantum order by disorder in the kitaev K1 - K2 honeycomb magnet," *Phys. Rev. X*, 2015, doi: 10.1103/PhysRevX.5.041035.

[111] J. Yoshitake, J. Nasu, and Y. Motome, "Fractional Spin Fluctuations as a Precursor of Quantum Spin Liquids: Majorana Dynamical Mean-Field Study for the Kitaev Model," *Phys. Rev. Lett.*, 2016, doi: 10.1103/PhysRevLett.117.157203.

[112] Y. Tian, W. Gao, E. A. Henriksen, J. R. Chelikowsky, and L. Yang, "Optically Driven Magnetic Phase Transition of Monolayer RuCl3," *Nano Lett.*, vol. 19, no. 11, pp. 7673–7680, 2019, doi: 10.1021/acs.nanolett.9b02523.

[113] L. Binotto, I. Pollini, and G. Spinolo, "Optical and transport properties of the magnetic semiconductor α-RuCl3," *Phys. Status Solidi*, vol. 44, no. 1, pp. 245–252, 1971, doi: 10.1002/pssb.2220440126.

[114] M. Ziatdinov *et al.*, "Atomic-scale observation of structural and electronic orders in the layered compound α-RuCl3," *Nat. Commun.*, 2016, doi: 10.1038/ncomms13774.

[115] X. Zhou *et al.*, "Angle-resolved photoemission study of the Kitaev candidate α-RuCl3," *Phys. Rev. B*, 2016, doi: 10.1103/PhysRevB.94.161106.

[116] A. Koitzsch *et al.*, "Jeff Description of the Honeycomb Mott Insulator α-RuCl3," *Phys. Rev. Lett.*, 2016, doi: 10.1103/PhysRevLett.117.126403.

[117] A. Banerjee *et al.*, "Proximate Kitaev quantum spin liquid behaviour in a honeycomb magnet," *Nat. Mater.*, 2016, doi: 10.1038/nmat4604.

[118] S. Mashhadi *et al.*, "Electrical Transport Signature of the Magnetic Fluctuation-Structure Relation in α-RuCl3 Nanoflakes," *Nano Lett.*, vol. 18, no. 5, pp. 3203–3208, 2018, doi: 10.1021/acs.nanolett.8b00926.

[119] L. Du *et al.*, "2D proximate quantum spin liquid state in atomic-thin α-RuCl3," *2D Mater.*, 2019, doi: 10.1088/2053-1583/aaee29.

[120] K. Park, J. J. Heremans, V. W. Scarola, and D. Minic, "Robustness of topologically protected surface states in layering of Bi 2Te3 thin films," *Phys. Rev. Lett.*, 2010, doi: 10.1103/PhysRevLett.105.186801.

[121] M. Gmitra and J. Fabian, "Graphene on transition-metal dichalcogenides: A platform for proximity spin-orbit physics and optospintronics," *Phys. Rev. B - Condens. Matter Mater. Phys.*, 2015, doi: 10.1103/PhysRevB.92.155403.

[122] R. Bistritzer and A. H. MacDonald, "Moiré bands in twisted double-layer graphene," *Proc. Natl. Acad. Sci. U. S. A.*, 2011, doi: 10.1073/pnas.1108174108.

[123] T. Frank, S. Irmer, M. Gmitra, D. Kochan, and J. Fabian, "Copper adatoms on graphene: Theory of orbital and spin-orbital effects," *Phys. Rev. B*, 2017, doi: 10.1103/PhysRevB.95.035402.

[124] G. Giovannetti, P. A. Khomyakov, G. Brocks, P. J. Kelly, and J. Van Den Brink, "Substrate-induced band gap in graphene on hexagonal boron nitride: Ab initio density functional calculations," *Phys. Rev. B - Condens. Matter Mater. Phys.*, 2007, doi: 10.1103/PhysRevB.76.073103.

[125] J. Zhang, C. Triola, and E. Rossi, "Proximity effect in graphene-topological-insulator heterostructures," *Phys. Rev. Lett.*, 2014, doi: 10.1103/PhysRevLett.112.096802.

[126] K. Zollner, M. Gmitra, and J. Fabian, "Heterostructures of graphene and hBN: Electronic, spin-orbit, and spin relaxation properties from first principles," *Phys. Rev. B*, 2019, doi: 10.1103/PhysRevB.99.125151.

[127] G. Giovannetti, M. Capone, J. Van Den Brink, and C. Ortix, "Kekulé textures, pseudospin-one Dirac cones, and quadratic band crossings in a graphene-hexagonal indium chalcogenide bilayer," *Phys. Rev. B - Condens. Matter Mater. Phys.*, 2015, doi: 10.1103/PhysRevB.91.121417.

[128] B. Yang *et al.*, "Strong electron-hole symmetric Rashba spin-orbit coupling in graphene/monolayer transition metal dichalcogenide heterostructures," *Phys. Rev. B*, 2017, doi: 10.1103/PhysRevB.96.041409.

[129] J. H. Garcia, A. W. Cummings, and S. Roche, "Spin hall effect and weak antilocalization in graphene/transition metal dichalcogenide heterostructures," *Nano Lett.*, 2017, doi: 10.1021/acs.nanolett.7b02364.

[130] J. H. Garcia, M. Vila, A. W. Cummings, and S. Roche, "Spin transport in graphene/transition metal dichalcogenide heterostructures," *Chem. Soc. Rev.*, vol. 47, no. 9, pp. 3359–3379, 2018, doi: 10.1039/c7cs00864c.

[131] C. K. Safeer *et al.*, "Room-Temperature Spin Hall Effect in Graphene/MoS2 van der Waals Heterostructures," *Nano Lett.*, 2019, doi: 10.1021/acs.nanolett.8b04368.

[132] L. Li *et al.*, " Gate-Tunable Reversible Rashba–Edelstein Effect in a Few-Layer Graphene/2H-TaS 2 Heterostructure at Room Temperature ," *ACS Nano*, 2020, doi: 10.1021/acsnano.0c01037.

[133] Y. K. Luo *et al.*, "Opto-valleytronic spin injection in monolayer MoS2/few-layer graphene hybrid spin valves," *Nano Lett.*, 2017, doi: 10.1021/acs.nanolett.7b01393.

[134] A. Avsar *et al.*, "Optospintronics in Graphene via Proximity Coupling," *ACS Nano*, 2017, doi: 10.1021/acsnano.7b06800.

[135] W. Yan, O. Txoperena, R. Llopis, H. Dery, L. E. Hueso, and F. Casanova, "A two-dimensional spin field-effect switch," *Nat. Commun.*, 2016, doi: 10.1038/ncomms13372.

[136] A. Dankert and S. P. Dash, "Electrical gate control of spin current in van der Waals heterostructures at room temperature," *Nat. Commun.*, 2017, doi: 10.1038/ncomms16093.

[137] L. A. Benítez *et al.*, "Strongly anisotropic spin relaxation in graphene-transition metal dichalcogenide heterostructures at room temperature," *Nat. Phys.*, 2018, doi: 10.1038/s41567-017-0019-2.

[138] T. S. Ghiasi, J. Ingla-Aynés, A. A. Kaverzin, and B. J. Van Wees, "Large Proximity-Induced Spin Lifetime Anisotropy in Transition-Metal Dichalcogenide/Graphene Heterostructures," *Nano Lett.*, 2017, doi: 10.1021/acs.nanolett.7b03460.

[139] A. W. Cummings, J. H. Garcia, J. Fabian, and S. Roche, "Giant Spin Lifetime Anisotropy in Graphene Induced by Proximity Effects," *Phys. Rev. Lett.*, 2017, doi: 10.1103/PhysRevLett.119.206601.

[140] S. Jafarpisheh, A. W. Cummings, K. Watanabe, T. Taniguchi, B. Beschoten, and C. Stampfer, "Proximity-induced spin-orbit coupling in graphene/ Bi1.5Sb0.5Te1.7Se1.3 heterostructures," *Phys. Rev. B*, 2018, doi: 10.1103/PhysRevB.98.241402.

[141] D. A. Solis, A. Hallal, X. Waintal, and M. Chshiev, "Proximity magnetoresistance in graphene induced by magnetic insulators," *Phys. Rev. B*, 2019, doi: 10.1103/PhysRevB.100.104402.

[142] A. Hallal, F. Ibrahim, H. Yang, S. Roche, and M. Chshiev, "Tailoring magnetic insulator proximity effects in graphene: First-principles calculations," *2D Mater.*, 2017, doi: 10.1088/2053-1583/aa6663.

[143] S. Biswas, Y. Li, S. M. Winter, J. Knolle, and R. Valentí, "Electronic Properties of α-RuCl3 in Proximity to Graphene," *Phys. Rev. Lett.*, 2019, doi: 10.1103/PhysRevLett.123.237201.

[144] E. Gerber, Y. Yao, T. A. Arias, and E. A. Kim, "Ab Initio Mismatched Interface Theory of Graphene on α-RuCl3: Doping and Magnetism," *Phys. Rev. Lett.*, 2020, doi: 10.1103/PhysRevLett.124.106804.

[145] K. W. Plumb *et al.*, "α- RuCl3: A spin-orbit assisted Mott insulator on a honeycomb lattice," *Phys. Rev. B - Condens. Matter Mater. Phys.*, vol. 90, no. 4, pp. 1–5, 2014, doi: 10.1103/PhysRevB.90.041112.

[146] S. Mashhadi *et al.*, "Spin-Split Band Hybridization in Graphene Proximitized with α-RuCl3 Nanosheets," *Nano Lett.*, vol. 19, no. 7, pp. 4659–4665, 2019, doi: 10.1021/acs.nanolett.9b01691.

[147] B. Zhou, J. Balgley, P. Lampen-Kelley, J. Q. Yan, D. G. Mandrus, and E. A. Henriksen, "Evidence for charge transfer and proximate magnetism in graphene- α-RuCl3 heterostructures," *Phys. Rev. B*, 2019, doi: 10.1103/PhysRevB.100.165426.

[148] T. Tynell *et al.*, "Rapid thermal annealing of Sb2Te3 thin films grown via atomic layer deposition," *Thin Solid Films*, 2020, doi: 10.1016/j.tsf.2020.137922.

[149] D. M. Dobkin and M. K. Zuraw, *Principles of Chemical Vapor Deposition*. 2003.

[150] A. K. Geim, "Nobel Lecture: Random walk to graphene," *Rev. Mod. Phys.*, 2011, doi: 10.1103/RevModPhys.83.851.

[151] S. J. Kang *et al.*, "Organic field effect transistors based on graphene and hexagonal boron nitride heterostructures," *Adv. Funct. Mater.*, 2014, doi: 10.1002/adfm.201400348.

[152] S. B. Kaemmar, "Introduction to Bruker's ScanAsyst and PeakForce Tapping AFM Technology," *Appl. note*, 2011.

[153] M. Hazle, "Practical Raman Spectroscopy D.J. Gardiner and P.R. Graves (Eds.), Springer Verlag, Berlin, 1989 (ISBN 3-540-50254-8). viii + 157 pp. Price DM 78.00.," *Anal. Chim. Acta*, 1990, doi: 10.1016/s0003-2670(00)82702-6.

[154] V. R. Manfrinato *et al.*, "Resolution limits of electron-beam lithography toward the atomic scale," *Nano Lett.*, 2013, doi: 10.1021/nl304715p.

[155] Z. R. Dai, Z. W. Pan, and Z. L. Wang, "Novel nanostructures of functional oxides synthesized by thermal evaporation," *Advanced Functional Materials*. 2003, doi: 10.1002/adfm.200390013.

[156] O. V. Lounasmaa and R. D. Parks, " Experimental Principles and Methods Below 1 K ," *Phys. Today*, 1975, doi: 10.1063/1.3069146.

[157] W. T. Hsu *et al.*, "Second harmonic generation from artificially stacked transition metal dichalcogenide twisted bilayers," *ACS Nano*, 2014, doi: 10.1021/nn500228r.

[158] E. J. H. Lee, K. Balasubramanian, R. T. Weitz, M. Burghard, and K. Kern, "Contact and edge effects in graphene devices," *Nat. Nanotechnol.*, 2008, doi: 10.1038/nnano.2008.172.

[159] J. Kerr, " XLIII. On rotation of the plane of polarization by reflection from the pole of a magnet ," *London, Edinburgh, Dublin Philos. Mag. J. Sci.*, 1877, doi: 10.1080/14786447708639245.

[160] Q. Wang *et al.*, "Room-Temperature Nanoseconds Spin Relaxation in WTe2 and MoTe2 Thin Films," *Adv. Sci.*, vol. 5, no. 6, pp. 1–7, 2018, doi: 10.1002/advs.201700912.

[161] W. Richter, H. Kohler, and C. R. Becker, "A Raman and Far-Infrared Investigation of Phonons in the Rhombohedral V2-VI3 Compounds," *Phys. Stat. Sol.*, 1977.

[162] S. Nakajima, "The crystal structure of Bi2Te3-xSex," *J. Phys. Chem. Solids*, 1963, doi: 10.1016/0022-3697(63)90207-5.

[163] M. L. H. Jones, Anthony C., "Chemical vapour deposition: precursors, processes and applications," *R. Soc. Chem.*, 2009, doi: 10.1109/NCIA.2013.6725337.

[164] M. M. Lucchese *et al.*, "Quantifying ion-induced defects and Raman relaxation length in graphene," *Carbon N. Y.*, 2010, doi: 10.1016/j.carbon.2009.12.057.

[165] L. Gao *et al.*, "Repeated growth and bubbling transfer of graphene with millimetre-size single-crystal grains using platinum," *Nat. Commun.*, 2012, doi: 10.1038/ncomms1702.

[166] L. M. Malard, M. A. Pimenta, G. Dresselhaus, and M. S. Dresselhaus, "Raman spectroscopy in graphene," *Physics Reports*. 2009, doi: 10.1016/j.physrep.2009.02.003.

[167] T. Park *et al.*, "Non-equilibrium fractal growth of MoS 2 for electrocatalytic hydrogen evolution," *CrystEngComm*, vol. 21, no. 3, pp. 478–486, 2019, doi: 10.1039/c8ce01952e.

[168] X. Fan *et al.*, "Controllable Growth and Formation Mechanisms of Dislocated WS2 Spirals," *Nano Lett.*, vol. 18, no. 6, pp. 3885–3892, 2018, doi: 10.1021/acs.nanolett.8b01210.

[169] R. Rao *et al.*, "Spectroscopic evaluation of charge-transfer doping and strain in graphene/ MoS2 heterostructures," *Phys. Rev. B*, vol. 99, no. 19, p. 195401, 2019, doi: 10.1103/PhysRevB.99.195401.

[170] K. M. F. Shahil, M. Z. Hossain, D. Teweldebrhan, and A. A. Balandin, "Crystal symmetry breaking in few-quintuple Bi2 Te3 films: Applications in nanometrology of topological insulators," *Appl. Phys. Lett.*, 2010, doi: 10.1063/1.3396190.

[171] W. Dang, H. Peng, H. Li, P. Wang, and Z. Liu, "Epitaxial heterostructures of ultrathin topological insulator nanoplate and graphene," *Nano Lett.*, vol. 10, no. 8, pp. 2870–2876, 2010, doi: 10.1021/nl100938e.

[172] A. Das *et al.*, "Monitoring dopants by Raman scattering in an electrochemically top-gated graphene transistor," *Nat. Nanotechnol.*, 2008, doi: 10.1038/nnano.2008.67.

[173] C. Casiraghi, S. Pisana, K. S. Novoselov, A. K. Geim, and A. C. Ferrari, "Raman fingerprint of charged impurities in graphene," *Appl. Phys. Lett.*, 2007, doi: 10.1063/1.2818692.

[174] S. Ryu *et al.*, "Atmospheric oxygen binding and hole doping in deformed graphene on a SiO2 substrate," *Nano Lett.*, vol. 10, no. 12, pp. 4944–4951, 2010, doi: 10.1021/nl1029607.

[175] C. H. Lui, L. Liu, K. F. Mak, G. W. Flynn, and T. F. Heinz, "Ultraflat graphene," *Nature*, 2009, doi: 10.1038/nature08569.

[176] N. Kumar *et al.*, "Second harmonic microscopy of monolayer MoS2," *Phys. Rev. B - Condens. Matter Mater. Phys.*, 2013, doi: 10.1103/PhysRevB.87.161403.

[177] K. S. Novoselov *et al.*, "Electric field in atomically thin carbon films," *Science (80-.).*, 2004, doi: 10.1126/science.1102896.

[178] K. Hatsuda *et al.*, "Evidence for a quantum spin Hall phase in graphene decorated with Bi 2 Te 3 nanoparticles," no. November, pp. 1–7, 2018.

[179] A. Pertsova and C. M. Canali, "Probing the wavefunction of the surface states in Bi2Se 3 topological insulator: A realistic tight-binding approach," *New J. Phys.*, 2014, doi: 10.1088/1367-2630/16/6/063022.

[180] D. Nandi *et al.*, "Signatures of long-range-correlated disorder in the magnetotransport of ultrathin topological insulators," *Phys. Rev. B*, 2018, doi: 10.1103/PhysRevB.98.214203.

[181] D. Niesner *et al.*, "Unoccupied topological states on bismuth chalcogenides," *Phys. Rev. B - Condens. Matter Mater. Phys.*, 2012, doi: 10.1103/PhysRevB.86.205403.

[182] Y. J. Yu, Y. Zhao, S. Ryu, L. E. Brus, K. S. Kim, and P. Kim, "Tuning the graphene work function by electric field effect," *Nano Lett.*, 2009, doi: 10.1021/nl901572a.

[183] H. Hirai, H. Tsuchiya, Y. Kamakura, N. Mori, and M. Ogawa, "Electron mobility calculation for graphene on substrates," *J. Appl. Phys.*, 2014, doi: 10.1063/1.4893650.

[184] N. Kim *et al.*, "Persistent topological surface state at the interface of Bi 2Se3 film grown on patterned graphene," *ACS Nano*, vol. 8, no. 2, pp. 1154–1160, 2014, doi: 10.1021/nn405503k.

[185] E. Rossi and S. Das Sarma, "Ground state of graphene in the presence of random charged impurities," *Phys. Rev. Lett.*, 2008, doi: 10.1103/PhysRevLett.101.166803.

[186] B. Zhou *et al.*, "Possible structural transformation and enhanced magnetic fluctuations in exfoliated α-RuCl3," *J. Phys. Chem. Solids*, 2019, doi: 10.1016/j.jpcs.2018.01.026.

[187] D. Weber, L. M. Schoop, V. Duppel, J. M. Lippmann, J. Nuss, and B. V. Lotsch, "Magnetic Properties of Restacked 2D Spin 1/2 honeycomb RuCl3 Nanosheets," *Nano Lett.*, vol. 16, no. 6, pp. 3578–3584, 2016, doi: 10.1021/acs.nanolett.6b00701.

[188] S. Mashhadi *et al.*, "Electrical Transport Signature of the Magnetic Fluctuation-Structure Relation in α-RuCl3 Nanoflakes," *Nano Lett.*, 2018, doi: 10.1021/acs.nanolett.8b00926.

[189] Y. Kim, P. Herlinger, T. Taniguchi, K. Watanabe, and J. H. Smet, "Reliable Postprocessing Improvement of van der Waals Heterostructures," *ACS Nano*, vol. 13, no. 12, pp. 14182–14190, 2019, doi: 10.1021/acsnano.9b06992.

[190] S. Masubuchi *et al.*, "Autonomous robotic searching and assembly of two-dimensional crystals to build van der Waals superlattices," *Nat. Commun.*, vol. 9, no. 1, pp. 4–6, 2018, doi: 10.1038/s41467-018-03723-w.

[191] S. Bae *et al.*, "Roll-to-roll production of 30-inch graphene films for transparent electrodes," *Nat. Nanotechnol.*, 2010, doi: 10.1038/nnano.2010.132.

[192] P. S. Steif, M. C. Palastro, and Y. Rabin, "The effect of temperature gradients on stress development during cryopreservation via vitrification," *Cell Preserv. Technol.*, 2007, doi: 10.1089/cpt.2007.9994.

[193] A. Mccollam, S. R. Julian, P. M. C. Rourke, D. Aoki, and J. Flouquet, "Anomalous de Haas – van Alphen Oscillations in CeCoIn 5," vol. 186401, no. May, pp. 6–9, 2005, doi: 10.1103/PhysRevLett.94.186401.

[194] F. Wu *et al.*, "Anomalous quantum oscillations and evidence for a non-trivial Berry phase in SmSb," *npj Quantum Mater.*, vol. 4, no. 1, pp. 1–6, 2019, doi: 10.1038/s41535-019-0161-4.

[195] B. S. Tan *et al.*, "Unconventional Fermi surface in an insulating state," *Science (80-.).*, vol. 349, no. 6245, pp. 287–290, 2015, doi: 10.1126/science.aaa7974.

[196] A. Wasserman and M. Springford, "The influence of many-body interactions on the de Haas-van Alphen effect," *Adv. Phys.*, vol. 45, no. 6, pp. 471–503, 1996, doi: 10.1080/00018739600101547.

[197] Y. Kubota, H. Tanaka, T. Ono, Y. Narumi, and K. Kindo, "Successive magnetic phase transitions in α-RuCl3: XY-like frustrated magnet on the honeycomb lattice," *Phys. Rev. B - Condens. Matter Mater. Phys.*, vol. 91, no. 9, pp. 1–9, 2015, doi: 10.1103/PhysRevB.91.094422.

[198] R. D. Johnson *et al.*, "Monoclinic crystal structure of α-RuCl3 and the zigzag antiferromagnetic ground state," *Phys. Rev. B - Condens. Matter Mater. Phys.*, 2015, doi: 10.1103/PhysRevB.92.235119.

[199] J. Knolle and N. R. Cooper, "Quantum Oscillations without a Fermi Surface and the Anomalous de Haas-van Alphen Effect," *Phys. Rev. Lett.*, 2015, doi: 10.1103/PhysRevLett.115.146401.

[200] Z. Dai *et al.*, "Crystal structure reconstruction in the surface monolayer of the quantum spin liquid candidate α-RuCl3," *2D Mater.*, 2020, doi: 10.1088/2053-1583/ab7e0e.

[201] D. J. O'Hara *et al.*, "Room Temperature Intrinsic Ferromagnetism in Epitaxial Manganese Selenide Films in the Monolayer Limit," *Nano Lett.*, 2018, doi: 10.1021/acs.nanolett.8b00683.

[202] S. Roche *et al.*, "Graphene spintronics: The European Flagship perspective," *2D Materials*. 2015, doi: 10.1088/2053-1583/2/3/030202.

[203] A. Avsar *et al.*, "Spin-orbit proximity effect in graphene," *Nat. Commun.*, 2014, doi: 10.1038/ncomms5875.

[204] M. Carrega, I. J. Vera-Marun, and A. Principi, "Tunneling spectroscopy as a probe of fractionalization in 2D magnetic heterostructures," pp. 1–26, 2020, [Online]. Available: http://arxiv.org/abs/2004.13036.

Curriculum Vitae

CONTACT INFORMATION   KATHARINA POLYUDOV
K.POLYUDOV@WEB.DE

PERSONAL INFORMATION

DATE OF BIRTH: 25.04.1991
NATIONALITY: GERMAN

EDUCATION

10/2014 - 09/2016
NANO-SCIENCE MASTER, EBERHARD KARLS UNIVERSITÄT TÜBINGEN

09/2011 - 10/2014
NANO-SCIENCE BACHELOR, EBERHARD KARLS UNIVERSITÄT TÜBINGEN

09/2008 – 07/2011
OTTO – HAHN GYMNASIUM TUTTLINGEN

PROFFESSIONAL EXPERIENCE

10/2016 – TODAY
NANOSCALE SCIENCE DEPARTMENT, MAX-PLANCK-INSTITUTE FOR SOLID STATE RESEARCH, STUTTGART, GERMANY DOCTORAL SCHOOL IN PHYSICS AT EPFL, LAUSANNE, SWITZERLAND

PUBLICATIONS

VAKLINOVA, K., POLYUDOV, K., BURGHARD, M., & KERN, K. (2018). SPIN FILTER EFFECT OF HBN/CO DETECTOR ELECTRODES IN A 3D TOPOLOGICAL INSULATOR SPIN VALVE. *JOURNAL OF PHYSICS: CONDENSED MATTER*, *30*(10), 105302.

MANGEL, S., SKRIPNIK, M., POLYUDOV, K., DETTE, C., WOLLANDT, T., PUNKE, P., & KERN, K. (2020). ELECTRIC-FIELD CONTROL OF SINGLE-MOLECULE TAUTOMERIZATION. *PHYSICAL CHEMISTRY CHEMICAL PHYSICS*, *22*(11), 6370-6375.

SKILLS

MATLAB, ORIGIN, PYTHON, LABVIEW, MATHEMATIKA, CORELDRAW, MICROSOFT OFFICE

ATOMIC FORCE MICROSCOPY, SCANNING TUNNELING MICROSCOPY, ELECTRON BEAM LITHOGRAPHY, PHYSICAL VAPOR DEPOSITION, EXTENSIVE CLEAN ROOM EXPERIENCE

GERMAN (C2), ENGLISH (C2), RUSSIAN (C2), FRENCH (B1)